Two Schiff Base Compounds Derived from 5-Aminoisophthalic Acid: Chemsensors Properties for Sensing of Metal Ions and Nitroaromatic Compounds

5-Aminoisoftalik Asitten Türetilen İki Schiff Bazı Bileşiği: Metal İyonları ve Nitroaromatic Bileşiklerin Saptanması İçin Sensör Özellikleri

Ayşegül Köse[1], **Mehmet Tümer[2]**

[1]Department of Property Protection and Safety, Elbistan Vocational School, Kahramanmaras Istiklal University, Kahramanmaras, Turkey.
[2]Department of Chemistry, Faculty of Art and Sciences, Kahramanmaras Sutcu Imam University, 46040, Kahramanmaras, Turkey.

ABSTRACT

In this work, two Schiff base ligands Z_{2a} and Z_{2b} derived from 5-aminoisophthalic acid were synthesized and their structures were characterized by FTIR, $^1H(^{13}C)$ NMR and mass spectrometries. The compounds were investigated for their chemosensor properties towards metal ions [Na^+, K^+, Al^{3+}, Cr^{3+}, Mn^{2+}, Fe^{3+}, Co^{2+}, Ni^{2+}, Cu^{2+}, Zn^2+, Cd^{2+}, Hg^{2+} and Pb^{2+}] were examined using colorimetric and spectrophotometric methods (UV-Vis absorption and florescence spectroscopy). Both compounds showed similar sensing properties towards metal ions and they have shown selective sensory properties for Fe^{+3} and Hg^{+2} ions. Moreover, the compounds were examined for their fluorimetric sensing abilities for nitroaromatic compounds [4-nitrofenol (NP), nitrobenzene (NB), 2,4-dinitrofenol (DNP), 1,3,5-trinitrophenol (TNP)]. Both compounds showed higher sensitivities for DNP and TNP than NP and NB. Compound Z_{2b} showed the highest sensitivity for DNP with K_{sv} value of 2.4×10^4 M^{-1}. Limit of detections for nitroaromatic compounds were calculated and both compounds showed LOD values in micromolar levels. Compound Z_{2b} has shown the lowest LOD value for DNP with 2.77 µM.

Key Words

Schiff base, 5-aminoisophthalic acid, chemosensor, fluorimetric sensor, metal ions, nitroaromatic compounds.

Ö Z

Bu çalışmada, 5-aminoizoftalik asitten türetilen iki Schiff bazı ligandı Z_{2a} ve Z_{2b} sentezlenmiş ve yapıları FTIR, $^1H(^{13}C)$ NMR ve kütle spektrometrileri ile karakterize edilmiştir. Bileşiklerin metal iyonlarına [Na^+, K^+, Al^{3+}, Cr^{3+}, Mn^{2+}, Fe^{3+}, Co^{2+}, Ni^{2+}, Cu^{2+}, Zn^{2+}, Cd^{2+}, Hg^{2+} ve Pb^{2+}] karşı kemosensör özellikleri kolorimetrik ve spektrofotometrik yöntemler (UV-Vis absorpsiyon ve floresans spektroskopisi) kullanılarak incelenmiştir. Her iki bileşikte metal iyonlarına karşı benzer algılama özellikleri göstermiş ve Fe^{+3} ve Hg^{+2} iyonları için seçici sensör özellikler göstermiştir. Ayrıca, bileşiklerin nitroaromatik bileşikler [4-nitrofenol (NP), nitrobenzen (NB), 2,4-dinitrofenol (DNP), 1,3,5-trinitrofenol (TNP)] için florimetrik saptama yetenekleri incelenmiştir. Her iki bileşikte DNP ve TNP için NP ve NB'den daha yüksek duyarlılık göstermiştir. Z_{2b} bileşiği, 2.4×10^4 M^{-1} K_{sv} değeriyle DNP için en yüksek hassasiyeti göstermiştir. Nitroaromatik bileşikler için tespit limiti hesaplandı ve her iki bileşik de mikromolar seviyelerde LOD değerleri göstermiştir. Z_{2b} bileşiği, 2.77 µM ile DNP için en düşük LOD değerini göstermiştir.

Anahtar Kelimeler

Schiff bazı, 5-aminoizoftalik asit, kemosensör, florimetrik sensör, metal iyonları, nitroaromatik bileşikler.

INTRODUCTION

Schiff base compounds are nitrogen analogues of aldehydes or ketones and are obtained by the condensation reaction of aldehydes or ketones with primary amines [1]. Schiff base compounds are widely used in pigments, catalysts, intermediates in organic synthesis, polymer stabilizers, dyes, biological activity, molecular memory storage, imaging systems, pharmaceutical and agro-industrial chemistry [2]. Since Schiff base compounds have the ability to form stable complexes with metal ions, they are used in molecular recognition and in the development of fluorescence sensors [3]. Schiff base derivatives with nitrogen-oxygen-rich coordination as a receptor site provide a powerful platform for detectable color change and fluorescence detection. In real samples, sensor structures containing Schiff base and capable of detecting metal ions by various mechanisms attract attention [4]. Schiff base compounds exhibit characteristic photophysical (absorption and emission) properties, have various binding sites, and are easy to synthesize, and these compounds are preferred in designing chemosensors as in many areas [5]. For example, a simply prepared quinoline hydroxyl derivative was used for selectively fluorescent "Off-On" recognition of Ag+ in aqueous medium [6].

Nitroaromatic compounds such as 2,4,6-trinitrotoluene (TNT) and 2,4-dinitrotoluene (DNT) are primary military explosives and also major components of unexploded landmines around the world [7]. The highest-energy explosives are nitro-substituted (nitrated) compounds that have the highest priority for detection and are therefore the focus of current investigation. The widespread use of military explosives also raises concerns about environmental pollution where they are produced and stored [8]. Major public health threat such as anemia, carcinogenicity, abnormal liver function, cataract development and skin irritation can occur to both animals and humans through short-term or long-term exposure to nitroaromatic explosives [9]. Detection of explosives in aqueous solution is of great importance due to the spread of terrorist activities from land to sea, the protection of underwater mines and the characterization of soil groundwater pollution [10]. Commercially available methods for detecting explosives are trained dogs, metal detectors, and ion mobility spectrometry (IMS) [11]. Therefore, there is an urgent need for innovative detection strategies that are not only cost-effective and convenient, but also highly sensitive and selective [12]. Explosive detection of optical sensors including absorbance (colorimetric) and fluorescence spectroscopy has begun to be used [13]. In addition, the source and detector of the fluorescent method can be easily incorporated into a hand-held device for field detection of explosives. Therefore, the fluorescence-based method has an important field of use in the rapid, sensitive and selective detection of explosives. Polyaromatic conjugated structures are widely used as fluorescent-based explosive sensors [14–16].

In this work, we prepared two Schiff base ligands derived from 5-aminoisophthalic acid (Scheme 1) and characterized their structures by spectroscopic and analytical methods. Sensing ability of the compounds toward metal ions and nitroaromatic compounds were investigated.
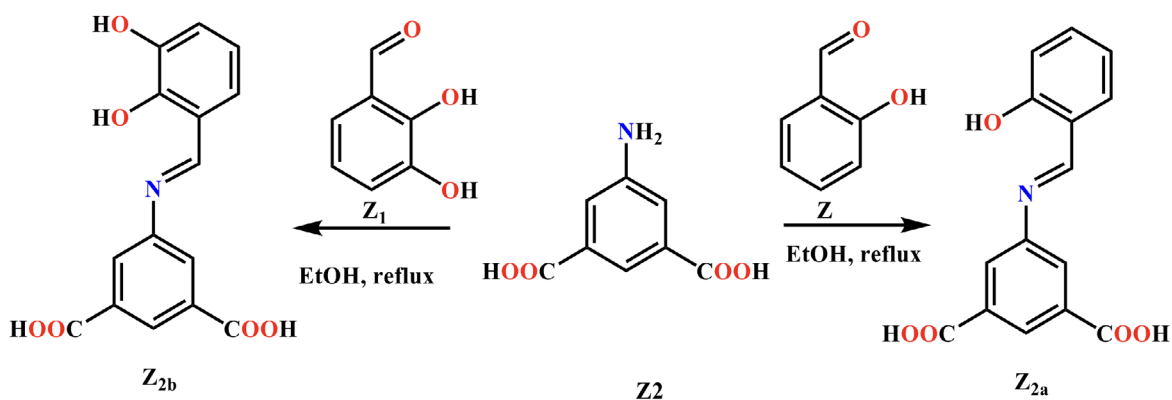
Scheme 1. Synthesis of Z_{2a} and Z_{2b}.

MATERIALS and METHODS

Materials and Instrumentation

All reagents and solvents were provided from commercial sources (Aldrich or Merck) and were used as received without further purification. A Perkin-Elmer FT-IR spectrometer (Spectrum 400) equipped with an ATR was used to record infrared spectra. ^{1}H(^{13}C) NMR spectra were obtained in d_6-DMSO solvent on a Bruker 400 MHz equipment and TMS was utilized as an internal standard. The Hitachi U3900H Spectrophotometer was used to measure UV-Vis absorption spectra.

Synthesis of Z_{2a} and Z_{2b}

5-aminoisophthalic acid (0.905 g, 5 mmol) was dissolved in ethanol (30 mL). To this solution, salicylaldehyde (0.610 g, 5 mmol) for Z_{2a} or 2,3-dihydroxybenzaldehyde (0.690 g, 5 mmol) for Z_{2b} dissolved in ethanol (20 mL) was added. The solution colours changed to orange with the addition of aldehyde. The reaction mixtures were refluxed for 24 hours. The consumption of the aldehydes in the reactions are followed by TLC [17]. After completion of reactions, the mixtures are cooled to the room temperature. The orange-coloured precipitates were filtered and dried in air.

Z_{2a}: Molecular Formula: $C_{15}H_{11}NO_5$. Molecular weight: 285.26 g/mol. Yield: 86%. Colour: Orange. m.p.: >300 °C (decomposed). FTIR (ATR, cm^{-1}): 3198, 3070, 1721, 1695, 1627, 1595, 1572, 1499, 1447, 1405, 1374, 1276, 1192, 1153, 1131, 970, 896, 788, 749, 726, 679, 662, 603, 568, 503. Elemental analysis found (calculated for $C_{15}H_{11}NO_5$) %: C, 62.96 (63.16); H, 3.72 (3.89); N, 4.78 (4.91). ^{1}H NMR (ppm, DMSO-d_6): δ 12.65 (1H, b, -COOH), 10.73 (1H, b, -OH), 8.39 (1H, s, CH=N$_{imine}$), 8.13 (2H, s, CH$_{aromatic}$), 7.76 (1H, d, CH$_{aromatic}$), 7.54 (1H, d, CH$_{aromatic}$), 7.50-7.44(1H, t, CH$_{aromatic}$), 7.37(1H, s, CH$_{aromatic}$), 6.99-6.94 (1H, t, CH$_{aromatic}$). ^{13}C NMR (ppm, DMSO-d_6): δ 192.41 ($\underline{C}$OOH), 167.53 ($\underline{C}$=N$_{imine}$), 166.84, 160.60, 149.23, 136.07, 131.92, 129.73, 126.34, 123.27, 119.77, 117.68. ESI-Q-TOF (m/z): 286.0748 [M + H]$^+$, 318.1734 [M + CH$_3$OH + Na]$^+$.

Z_{2b}: Molecular Formula: $C_{15}H_{11}NO_6$. Molecular weight: 301.25 g/mol. Yield: %83. Colour: Orange. m.p.: 256-260 °C (decomposed). FTIR (ATR, cm^{-1}): 3190, 2887, 1723, 1695, 1644, 1616, 1548, 1462, 1361, 1283, 1198, 1220, 1027, 969, 911, 855, 775, 724, 675, 609, 500. Elemental analysis found (calculated for $C_{15}H_{11}NO_6 \cdot C_2H_5OH$) %: C, 58.65 (58.79); H, 4.83 (4.93); N, 3.95 (4.03). ^{1}H NMR (ppm, DMSO-d_6): δ 12.76 (1H, b, -COOH), 10.21(1H, b, -OH), 9.07(1H, s, CH$_{aromatic}$), 8.39(1H, s, CH=N$_{imine}$), 8.12(2H, s, CH$_{aromatic}$), 7.65(1H, d, CH$_{aromatic}$), 7.20(1H, d, CH$_{aromatic}$), 6.84(1H, t, CH$_{aromatic}$), 3.47-4.43(2H, q, -CH$_{2ethanol}$), 0.99(3H, t, -CH$_{3ethanol}$). ^{13}C NMR (ppm, DMSO-d_6): δ 193.19 ($\underline{C}$OOH), 167.68 ($\underline{C}$=N$_{imine}$), 166.66 ($\underline{C}$-O), 166.35 ($\underline{C}$-O), 149.56, 146.48, 133.28, 131.81, 127.95, 126.31, 123.51, 117.38, 56.13 (-$\underline{C}$H$_2$-O$_{ethanol}$), 19.08 ($\underline{C}$H$_3$-$_{ethanol}$). ESI-Q-TOF (m/z): 353.2715 [M + CH$_3$OH + H$_2$O + H]$^+$, 381.3046 [M + 2CH$_3$OH + H$_2$O]$^+$.

RESULTS and DISCUSSION

In the context of this study, we have prepared two Schiff base ligands (Z_{2a} and Z_{2b}) by condensation reaction of 5-aminoisophthalic acid with salicylaldehyde (Z_{2a}) or 2,3-dihydroxybenzaldehyde (Z_{2b}) (Scheme 1). The compounds were obtained in high yield and purity [18]. The structural characterizations of the compounds were done by FT-IR, ^{1}H/^{13}C NMR and mass spectral analysis. The compounds were tested for their sensing abilities towards metal ions and nitroaromatic compounds [19].

FTIR spectra of Schiff base compounds (Z_{2a} and Z_{2b}) were taken in order to address the characteristic bond stretching's in the structures. FTIR spectral data were given in the experimental section and spectra of the compounds were provided in the supplementary documents (Figs. S1 and S2). The characteristic imine bond (C=N) stretching's were observed at 1627 and 1616 cm^{-1}, respectively [20–23]. The sharp peaks observed in 1721 and 1695 cm^{-1} for Z_{2a}, 1723 and 1695 cm^{-1} for Z_{2b} are assigned to the carboxy group stretching's n(COO) [24]. Observing carboxyl group stretching's n(C=O) peaks as two separate peaks was interpreted as the co-existence of the solid form phenol-imine tautomeric form and the keto-amin/zwitter ion form for these compounds. Peaks observed in FTIR spectrums of Z_{2a}-Z_{2b} compounds are in harmony with similar compound spectrums found in the literature [24].

In order to characterize the synthesized Schiff base compounds, their ^{1}H(^{13}C) NMR spectra were taken in d_6-DMSO. The ^{1}H(^{13}C) NMR spectra of the compounds are given in Figures 1&2.

In the ^{1}H NMR spectra of Z_{2a} and Z_{2b}, the carboxyl group protons (-COOH) were observed as peaks at 12.65 and 12.76 ppm, respectively [24–26]. The phenolic group protons were observed at 10.73 and 10.21 ppm respectively [21, 27]. A singlet peak at 8.39 ppm for both
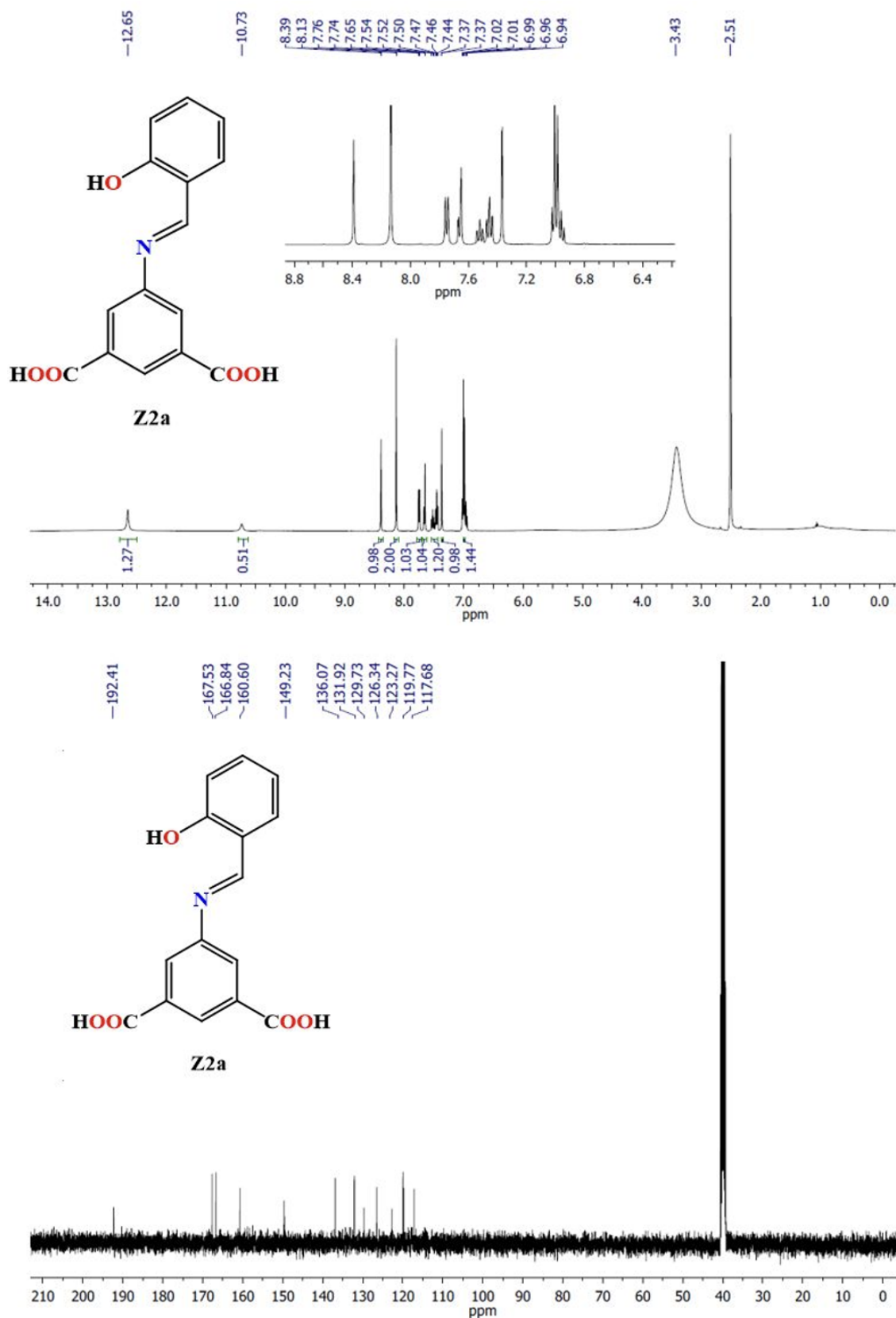
Figure 1. $^1H(^{13}C)$ NMR spectra of Z_{2a}.
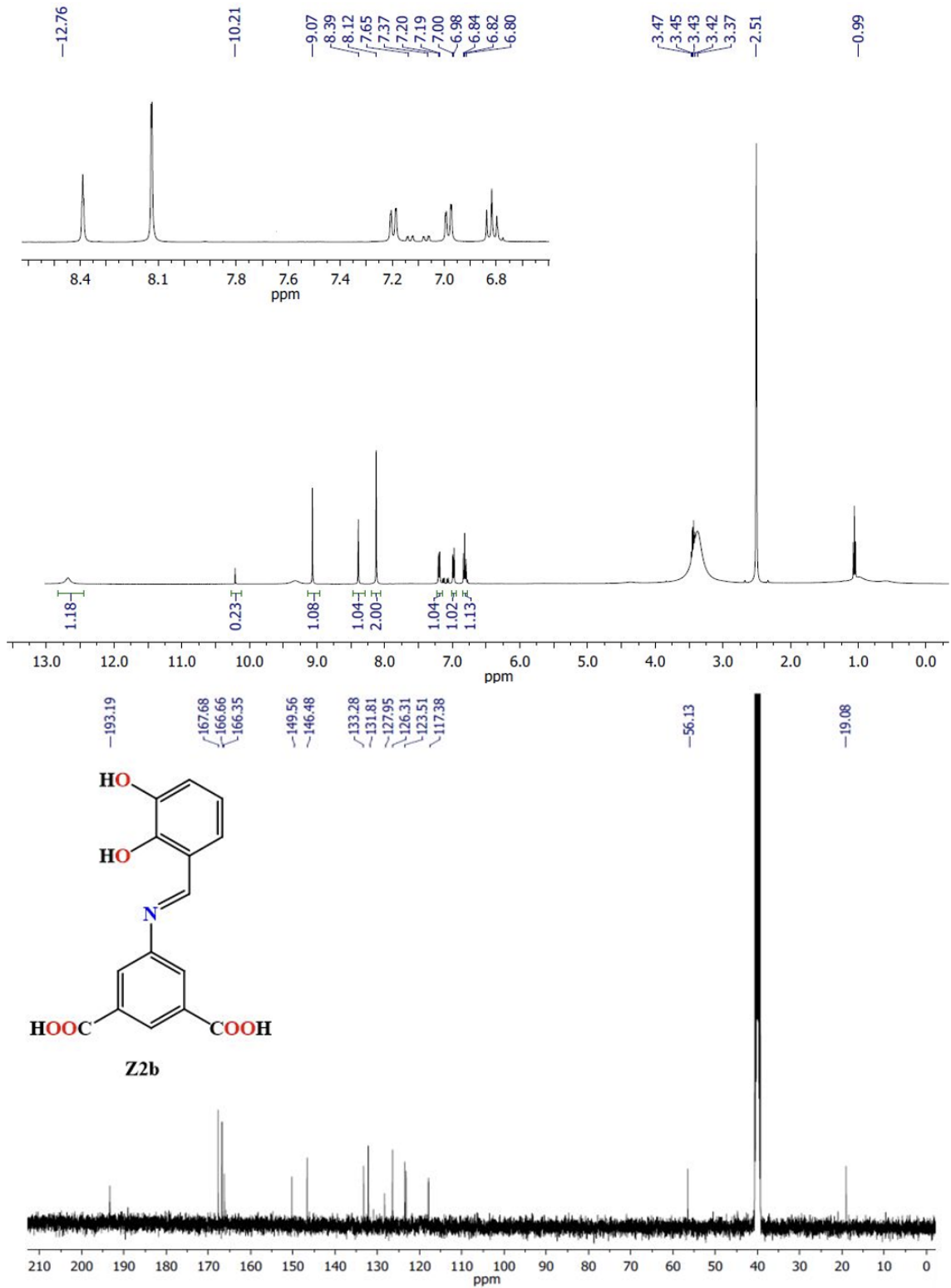
Figure 2. ^{1}H(^{13}C) NMR spectra of Z$_{2b}$.

ligands were assigned to the imine group protons. Aromatic proton signals in the range of 8.13-6.84 ppm were observed in the spectrums of both compounds. In the spectrum of Z_{2b}, two multiplet peaks at 4.43 and 0.99 ppm are due to the proton signals of ethanol solvent and integration values suggest that there is one ethanol solvent per molecule in the compound sample. The integration values for proton assignments were in good agreement with their proposed structure.

When the ^{13}C NMR spectrums of the compounds were examined, carbon atomic signals observed at 192.41 (Z_{2a}) and 193.19 (Z_{2b}) ppm were caused by the carboxyl (-COOH) group [24]. The peaks at 167.53 for Z_{2a} and 167.68 for Z_{2b} ppm are attributed to the bond of imine group carbon atom (C=N) [28, 29]. In the spectra of the compounds, aromatic carbon atom signals were observed in the range of 166.84-117.38 ppm. It has been observed that the compounds are compatible with peak numbers structures observed in the ^{13}C NMR spectra. The two signals observed at 56.13 and 19.08 ppm in the ^{13}C NMR spectrum of Z_{2b} are carbon atom signals from the ethanol solvent found in the sample.

The structure of the compounds was further characterized by ESI-Q-TOF mass spectral analysis and molecular ion peaks were observed for both compounds. ESI-Q-TOF mass spectra of the compounds were given in Figure 3. In the spectrum of Z_{2a}, peaks at m/z 286.0748 and 318.1734 were assigned to the molecular ions
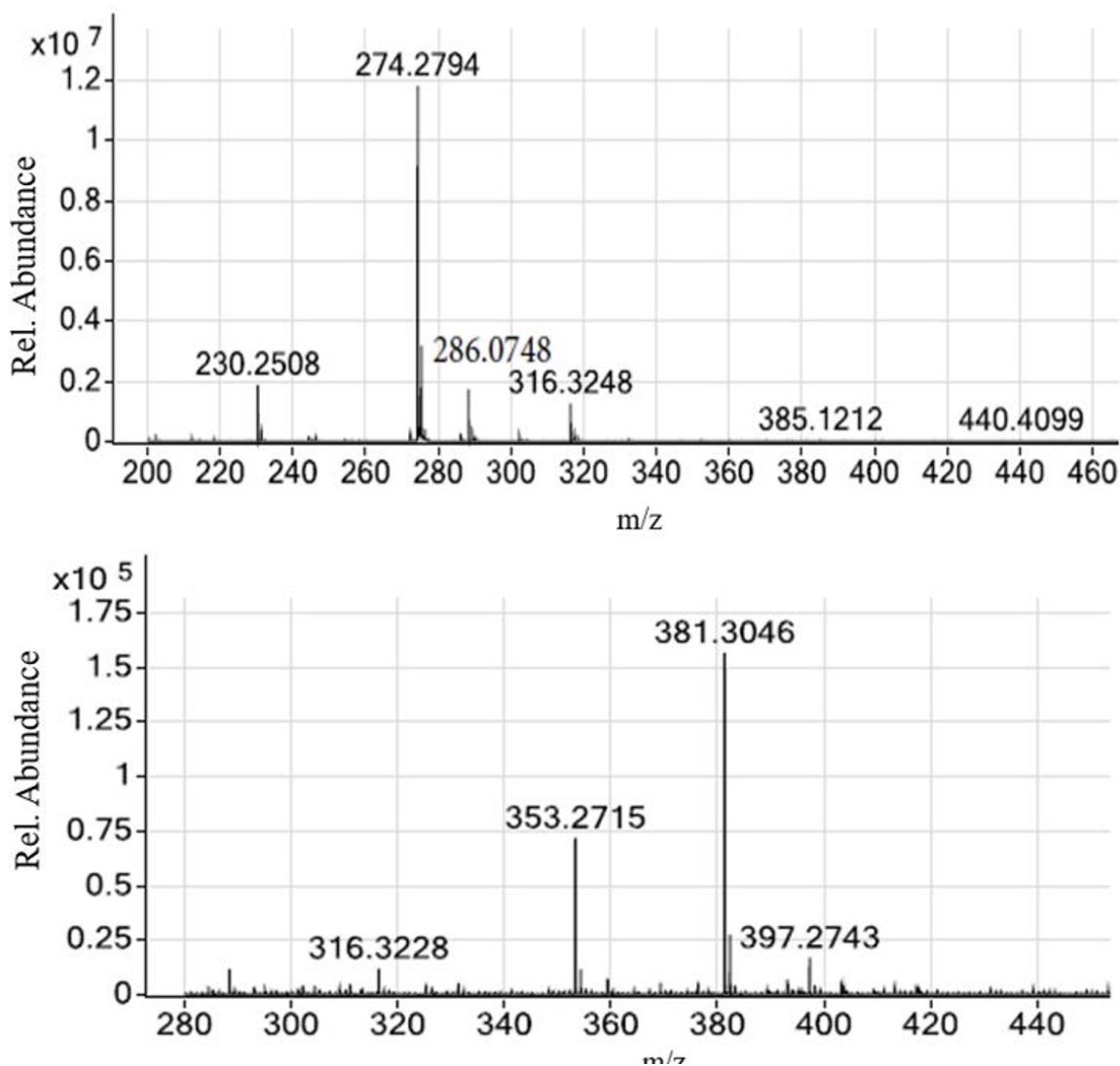
Figure 3. ESI-Q-TOF spectra of Z_{2a} (top) and Z_{2b} (bottom).
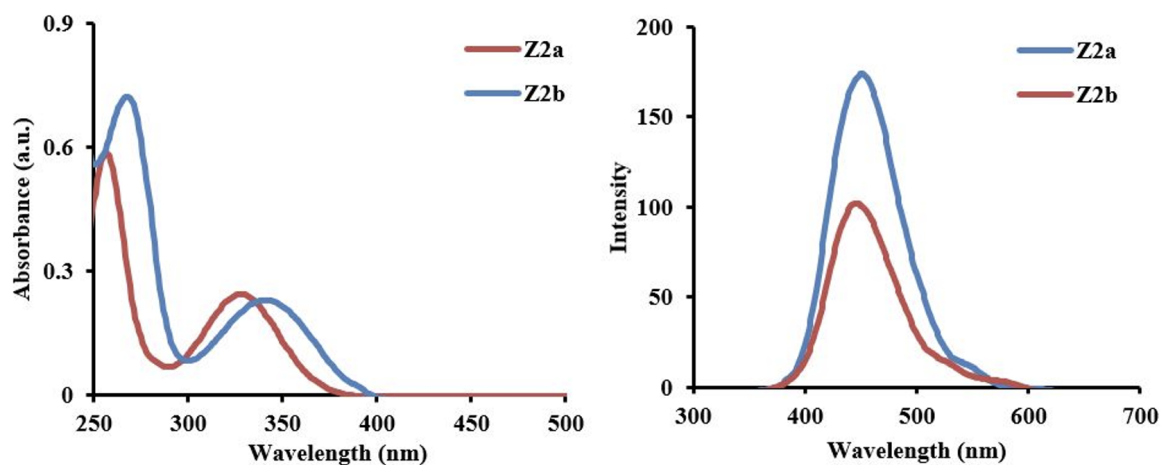
Figure 4. UV-Vis absorption (up) and emission spectra (down) of Z_{2a} and Z_{2b} in DMSO (10^{-5} M).

[M+H]$^+$ and [M+Na]$^+$, respectively. In the spectrum of Z_{2b}, two peaks at m/z 353.2715 and 381.3046 were assigned to the positively charged molecular ions species [M+CH$_3$OH, H]$^+$ and [M+2CH$_3$OH, H]$^+$, respectively.

UV-Vis absorption and photoluminescence properties of the Schiff base were investigated compounds in DMSO (10^{-5} M). UV-Vis absorption and photoluminescence spectra of Z_{2a} are shown in Figure 4. The spectra of Z_{2b} are provided in the supplementary documents. In the UV-Vis absorption spectra of the compounds Z_{2a} and Z_{2b}, there are two absorption bands in the range of 250-380 nm [26, 28]. The first band was observed at 250-300 nm range and this absorption band was assigned to the π-π* electronic transitions of π-electrons in the structures. The second absorption band was seen at 300-380 nm with lower absorption values. This absorption band can be attributed to the n-π* electronic transitions. The compounds are also emissive when excited in the UV region. Both compounds gave emission maximums in the blue region (400-500 nm) when they were excited in the range of 250-274 nm. Although emission wavelengths are similar for both compounds, the emission intensity of Z_{2a} are considerably higher than that of Z_{2b}. This may be due to the second hydroxyl group in Z_{2b} which may cause energy transfer in the excited state.

Sensor properties towards metal ions

The chemosensory properties of Z_{2a} and Z_{2b} against metal cations were investigated colorimetric and spectrophotometric methods. Color changes of ligands in the presence of metal ions (1:1 ratio) were investigated under daylight, 254 (short wavelength) and 365 nm (long wavelength) light.

Color changes of the DMSO solution (10^{-5} M) of the compounds Z_{2a} and Z_{2b} in the presence of various metal ions are given in Figure 5. DMSO solutions (10^{-5} M) of both the Z_{2a} and Z_{2b} are yellow in under daylight. With the addition of Fe^{3+}, the color of both ligands has turned to yellow-brown. The addition of Hg^{2+} turns Z_{2a}'s solution color slightly yellow, while the solution color of Z_{2b} is noticeably brown. No noticeable change in the solution colors of both ligands was observed in the presence of other metal ions. Under short wavelength light (254 nm), the Z_{2a} and Z_{2b} compounds showed blue fluorescence. While there was a slight dampening of blue fluorescence in the presence of Fe^{+3} and Hg^{+2} ions, no color change was observed in the presence of other metal ions. Under long wavelength light (365 nm), both ligands showed blue-turquoise fluorescence. Na$^+$, K$^+$, Al^{3+}, Cr^{3+}, Mn^{2+}, Co^{2+}, Ni^{2+}, Cu^{2+}, Zn^{2+}, Cd^{+2} and Pb^{2+} ions were observed with turquoise fluorescence and no noticeable color changes were observed. In the presence of Fe^{3+} and Hg^{2+} ions, quenching of fluorescence characteristics of both compounds was detected. Fluorescence quenching in the presence of Fe^{3+} and Hg^{2+} ions was also observed in emission spectra.

When the UV-Vis spectra of receptor compounds were examined in the presence of metal ions, no significant change was observed in the wavelengths of the absorption bands of the receptor compounds. In the presence of Fe^{3+} and Hg^{2+} ions, a significant increase in the absorbance values of the absorption bands of the ligand was observed. The emission spectral changes of Z_{2a} and Z_{2b} solutions in the range of 400-550 nm (excited at 256 nm for Z_{2a} and 269 nm for Z_{2b}) with the addition of metal ions were investigated. In the presence of all metal ions, the emission intensities of
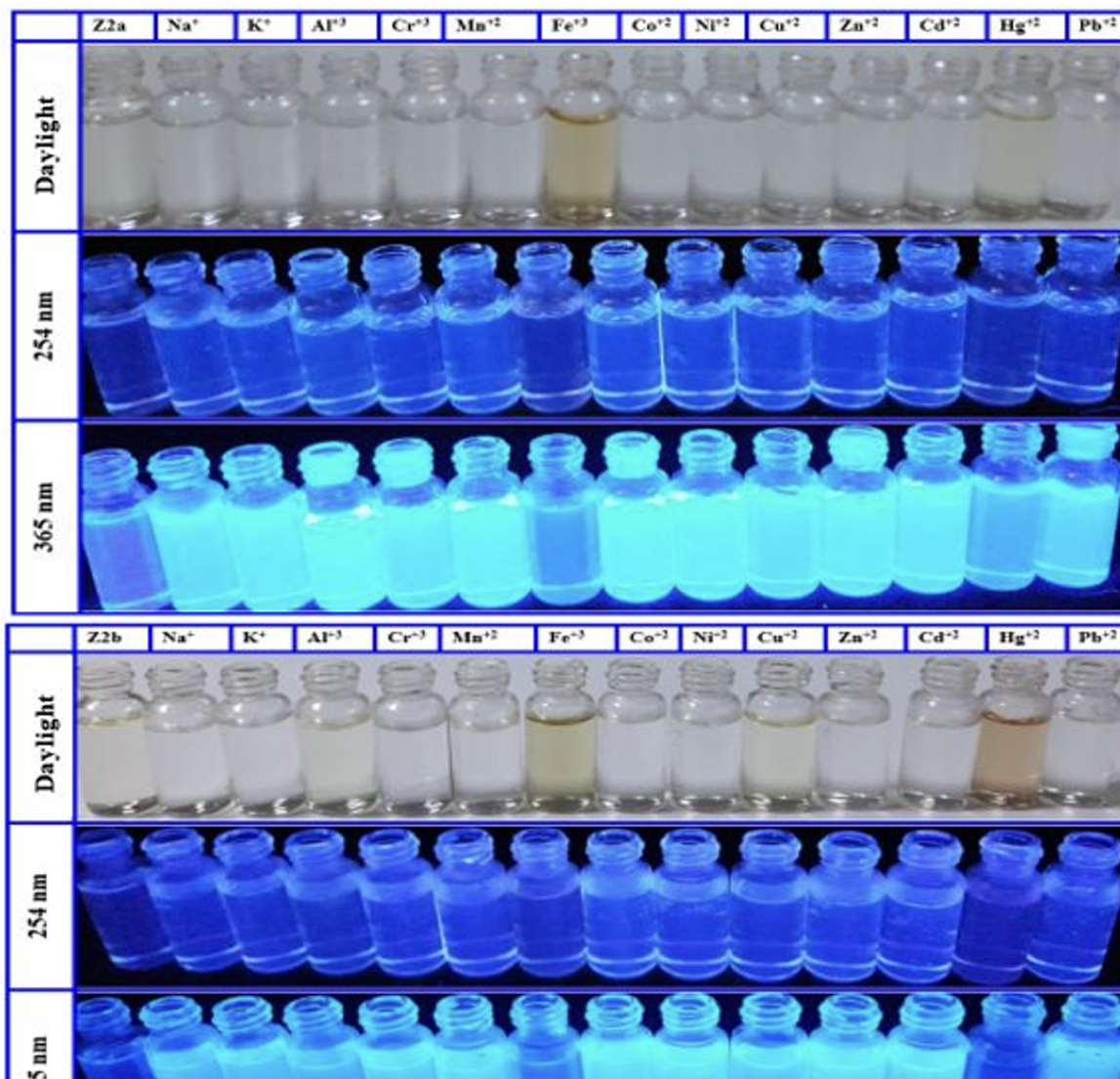
Figure 5. Color changes of Z_{2a} and Z_{2b} in the presence of metal ions under day light and UV-lamp (254 and 365 nm).

Z_{2a} and Z_{2b} decreased. However, in the presence of Fe^{3+} and Hg^{2+} ions, the emission of Z_{2b} is almost turned off. Z_{2b} compounds showed colorimetric and fluorimetric sensor properties against Fe^{3+} and Hg^{2+} ions in solution environment.

Fluorimetric sensing of nitro-aromatic compounds

Fluorescent quenching-based fluorimetric sensing are one of the selective and sensitive methods that have been frequently studied in recent years for the detection of nitro-aromatic explosives [30]. The quenching effect occurs in the emission band mainly due to the interaction of the fluorescence sensor with the nitroaromatic compounds [31]. Usually hydrogen bonding and π-π interactions occur between the fluorimetric sensor and the analyte. Monomers, polymers and metal-organic frameworks with highly conjugated π-electrons are often used for the detection of nitroaromatic compounds. There are many reported fluorescence quenching-based fluorimetric sensors for the detection of nitroaromatic compounds in the literature [31]. However, they have several drawbacks such as high cost, multi-step synthesis, reusability, lack of selectivity, and low sensitivity. The fluorimetric sensing properties of the Schiff base-based compounds that were synthesized within the scope of the work were investigated by fluorescence spectroscopy in the detection of nitroaromatic compounds. DMSO solutions of nitroaromatic compounds were added to the DMSO solution of the compounds (keeping the ligand concentration constant). The emission spectra of the obtained mixtures were taken
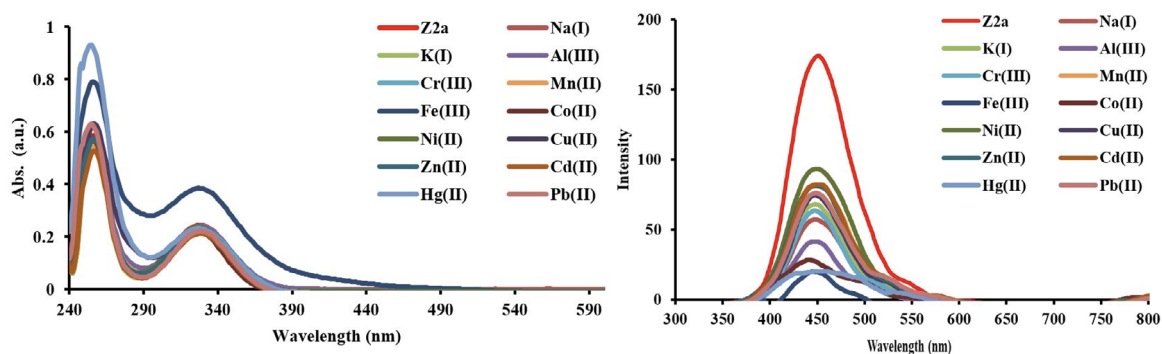
Figure 6. Absorbance and emission spectra changes of Z_{2a} in the presence of metal ions.

Table 1. Figure-of-merit (FOM) calculation of the sensor at different glycerol concentrations (FWHM represents full width at half maximum of the curves).

	K_{SV} M^{-1} (R^2)			
Compound	NB	NP	DNP	TNP
Z_{2a}	8.30x10^3(0.9897)	1.80x10^3(0.9900)	1.84x10^4(0.9906)	1.66x10^4 (0.9835)
Z_{2b}	3.09x10^3(0.9868)	3.40x10^3(0.9928)	2.4x10^4(0.9892)	1.93x10^4 (0.9970)
	Limit of detections (LOD, µM)			
	NB	NP	DNP	TNP
Z_{2a}	16.89	66.42	10.16	15.75
Z_{2b}	3.84	25.72	2.77	7.25

at the excitation wavelength of the fluorescent compound, and fluorometric titrations in the presence of incremental addition of nitroaromatic compounds were performed. In this study, nitrobenzene (NB), 4-nitrophenol (NP), 2,4-dinitrophenol (DNP) and 1,3,5-trinitrophenol (TNP) available in our laboratory were selected as nitroaromatic compounds. The emission band of the ligands decreased with gradual addition of nitroaromatic compounds. The nitroaromatic compounds caused a quenching effect in the emission spectra. It was observed that this decrease was linear for all nitroaromatic compounds.

In order to examine the quenching efficiency of the compounds for sensitivities towards nitroaromatic compounds, Stern-Volmer plots (I_0/I vs [A]) were drawn and quenching constants (K_{sv}) were obtained. The obtained K_{sv} values are given in Table 1.

When the obtained K_{sv} values were examined, it can be seen that both compounds showed higher sensitivities to DNP and TNP than the other nitroaromatics. Compound Z_{2b} showed better sensitivity towards DNP

and TNP than compound Z_{2a}. Emission spectral change, Stern-Volmer plot (I_0/I vs [A]) and emission quenching percentages of compound Z_{2b} in the presence of 5-100 mM TNP are given in Figure 7. As the TNP concentration increased, there was a linear decrease in the emission intensity of compound Z_{2b}. Emission intensity at 435 nm decreased by 10% in the presence of 5 µM TNP. Addition of 100 µM TNP, the emission intensity decreased by 70%. Compound Z_{2b} exhibit the highest sensitivity for DNP amongst the studied nitroaromatic compounds. The higher sensitivity of the compounds towards DNP can be explained better energy transfer in the excited state between the florescent receptor compounds (Z_{2a} and Z_{2b}) and DNP. Based on the fluorescence titration data in the presence of nitroaromatic compounds, we also calculated the limit of detections (LOD) for nitroaromatic compounds and LOD values are given in Table 1. The compound Z_{2a} and Z_{2b} showed LOD in micromolar levels. Compound Z_{2b} showed lower LOD values for studied nitroaromatic compounds than compound Z_{2a}. Compound Z_{2b} showed the lowest LOD value for DNP (LOD: 2.77 mM). Compound Z_{2b} showed best sensitivity and lowest LOD for DNP.
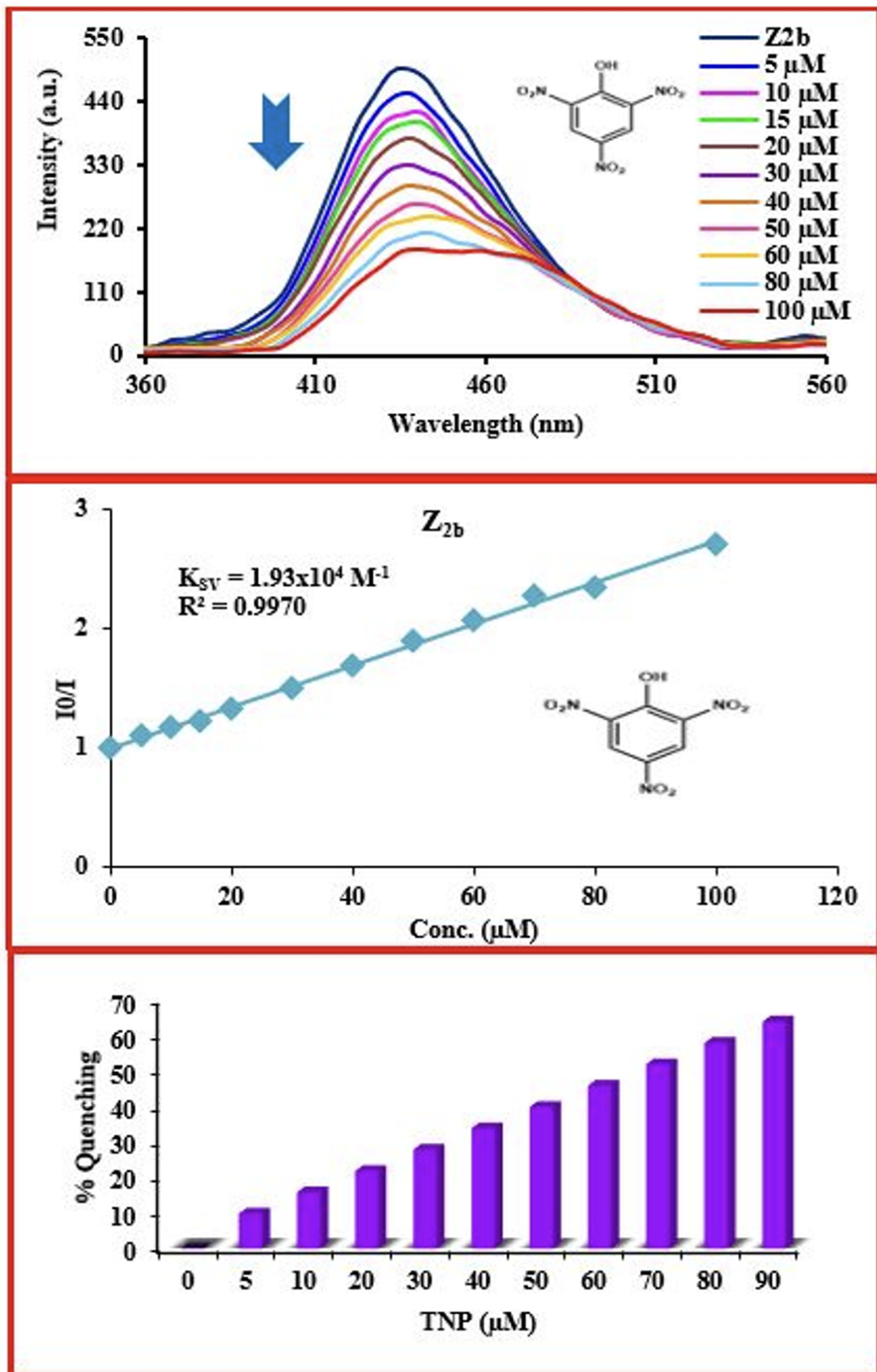
Figure 7. a) Emission spectra change of Z_{2b} upon incremental addition of TNP. b) Stern-Volmer plot (I0/I vs [A] c) Emission quenching percentage upon increased amount of TNP.

CONCLUSIONS

In this work, we prepared two Schiff base ligands from the reaction 5-aminoisophthalic acid and salicylaldehyde (Z_{2a}) or 2,3-dihydroxybenzaldehyde (Z_{2b}). The compounds were characterized by elementel analysis, FTIR, $^1H/^{13}C$ NMR and mass spectral studies. The compounds were screened for their sensing properties towards cations and nitroaromatic compounds. Colorimetric and fluorimetric studies revealed that both compounds (Z_{2a} and Z_{2b}) have selective sensing abilities towards Fe^{3+} and Hg^{2+} ions. Both Fe^{3+} and Hg^{2+} ions caused quenching of emission band of the free ligands. Fluorimetric sensing properties of the synthesized compounds towards nitroaromatic compounds [nitrobenzene (NB), 4-nitrophenol (NP), 2,4-dinitrophenol (DNP) and 1,3,5-trinitrophenol (TNP)] have also been investigated and data showed that compound Z_{2b} showed the best sensitivity and lowest LOD values for DNP. Compound Z_{2b} showed the lowest LOD value for DNP (LOD: 2.77 mM).

R e f e r e n c e s

1. S. Afrin Dalia, B. Farhana Afsan, B. Md Saddam Hossain, M. Nuruzzaman Khan, B. Md Kudrat-E-Zahan, B. Md Mahasin Ali, C. Md Kudrat-E-Zahan, F. Afsan, M. Saddam Hossain, C. Zakaria, M. Kudrat-E-Zahan, M. Mahasin Ali, A short review on chemistry of schiff base metal complexes and their catalytic application, Int. J. Chem. Stud., 6 (2018) 2859-2866.

2. D. Udhayakumari, V. Inbaraj, A Review on Schiff Base Fluorescent Chemosensors for Cell Imaging Applications, J. Fluoresc., 30 (2020) 1203-1223.

3. D. Udhayakumari, S. Naha, S. Velmathi, Colorimetric and fluorescent chemosensors for Cu2+. A comprehensive review from the years 2013-15, Anal. Methods, 9 (2017) 552-578.

4. B. Das, A. Jana, A. Das Mahapatra, D. Chattopadhyay, A. Dhara, S. Mabhai, S. Dey, Fluorescein derived Schiff base as fluorimetric zinc (II) sensor via 'turn on' response and its application in live cell imaging, Spectrochim. Acta - Part A Mol. Biomol. Spectrosc., 212 (2019) 222-231.

5. B.K. Paul, S. Kar, N. Guchhait, A Schiff base-derived new model compound for selective fluorescence sensing of Cu(II) and Zn(II) with ratiometric sensing potential: Synthesis, photophysics and mechanism of sensory action, J. Photochem. Photobiol. A Chem., 220 (2011) 153-163.

6. M. Bhuvanesh Kumar, R. Parameshwaran, Fuzzy integrated QFD, FMEA framework for the selection of lean tools in a manufacturing organisation, Prod. Plan. Control, 29 (2018) 403-417.

7. A.J. Leggett, Bose-Einstein condensation in the alkali gases: Some fundamental concepts, Rev. Mod. Phyhsics, 73 (2001) 307-356.

8. K. Sarkar, M. Debnath, P.P. Kundu, Preparation of low toxic fluorescent chitosan-graft-polyethyleneimine copolymer for gene carrier, Carbohydr. Polym., 92 (2013) 2048-2057.

9. K. Thakur, S.K. Tomar, A.K. Singh, S. Mandal, S. Arora, Riboflavin and health: A review of recent human research, Crit. Rev. Food Sci. Nutr., 57 (2017) 3650-3660.

10. S. Singh, Sensors-An effective approach for the detection of explosives, J. Hazard. Mater., 144 (2007) 15-28.

11. K.G. Furton, L.J. Myers, The scientific foundation and efficacy of the use of canines as chemical detectors for explosives, Talanta, 54 (2001) 487-500.

12. J. Feng, Y. Tao, X. Shen, H. Jin, T. Zhou, Y. Zhou, L. Hu, D. Luo, S. Mei, Y.I. Lee, Highly sensitive and selective fluorescent sensor for tetrabromobisphenol-A in electronic waste samples using molecularly imprinted polymer coated quantum dots, Microchem. J., 144 (2019) 93-101.

13. M.E. Germain, M.J. Knapp, Optical explosives detection: From color changes to fluorescence turn-on, Chem. Soc. Rev., 38 (2009) 2543-2555.

14. T. Rasheed, F. Nabeel, K. Rizwan, M. Bilal, T. Hussain, S.A. Shehzad, Conjugated supramolecular architectures as state-of-the-art materials in detection and remedial measures of nitro based compounds: A review, TrAC - Trends Anal. Chem., 129 (2020) 115958.

15. M. Aghaei, A.H. Kianfar, M. Dinari, Synthesis and characterization of a novel Schiff base polyamide ligand and its copper(II) complex for comparative removal of Pb(II) ions from aqueous solutions, J. Polym. Res., 27 (2020) 1-13.

16. Z. Yu, F. Wang, X. Lin, C. Wang, Y. Fu, X. Wang, Y. Zhao, G. Li, Selective fluorescence sensors for detection of nitroaniline and metal Ions based on ligand-based luminescent metal-organic frameworks, J. Solid State Chem., 232 (2015) 96-101.

17. E.J. Lenardão, J. de O. Feijó, S. Thurow, G. Perin, R.G. Jacob, C.C. Silveira, Selenonium ionic liquid as efficient catalyst for the Baylis-Hillman reaction, Tetrahedron Lett., 50 (2009) 5215-5217.

18. M. Hirata, T. Gotou, S. Horiuchi, M. Fujiwara, M. Ohba, Thin-film particles of graphite oxide 1: High-yield synthesis and flexibility of the particles, Carbon N. Y., 42 (2004) 2929-2937.

19. L.Q. Zhang, X.W. Wang, L. Gu, Y.H. Yu, J.S. Gao, Three pairs of luminescent coordination polymers based on CoII and CdII clusters for the detection of antibiotics, pesticides and chiral nitro aromatic compounds, RSC Adv., 10 (2020) 9476-9485.

20. A. Lewanowicz, A. Olszowski, P. Dziekoński, J. Leszczyński, Spectroscopic characteristics of the micro-environmentally induced H-bond transformation in anil-type species: Experimental and theoretical study, J. Mol. Model., 11 (2005) 398-406.

21. E. İspir, M. Kurtoğlu, F. Purtaş, and S. Serin, Synthesis and antimicrobial activity of new Schiff bases having the -SiOR group (R = CH_3 or CH_2CH_3), and their transition metal complexes, Transit. Met. Chem., 30 (2005) 1042-1047.

22. A. Golcu, M. Tumer, H. Demirelli, and R. A. Wheatley, Cd(II) and Cu(II) complexes of polydentate Schiff base ligands: Synthesis, characterization, properties and biological activity, Inorganica Chim. Acta, 358 (2005) 1785-1797.

23. M. Köse, S. Purtas, S. A. Güngör, G. Ceyhan, E. Akgün, and V. McKee, A novel Schiff base: Synthesis, structural characterisation and comparative sensor studies for metal ion detections, Spectrochim. Acta - Part A Mol. Biomol. Spectrosc., 136 (2015) 1388-1394.

24. M. Tümer, E. Akgün, S. Toroğlu, A. Kayraldiz, and L. Dönbak, Synthesis and characterization of Schiff base metal complexes: Their antimicrobial, genotoxicity and electrochemical properties, J. Coord. Chem., 61 (2008) 2935-2949.

25. E.O. Hamed, M.G. Assy, M.M. Galahom, Heterocyclization of Aromatic Amino Acids: Novel Syntheses and Antibacterial Activity of Fused, Non-fused, and Spiro Polyheterocyclic Derivatives, Russ. J. Org. Chem., 56 (2020) 1062-1069.

26. I. Gonul, M. Kose, G. Ceyhan, and S. Serin, "Methoxy group containing bidentate Schiff base ligands and their transition metal complexes: Synthesis, structural characterisation, photoluminescence, antioxidant capacity and superoxide dismutase activity studies," Inorganica Chim. Acta, 453 (2016) 522-530.

27. V.P. Singh, P. Singh, Synthesis, spectral characterization and thermal studies of Co(II), Ni(II), Cu(II) and Zn(II) complexes with 2-amino benzoic acid- and 2-hydroxy benzoic acid thiophen-2-ylmethylene hydrazide, J. Mol. Struct., 1035 (2013) 363-370.

28. M. Köse, G. Ceyhan, M. Tümer, I. Demirtaş, I. Gönül, and V. McKee, Monodentate Schiff base ligands: Their structural characterization, photoluminescence, anticancer, electrochemical and sensor properties, Spectrochim. Acta - Part A Mol. Biomol. Spectrosc., 137 (2015) 477-485.

29. G. Ceyhan, C. Çelik, S. Uruş, I. Demirtaş, M. Elmastaş, and M. Tümer, Antioxidant, electrochemical, thermal, antimicrobial and alkane oxidation properties of tridentate Schiff base ligands and their metal complexes, Spectrochim. Acta - Part A Mol. Biomol. Spectrosc., 81 (2011) 184-198.

30. F. Akhgari, H. Fattahi, and Y.M. Oskoei, Recent advances in nanomaterial-based sensors for detection of trace nitroaromatic explosives, Sensors Actuators, B Chem., 221 (2015) 867-878.

31. B. Gole, A.K. Bar, P.S. Mukherjee, Modification of extended open frameworks with fluorescent tags for sensing explosives: Competition between size selectivity and electron deficiency, Chem. A Eur. J., 20 (2014) 2276-2291.

Systematic Studies on the Male Genital Organs of some Blister Beetles (Coleoptera: Meloidae) of Ankara Province (Turkey)

Ankara İli (Türkiye) Bazı Yakı Böceklerinin (Coleoptera: Meloidae) Erkek Genital Organları Üzerinde Sistematik Çalışmalar

Muhammed Arif Demir[1] **and Mahmut Kabalak**[2,3]

[1]Graduate School of Science and Engineering, Hacettepe University, Beytepe, Ankara, Turkey.
[2]Department of Biology, Hacettepe University, Beytepe, Ankara, Turkey.
[3]Hacettepe University Biodiversity Research and Application Center, Beytepe, Ankara, Turkey.

ABSTRACT

The focus of this study is to make important contributions to Meloidae taxonomy. Specimens belonging to thirty-two species of the family Meloidae (Coleoptera) were collected from Ankara province in 2018-2019. Male genital structures of these species were examined. Photographs and drawings of the male genital organ structures of all these species (32 species), and descriptions of some of them, which were found to be missing in the current literature, were given. The taxonomic key has been constructed for these species from the present literature and examined materials. Also, male genital organs of all species were compared to the literature. Photographs and drawings of the male genital organs of *Alosimus luteus* (Waltl, 1838), *A. marginicollis* (Haag-Rutenberg, 1880) and *Euzonitis rubida* (Ménétriés, 1832) were given for the first time with this study.

Key Words
Ankara, Meloidae, Systematic evaluations, Turkey.

ÖZ

Bu çalışmanın odak noktası Meloidae taksonomisine önemli katkılarda bulunmaktır. Meloidae (Coleoptera) familyasına ait otuz iki türe ait örnekler, 2018-2019 yıllarında Ankara ilinden toplanmıştır. Bu türlerin erkek genital yapıları incelenmiştir. Bu türlerin tamamının (32 tür) erkek genital organ yapılarının fotoğrafları ve çizimleri ile güncel literatürde eksik bulunan bazılarının tanımlamaları verilmiştir. Bu türler için mevcut literatürden ve incelenen materyallerden taksonomik anahtar oluşturulmuştur. Ayrıca tüm türlerin erkek genital organları güncel literatürle karşılaştırılmıştır. *Alosimus luteus* (Waltl, 1838), *A. marginicollis* (Haag-Rutenberg, 1880) ve *Euzonitis rubida* (Ménétriés, 1832) erkek genital organlarının fotoğrafları ve çizimleri ilk kez bu çalışmada verilmiştir.

Anahtar Kelimeler
Ankara, Meloidae, Sistematik değerlendirmeler, Türkiye.

INTRODUCTION

The family Meloidae (Coleoptera) has about 3000 species belonging to 120 genera [1]. This family, known as blister beetles, is cosmopolitan (except New Zealand, Antarctica and most Polynesian islands) [2]. This family has the tenebrionoid type of male genitalia, and parameres partly or entirely fused but articulated with phallobase. Aedeagus is elongate and generally with two dorsal hooks, or uncommonly one, and with usually one ventral endophallic hook. Nemognathinae lacks both aedeagal dorsal hooks and endophallic hooks. Parameres distinct, fused only basally in Eleticinae, Meloinae and Tetraonycinae; completely fused in most Nemognathinae except in certain genera [2]. The focus of this study is to make important contributions to Meloidae taxonomy by examining with the drawing and describing of male genital organs of specimens collected from Ankara.

MATERIALS and METHODS

Specimens were collected from Ankara for 69 days (May-October 2018 (33 days) and April-October 2019 (36 days)) with field studies. The male genital organs were dissected and compared with the drawings in the current literature for confirmation of species diagnosis. The male genitals were prepared by using standard methods. These were examined by separating, photos of them were taken and drawings were made from ventral and lateral views. Morphological structures of male genital organs for differential diagnosis are also given briefly in tables. Photographs of male genitalia and small-sized specimens were taken with the Euromex SB-1903 Stereoblue microscope. Large specimens were taken with the Nikon Coolpix P900. The taxonomic key has been prepared considering the examined materials and related literature [3-14]. The differential diagnosis characters in male genital organs are placed on the keys. Detailed differences are given in the tables.

RESULTS and DISCUSSION

In this study, 32 species belonging to 2 subfamilies, 5 tribe and 11 genera from Ankara were systematically examined. Photographs and drawings of the male genital organ structures of all these species, and descriptions of some of them, which were found to be missing in the current literature, were given. Photographs and drawings of the male genital organs of *Alosimus luteus*, *A. marginicollis* and *Euzonitis rubida* species were given for the first time in this study. Also, *Alosimus armeniacus*, *A. chalybaeus*, *Lydus turcicus*, *Hycleus polymorphus*, *Mylabris* (*Eumylabris*) *cincta*, *M.* (*E.*) *crocata*, *M.* (*E.*) *fabricii*, *M.* (*Micrabris*) *laevicollis*, *M.* (*Micrabris*) *concolor*, *Meloe* (*Eurymeloe*) *glazunovi*, *Euzonitis sexmaculata*, *Zonitis* (s.str.) *flava* and *Z.* (s.str.) *immaculata* male genital organ structures were photographed and drawn for the first time in detail (evaluation of aedeagus and tegmen separately, and spiculum gastrale).

Key to the species

1. Antennae elongate and usually filiform; maxillary galeae rather modified and in usually elongate and forming a suction tube; outer angle of anterior tibiae of female blunt and short; the dorsal blade of tarsal claws with a double row of teeth along lower margin; aedeagus semi-membranous, without hook, endophallus only slightly sclerotized, never hooked; parameres usually completely fusioning……………………………………………**2**

1'. Antennae variously shaped, usually not filiform; maxillary galeae usually not modified or elongate (except for *Cerocoma*); outer angle of anterior tibiae of female pointed and elongate (except for *Meloe*); the dorsal blade of tarsal claws smooth in lower margin (except for Lyttini, and *Eumylabris* subgenus belonging to *Mylabris*); aedeagus strongly sclerotized, with 2-1 hooks, endophallus well sclerotized and also hooked; parameres not completely fusioning…………………………………………**6**

2. Galeae quite elongate, longer than maxillary palpi (Figure 31 in Bologna and Pinto [9]); gonoforceps cylindrical in lateral view (Figure 3) …………………………………………***Nemognatha chyrsomelina***

2'. Galeae slightly elongate, shorter than maxillary palpi; gonoforceps conical in lateral view …………………… **3**

3. Outer hind tibial spur much longer, wider apically than inner spur …………………………………………… **4**

3'. Outer hind tibial spur about as long as an inner spur, variable in width …………………………………… **5**

4. Head and pronotum black; pronotum spotless; antenna completely black; gonoforceps completely fused in ventral view; aedeagus pointed at the apex (Figure 1) …………………………………………… ***Euzonitis rubida***

4'. Head and pronotum yellow-ocher; pronotum with two black slightly spots on the lateral; antenna brown, only first segment black; gonoforceps slightly separated in ventral view; aedeagus not pointed at the apex (Figure 2) ……………………… ***Euzonitis sexmaculata***

5. Prosternum short, not elongated between posteriorly anterior coxa; pronotum narrowing roundly the antero-laterally in viewed dorsally (Figure 156 in Bologna [8]); outer hind tibial spur wider than the inner (Figure 86 in Bologna and Pinto [9]); gonoforceps pointed at the apex in ventral view (Figure 4) …………………………………………… ***Zonitis*** (s.str.) ***flava***

5'. Prosternum long, clearly posteriorly elongated and pointed between the anterior coxa; pronotum narrowing suddenly antero-laterally in viewed dorsally (Figure 156 in Bologna [8]); outer hind tibial spurs almost equal width (Figure 87 in Bologna and Pinto [9]); gonoforceps blunt at the apex in ventral view (Figure 5) ………………………………… ***Zonitis*** (s.str.) ***immaculata***

6. Elytra short and basally imbricate, not completely covering abdomen; metathoracic wings absent; metasternum short; the endophallic hook of the aedeagus is too small, not visible clearly in the lateral view …… ………………………………………………………………………… **7**

6' Elytra normally developed and basally non-imbricate, covering abdomen; metathoracic wings developed; metasternum elongate; the endophallic hook of aedeagus is not small, clearly visible in the lateral view (except *Actenodia confluens*) …………………………… **8**

7. Elytral humeral depression very pronounced ……………………………………… ***Meloe (Eurymeloe) glazunovi***

7'. Elytral humeral depression less pronounced …………………………… ***Meloe (Eurymeloe) mediterraneus***

8. Antenna inserted in front of frontal suture, far from eyes, the segments strongly modified in male; aedeagus with two endophallic hooks ………………… **9**

8'. Antenna behind frontal suture, near eyes, the segments moderately or not modified in male; aedeagus with one endophallic hook……………………… **12**

9. (Male) Frontal calli scarcely developed and raised over the head, with a frontal area well visible between them; antennae and maxillary palpi scarcely modified; protibiae not modified or only slightly swollen dorsally; the apex of aedeagus rounded …………… **10**

9'. (Male) Frontal calli only slightly raised over the head and not very close to each other, frontal area clearly visible between them; antennae and maxillary palpi strongly modified; protibiae with a high dorsal keel, variously shaped and not directed outwards; the apex of aedeagus pointed………………………………………………… **11**

10. Maxillary palpomere II and III weakly enlarged; antennae only slightly modified within the *Cerocoma* subgenus (Figures 2-V and 3-V in Turco and Bologna [12]); apical lobes of parameres distinctly swollen (Figure 6) ……………………………… ***Cerocoma*** (s.str.) ***bernhaueri***

10'. Maxillary palpomere II and III distinctly enlarged; antennae visibly modified within the *Cerocoma* subgenus (Figures 2-S and 3-S in Turco and Bologna [12]); apical lobes of parameres slightly swollen (Figure 7) ……………………………… ***Cerocoma*** (s.str.) ***schaefferi***

11. Protarsomere III about as long as V, excluding claws; maxillary palpi IV thin, slightly widened in medio-distal (Figures 3-I and 4-I in Turco and Bologna [12]); aedeagal hooks equal in size; endophallic hooks equal in size (Figure 8) ………… ***Cerocoma*** (Meloides) ***longiseta***

11'. Protarsomere III distinctly shorter than V, excluding claws; maxillary palpi IV wide, widened in medio-proximal (Figures 3-Q and 4-Q in Turco and Bologna [12]); aedeagal hooks not equal, subapical hook slightly larger than the apical; endophallic hooks not equal, subapical hook slightly larger than the apical (Figure 9) …………………………………………***Cerocoma*** (Meloides) ***turcica***

12. Antennae moniliform, fusiform or subfiliform, not enlarged apically; mesepisterna separated or touching along the middle, in front of mesosternum; the dorsal blade of tarsal claws with one row of teeth along ventral margin; endophallic hook large and strongly sclerotize ……………………………………………………… **13**

12'. Antennae claviform, slightly enlarged apically; mesepisterna separated in middle, in front of mesosternum, this latter usually with distinct scutum; the dorsal blade of tarsal claws smooth in the ventral margin (except for *Eumylabris* subgenus belonging to *Mylabris*); endophallic hook not as large as above and less sclerotize …………… **18**

13. The last segment of maxillary palpi clearly narrowed apically; antennae short, not attaining the base of pronotum, V–X. segment transverse and symmetrical; male head strongly impressed behind the eye (Figure 58 in Bologna [8]) ……………………… ***Oenas crassicornis***

13'. The last segment of maxillary palpi not clearly narrowed apically; antennae long, attaining the base of pronotum, V–X. segment more elongate or if transverse then at least slightly asymmetrical; male head not impressed behind eye ……………………………………… **14**

14. Pronotum longer than wide; antennal segments VI–X more elongate, asymmetrical at the basal; colour not metallic ……………………………… ***Lydus turcicus***

14'. Pronotum wider than long; antennal segments VI–X more enlarge, symmetrical at the basal; colour metallic …………………………………………………… **15**

15. Frontal red spot present; first middle-tarsomere shorter than II in male (Figure 15) ……………………… …………………………………………… ***Alosimus marginicollis***

15'. Frontal red spot absent; first middle-tarsomere equal with II, or longer than in male …………………… **16**

16. Protibia with apically one spur; first middle-tarsomere relatively equal with II in male; aedeagal hooks almost equal-sized (Figure 14) ……………………………… ………………………………………………… ***Alosimus luteus***

16'. Protibia with apically two spurs; first middle-tarsomere longer than II in male; aedeagal hooks different-sized …………………………………………………… **17**

17. In the male, middle-tarsomere I thin, clearly longer than II; the distal hook of aedeagus larger than the proximal one (Figure 12); body in metallic green or blue-green colours …………………… ***Alosimus armeniacus***

17'. In the male, middle-tarsomere I wide, slightly longer than II; the distal hook of aedeagus smaller than the proximal one (Figure 13); body in black-blue or black-green colours …………………… ***Alosimus chalybaeus***

18. Pronotum wider than long; antennae 9 segmented ………………………………… ***Actenodia confluens***

18'. Pronotum longer than wide; antennae 11 segmented ………………………………………………………… **19**

19. Mesepisterna with a relatively wide and distinctly furrowed anterior border area (Figures 66–67 in Bologna and Pinto [9]); pronotum with a very fine median furrow and depression at the central of disk ……… **20**

19'. Mesepisterna with anterior edge sometimes narrowly grooved, without a wide and furrowed anterior border area (Figures 68–69 in Bologna and Pinto [9]); pronotum without a fine median furrow at the central of disk ………………………………………………………… **23**

20. Mesosternum without a clear fore modified portion named scutum; last antennal segment thin, rounded at apex, not appears contiguous to before the last; gonoforceps proximally fused in ventral view (Figure 22…………………………………… ***Hycleus sexmaculatus***

20'. Mesosternum with a wide fore modified portion named scutum; last antennal segment of swollen, pointed at apex, appears contiguous to before the last; gonoforceps medially or medio-proximally fused in ventral view ……………………………………………… **21**

21. Antennomere I shorter than twice II; elytra patterning with two spots on anterior 1/3; temples wider than eyes ………… ***Hycleus scabiosae***

21'. Antennomere I as long or longer than twice II; elytra patterning with the black fascia on anterior 1/3; temples not wider than eyes …………………………… **22**

22. Pronotum with transverse depression in anterior; only the distal hook of the aedeagus at the apex; gonoforceps medially fused in ventral view (Figure 19) ……………………………………… ***Hycleus polymorphus***

22'. Pronotum without depression in anterior; both hooks of the aedeagus at the apex; gonoforceps medio-proximally fused in ventral view (Figure 21) ……………………………***………………. Hycleus zebraeus***

23. Mesosternal scutum smooth; hooks of aedeagus similar or only slightly different, distal one far from apex ………………………………………………………… **24**

23'. Mesosternal scutum with punctate and pubescent posterior middle area; hooks of aedeagus different from one another, distal one apical or subapical (Subgenus: *Mylabris*) **30**

24. Dorsal blade of tarsal claws with teeth along ventral margin; medium or large-sized species (Subgenus: Eumylabris) **25**

24'. Dorsal blade of tarsal claws with smooth along ventral margin; small-sized species (Subgenus: Micrabris) **28**

25. Head with small two red spots in between the eyes; elytral pattern with two spots in anterior and black fasciae in middle and posterior........................... **26**

25'. Head without a spot in between the eyes; elytral pattern with 5 black spots (2:2:1) **27**

26. Antennomere III longer than IV; elytral pattern with two spots in anterior, wide fasciae in the median and subapical, which not reach the lateral margin; aedeagal hooks almost equal-sized (Figure 23) .... ***Mylabris calida***

26'. Antennomere III as long as IV; elytral pattern with fascia in anterior, which not reach the lateral margin, wide fasciae in median and subapical, which reach the lateral margin; aedeagal hooks different-sized, the proximal one distinctly larger (Figure 24) .... ***Mylabris (E.) cincta***

27. Lateral appendages of mesosternum short and blunt; elytral posterior spot wider than others; gonoforceps almost conical, suddenly narrowing from basal to proximal, gradually narrowing from proximal to apical in lateral view; aedeagal hooks almost equal-sized (Figure 25) .... ***Mylabris (E.) fabricii***

27'. Lateral appendages of mesosternum long and pointed; elytral posterior spot as wide as, or narrower than others gonoforceps almost cylindrical at the basal, gradually narrowing towards the apical in lateral view; aedeagal hooks different-sized, the proximal one slightly larger (Figure 26) .... ***Mylabris (E.) crocata***

28. Elytra unicolour yellow-brown; antenna long, reaches the basal of the elytra; the basal part of gonoforceps deeply emarginated in ventral view (Figure 29) .... ***Mylabris (Mic.) unicolor***

28'. Elytra with brown but with black spots or fasciae; antenna short, reaches the medial of the pronotum; the basal part of gonoforceps shallow emarginated or straight in ventral view **29**

29. Elytral pattern with two spots in anterior and posterior, one middle greatly sinuous narrow fascia; gonoforceps medio-proximally fused in ventral view; aedeagal hooks almost equal-sized (Figure 27) .... ***Mylabris (Mic.) geminata***

29'. Elytral pattern with 6 spots (2:2:2); gonoforceps proximally fused in ventral view; aedeagal hooks different-sized, the distal one wider and shorter (Figure 28) .... ***Mylabris (Mic.) laevicollis***

30. Elytral black apical fascia narrow; antennomeres III-X reddish; gonoforceps medially fused in ventral view; the apical lobe of gonoforceps distinctly curved in lateral view (Figure 30) .... ***Mylabris (s.str.) olivieri***

30'. Elytral black apical fascia wide; antennomeres black; gonoforceps proximally fused in ventral view; the apical lobe of gonoforceps slightly curved in lateral view **31**

31. Pronotum with a shallow anterior transverse depression; gonoforceps very wide in lateral view (Figure 31) .... ***Mylabris (s.str.) quadripunctata***

31'. Pronotum without anterior transverse depression; gonoforceps almost slender in lateral view (Figure 32) .... ***Mylabris (s.str.) variabilis***

Subfamily: **NEMOGNATHINAE** Laporte, 1840
Tribe: Nemognathini Laporte, 1840
Genus: *Euzonitis* Semenov, 1893

This genus is represented by 17 species in the Palaearctic Region, 5 species in Turkey [15]. In this study, male specimens of two species belonging to this genus were examined. These species are *Euzonitis rubida* and *E. sexmaculata.* Differential diagnosis characters on male genital structures of examined species belonging to this genus were given Table 1.

Euzonitis rubida (Ménétriés, 1832)

Male Genital Organ Morphology (Figure 1): Gonoforceps completely fused in ventral view; phallobase convex and long; in lateral view gradually narrowing from basal to distal, rotated position in the apically, the phallobase is narrow, the ventral flat, is different in shape; aedeagus large, sclerotized and dense setae, pointed at the apex; spiculum gastrale long, the apodeme quite long and converged.
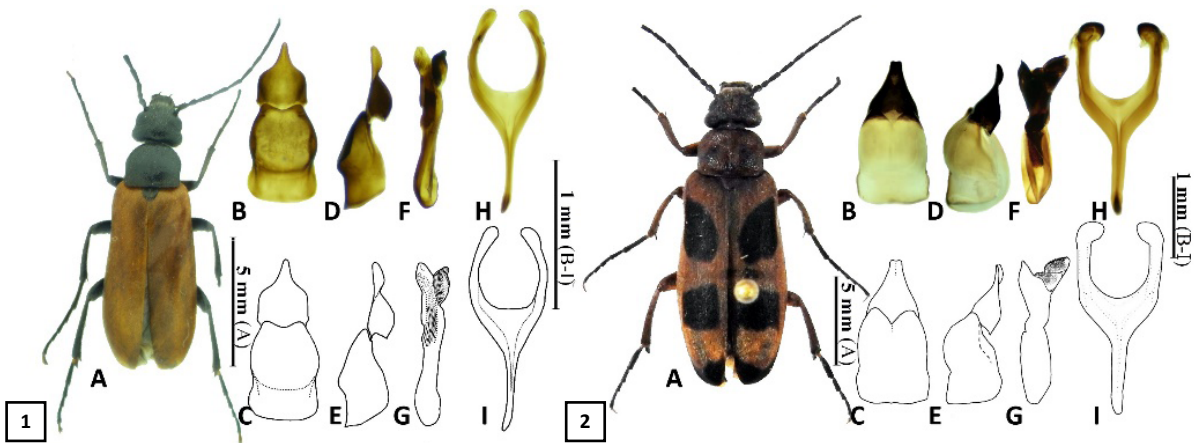
Figure 1-2. 1. *E. rubida*, 2. *E. sexmaculata*. A. Habitus (♂), B-I. Male genitalia photos and drawings (B-C. Tegmen (ventral view), D-E. Tegmen (lateral view), F-G. Aedeagus (lateral view), H-I. Spiculum gastrale).

Table 1. Differential diagnosis characters on male genital structures of examined species belonging to *Euzonitis*.

Male genital structures/Species	*E. rubida*	*E. sexmaculata*
Gonoforceps (Ventral view)	Completely fused, pointed at the apex	Almost completely fused, only slightly separated and blunt at the apex
Phallobase (Ventral view)	Convex and long	Slightly convex and short
Gonoforceps (Lateral view)	Gradually narrowing from basal to distal	Gradually narrowing from basal to apical
Phallobase (Lateral view)	Narrow and ventral side straight	Wide and ventral side convex
Aedeagus	Pointed at the apex	Not pointed at the apex
Apodeme of the spiculum gastrale	Closer to each other	Parallel to each other

Remarks: There is no information on the male genital organ of this species in the available literature, and photos, drawings and detailed description of the male genital organ are given, for the first time by this study.

Euzonitis sexmaculata (Olivier, 1789)
Male Genital Organ Morphology (Figure 2): For detailed description, see Bologna [8].

Remarks: With the drawing included in the findings of Bologna [8], it is seen that the aedeagus is quite similar, but the phallobase is narrower and less curved in the lateral view. With the drawing in the findings of Iablokoff-Khnzorian [16], it is seen that the structure of the gonoforceps is similar, but the aedeagus is different. It is thought that the reason for this difference is because the aedeagus cannot be drawn laterally. In the findings of Serri et al. [17], it is thought that the lateral view of the gonoforceps is not included and the aspect ratio of the drawing is not preserved in the ventral view, so it is thought to be rather narrow and long.

Genus: **Nemognatha** Illiger, 1807
This genus is represented by 6 species in the Palaearctic Region, one species in Turkey [15]. In this study, male specimens of one species belonging to this genus were examined.

Nemognatha chrysomelina (Fabricius, 1775)
Male Genital Organ Morphology (Figure 3): For detailed description, see Bologna [8].

Remarks: It was observed that the drawings in this study were compatible with the drawings in the findings of Bologna [8, 18].
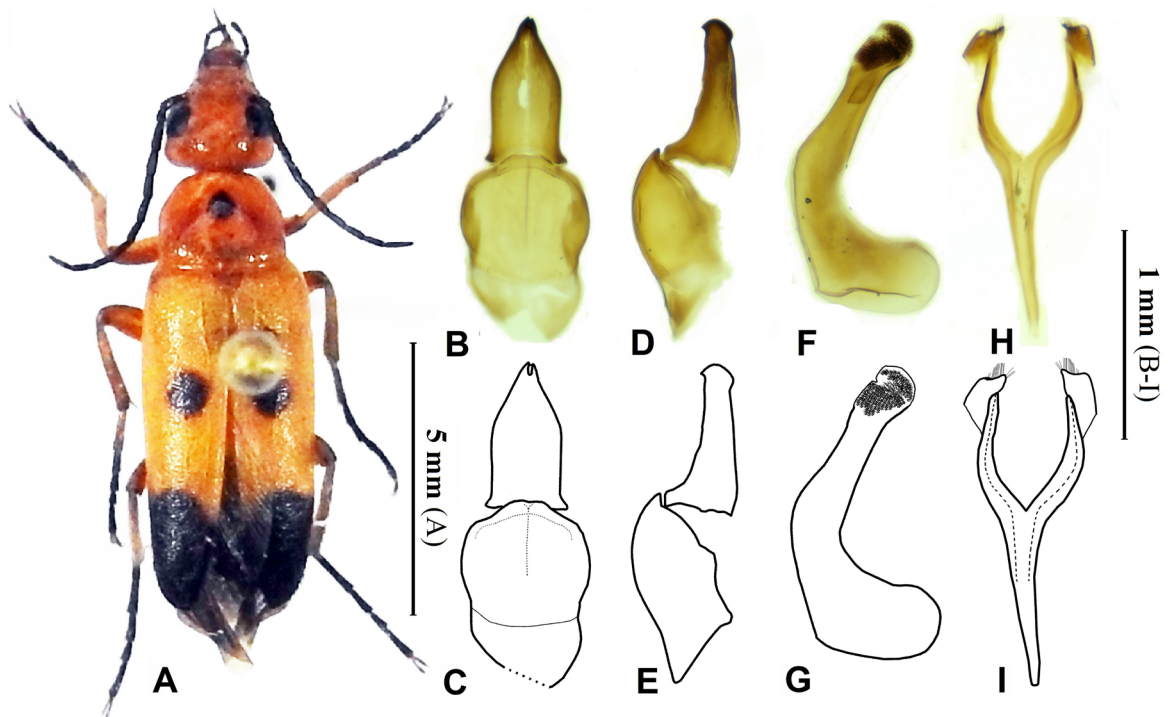
Figure 3. *Nemognatha chrysomelina*. A. Habitus (♂), B-I. Male genitalia photos and drawings (B-C. Tegmen (ventral view), D-E. Tegmen (lateral view), F-G. Aedeagus (lateral view), H-I. Spiculum gastrale).
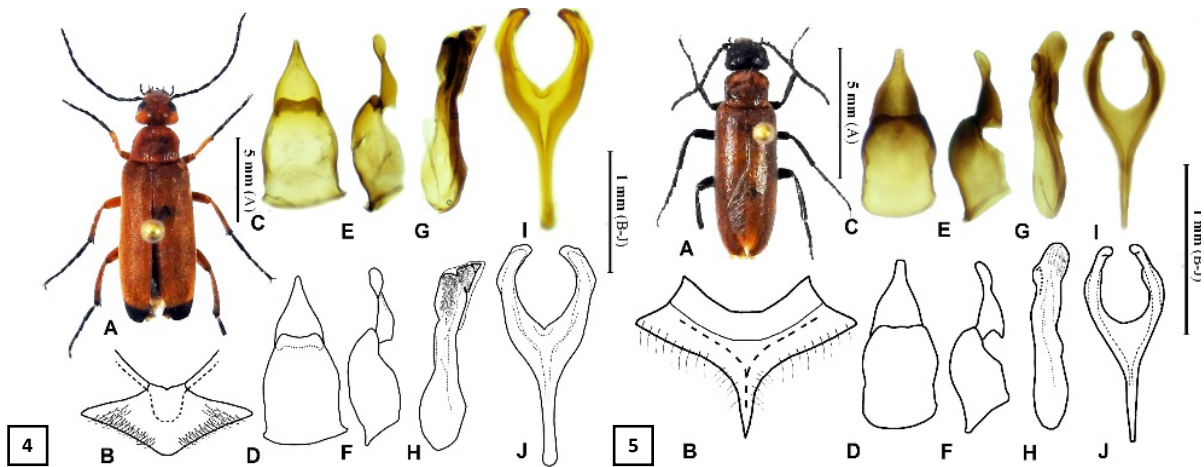
Figure 4-5. 4. Z.(s.str.) *flava*, 5. Z. (s.str.) *immaculata*. A. Habitus (♂), B. Prosternum, C-J. Male genitalia photos and drawings (C-D. Tegmen (ventral view), E-F. Tegmen (lateral view), G-H. Aedeagus (lateral view), I-J. Spiculum gastrale).

Table 2. Differential diagnosis characters on male genital structures of examined species belonging to *Zonitis*

Male genital structures/Species	Z. (s.str.) flava	Z. (s.str.) immaculata
Gonoforceps (Ventral view)	Slightly narrowing from basal to proximal, suddenly narrowing from proximal to apical, pointed at the apex	Slightly narrowing from basal to medial, suddenly narrowing from medial to apical, blunt at the apex
Phallobase (Ventral view)	Convex	Medially arched
Gonoforceps (Lateral view)	Narrow at the basal	Wide at the basal
Aedeagus	Pointed at the apex	Rounded at the apex

Genus: **Zonitis** Fabricius, 1775

This genus is represented by 29 species in the Palaearctic Region, 8 species in Turkey [15]. Male specimens of two species were examined in this study. These species are *Zonitis* (s.str.) *flava* and *Z.* (s.str.) *immaculata.* Differential diagnosis characters on male genital structures of examined species belonging to this genus were given Table 2.

Zonitis (s.str.) **flava** Fabricius, 1775

Male Genital Organ Morphology (Figure 4): For detailed description, see Bologna [8].

Remarks: The drawings in this study showed differences in the apex of the aedeagus with the drawings included in the findings of Bologna [8] and Ruiz [19]. It was observed that the male genital organ structure of the determined species was more similar to the drawing in the findings of Ruiz [19].

Zonitis (s.str.) **immaculata** (Olivier, 1789)

Male Genital Organ Morphology (Figure 5): For detailed description, see Bologna [8].

Remarks: It was observed that the drawings in this study were compatible with the drawing in the findings of Bologna [8].

Subfamily: **MELOINAE** Gyllenhal, 1810
Tribe: Cerocomini Leach, 1815
Genus: ***Cerocoma*** Geoffroy, 1762

The genus *Cerocoma* is the most species-rich genus of the Cerocomini tribe. This genus is represented by 29 species belonging to 5 subgenera in the Palaearctic Region, and 23 species belonging to four subgenera in Turkey [12, 15]. In this study, male specimens of four species belonging to this genus were examined. These species are *C.* (s.str.) *bernhaueri*, *C.* (s.str.) *schaefferi*, *C.* (*Meloides*) *longiseta* and *C.* (*Meloides*) *turcica*. Differen-

tial diagnosis characters on male genital structures of examined species belonging to this genus were given Table 3.

Cerocoma (s.str.) bernhaueri Pardo Alcaide, 1977
Male Genital Organ Morphology (Figure 6): For detailed description, see Turco and Bologna [12].

Remarks: Turco and Bologna [12] were reported that *Cerocoma* (s.str.) *bernhaueri* is quite similar to *C.* (s.str.) *dahli*, and these two species were confused so much so far. Compared to the current literature, the external
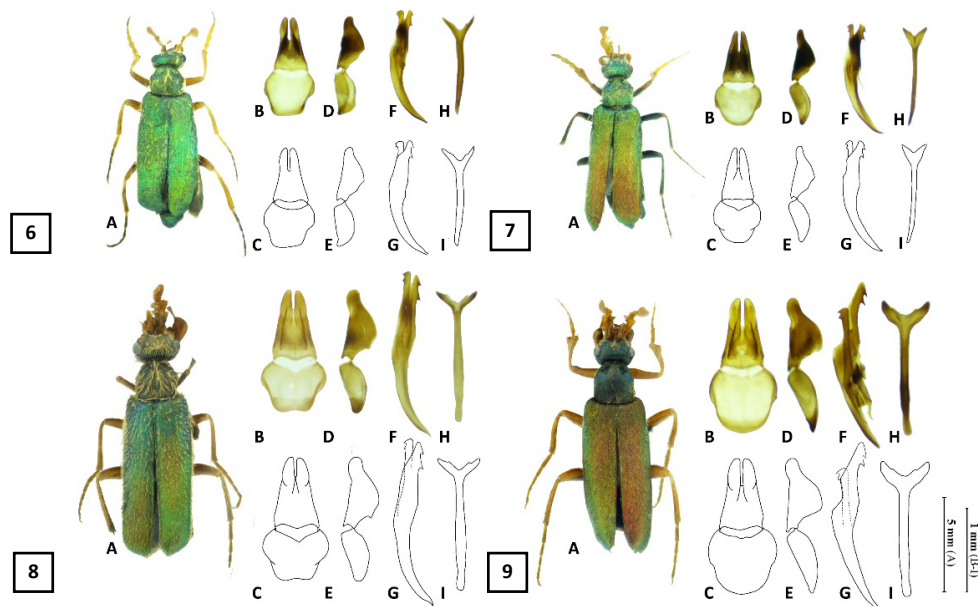
Figure 6-9. Male habitus and genitalia. 6. *Cerocoma* (s.str.) bernhaueri, 7. C. (s.str.) *schaefferi*, 8. C. (*Meloides*) longiseta, 9. C. (*Meloides*) turcica; A. Habitus (♂), B-I. Male genitalia photos and drawings (B-C. Tegmen (Ventral view), D-E. Tegmen (Lateral view), F-G. Aedeagus (Lateral view), H-I. Spiculum gastrale).

Table 3. Differential diagnosis characters on male genital structures of examined species belonging to *Cerocoma*.

Male genital structures /Species	C. bernhaueri	C. schaefferi	C. longiseta	C. turcica
Apical lobes of parameres (Ventral)	Swollen	Slightly swollen	Swollen	Swollen
Apical lobes of parameres (Lateral)	Straight, with apical lobes directed forward	Straight, with apical lobes directed forward	Straight, with apical lobes directed forward	Slightly curved, with apical lobes dorsally directed
Apex of aedeagus	Rounded	Rounded	Pointed	Pointed
Dorsal hooks of aedeagus	Subapical hook slightly larger than the apical	Almost equal (subapical hook slightly larger than the apical)	Equal in size	Subapical hook slightly larger than the apical
Endophallic hooks of aedeagus	Equal in size	Equal in size	Equal in size	Subapical hook slightly larger than the apical

morphologies (antenna and maxillary palpus segments, the structure of the protibia) and the male genital organ of this species appear to be compatible with the drawings of Turco and Bologna [12].

Cerocoma (s.str.) schaefferi (Linnaeus, 1758)
Male Genital Organ Morphology (Figure 7): For detailed description, see Turco and Bologna [12].
Remarks: It was observed that this species detected in this study is compatible with the drawings of Turco and Bologna [12] rather than the drawing of Bologna [8].

Cerocoma (Meloides) longiseta Turco & Bologna, 2011
Male Genital Organ Morphology (Figure 8): For detailed description, see Turco and Bologna [12].
Remarks: It was observed that this species detected in this study is compatible with the drawings of Turco and Bologna [12].

Cerocoma (Meloides) turcica Pardo Alcaide, 1977
Male Genital Organ Morphology (Figure 9): For detailed description, see Turco and Bologna [12].
Remarks: It was observed that this species detected in this study is compatible with the drawings of Turco and Bologna [12].

Tribe: Meloini Gyllenhal 1810
Genus: **Meloe** Linnaeus, 1758
This genus is represented by 122 species in the Palaearctic Region, 20 species in Turkey [15]. In this study, male specimens of two species belonging to this genus were examined. These species are *Meloe (Eurymeloe) glazunovi* and *M. (Eurymeloe) mediterraneus*. Differential diagnosis characters on male genital structures of examined species belonging to this genus were given Table 4.
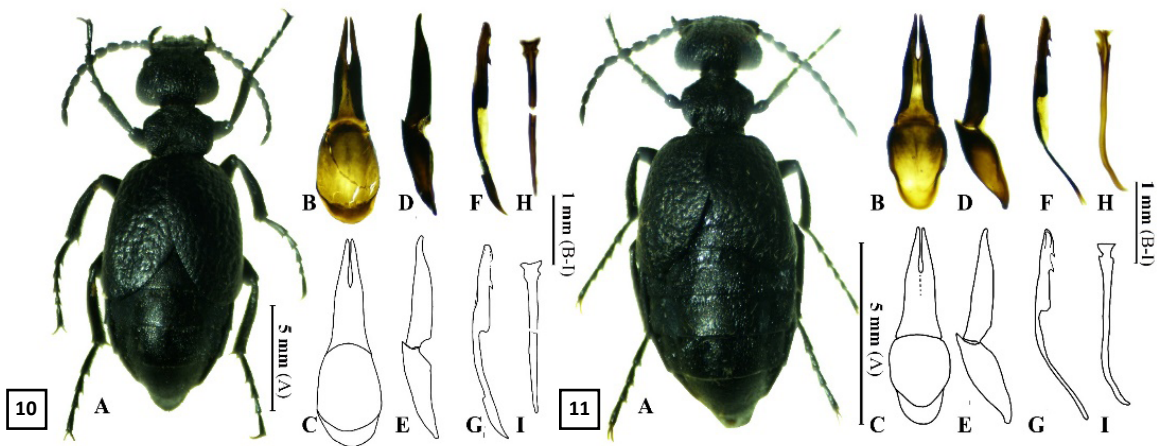
Figure 10-11. 10. M. (*Eurymeloe*) *glazunovi*, 11. M. (*Eurymeloe*) *mediterraneus*. **A.** Habitus (♂), **B**-I. Male genitalia photos and drawings (**B-C**. Tegmen (ventral view), **D-E**. Tegmen (lateral view), **F-G**. Aedeagus (lateral view), **H-I**. Spiculum gastrale).

Table 4. Differential diagnosis characters on male genital structures of examined species belonging to *Meloe*.

Male genital structures/Species	*M. (E.) glazunovi*	*M. (E.) mediterraneus*
The basal part of parameres (Ventral view)	Slightly wide	Very wide
Phallobase (Ventral view)	Gradually wider towards the apical	Gradually narrower towards the apical
Parameres (Lateral view)	Slender, prominently curved in before apical lobe	Slightly wider, slightly curved in before apical lobe
Phallobase (Lateral view)	Slender	Wide

Meloe (Eurymeloe) glazunovi Pliginskij, 1910

Male Genital Organ Morphology (Figure 10): Gonoforceps fused medio-distally in ventral view, parameres parallel, narrows in the medio-distal, basal of parameres deeply emarginated; in lateral view parameres slender, prominently curved in before apical lobe; the proximal hook of the aedeagus curved, the endophallic hook is at the apex, very small, within the membrane; spiculum gastrale thin, blunt at the apex.

Remarks: Compared to the current literature of the male genital organ of this species, it was found to be compatible with the drawing included in the findings of Iablokoff-Khnzorian [16], although it is somewhat without details and confusion.

Meloe (Eurymeloe) mediterraneus G. Müller, 1925

Male Genital Organ Morphology (Figure 11): For detailed description, see Bologna [8, 20].

Remarks: Compared to the current literature of the male genital organ of this species, it was found to be compatible with the drawings included in the findings of Iablokoff-Khnzorian [16] and Bologna [8, 20].

Tribe: Lyttini Solier, 1851

Genus: ***Alosimus*** Mulsant, 1857

The genus *Alosimus* described as the subgenus of the genus *Lydus* in the early literature, such as Escherich (1896) and Mařan (1942) [9]. The received taxonomic status has been defined by Kaszab [7] and some taxonomic problems have been clarified by studies of Bologna [8, 18, 21]. This genus represented by 27 species in the Palaearctic Region and 15 species in Turkey [15]. In this study, male specimens of four species belonging to this genus were examined. These species are *Alosimus armeniacus* (Falderman, 1837), *A. chalybaeus* (Tauscher, 1812), *A. luteus* (Waltl, 1838) and *A. marginicollis* (Haag-Rutenberg, 1880). Differential diagnosis characters on male genital structures of examined species belonging to this genus were given Table 5.

Alosimus armeniacus (Faldermann, 1837)

Male Genital Organ Morphology (Figure 12): Gonoforceps fused medially in ventral view, the width of the middle cavity is narrower than the width of a paramere; in lateral view proximally arched, apical lobe curved; aedeagal distal hook positioned almost at the apex, different in shape and size from the proximal hook, the
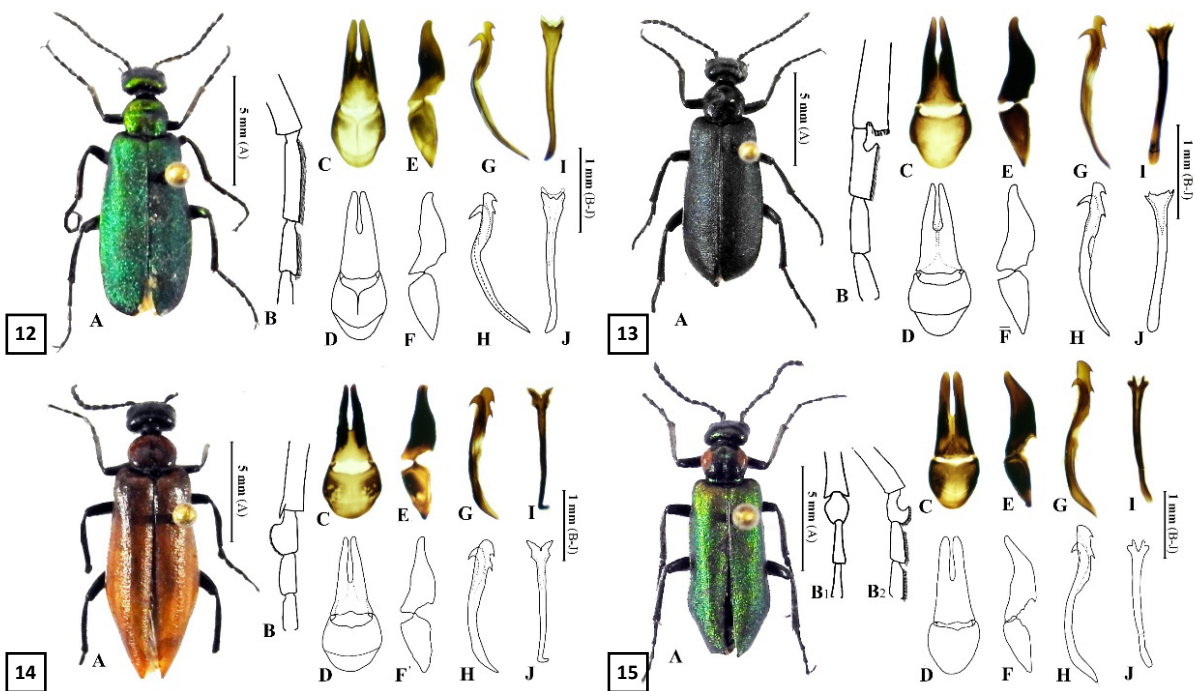
Figure 12-15. Male habitus and genitalia. 12. *Alosimus armeniacus*, 13. *A. chalybaeus*, 14. *A. luteus*, 15. *A. marginicollis*, A. Habitus (♂), B. First middle-tarsomere (B_1. dorsal view, B_2. lateral view), C-J. Male genitalia photos and drawings (C-D. Tegmen (ventral view), E-F. Tegmen (lateral view), G-H. Aedeagus (lateral view), I-J. Spiculum gastrale).

Table 5. Differential diagnosis characters on male genital structures of examined species belonging to *Alosimus*.

Male genital structures /Species	*A. armeniacus*	*A. chalybaeus*	*A. luteus*	*A. marginicollis*
Fusion state of Gonoforceps (Ventral view)	Medially fused	Medially fused	Medio-proximally fused	Medially fused
Width of the cavity between parameres (Ventral view)	Narrower than the width of a paramere	Clearly as wide as paramere	Almost as wide as paramere	Narrower than the width of a paramere
Gonoforceps (Lateral view)	Proximally arched, apical lobe curved	Medially arched, apical lobe relatively curved	Distally and proximally arched, apical lobe slightly curved	Proximally slight arched, very strongly curved distally towards the ventral
Dorsal hooks of aedeagus	Distal hook distinctly larger	Proximal hook distinctly larger	Hooks almost equal-sized	Proximal hook larger
Distance between the dorsal hooks	Relatively far	Far	Relatively close	Distinctly far
Endophallic hook of aedeagus	Thin and elongated straight down	Thin and elongated straight down	Short and curved downward	Short and curved downward
Apodeme of the spiculum gastrale	Relatively short	Short	Relatively long	Relatively short

proximal hook directed downward, the distal hook of aedeagus clearly larger than the proximal one, the distance between them relatively far, endophallic hook thin and elongated straight down; apodeme of the spiculum gastrale relatively short.

Remarks: Compared to the present literature, the male genital organ was found to be compatible with the drawing of Bologna [18]. Since the aedeagus and tegmen were drawn as a whole without separation in the study by Bologna [18], the tegmen could not be compared ventrally. Also, in several studies were conducted by various researchers from different regions of Iran [17, 22, 23] drawings of male genital organ structures of this species are included. However, in these studies, it is seen that the aspect ratios of the drawings cannot be maintained and therefore the aedeagus is quite bulging from the medial and the proximal hook is larger than the distal hook.

Alosimus chalybaeus (Tauscher, 1812)
Male Genital Organ Morphology (Figure 13): Gonoforceps fused medially in ventral view, the width of middle cavity width of a paramere; in lateral view medially arched, apical lobe relatively curved; aedeagal distal hook positioned almost at the apex, different in shape and size from the proximal hook, proximal hook directed

downward, the distal hook of aedeagus clearly smaller than proximal one, the distance between them far, endophallic hook thin and elongated straight down; apodeme of the spiculum gastrale are short.

Remarks: The specimens examined in this study was more similar to the drawing in Bologna [18] than in the drawing of Gupta [24]. However, in both studies, aedeagus and gonoforceps were evaluated only laterally and the ventral view of gonoforceps could not be compared. When looking at the drawing of this species in the findings of Iablokoff-Khnzorian [16], it was observed that the proximal hook of aedeagus was smaller than the distal one and was more similar to the *A. armeniacus* species detected in this study.

Alosimus luteus (Waltl, 1838)
Male Genital Organ Morphology (Figure 14): Gonoforceps fused medio-proximally in ventral view, width of middle cavity relatively width of a paramere; in lateral view distally and proximally arched, apical lobe slightly curved; aedeagal distal hook positioned almost at the apex, similar in shape and size with proximal hook, the proximal hook directed downward and significantly smaller than the distal hook, the distance between them relatively near, with the small prominent protrusion on the proximal hook, endophallic hook short and
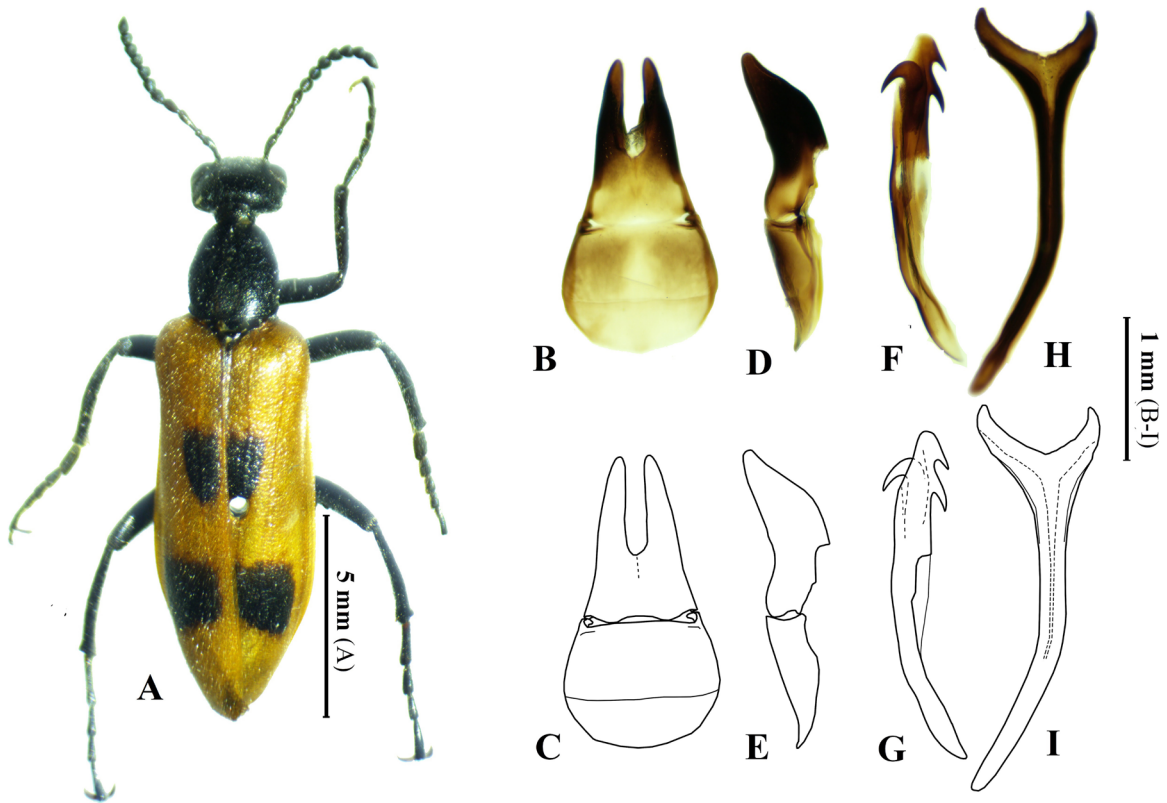
Figure 16. *Lydus turcicus*; A. Habitus (♂), B-I. Male genitalia photos and drawings (B-C. Tegmen (ventral view), D-E. Tegmen (lateral view), F-G. Aedeagus (lateral view), H-I. Spiculum gastrale).

curved downward; spiculum gastrale emarginated in the apex, and its apodeme relatively long.

Remarks: *Alosimus luteus*, differs from other species of the genus with a protibial spur, pronotum and elytra yellowish-brown, and two black spots on the pronotum [7]. In the studied specimens, the black spots on the pronotum are seen as a large, slightly pronounced black spot. No information has been found and compared in the literature regarding the male genital organ of this species. For the first time in this study, the photo, drawing and detailed description of the male genital organ were given. This species was morphologically similar to *Alosimus decolor* (Abeille de Perrin, 1880) and most distinctly distinguished by the presence of black spots on the pronotum [7]. The examined specimen was compared with the male genital organ of the *A. decolor* in the findings of Bologna [18]. In the drawing of Bologna [18], it was observed to be different than the different were aedeagus hooks of *A. decolor* was short and gonoforceps was prominent curved in the medial position in the lateral view, compared to the *A. luteus* detected in this study.

Alosimus marginicollis (Haag-Rutenberg, 1880)
Male Genital Organ Morphology (Figure 15): For detailed description, see Mařan [6].

Remarks: *A. marginicollis*, is easily distinguished from other species of the genus with its two large, distinctive lemon yellow-orange spots in the pronotum [7]. This species is endemic to Turkey, photos and drawings of the male genital organ are given, for the first time by this study.

Genus: ***Lydus*** Dejean, 1821
The genus *Lydus* is represented by 16 species in the Palaearctic Region and 10 species in Turkey [15]. In this study, male specimens of one species belonging to this genus were examined.

Lydus turcicus Kaszab, 1952
Male Genital Organ Morphology (Figure 16): Gonoforceps fused medio-proximally in ventral view, the width of the middle cavity is the width of a paramere; in lateral view proximally strongly arched, phallobase narrow; aedeagal distal hook positioned at the apex, different

in shape and size from the proximal hook, the proximal hook directed downward and almost twice the distal hook, the distance between them relatively near, endophallic hook long and directed downward; spiculum gastrale deeply emarginated in the apex, and its apodeme large.

Remarks: In the current literature [18, 25], it is reported that *L. trimaculatus*, *L. quadrimaculatus* Tauscher, 1812 and *L. turcicus* can be confused with each other. Pronotum of *Lydus turcicus* is widest just behind the medial, significantly narrowed towards the anterior; head is long; the temple is very long and longer than the longitudinal diameter of the eye, and differs from other species of this genus [25]. Compared to the current literature of the male genital organ of this species, it was found to compatible with the drawing in the findings of Bologna [18]. Kaszab [25] mentioned only the dorsal hooks of the aedeagus when described this species.

Genus: **Oenas** Latreille, 1802

The genus *Oenas* is represented by 12 species in the Palaearctic Region and 3 species in Turkey [15]. In this study, male specimens of one species belonging to this genus were examined.

Oenas crassicornis (Illiger, 1800)

Male Genital Organ Morphology (Figure 17): For detailed description, see Bologna [8].

Remarks: This species differs from other species of this genus by the fact that I. segment of middle tarsi in the male is laterally compressed and enlarged considerably towards the ventral, furrow under the eye of male deeper and the pronotum and elytra are yellow-ochre [8, 26]. According to current literature, there are differences between the drawings of the male genitalia of this species [8, 18, 23]. In particular, it is seen in some studies that the apex of the aedeagus is round [8, 18] or pointed [23]. Also, it is seen that, positions and sizes of the dorsal hooks of aedeagus are different. Aedeagus of examined specimens was seen to be compatible with the aedeagus of specimens collected from Turkey by [8, 18]. However, it differs with gonoforceps being thinner in lateral view. This suggests that the *Oenas*, whose external morphological characters were revealed by Kaszab [26], requires a re-examination and taxonomic revision with current methods.
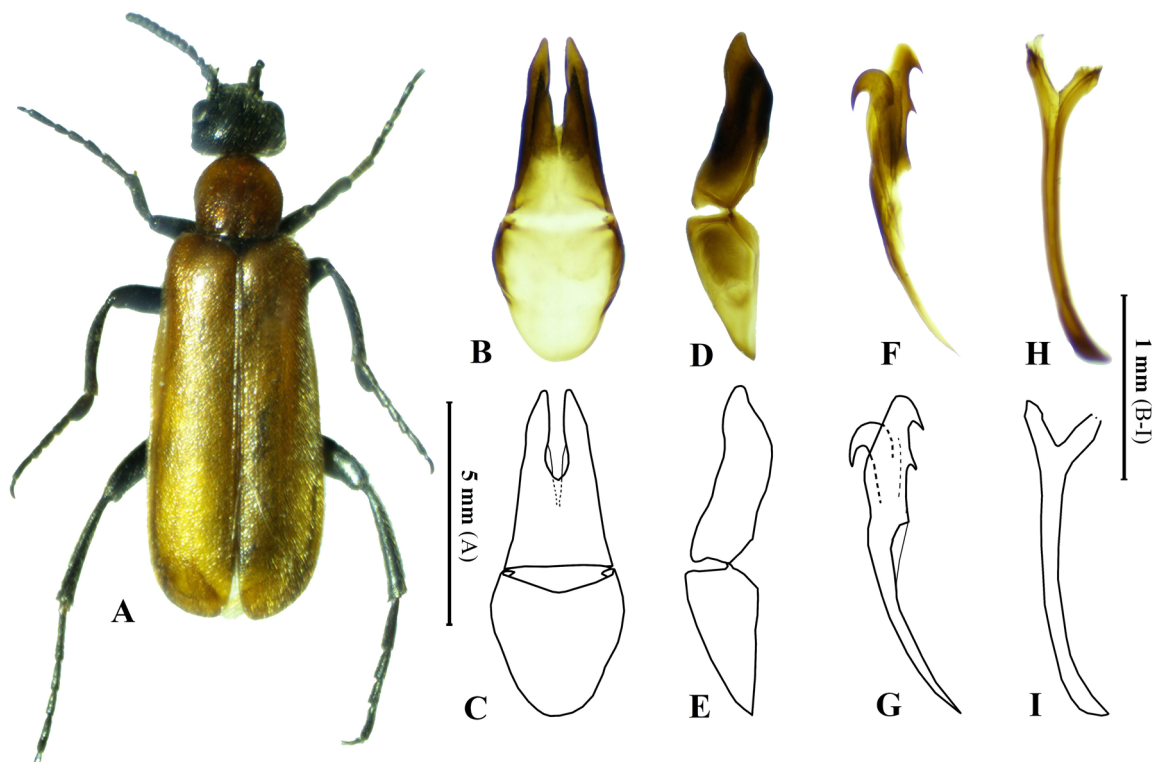
Figure 17. *Oenas crassicornis*; A. Habitus (♂), B-I. Male genitalia photos and drawings (B-C. Tegmen (ventral view), D-E. Tegmen (lateral view), F-G. Aedeagus (lateral view), H-I. Spiculum gastrale).

Tribe: Mylabrini Laporte, 1840
Genus: **Actenodia** Laporte, 1840
This genus is represented by 9 species in Palaearctic Region, 18 species in World and 2 species in Turkey [10, 15]. In this study, male specimens of one species belonging to this genus were examined.

Actenodia confluens (Reiche, 1866)
Male Genital Organ Morphology (Figure 18): For detailed description, see Bologna et al. [10].

Remarks: Compared to the current literature of the male genital organ of this species, it was found to compatible with the drawings of Bologna et al. [10].

Genus: **Hycleus** Latreille, 1817
The hyper-diverse genus *Hycleus* is the most species-rich genus of Meloidae. This genus is represented by more than 500 species and widely distributed in the Old World [27]. This genus is represented by 117 species in the Palaearctic Region, and 10 species in Turkey [15]. In this study, male specimens of four species belonging to this genus were examined. These species are *Hycleus polymorphus*, *H. scabiosae*, *H. zebraeus* and *H. sexma-*

culatus. In the current literature [3, 5, 8, 18, 28-30] no diagnostic keys are covering all of the detected species. Species diagnoses were made by comparing species descriptions and some taxonomic characters such as structures of mesosternum and drawings of male genital organ. Differential diagnosis characters on male genital structures of examined species belonging to this genus was given Table 6.

Hycleus polymorphus (Pallas, 1771)
Male Genital Organ Morphology (Figure 19): For detailed description, see Bologna [8].

Remarks: Compared with the current literature, it is seen that the genitalia of the detected species is compatible with the drawing in the findings of Bologna [8]. This species, which is included in the findings of Iablokoff-Khnzorian [16] and given as *Mylabris polymorpha*, is thought to be *H. zebraeus*, since the aedeagus does not have a distal longitudinal area between the distal and proximal hooks in the male genital organ drawing. However, in both studies, aedeagus and gonoforceps were evaluated only laterally and the ventral view of gonoforceps could not be compared.
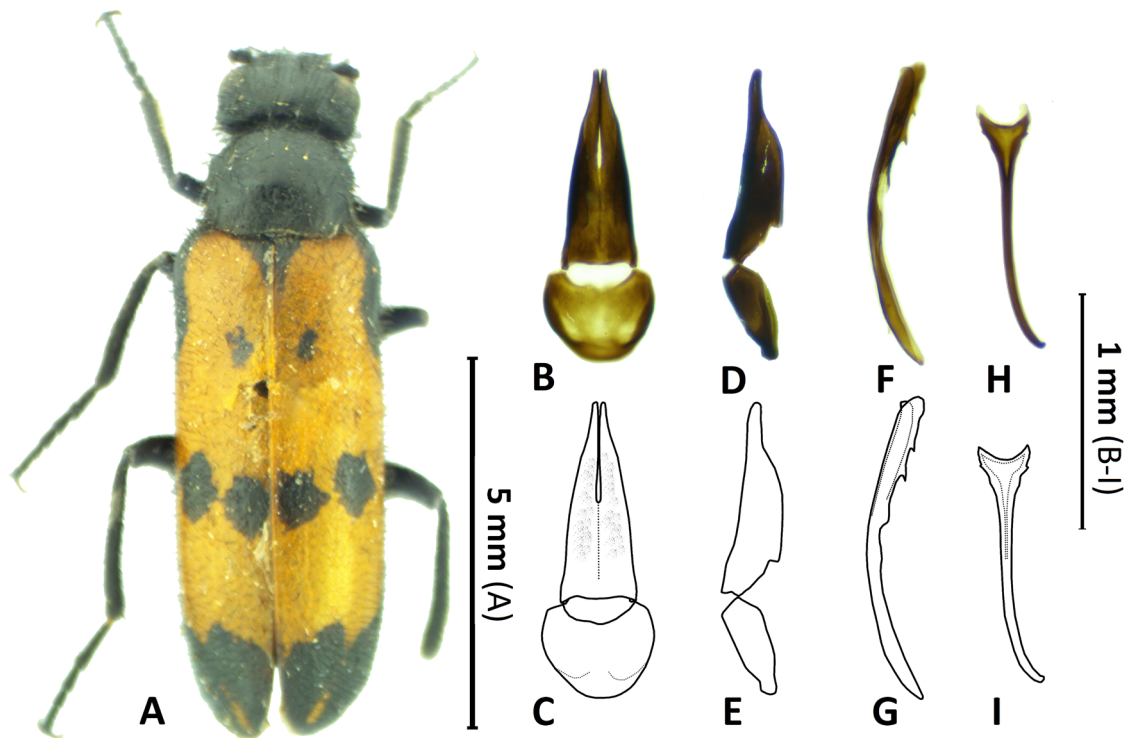
Figure 18. *Actenodia confluens* (Reiche, 1866); A. Habitus (♂), B-I. Male genitalia photos and drawings (B-C. Tegmen (Ventral view), D-E. Tegmen (Lateral view), F-G. Aedeagus (Lateral view), H-I. Spiculum gastrale).
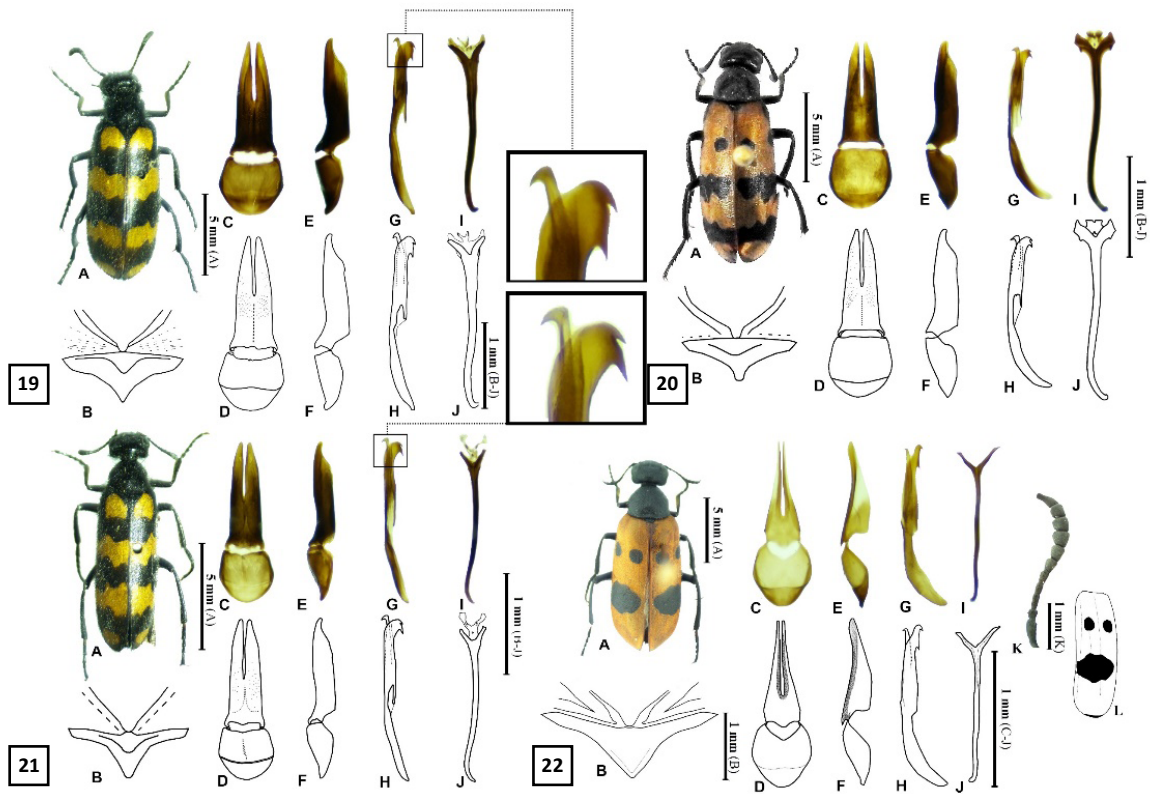
Figure 19-22. 19. *Hycleus polymorphus*, 20. *H. scabiosae,* 21. *H. zebraeus*, 22. *H. sexmaculatus*. A. Habitus (♂), B. Mesosternum, C-J. Male genitalia photos and drawings (C-D. Tegmen (ventral view), E-F. Tegmen (lateral view), G-H. Aedeagus (lateral view), I-J. Spiculum gastrale), K. Antenna, L. Elytra.

Table 6. Differential diagnosis characters on male genital structures of examined species belonging to *Hycleus*.

Male genital structures/Species	*H. polymorphus*	*H. scabiosae*	*H. zebraeus*	*H. sexmaculatus*
Fusion state of Gonoforceps (Ventral view)	Medially fused	Medio-proximally fused	Medio-proximally fused	Proximally fused
Location of the dorsal hooks of aedeagus	The distal hook at the apex	Both hooks at the apex	Both hooks at the apex	The distal hook at the apex
Dimensions of the dorsal hooks of aedeagus	The proximal hook longer and pointed downwards	The proximal hook longer, wider, and downward curved	The proximal hook longer, wider, and downward curved	The proximal hook longer, wider and pointed downwards
Distal dent placed between the dorsal hooks	Present	Absent	Present (very small)	Absent

Hycleus scabiosae (Olivier, 1811)
<u>Male Genital Organ Morphology (Figure 20):</u> For detailed description, see Bologna [18].

<u>Remarks:</u> Compared with the current literature [16-18, 22, 23, 30], it is seen that between genitalia drawings of this species is very little difference between, and

it appears to be consistent with the male genitalia of the specimens collected in the findings by Bologna [18] from Turkey.

Hycleus zebraeus (Marseul, 1870)
<u>Male Genital Organ Morphology (Figure 21):</u> For detailed description, see Bologna [18].

Remarks: In the current literature, this species has been seen to be very confused with *H. polymorphus* [8, 18, 27, 31]. Bologna [31] stated the distinctive characters of these two species. In the specimens examined, it is thought that it is very difficult to distinguish these species by both the width of the basal yellow point of the elytra and the width of the antenna. It is thought that male genital organ and mesosternum structures can give a clearer distinction character. In this study, it is thought that the visual (dorsal hooks of the aedeagus) which is given in figures 19 and 21, to differentiate from the male genitalia, can contribute to the current literature. Also, compared to the current literature of the male genital organ of this species, it was found to compatible with the drawings of Bologna [18] rather than the drawing of Moslemi et al. [23].

Hycleus sexmaculatus (Olivier, 1811)

Male Genital Organ Morphology (Figure 22): For detailed description, see Serri et al. [32].

Remarks: Compared to the current literature of the male genital organ of this species, it was found to compatible with the drawing in the findings of Serri et al. [32] and Iablokoff-Khnzorian [16]. Also, the elytral pattern of this species varies. The elytral pattern of the examined specimens in this study is compatible with the drawing of Marseul [3], Iablokoff-Khnzorian [16] and Serri et al. [32] rather than drawing in the findings of Bologna [18]. Iablokoff-Khnzorian [16] was drawn the antenna of this species, but it is seen that the last segment is quite short and chunk and this drawing is thought to belong to the female specimen.
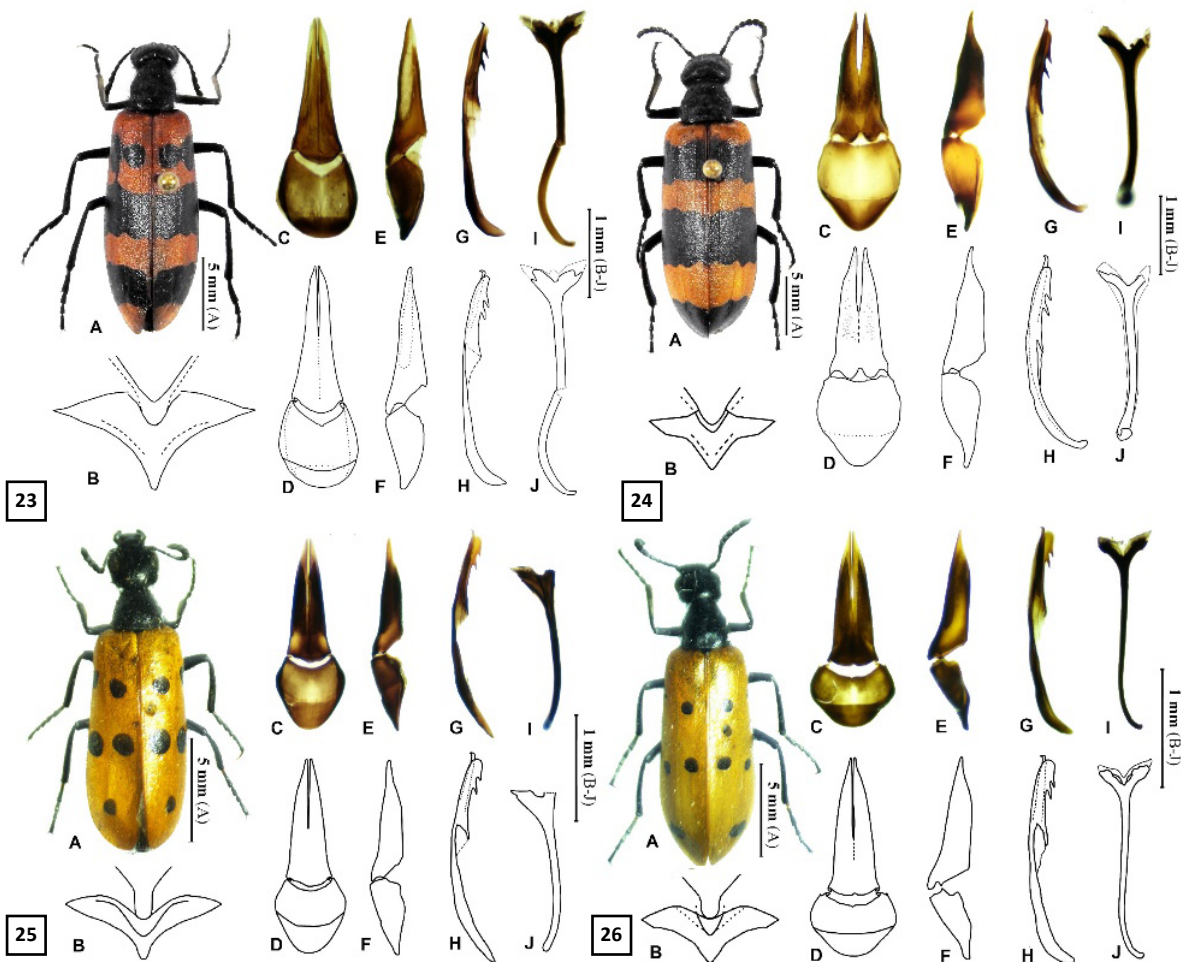
Figure 23-26. 23. *Mylabris (E.) calida*, 24. M. *(E.) cincta*, 25. M. *(E.) crocata*, 26. M. *(E.) fabricii*. A. Habitus (♂), B. Mesosternum, C-J. Male genitalia photos and drawings (C-D. Tegmen (ventral view), E-F. Tegmen (lateral view), G-H. Aedeagus (lateral view), I-J. Spiculum gastrale).

Table 7. Differential diagnosis characters on male genital structures of examined species belonging to *Mylabris (Eumylabris).*

Male genital structures/Species	M. (E.) calida	M. (E.) cincta	M. (E.) crocata	M. (E.) fabricii
Fusion state of Gonoforceps (Ventral view)	Medio-distally fused	Medially fused	Medio-proximally fused	Proximally fused
Gonoforceps (Lateral view)	Gradually narrowing from basal to apical	Narrowing from basal to proximal, almost parallel from proximal to distal, suddenly narrowing from distal to apical	Almost cylindrical at the basal, gradually narrowing towards the apical	Almost conical, suddenly narrowing from basal to proximal, gradually narrowing from proximal to apical
Dorsal hooks of aedeagus	Hooks almost equal-sized, differently curved	Proximal hook distinctly larger	Proximal hook slightly larger	Hooks almost equal-sized
Spiculum gastrale (Ventral view)	Spiculum gastrale deeply "V" shaped notched at apex	Spiculum gastrale deeply "V" shaped notched at apex	Spiculum gastrale slightly deep "V" shaped notched at apex	Spiculum gastrale deeply "V" shaped notched at apex
Apodeme of the spiculum gastrale	Relatively long	Relatively long	Wide and relatively short	Relatively long

Genus: **Mylabris** Fabricius, 1775
This genus is represented by 16 subgenera and 173 species in Palaearctic Region [13-15, 33, 34], and is represented by 6 subgenera and 33 species in Turkey [13, 15, 35]. In this study, male specimens of 10 species (most species) and 3 subgenera belonging to this genus were examined. These subgenera are *Eumylabris* Kuzin, 1954, *Micrabris* Kuzin, 1954 and *Mylabris* Fabricius, 1775.

Subgenus: **Eumylabris** Kuzin,1954
This subgenus is represented by 19 species in the Palaearctic Region, 5 species in Turkey [15]. Bologna et al. [36] reported that this subgenus needs revision, there are many undefined species, and some defined taxa may also be synonymous. In this study, male specimens of four species belonging to this subgenus were examined. These species are *Mylabris (Eumylabris) calida, M. (E.) cincta, M. (E.) crocata* and *M. (E.) fabricii*. There is no taxonomic key covering all species identified in the current literature [3, 5, 8, 16-18, 22, 23, 29, 30]. While the species were determined, descriptions, drawings of mesosternum, and male genitalia were compared. Also, as seen below, male genital organs show some differs in the current literature. Whether this difference is due to drawings, whether it is due to variation in male genital organs of different populations, or if it is drawings of different taxa, by re-examining all species of this subge-

nus and, as reported by Bologna et al. [36], it is thought that the subgenus can be understood by revision. Differential diagnosis characters on male genital structures of examined species belonging to this subgenus were given Table 7.

Mylabris (Eumylabris) calida (Pallas, 1782)
Male Genital Organ Morphology (Figure 23): Gonoforceps fused medio-distal in ventral view; in lateral view relatively flat, gradually narrowing from basal to apical; aedeagal distal hook far from the apex, is same in shape, differently curved from the proximal hook, the endophallic hook is almost at the apex; spiculum gastrale deeply "V" shaped notched at apex, the apodeme relatively long.

Remarks: It was reported by Bologna [18] that description and important taxonomic drawings of this species were given by Pardo Alcaida (1954). However, due to the difficulty of accessing this publication, the description of the male genital organ is also given here. Compared to the current literature, it is very similar to the male genital organ drawing (given as *M. (E.) posticalis* (Dokhtouroff, 1889)) in the findings of Pan et al. [11]. Also, the drawing in this study was observed that the drawings of Kuzin [30] and Iablokoff-Khnzorian [16] were compatible with except for minor differences.

Mylabris (Eumylabris) cincta Olivier, 1795

Male Genital Organ Morphology (Figure 24): Gonoforceps fused medially in ventral view; in lateral view narrowing from basal to proximal, almost parallel from proximal to distal, suddenly narrows from distal to apical; aedeagal distal hook far from the apex, is different in shape, the distal hook of aedeagus clearly short and thick than the proximal one, the endophallic hook is at the apex; spiculum gastrale deeply "V" shaped notched at apex, the apodeme relatively long.

Remarks: It was reported by Bologna [18] that description and important taxonomic drawings of this species were given by Pardo Alcaida (1954). However, due to the difficulty of accessing this publication, the description of the male genital organ is also given here. Compared to the current literature, it has been observed that there are quite different drawings. Although the hooks of Aedeagus are compatible with the drawing given by findings of Iablokoff-Khnzorian [16] from Armenia, the proximal hook of the aedeagus looks quite long and curved; in the drawing in Moslemi et al. [23] findings, the proximal hook is quite short and chunk.

Mylabris (Eumylabris) crocata (Pallas, 1781)

Male Genital Organ Morphology (Figure 25): For detailed description, see Bologna [8].

Remarks: Elytral pattern of specimens belonging to this species, with five (2:2:1) spots are similar to *M. fabricii*. This species was determined with examining mesosternum structure and male genital organ. Compared with the current literature, male genitalia of this species is compatible with the drawing and description in the findings of Bologna [8, 18]. However, in both studies, aedeagus and gonoforceps were evaluated only laterally and the ventral view of gonoforceps could not be compared. In the studies of Serri et al. [17], the aedeagus was not drawn, and the drawing of the gonoforceps structure from the ventral and lateral is more similar to the male
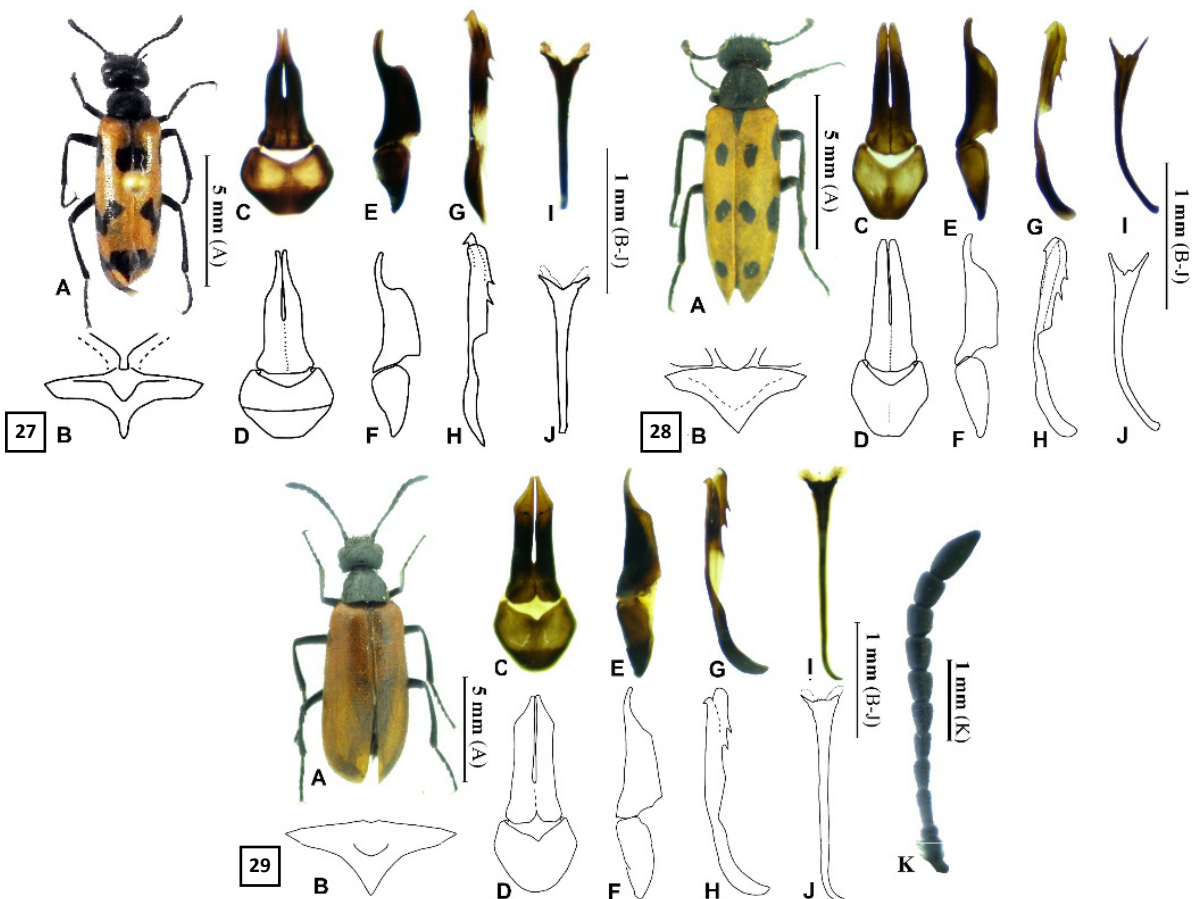
Figure 27-29. 27. *Mylabris (Mic.) geminata*, 28. *M. (Mic.) laevicollis*, 29. *M. (Mic.) unicolor*. A. Habitus (♂), B. Mesosternum, C-J. Male genitalia photos and drawings (C-D. Tegmen (ventral view), E-F. Tegmen (lateral view), G-H. Aedeagus (lateral view), I-J. Spiculum gastrale).

Table 8. Differential diagnosis characters on male genital structures of examined species belonging to *Mylabris (Micrabris).*

Male genital structures / Species	M. (Mic.) geminata	M. (Mic.) laevicollis	M. (Mic.) unicolor
Fusion state of Gonoforceps (Ventral view)	Medio-proximally fused	Proximally fused	Proximally fused
Gonoforceps (Ventral view)	Narrowing from basal to proximal, parallel from proximal to distal, suddenly narrowing from distal to apical, separated apex	Narrowing from basal to proximal, relatively parallel from proximal to apical, narrowing at the apical, rounded apex	Narrowing from basal to proximal, parallel from proximal to distal, narrowing at the apical, parallel in the apex
The basal part of gonoforceps (Ventral view)	Straight	Shallow emarginated	Deeply emarginated
Gonoforceps (Lateral view)	Gradually narrowing from basal to distal, distally with large round grooves	Relatively parallel from basal to the distal, sharp narrowing at distal, thin apical	Parallel from basal to the distal, sharp narrowing at distal, thin apical
Dorsal hooks of aedeagus	Hooks almost equal-sized	The distal hook wider and shorter	Hooks almost equal-sized, the distal hook thinner

Mylabris (Eumylabris) fabricii Soumacov, 1924
Male Genital Organ Morphology (Figure 26): For detailed description, see Bologna [8].

Remarks: Compared with the current literature, male genitalia of this species is compatible with the drawing and description in the findings of Bologna [8, 18]. However, in both studies, aedeagus and gonoforceps were evaluated only laterally and the ventral view of gonoforceps could not be compared. In studies in Iran [17, 22, 23], the male genital organ drawings are quite similar to the *M. (E.) crocata* determined in this study.

Subgenus: ***Micrabris*** Kuzin, 1954
This subgenus is represented by 19 species in the Palaearctic Region, 5 species in Turkey [15]. In this study, male specimens of three species belonging to this subgenus were examined. These species are *Mylabris (Micrabris) geminata, M. (Micrabris) laevicollis* and *M. (Micrabris) unicolor.* Differential diagnosis characters on male genital structures of examined species belonging to this subgenus were given Table 8.

Mylabris (Micrabris) geminata Fabricius, 1798
Male Genital Organ Morphology (Figure 27): For detailed description, see Bologna [8].

Remarks: Compared to the current literature of the male genital organ of this species, it was found to compatible with the drawings included in the findings of Bologna [8, 18] and Iablokoff-Khnzorian [16]. However, in both studies, aedeagus and gonoforceps were evaluated only laterally and the ventral view of gonoforceps could not be compared.

Mylabris (Micrabris) laevicollis Marseul, 1870
Male Genital Organ Morphology (Figure 28): Gonoforceps fused proximally in ventral view, narrowing from basal to proximal, relatively parallel to proximal to apical, narrowing at the apical, rounded apex; in lateral view relatively parallel to basal to distal, sharp narrowing at distal, thin apical; aedeagal distal hook far from the apex, is different in shape, the distal hook of aedeagus clearly long and thick than the proximal one, the endophallic hook is almost at the apex, wide and sharply curved; the apodeme of the spiculum gastrale are thinning, relatively short

Remarks: Compared to the current literature of the male genital organ of this species, it was found to compatible with the drawing included in the finding of Iablokoff-Khnzorian [16]. However, aedeagus and gonoforceps were evaluated only laterally and the ventral view of gonoforceps could not be compared.

Mylabris (Micrabris) unicolor Faldermann, 1837

Male Genital Organ Morphology (Figure 29): Gonoforceps fused proximally in ventral view, narrowing from basal to proximal, parallel to proximal to distal, narrowing at the apical, parallel in apex; basal of parameres deeply emarginated; in lateral view parallel to basal to the distal, sharp narrowing at distal, thin apical; aedeagal distal hook far from the apex, is almost equal in length, the distal hook of aedeagus narrower than the proximal one, the endophallic hook is at the apex, wide and sharply curved; the apodeme of the spiculum gastrale are thin and short

Remarks: This species, as reported by Pan and Bologna [13], *M.* (s.str.) *concolor* Marseul 1870 is very similar and morphological characters of these species, especially the male genital organ and mesosternum, should be examined carefully. Compared to the current literature of the male genital organ of this species, it was found to compatible with the drawing included in the finding of Iablokoff-Khnzorian [16]. However, aedeagus and go-

Subgenus: ***Mylabris*** Fabricius, 1775

This subgenus is represented by 26 species in Palaearctic Region [13, 15, 33, 34, 37, 38] and 9 species in Turkey [13, 15]. This subgenus was revised Pan and Bologna [13] and species descriptions, diagnostic keys and drawings of some taxonomic characters (male genitals, mesosternums and elytral patterns) are given. In this study, male specimens of three species belonging to this subgenus were examined. These species are *Mylabris* (s. str.) *olivieri, M.* (s. str.) *quadripunctata* and *M.* (s. str.) *variabilis*. Differential diagnosis characters on male genital structures of examined species belonging to this subgenus were given Table 9.

Mylabris (s.str.) ***olivieri*** Billberg, 1813

Male Genital Organ Morphology (Figure 30): For detailed description, see Bologna [8] and Pan and Bologna [13].

Remarks: Compared to the current literature of the male genital organ of this species, it was found to com-
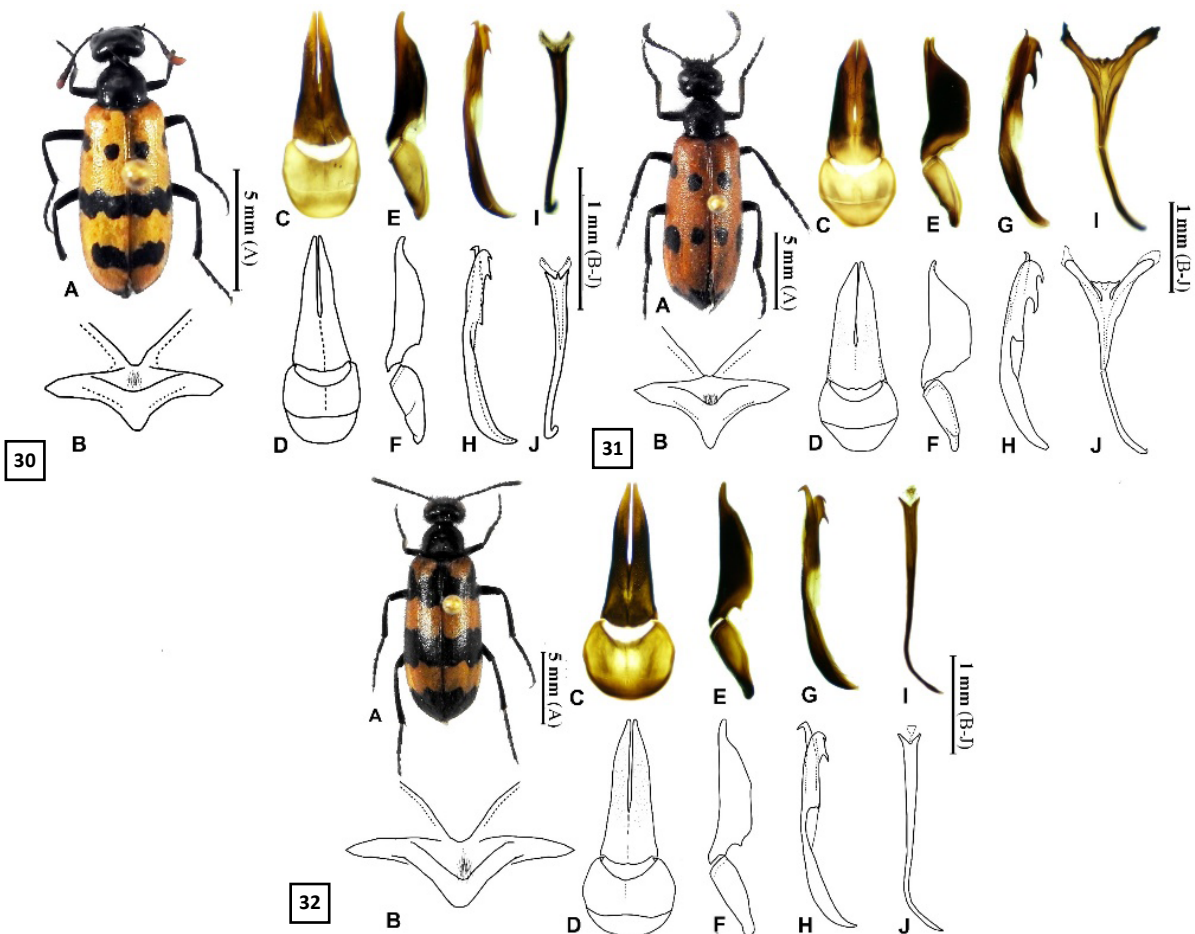
Figure 30-32. 30. *Mylabris (s.str.) olivieri*, 31. *M. (s.str.) quadripunctata*, 32. *M. (s.str.) variabilis*. A. Habitus (♂), B. Mesosternum, C-J. Male genitalia photos and drawings (C-D. Tegmen (ventral view), E-F. Tegmen (lateral view), G-H. Aedeagus (lateral view), I-J. Spiculum gastrale).

Table 9. Differential diagnosis characters on male genital structures of examined species belonging to *Mylabris (Mylabris)*.

Male genital structures/ Species	M. (s.str.) olivieri	M. (s.str.) quadripunctata	M. (s.str.) variabilis
Fusion state of Gonoforceps (Ventral view)	Medially fused	Proximally fused	Proximally fused
Gonoforceps (Ventral view)	Gradually narrowing from basal to medial, almost parallel from medial to distal, gradually narrowing from distal to apical	Slightly narrowing from basal to distal, suddenly from distal to apical	Gradually narrowing from basal to medial, almost parallel from medial to distal, gradually narrowing from distal to apical
Gonoforceps (Lateral view)	Slender	Very wide	Slender
The apical lobe of Gonoforceps (lateral view)	Curved	Slightly curved	Slightly curved
Dorsal hooks of Aedeagus	Proximal hook slightly larger	Proximal hook much larger	Proximal hook larger

Mylabris (s.str.) ***quadripunctata*** (Linnaeus, 1767)
Male Genital Organ Morphology (Figure 31): For detailed description, see Bologna [8] and Pan and Bologna [13].

Remarks: Compared to the current literature of the male genital organ of this species, it was found to compatible with the drawing included in the finding of Bologna [8] and Pan and Bologna [13]. According to Pan and Bologna [13], this species is very similar to *M.* (s. str.) *cernyi* Pan and Bologna, 2014, and is distinguished by examined their genitalia. In this study, many specimens were examined, and diagnoses were supported.

Mylabris (s.str.) ***variabilis*** (Pallas, 1782)
Male Genital Organ Morphology (Figure 32): For detailed description, see Bologna [8] and Pan and Bologna [13].

Remarks: According to Pan and Bologna [13], this species is similar to *M.* (s.str.) *ciliciensis* (Escherich, 1899) and commonly confused with it, being distinguished with frontal red spot wide, antennomeres usually black, structures of scutum and male genitalia. Compared to the current literature of the male genital organ of this species, it was found to compatible (except minor differs) with the drawing included in the finding of Bologna

[8] and Pan and Bologna [13]. It is thought that these small differences, especially in the proximal hook of the aedeagus, may be due to the position of the aedeagus.

CONCLUSION

When the current literature on genital organs of this family is examined, Gupta [24] 's a higher classification based on the structure of male and female genital organs draws attention. In the publication of Gupta [24], a total of 15 tribe and many genera belonging to Meloinae and Nemognathinae subfamilies were studied. However, since only the structure of the genital organs was examined, differences were observed in the taxonomic situations of many higher taxa and therefore this classification was not accepted [8]. In the current classification of the family, first-instar morphology, adult morphology and adult behavior characters were used [39], then this classification as combined with the molecular data set (nuclear ITS2 and mitochondrial 16S) was supported [1].

Male genital organs from species determined in this study and current literature [8, 11, 13, 16-19, 22-24, 30] were examined. As a result, it is thought that they give important taxonomic characters for the Meloidae family as well as in many other Coleoptera families. Ho-

wever, this does not mean that other taxonomic characters are less important or not and that species determine can only be made on the male genital organ. The combined use of taxonomic characters gives the most accurate results.

R e f e r e n c e

1. M.A. Bologna, M. Oliverio, M. Pitzalis, P. Mariottini, Phylogeny and evolutionary history of the blister beetles (Coleoptera, Meloidae), Mol. Phylogenet. Evol., 48 (2008) 679-693.
2. M.A. Bologna, F. Turco, J.D. Pinto, 11.19. Meloidae Gyllenhal 1810. In Leschen RAB, Beutel RG, Lawrence JF, editors. Handbook of Zoology. Coleoptera, Beetles. Berlin, Germany, 681-693, 2010.
3. S.A. de Marseul, Monographie des Mylabrides d'Europe, et des contrées limitrophes en Afrique et en Asie, L'Abeille, vol 7, 1870.
4. K. Escherich, Revision der palaearktischen Zonitiden, einer Unterfamilie der Meloiden, Verh. Naturf. Vereins. Brünn. 35 (1897) 96-132.
5. G. Sumakov, Les espèces paléarctiques du genre Mylabris Fabr.(Coleoptera, Meloidae), Hor. Soc. Ent. Rossicae, 42 (1915) 1-71.
6. J. Mařan, Specie rum generis Lydus (Subg. Alosimus Muls.) ex affinitate speciei Lydus syriacus L. revisio. Coleoptera Meloidae Sb. Entomol. Odd. Zem. Mus. Praze, 20 (1942) 78-98.
7. Z. Kaszab, Neue Revision der Gattung Alosimus Muls.(Col., Meloidae), Annls. Hist-Nat. Mus. Natn. Hung., 1 (1951) 138-150.
8. M.A. Bologna, Coleoptera Meloidae, Edizioni Calderini, Italy, vol 28, 1991.
9. M.A. Bologna, J.D. Pinto, The Old World genera of Meloidae (Coleoptera): a key and synopsis, J. Nat. Hist., 36 (2002) 2013-2102.
10. M.A. Bologna, A. Di Giulio, M. Pitzalis, Systematics and biogeography of the genus Actenodia (Coleoptera: Meloidae: Mylabrini), Syst. Entomol., 33 (2008) 319-360.
11. Z. Pan, X. Wang, G. Ren, Taxonomy of Mylabris (Eumylabris) Kuzin (Coleoptera: Meloidae) from China, Entomotaxonomia, 32 (Suppl.) (2010) 34-42.
12. F. Turco, M.A. Bologna, Systematic revision of the genus Cerocoma Geoffroy, 1762 (Coleoptera: Meloidae: Cerocomini), Zootaxa, 2853 (2011) 1-71.
13. Z. Pan, M.A. Bologna, Taxonomy, Bionomics and Faunistics of the Nominate Subgenus of Mylabris Fabricius, 1775, with the description of five new species (Coleoptera: Meloidae: Mylabrini), Zootaxa, 3806 (2014) 1-78. Bologna, Phylogenetic systematics of Mylabris blister beetles (Coleoptera, Meloidae): a molecular assessment using species trees and total evidence, Cladistics, 35 (2019) 243-268. https://doi.org/10.1111/cla.12354
14. M.A. Bologna, Meloidae, in Catalogue of Palaearctic Coleoptera (Volume 5: Tenebrionoidea), Editors I. Löbl and A. Smetana, Apollo Books, Strenstrup, 384-390, 2008.
15. S. Iablokoff-Khnzorian, Fauna Armenia SSR. Meloidae and Alleculidae, Akademia Nauk Armeniskoye SSR, Institut Zoologii, Vol 5, 1-155, 1983.
16. S. Serri, H. Boroumand, S. Pashaeirad, P. Kharazi, An Identification Guide to Meloid Beetles (Coleoptera: Meloidae) of Tehran Province Iran J. Biol., 19 (2006) 87-97.
17. M.A. Bologna, Meloidae di Turchia. I.(Coleoptera), Fragm. Entomol., 15 (1979) 143-199.
18. J. Ruiz, Nuevos datos sobre Zonitis fernancastroi Pardo Alcaide, 1950 en el sur de la Península Ibérica (Coleoptera, Meloidae), Boletín de la S.E.A., 33 (2003) 95-99.
19. M.A. Bologna, Note su Eurymeloe e revisione delle specie euromediterranee del gruppo rugosus (Coleoptera, Meloidae), Fragm. Entomol., 20 (1988) 233-301.
20. M.A. Bologna, Un nuovo Alosimus del litorale tirrenico e note tassonomiche su altre specie congeneriche nord africane (Coleoptera, Meloidae), Fragm. Entomol., 21 (1989) 191-204.
21. A. Faraji, S. Pashaie, A. Shayestehfar, Taxonomic study of blister beetles (Coleoptera: Meloidae) in Arak county, Iran, Exp. Anim. Biol. 1 (2012) 55-68.
22. R. Moslemi, S. Pashaie Rad, S. Serri, An identification guide to meloid beetles (Coleoptera: Meloidae) (Insecta; Coleoptera) of Markazi province, J. Anim. Res. (Iran J. Biol.), 28 (2015) 105-115.
23. A. Gupta, External Genitalia of Meloidae (Coleoptera) III. Significance of some genitalic components in the higher classification of the family, Dtsch. entomol. Z., 25 (1978) 131-157.
24. Z. Kaszab, Eine neue Lydus-Art aus Kleinasien, nebst einer Bestimmungstabelle der bisher bekannten Arten der Gattung Lydus sensu stricto (Col., Meloidae), Annls. Hist-Nat. Mus. Natn. Hung., 43 (1952) 95-99.
25. Z. Kaszab, Über die Arten der Gattüng Oenas, Acta Biol. Acad. Sci. Hung., 2 (1951) 275-279.
26. A. Riccieri, E. Mancini, D. Salvi, M.A. Bologna, Phylogeny, biogeography and systematics of the hyper-diverse blister beetle genus Hycleus (Coleoptera: Meloidae), Mol. Phylogenet. Evol., 144 (2020) 106706.
27. A.G. Olivier, Encyclopédie méthodique, ou par ordre de matières; par une société de gens de lettres, de savans et d'artistes; précédée d'un vocubulaire universel, servant de table pour tout l'ouvrage, ornée des portraits de Mm. Diderot & d'Alembert, premiers éditeurs de l'Encyclopédie. Histoire naturelle. Insectes. Tome Huitième. H. Agasse, Paris, 722, 1811.
28. S.A. de Marseul, Monographie des Mylabrides. Mémoires de la Société royale des Sciences de Liège, 363–662, 1872.
29. V. Kuzin, K posnanyju systemy narybnikov (Coleoptera, Meloidae, Mylabrini), Trudly Usesojnogo Entomologizesko Obzestva, 44 (1954) 336-379.
30. M.A. Bologna, I Meloidae della Grecia (Coleoptera), Fragm. Entomol., 25 (Suppl.) (1994) 1-119.

31. S. Serri, M.A. Bologna, A. Riccieri, Revision of the *Hycleus sexmaculatus* species group (Coleoptera: Meloidae, Mylabrini), Zootaxa, 4790 (2020) 1-42.

32. S. Serri, Z. Pan, M.A. Bologna, A new *Mylabris* species from south-eastern Iran and a key to the Iranian species of the nominate subgenus (Coleoptera, Meloidae), ZooKeys, 219 (2012) 81-86.

33. L. Černý, V. Vrabec, *Mylabris* (*Mylabris*) *snizeki* sp. nov. from Jordan, with a key to the Jordanian species of the nominotypical subgenus (Coleoptera: Meloidae), Zootaxa, 4555 (2019) 146-150.

34. 35. M. Kemal A.Ö. Koçak, A new *Mylabris* species and subgenus for the fauna of Turkey, Cesa News 84 (2012) 12-14.

35. M.A. Bologna, L. Cerny, A. Zubair, Meloidae (Coleoptera) of Pakistan and Kashmir with the description of three new species, new faunistic and taxonomic records, and a zoogeographic analysis, Turk J. Zool., 42 (2018) 637-660.

36. M.A. Bologna, F. Turco, The Meloidae (Coleoptera) of the United Arab Emirates with an updated Arabian checklist, Zootaxa, 1625 (2007) 1-33.

37. M.A. Bologna, The Meloidae (Coleoptera) of Libya: an annotated catalogue and description of three new species, Ann. Soc. Entomol. Fr., 45 (2009) 345-364.

38. M.A. Bologna, J.D. Pinto, Phylogenetic studies of Meloidae (Coleoptera), with emphasis on the evolution of phoresy, Syst. Entomol., 26 (2001) 33-72.

Research Article

Automated Cell Viability Analysis in Tissue Scaffolds

Doku İskelelerinde Otomatik Hücre Canlılığı Analizi

Tansel Uyar[1,2], **Aykut Erdamar[2]**, **Menemşe Gümüşderelioğlu[1]**, **Mehmet Fevzi Akşahin[2]**,
Gülseren Irmak[1,3], **Osman Eroğul[4]**

[1]Department of Bioengineering, Hacettepe University, Ankara, Turkey.

[2]Department of Biomedical Engineering, Başkent University, Ankara, Turkey.

[3]Department of Bioengineering, Turgut Özal University, Malatya, Turkey.

[4]Department of Biomedical Engineering, TOBB University of Economics and Technology, Ankara, Turkey.

ABSTRACT

Image analysis of cell biology and tissue engineering is time-consuming and requires personal expertise. However, evaluation of the results may be subjective. Therefore, computer-based learning and detection applications have been rapidly developed in recent years. In this study, Confocal Laser Scanning Microscope (CLSM) images of the viable pre-osteoblastic mouse MC3T3-E1 cells in 3D bioprinted tissue scaffolds, captured from a bone tissue regeneration study, were analyzed by using image processing techniques. The aim of this study is to develop a reliable and fast algorithm for the automated analysis of live/dead assay CLSM images. Percentages of live and dead cell areas in the scaffolds were determined, and then, total cell viabilities were calculated. Furthermore, manual measurements of four different analysts were obtained to evaluate subjectivity in the analysis. The measurement variations of analysts, also known as the coefficient of variation, were determined from 13.18% to 98.34% for live cell images and from 9.75% to 126.02% for dead cell images. Therefore, an automated algorithm was developed to overcome this subjectivity. The other aim of this study is to determine the depth profile of viable cells in 3D tissue scaffolds. Consequently, cross-sectional image sets of three different types of tissue scaffolds were analyzed.

Key Words

Image correlation; edge detection; cell area counting; tissue engineering.

ÖZ

Hücre biyolojisi ve doku mühendisliğinde görüntü analizi zaman alan ve kişisel uzmanlık gerektiren bir işlemdir. Ancak sonuçların değerlendirilmesi öznel olabilir. Bu nedenle bilgisayar destekli öğrenme ve tespit uygulamaları son yıllarda hızla gelişmiştir. Bu çalışmada, bir kemik dokusu rejenerasyon çalışmasından yakalanan, 3D biyo-baskılı doku iskelelerinde canlı pre-osteoblastik fare MC3T3-E1 hücrelerinin Konfokal Lazer Taramalı Mikroskop (CLSM) görüntüleri, görüntü işleme teknikleri kullanılarak analiz edilmiştir. Bu çalışmanın amacı, canlı/ölü analizi CLSM görüntülerinin otomatik analizi için güvenilir ve hızlı bir algoritma geliştirmektir. İskelelerdeki canlı ve ölü hücre alanlarının yüzdeleri belirlenmiş ve ardından toplam hücre canlılıkları hesaplanmıştır. Ayrıca, analizde öznelliği değerlendirmek için dört farklı analistin manuel ölçümleri yapılmıştır. Varyasyon katsayısı olarak da bilinen analistlerin ölçüm varyasyonları, canlı hücre görüntüleri için % 13.18 ile % 98.34 ve ölü hücre görüntüleri için % 9.75 ile % 126.02 arasında belirlenmiştir. Bu nedenle, bu öznelliği aşmak için otomatik bir algoritma geliştirilmiştir. Bu çalışmanın diğer amacı, 3 boyutlu doku iskelelerindeki canlı hücrelerin derinlik profilini belirlemektir. Sonuç olarak, üç farklı doku iskelesinin kesitsel görüntü setleri analiz edilmiştir.

Anahtar Kelimeler

Görüntü korelasyonu; Kenar algılama; hücre alanı sayımı; doku mühendisliği.

INTRODUCTION

Biological images contain patterns, objects and/or living cells that provide functional information about the structure or system being viewed. Some of these images may belong to artificial materials, while others may belong to the culture images of cellular structures. Various imaging techniques such as confocal laser scanning microscopy (CLSM), scanning electron microscopy, and optical microscopy can be used to obtain images of materials or cells [1,2]. These images can be examined using semi-automatic and/or fully-automatic software [3–5]. Many researchers use image analysis programs such as ImageJ to perform manual analysis [6]. Various information about abiotic environments, such as cells and tissue, can be obtained from this software. For example, some tissue scaffold properties such as fiber diameter, pore diameter and permeability can be determined, and also cell and tissue properties such as the amount of cell, percentage of cell viability, area covered by cells can be analyzed [7-20]. There are several approaches to analyze these properties and obtain the analytical data. One of these approaches is user-dependent utilities (Image J, etc). In user-dependent approach, analyses take a very long time and also require personal expertise [21]. Other approaches are semi-automated and fully-automated analysis software which user does not have direct influence. They shorten the analysis time and reduce the dependency on the user. Thus, subjective results derived from the user can be avoided. There are various studies in the literature about automatic approaches [22]. Confocal microscopy images were used to identify glial fibrillary acidic proteins (GFAP) found in brain astrocytes in one of the studies and an algorithm was developed to classify cells [23]. In a similar study, the region of the cell nucleus was identified in an image obtained from mouse hippocampus by staining cell nuclei and RNA in different colors [24]. Piccinini et al. studied optical microscopy images obtained by staining dead cells with trypan blue. These images were analyzed and live and dead cells were classified [25]. In another study, an algorithm was developed to distinguish myelin sheath and nerve itself from the nerve through the SEM images of a nerve bundle. The axons in the inner part of the nerve bundle and the myelin sheaths that surrounding these axons were determined separately and a distribution graph of the diameters of the nerve fibers in the nerve bundle was extracted [26].

In this study, CLSM images obtained from MC3T3-E1 pre-osteoblastic cells (osteoblast precursor) on alginate and alginate-HAp (hydroxyapatite) tissue scaffolds were used. At first, the percentages of the area of the live and dead cells were calculated by four different analysts using ImageJ utility. Then, the developed algorithm was performed semi-automatically for the same analysis and the percentages of the area that belongs to the live and dead cells were calculated. The innovative approach of the developed method is adaptive and calculates the area percentages of the dead cells according to similar studies in the literature. In the presented method, firstly raw images were separated by the pre-processing step. Afterwards, an image correlation algorithm for living cells, and an adaptive statistical approach for dead cells were developed. Then, the results of the algorithm and visual scoring were compared. Moreover, the coefficient variance was calculated to determine the measurement deviation between manual analyses. After the algorithm was successfully developed, cross-sectional CLSM images of live MC3T3-E1 cells in three different tissue scaffolds (alginate-HAp, conventional Gel-MA and microwave-assisted Gel-MA) were analyzed. Using these image sets, it was determined how the viability of the cells changed depending on the depth of the tissue scaffold in further studies. All cross-sectional images were examined, and a percentage of the viability related to depth was calculated. This characterization process is another innovative aspect of this study. The maximum and minimum cell viability was determined as a function of depth.

MATERIALS and METHODS

Production of Tissue Scaffolds
Alginate and Alginate-Hydroxyapatite (HAp) scaffolds
Alginate and alginate-HAp tissue scaffolds were produced by cross-linking reaction. Sodium alginate was dissolved in PBS (pH: 7.4) at a concentration of 3% (w/v). $CaSO_4$ (1%,w/v) was added into the sodium alginate solution to initiate internal gelation. Then, internal cross-linking was carried out by mixing the two solutions via a three-way valve. The mixing ratios of $CaSO_4$ and sodium alginate solutions were optimized in terms of printability and gelation. For encapsulation of cells, MC3T3-E1 pre-osteoblasts were dispersed in hydrogels at a density of 3×10^7 cells/mL. The resulting viscous solution was imprinted in 24-well Petri dishes via Fab@Home bioprinter. As a result of the extruder-based imprinting

process, cell-entrapped constructs in cylindrical geometry (6 mm x 1 mm) were obtained. These constructs were cross-linked with $CaCl_2$ and transferred to the cell culture stage in the presence of nutrient medium in a CO_2 incubator. The same process was repeated with the addition of the nano-HAp, which was produced by the biomimetic approach [27], into the sodium alginate solution, thus alginate-HAp tissue scaffolds including MC3T3-E1 cells were obtained.

Methacrylated gelatin (Gel-MA) scaffolds

Gelatin was methacrylated by two ways: Conventional method [28] and microwave-assisted methacrylation [29]. The reaction products, conventional Gel-MA and microwave-assisted Gel-MA, were dried in a freeze-dryer (Christ, Germany) and stored at -80ºC until hydrogel preparation steps. Methacrylated gelatin (Gel-MA) hydrogels were prepared by photo-crosslinking in the present of photo-initiator (Irgacure, 0.3 w/v). Irgacure was completely dissolved in PBS (pH: 7.4) at 50ºC. Gel-MA was dissolved in this solution at 37 ºC. MC3T3-E1 mouse pre-osteoblast cells were gently dispersed and mixed into sterile hydrogel solutions at a density of 2×10^7 cells/mL A cell-bio-ink mixture was loaded into the deposition syringes of Fab@Home bioprinter and printed along the X–Y–Z target paths. After printing, cell-laden hydrogel disks (6 mm × 1 mm) were immediately crosslinked with UV (320-480 nm) light at an intensity of 200 mW/cm² for 40 s.

Imaging of Cell Viability

Alginate and alginate-HAp hydrogel scaffolds

In this study, the images that were used for viability analysis were captured by using a confocal laser scanning microscope (Zeiss, LSM510) with a live / dead analysis molecular probe (Life Technology). Images were captured in sequential scanning mode using 0.5, 20x/0.5 and 1 AU values in numerical aperture number, objective magnification (Zeiss Plan-Neofluar objecti-

ve) and pinhole size parameters, respectively. On days 3 and 9 of the culture, cell-containing hydrogels were washed with PBS (pH: 7.4) and incubated with 2 µM calcein AM and 4 µM ethidium homodimer (EthD-1) before imaging. In this protocol, live cells were stained green with fluorescein marker calcein acetoxymethyl (calcein AM), while dead cells were stained red with EthD-1 [27]. The true color (RGB) images obtained by the aforementioned technique were recorded in a 'tif' image format with a size of 1024x1024 (Real size equivalent in material: 460 µm x 490 µm) pixels.

Conventional and microwave-assisted Gel-MA hydrogel scaffolds

The cell viability of these group of hydrogels were examined using a live/dead viability kit. The cell-laden hydrogels were washed in PBS and incubated in 2 µM Calcein AM and 4 µM ethidium homodimer (Ethd-1) solution for 30 min. The cell-loaded Gel-MA hydrogels were observed under a confocal microscope (Zeiss, LSM 510) with the same parameters that detailed above. Two image sets of 3D bioprinted tissue scaffolds were taken from on day 3.

Image Processing Techniques for Analysis of Live or Dead Cell Percentages

CLSM images were analyzed using MATLAB 2015b. Images used in the study were obtained from pre-osteoblastic MC3T3-E1 cell cultures. In the cell culture study, 35 different images obtained from 3D bioprinted tissue scaffolds were analyzed. Then, 25 cross-sectional images of three different tissue scaffolds at every 9 µm were taken from each tissue scaffold for cell viability characterization. This process was carried out to investigate the depth-dependent variation of the cell growth rate in experimental cell culture studies. During characterization, the same algorithm was used to determine viability as the function of depth. The block diagram for the developed algorithm was given in Figure 1.
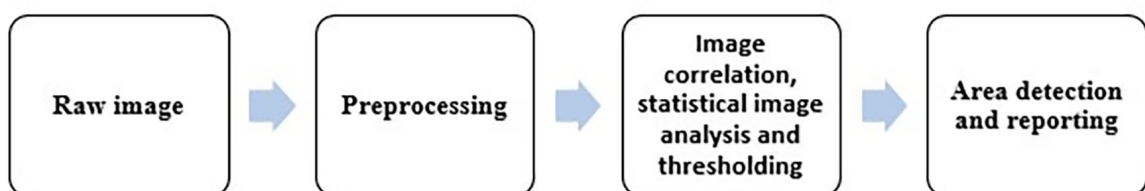
Figure 1. Block diagram of the image analysis algorithm.

Preprocessing

The following algorithm steps were applied to the cell images in the preprocessing part.

Splitting RGB image into layers: RGB image consists of three layers which are red, green, and blue channels. Based on the current staining technique, a green layer for the live cell and a red layer for the dead cell were obtained from the RGB image [27]. In splitting process, overlapped regions were excluded owing to the uncertainty about viability condition.

Removing noises from the image: The noise on the images which was caused by the imaging technique was removed using Wiener adaptive filter. This filter is an effective tool for removing signal-independent zero-mean white Gaussian noise [30]. Noisy image can be modeled as in Eq.1.

$$x_{i,j} = y_{i,j} + n_{i,j}$$

(1)

$x_{i,j}$ is the noisy image, $y_{i,j}$ is the noise-free image and $n_{i,j}$ is the additive Gaussian noise. The aim of the noise removal process is to suppress the noise stemming from noisy image ($x_{i,j}$) by minimizing the mean squared error (MSE). A linear estimate $\hat{y}_{i,j}$ of $y_{i,j}$ is derived from Eq.2 where N is the number of elements in $y_{i,j}$ At this point, Wiener filter minimizes the mean square error between the estimated image $\hat{y}_{i,j}$ and the original image $y_{i,j}$ in Eq.2 [31].

$$MSE(\hat{y}) = \frac{1}{N} \sum_{i,j=1}^{N} (\hat{y}_{i,j} - y_{i,j})^2$$

(2)

$x_{k,l}$ is the density value of a pixel in the NxN image. Pixel-wise adaptive Wiener filter use neighborhoods of size (2n+1)x(2m+1) window to estimate the local image mean and standard deviation. In this study, window size was chosen as 5x5 [32]. It assumes that the noise is stationary with zero mean and variance $\sigma_{i,j}$ and uncorrelated with the original image $x_{k,l}$. Based on these assumptions, Wiener adaptive filter estimates the local mean and variance around each pixel using Eq.3 and Eq.4 [32–34]. If the variance is large, the Wiener filter performs little smoothing. If the variance is small, the Wiener filter performs more smoothing.

$$m_{i,j} = \frac{1}{(2n+1)(2m+1)} \sum_{k=i-n}^{n+i} \sum_{l=j-m}^{m+j} x_{k,l}$$

(3)

$$\sigma_{i,j} = \frac{1}{(2n+1)(2m+1)} \sum_{k=i-n}^{n+i} \sum_{l=j-m}^{m+j} (x_{k,l} - m_{i,j})^2$$

(4)

$$x'_{i,j} = m_{i,j} + \frac{\sigma_{i,j} - v_{i,j}}{\sigma_{i,j}} (x_{i,j} - m_{i,j})$$

$m_{i,j}$ is the local mean in Eq.3 and $\sigma_{i,j}$ is the local variance in Eq.4. Then Wiener filter creates a pixel-wise filtering using these estimates and estimated image is obtained according to Eq.5.

$$x'_{i,j} = m_{i,j} + \frac{\sigma_{i,j} - v_{i,j}}{\sigma_{i,j}} (x_{i,j} - m_{i,j})$$

(5)

$v_{i,j}$ is the local noise variance in Eq.5, was obtained using the mean value of all local estimated variances [32–34].

Smoothing the image with Gaussian filter: After the noise removal step, Gaussian type low-pass filter was applied to fill tiny gaps in cells and to remove high frequency noise. Most edge-detection algorithms are sensitive to noise [35]. This filtering was used because of the edge-detection in the next part. Gaussian matrix (h_g) was generated with 5x5 kernel size due to σ=1 standard deviation in Eq.6 [36]. Gaussian matrix formed in before was convolved with image according to Eq.7 and new softened image (h) was obtained.

$$h_g(n_1, n_2) = e^{\frac{-(n_1^2 + n_2^2)}{2\sigma^2}}$$

(6)

$$h(n_1, n_2) = \frac{h_g(n_1, n_2)}{\sum_{n_1} \sum_{n_2} h_g}$$

(7)

Image correlation, statistical image analysis and thresholding process

In order to obtain live cells contour on the preprocessed image cross-correlation, statistical image analysis and then thresholding steps were performed. Two dimensional cross-correlation function was calculated with Eq.8. X is the MxN sized preprocessed image and H is the PxQ sized template which was selected as a mask in Eq.8. Template was selected in based on pixel size to cover the whole cell. For this reason, P and Q values may change according to the size of the template. At the end of this process, the correlation matrix was obtained in (N+Q-1) x (M+P-1) dimensions [37].

$$C(k,l)=\sum_{m=0}^{M-1}\sum_{n=0}^{N-1}X(m,n)\bar{H}(m-k,n-l)$$

$$-(P-1)\leq k \leq M-1,$$

$$-(Q-1)\leq l \leq N-1, \tag{8}$$

Afterwards, normalization process was performed to the correlated image by using Eq. 9. Where, X' is the normalized cross-correlation matrix, μ is the mean of the cross-correlation matrix and σ is the standard deviation of the cross-correlation matrix.

$$X'=\frac{X-\mu}{\sigma} \tag{9}$$

In the normalization process, the average pixel value of the image was subtracted from each pixel value and the calculated difference was divided by the standard deviation. With this process live cells were identified by positive values. Also, non-viable regions were identified by negative values. Owing to this situation, the threshold value has been set to zero.

Then, edge detection functions were used to extract contours from the thresholded image. For edge detection process, three different algorithms (Sobel, Prewitt and Canny) were applied [37]. For the edge detection process, Sobel kernels in Figure 2a, Prewitt kernels in Figure 2b and Canny kernels in Figure 2c were used for convolution.

In order to minimize the methodological error, three methods were separately used. Then three edge detected images were combined with each other by adding one image. The final edge detected image was superimposed on the raw image.

Adaptive thresholding for dead cells: The thresholding method for living cells has been insufficient for the detection of dead cells. Therefore, a different approach has been developed. In this approach, threshold values for detecting dead cells were obtained adaptively from the images. These threshold values were determined using the statistical analysis of the pixel density histograms of dead cell images. Accordingly, two threshold levels were designated for adaptive thresholding based on dead cell images. is the value obtained by dividing the average values of the image matrix by the standard deviation of the matrix values (Eq.10) and is the average value of the image matrix (Eq.11).

$$threshold1=\left|\frac{mean(matrix)}{standartdeviation(matrix)}\right| \tag{10}$$

$$threshold2=\left|mean(matrix)\right| \tag{11}$$
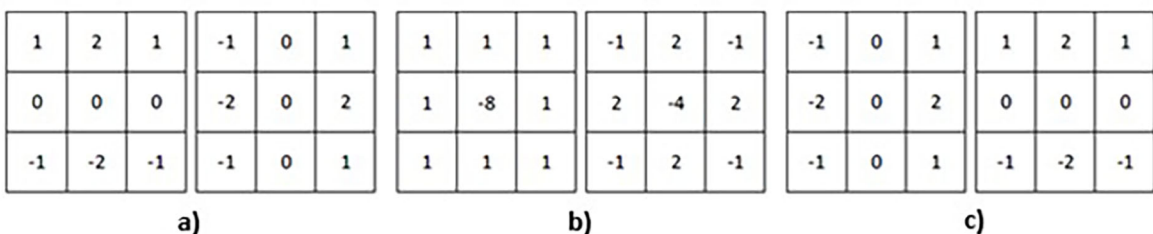
Figure 2. Edge detection kernels used for convolution, a) Sobel kernels, b) Prewitt kernels,   c) Canny kernels.

After these threshold values were calculated, the median values of intensity levels in each line of the image were selected for each row and they were obtained as an one-dimensional vector. The highest value of this vector was selected as a selector for the adaptive thresholding. This value was used for threshold selection. The operation used in the algorithm was explained as a conditional expression in Eq.12.

$$If\ maximum\ value\ median \geq threshold\ 2 \qquad \Rightarrow use\ threshold\ 1;$$
$$If\ maximum\ value\ median < threshold\ 2 \qquad \Rightarrow use\ threshold\ 2;$$
$$(12)$$

Once the threshold value has been selected, dead-cell areas were detected by applying an image thresholding process. After cell lines were identified, dead cell contours were determined with the edge detection method that was explained in advance. Then cell contour image was placed on the gray level image of dead cells.

Detection of cell area and calculation
Calculation of live and dead cell percentages
According to the thresholding process, pixel densities higher than the threshold were set to '1' and the others were set to '0'. On the thresholded images of live and dead cells, cell areas were calculated by counting the values of '1's on image with $pixel^2$ unit. Percentages of cell areas were calculated by dividing the whole pixel on image into cell areas. After the counting process, the area percentages of the cells were reported.
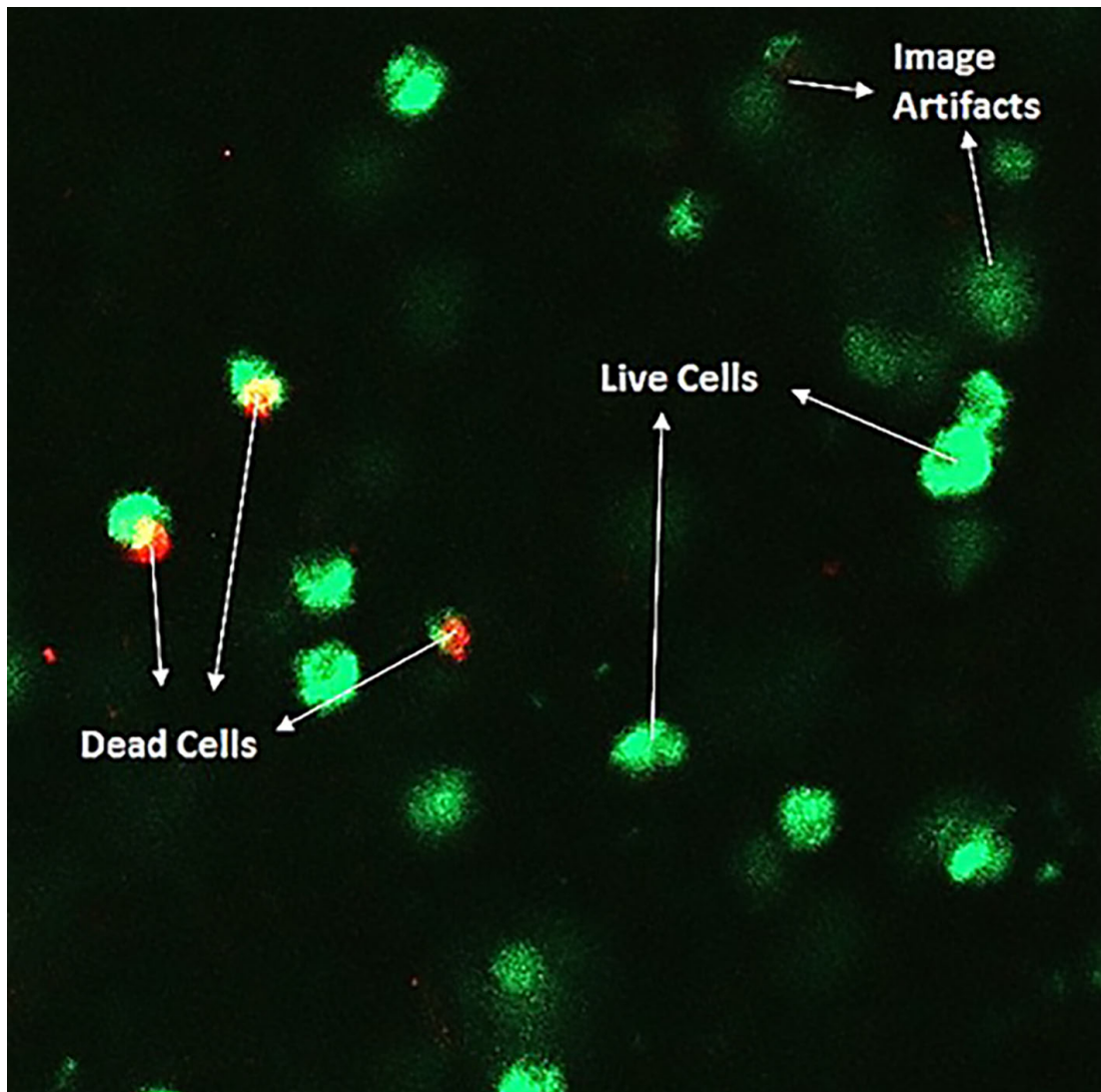
Figure 3. An example of a raw image (3D bioprinted tissue scaffold of alginate-HAp on day 3, Surface image).

Inspection of analysts and reporting of live and dead cell percentages

Images of live and dead cells were analyzed with ImageJ program by four analysts. Each analyst reported his/her measurements and according to these measurements, some of the statistical parameters have been calculated. In this evaluation, average values of calculations, standard deviations and variation coefficient percentages of the numerical values were calculated by the analysts. The variation coefficients, calculated by the mean value ratio of the standard deviation, express how much the distributions in the manual measurements change with respect to the average. The percentage of variation coefficient is the measure of how different analyst are deviating from the average measured value for the same measurement. In other words, it can be described as subjectivity in measurement. Thence, the metrics of the analysts were reported in Experimental Results part.

RESULTS and DISCUSSION

A raw image sample was given in Figure 3. According to the assay protocol, the live cells stained green with calcein AM and the locations of the dead cells stained red with EthD-1 were shown in the Figure 3. Non-cell image artifacts, which produce fluorescence effect by interacting with HAp in the tissue scaffold, were also indicated in this raw image (Figure 3).

In the preprocessing step, firstly the raw image was divided into red, green and blue layers so that dead and living cells can be analyzed separately. In addition, the overlapping parts of the living and dead cells in the red and green layers were also removed to prevent mistakes that may be caused by the dyeing technique or the imaging technique. Then, the Wiener adaptive noise filter was applied to the images. As the last step of preprocessing, Gaussian type low pass filter was applied to soften the images. The images obtained as a result of the preprocessing steps were given in Figure 4.

After the preprocessing step of the algorithm, the green and red image layers were converted to gray level. Correlation, normalization, and thresholding steps were performed for live cells as described in Image correlation, statistical analysis and thresholding section. For dead cells, as described in Image correlation, statistical analysis and thresholding section, an adaptive threshold value derived from images containing dead cells and varying with each image was used. Eventually, the contours of the live and dead cells in the images were determined and the superimposed-on images obtained as a result of preprocessing, and they were converted to gray level (Figure 5).
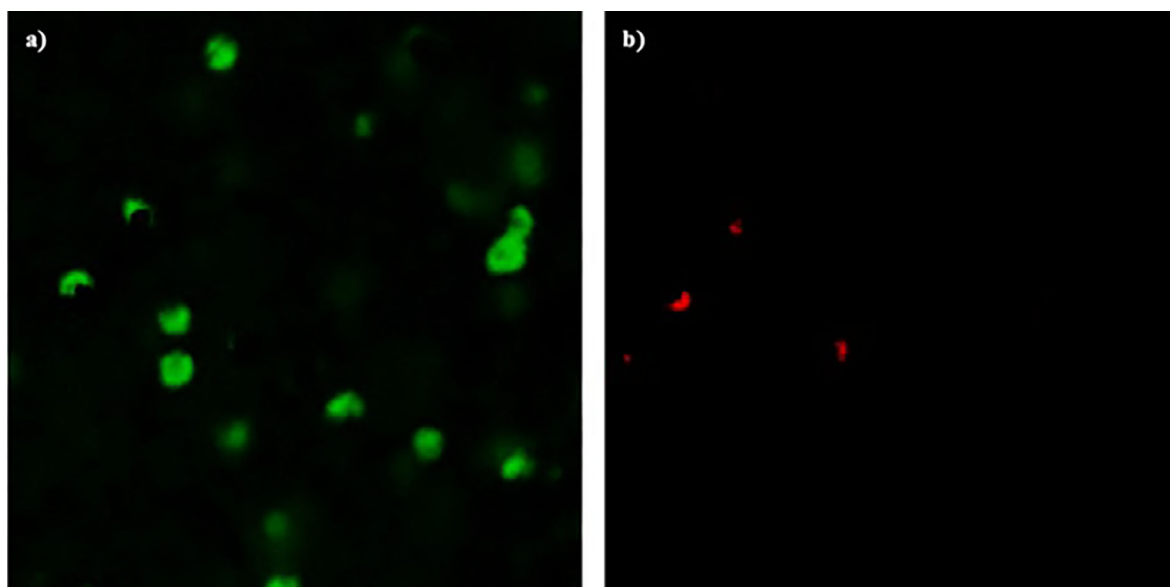
Figure 4. Images obtained as a result of preprocessing steps, a) Live cells, b) Dead cells.
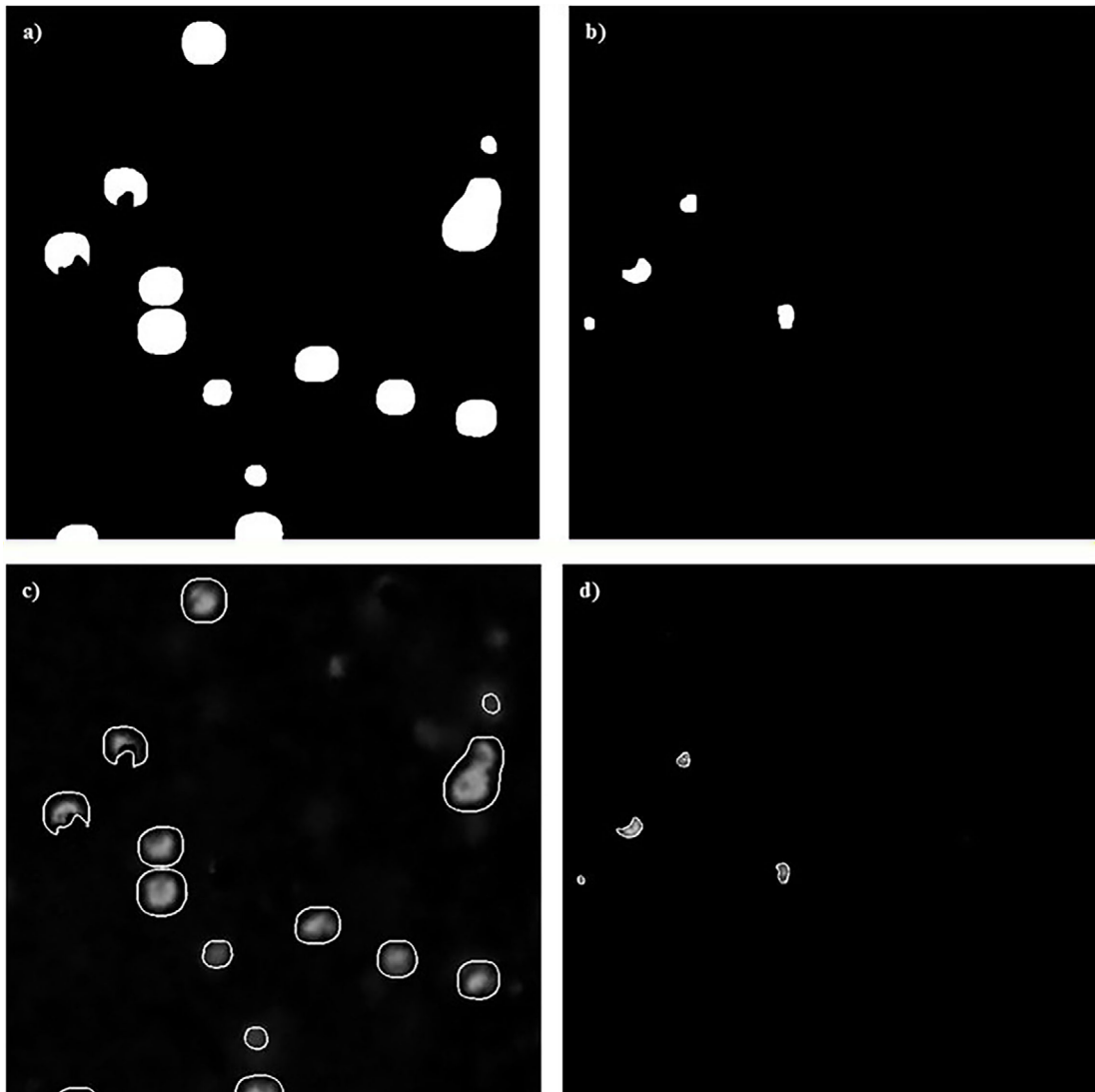
Figure 5. Images obtained as a result of thresholding and edge detection process, a-c) Live cells, b-d) Dead cells.

Thirty-five CLSM images of alginate and alginate-HAp tissue scaffolds were analyzed using the developed algorithm and live and dead cell percentages were calculated. In addition, the same image set was analyzed manually by four different analysts with ImageJ mentioned in Detection of cell area and calculation section. The results acquired from the algorithm were evaluated on the basis of analysts' results and statistical analysis. The measurements and calculations for image the set were given in Table 1.

As a result of this calculation process; intervals of variation coefficient percentages were obtained and average values of variation coefficient percentages were calculated (Table 2).

The other goal of this study is to determine the cell viability depending on the depth of the tissue scaffold. For this purpose, the change in the viability percentages of MC3T3-E1 cells in tissue scaffolds was investigated based on the depth of the tissue scaffold. For this characterization, the MC3T3-E1 cells implanted into the produced three different tissue scaffolds (alginate-HAp, traditional gel-MA, and microwaved gel-MA) were visualized with CLSM. Cross-section images were taken at every 9 μm and an image set was created for each tissue scaffold with 25 individual cross-sectional image. Each cross-sectional image in this set was examined separately and the viability percentages of the cross-sectional areas were calculated. The percentage of the live cell area depending on the depth of the tissue scaffolds was shown in Figure 6.

Table 1. Calculations for the image set (The variables given in the table are A1: Analyst 1, A2: Analyst 2, A3: Analyst 3, A4: Analyst 4, MA = Mean of Analysts, ASD = Standard Deviation of Analysts, AL: Algoritma Result, VC = Percentage of Variation Coefficient, CC:Cell Condition, LCI=Live Cell Image, DCI=Dead Cell Image, Calculation of all measurements are given in percentages).

Image No.	CC	A1%	A2%	A3%	A4%	MA%	SD	VC%	AL%
1	LCI	3.228	4.277	4.034	5.863	4.351	0.956	21.97	4.740
	DCI	0.205	0.246	0.318	0.420	0.297	0.081	27.40	0.394
2	LCI	3.335	3.613	3.387	5.332	3.917	0.824	21.03	4.156
	DCI	0.277	0.756	0.491	0.041	0.391	0.264	67.47	0.301
3	LCI	3.922	6.554	6.76	13.971	7.802	3.733	47.85	6.336
	DCI	0.254	0.331	0.572	0.439	0.399	0.120	29.96	0.219
4	LCI	5.037	3.648	4.189	5.668	4.635	0.775	16.72	4.936
	DCI	0.343	0.227	0.673	0.230	0.368	0.182	49.47	0.142
5	LCI	4.438	7.670	6.146	4.531	5.696	1.327	23.29	5.883
	DCI	0.202	0.658	0.522	0.124	0.376	0.221	58.64	0.122
6	LCI	5.649	6.351	8.107	11.235	7.835	2.157	27.53	7.201
	DCI	0.538	0.658	1.457	0.311	0.741	0.432	58.25	0.620
7	LCI	2.234	3.837	4.592	12.415	5.770	3.930	68.12	6.896
	DCI	0.105	0.114	0.251	1.175	0.411	0.445	108.13	0.432
8	LCI	6.028	7.669	10.801	8.848	8.337	1.740	20.87	6.767
	DCI	0.357	0.249	1.213	0.066	0.471	0.441	93.51	0.306
9	LCI	3.804	3.858	8.435	12.584	7.170	3.647	50.87	8.238
	DCI	0.021	0.060	0.659	0.878	0.404	0.372	92.06	0.137
10	LCI	5.028	6.489	10.361	7.683	7.390	1.956	26.47	7.770
	DCI	0.5	0.328	0.827	0.061	0.429	0.278	64.78	0.288
11	LCI	2.402	3.273	2.811	11.208	4.924	3.641	73.96	6.051
	DCI	0.167	0.163	0.277	0.838	0.361	0.279	77.23	0.581
12	LCI	1.238	1.566	2.033	3.561	2.100	0.890	42.39	3.340
	DCI	0.083	0.166	0.158	0.143	0.138	0.033	23.65	0.059
13	LCI	1.543	2.740	2.871	2.030	2.296	0.540	23.51	3.347
	DCI	0.233	0.193	0.348	0.108	0.221	0.086	39.10	0.166
14	LCI	2.453	3.526	3.064	3.358	3.100	0.409	13.18	4.362
	DCI	0.501	0.878	0.381	0.188	0.487	0.252	51.68	0.215
15	LCI	1.155	1.212	0.848	1.546	1.190	0.248	20.81	1.614
	DCI	0.099	0.217	0.206	0.300	0.206	0.071	34.76	0.094
16	LCI	1.165	2.697	3.173	3.540	2.644	0.905	34.21	2.354
	DCI	0.373	0.147	0.391	0.513	0.356	0.132	37.12	0.429
17	LCI	3.814	3.090	4.776	5.230	4.228	0.832	19.69	5.024
	DCI	0.145	0.401	0.386	0.235	0.292	0.107	36.59	0.259
18	LCI	4.202	4.817	6.591	6.726	5.584	1.097	19.65	5.957
	DCI	0.109	0.063	0.232	0.323	0.182	0.102	56.29	0.044
19	LCI	3.685	3.729	4.874	3.324	3.903	0.582	14.92	4.533
	DCI	0.217	0.225	0.839	0.921	0.551	0.331	60.09	0.832
20	LCI	4.128	3.031	5.111	6.279	4.637	1.200	25.88	4.962
	DCI	0.105	0.225	0.383	0.264	0.244	0.099	40.63	0.134

Table 1. Continue.

Image No.	CC	A1%	A2%	A3%	A4%	MA%	SD	VC%	AL%
21	LCI	1.948	4.002	3.126	5.632	3.677	1.344	36.54	3.915
	DCI	0.115	0.100	0.334	0.236	0.196	0.095	48.62	0.322
22	LCI	3.028	4.981	2.981	5.863	4.213	1.249	29.63	4.740
	DCI	0.251	0.202	0.423	0.516	0.348	0.127	36.51	0.394
23	LCI	1.162	1.212	2.903	2.236	1.878	0.731	38.90	2.532
	DCI	0.122	0.571	0.302	0.782	0.444	0.252	56.75	0.179
24	LCI	10.666	10.997	12.548	16.502	12.678	2.319	18.29	10.279
	DCI	0.2	0.252	0.2	0.221	0.218	0.021	9.75	0.091
25	LCI	2.048	4.351	5.755	12.731	6.221	3.985	64.047	7.711
	DCI	0.203	0.145	0.203	0.476	0.257	0.129	50.166	0.000
26	LCI	6.657	5.187	12.197	7.388	7.857	2.628	33.446	6.282
	DCI	1.545	1.142	2.279	2.252	1.804	0.483	26.743	0.058
27	LCI	4.236	4.021	7.349	10.574	6.545	2.673	40.843	7.320
	DCI	0.964	0.140	3.933	0.000	1.259	1.587	126.029	0.657
28	LCI	3.598	2.651	4.960	9.390	5.150	2.582	50.140	6.453
	DCI	0.833	0.894	2.993	1.557	1.569	0.870	55.417	0.504
29	LCI	4.980	2.412	7.827	7.308	5.632	2.146	38.105	5.546
	DCI	0.539	0.104	4.008	0.695	1.337	1.557	116.525	2.230
30	LCI	1.576	1.529	6.760	6.340	4.051	2.503	61.789	6.530
	DCI	0.555	0.471	1.495	0.245	0.691	0.478	69.066	2.234
31	LCI	1.220	0.570	7.190	5.046	3.507	2.729	77.826	6.527
	DCI	0.109	0.375	0.435	0.183	0.276	0.134	48.558	0.018
32	LCI	2.137	3.310	11.083	2.444	4.744	3.685	77.688	4.727
	DCI	0.103	0.145	0.843	0.587	0.420	0.309	73.751	0.000
33	LCI	0.816	0.626	3.326	9.023	3.448	3.390	98.342	5.751
	DCI	0.333	0.086	0.527	0.156	0.275	0.171	62.055	0.911
34	LCI	0.581	0.478	4.302	3.563	2.231	1.722	77.177	3.484
	DCI	0.034	0.031	0.109	0.229	0.101	0.080	79.672	0.511
35	LCI	1.922	2.021	7.878	2.500	3.580	2.491	69.573	2.471
	DCI	0.153	0.196	1.500	0.372	0.555	0.552	99.345	0.651

Table 2. Statistical analysis of analysts' measurements results.

Glycerol Concentrations (%)	Intervals of Variation Coefficient Percentages (%)	Average Values of Variation Coefficient Percentages (%)
Live Cell Images	13.18 - 98.34	40.72
Dead Cell Images	9.75 – 126.02	59.02
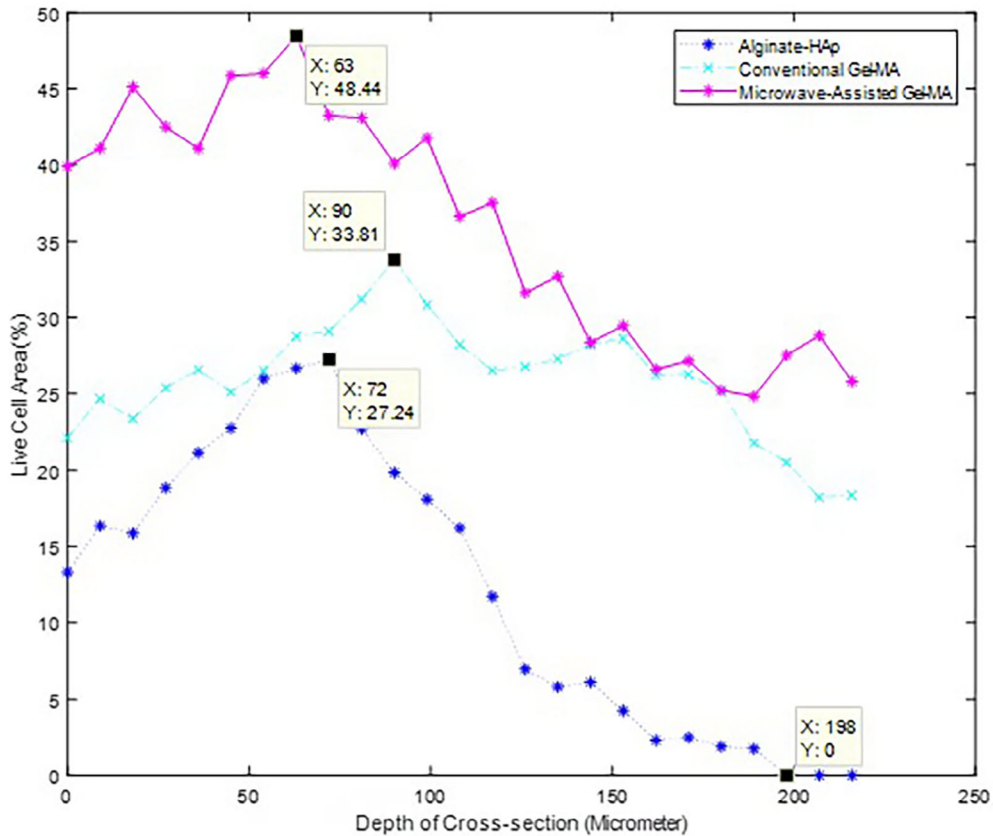
Figure 6. Cell viability change depending on the depth of tissue scaffolds.

Maximum cell viabilities were obtained down from the tissue scaffold at intervals of 63 μm and 90 μm. Maximum cell viability of Alginate-HAp was obtained at 72 μm and viability of the cells rapidly decreased until 198 μm. After this depth, there was no viability observed. For Traditional Gel-MA and Microwaved Gel-MA, the maximum cell viabilities were obtained at 90 μm and 63 μm, respectively. After these points, viability of cell rapidly decreased but never reached zero for either tissue scaffolds. Three images of maximum cell viability for tissue scaffolds were shown in Figure 7.

DISCUSSION

In this work, study was designed to semi-automatically detect cell viability based on the depth of the 3D bioprinted tissue scaffold. Firstly, an algorithm has been developed which enables accurate detection of live and dead cells. The algorithm can easily distinguish separate

cells. However, it may be insufficient to distinguish adjacent intertwined cells in some cases. To overcome this problem, detected cell areas were used instead of cell number in calculations. In this way, a relative cell viability evaluation can be made. In the continuation of the study, the cell viability in the 3D bioprinted tissue scaffold was determined depending on the depth. Contrary to the studies frequently encountered in the literature, in which the scaffold material structure was examined in the 3D plane, the efficiency of cell activity was examined in the 3D plane in the presented study [22,28,39]. In this study, the examination of cell activity, which changes due to different material properties, along the 3d section plane, constitutes its distinguishing aspect from other material-cell interaction studies in the literature [22,29,40]. However, unlike the manual evaluations performed with user-based software in the literature for cell detection, in the presented study, multiple evaluations could be made in a short time with a semi-automa-
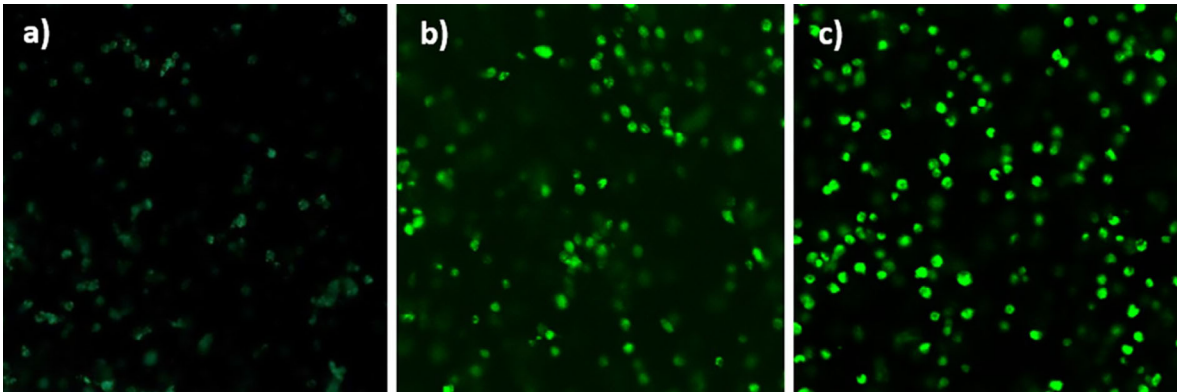
Figure 7. Depth images of tissue scaffolds with the highest percentage of cell viability, a) Alginate-HAp (72 μm) b) Conventional Gel-MA (90 μm) c) Microwave-assisted Gel-MA (63 μm).

tic software design that is least dependent on the user (analyst) [41]. At this point, user reliability, which is another perspective of the study, is also discussed in order to make user (analyst) and software comparisons. The reliability of the analysis in such studies depends on the segmentation accuracy of live and dead cells. Analysts who are experts in their fields inspect these cell images with a visual examination. Visual inspection may cause subjective results and affect the outcome of the study [6,38]. Furthermore, these results are not reproducible because of the personal expertise of the analysts. One of the goals of this study is to evaluate the results of a person-to-person variation (analyst effect) in the visual analysis. The results of our study showed that analysts may make different interpretations in the examination. These subjective interpretations can cause faulty evaluations that may lead researchers to mislead in their studies. The obtained results were compared with the percentage of the variation coefficient, which represents the measurement difference between four different analysts. The coefficients of the variation were obtained from 13.18 % to 98.34 % for live cells and from 9.75% to 126.02% for dead cells with respect to measurements of the analysists. In addition, the average values of variation coefficient percentages are 40.72% for live cell images and 59.02% for dead cell images. These results indicate the inter-analysts' variabilities. It is thought that the reason for this difference is that the perception of human eyes differs from each other during visual evaluation. Another reason for the high rate of deviation in dead cell images is that the number of cells in the dead cell images is small compared to that of live cell images, and this increases the rate of mis-detection. Also, it is determined that the mean values of the analysts' measurements were close to algorithm

results when Table 1 was examined. In cases where the coefficient of the variation in manual measures is low, the algorithm results are converging the average of the manual results.

CONCLUSIONS

In the study, area percentages of live and dead cells in CLSM images of cell cultures that were implanted to alginate and alginate-HAp tissue scaffolds were calculated semi-automatically. The results show that there were too many deviations between the manual evaluations of the analysts. Conversely, it has been shown that reproducible results can be obtained with the developed algorithm. Moreover, depth-dependent cell viability analyses were performed on the tissue scaffold. The maximum cell viability was obtained at 63 μm, 72 μm and 90 μm for microwave-assisted Gel-MA, alginate-HAp, conventional Gel-MA scaffolds, respectively. For Alginate-HAp scaffold cell viability began to decrease and there was no viability deeper than 198 μm. For conventional Gel-MA and Microwave-assisted Gel-MA tissue scaffolds, cell viability began to decrease but never reached zero percentage. Depending on the depth of the tissue scaffold, a reduction in viability is expected. This situation can be explained by the reduced transport of the nutrition substances needed by the cells based on diffusion physics.

References

1. V. Ntziachristos, Fluorescence Molecular Imaging, Annu. Rev. Biomed. Eng., 8 (2006) 1–33.

2. G.Y. Wiederschain, The Molecular Probes handbook A guide to fluorescent probes and labeling technologies, 11th ed., Thermo Fisher Scientific, 2010.

3. W. Grootjans, E.A. Usmanij, W.J.G. Oyen, E.H.F.M. van der Heijden, E.P. Visser, D. Visvikis, M. Hatt, J. Bussink, L.F. de Geus-Oei, Performance of automatic image segmentation algorithms for calculating total lesion glycolysis for early response monitoring in non-small cell lung cancer patients during concomitant chemoradiotherapyFDG-PET in early NSCLC response assessment, Radiother. Oncol., 119 (2016) 473–479.

4. Y. Liu, Y. Chen, B. Han, Y. Zhang, X. Zhang, Y. Su, Fully automatic Breast ultrasound image segmentation based on fuzzy cellular automata framework, Biomed. Signal Process. Control, 40 (2018) 433–442.

5. X. Li, J. Liu, Z. Liu, X. He, C. Zhang, H. Yuan, F. Liu, C. Zheng, Automatic detection of leukocytes for cytometry with color decomposition, Optik (Stuttg)., 127 (2016) 11901–11910.

6. G. Narayanan, M.Y. Tekbudak, Y. Caydamli, J. Dong, W.E. Krause, Accuracy of electrospun fiber diameters: The importance of sampling and person-to-person variation, Polym. Test., 61 (2017) 240–248.

7. S. Nazlibilek, D. Karacor, T. Ercan, M.H. Sazli, O. Kalender, Y. Ege, Automatic segmentation, counting, size determination and classification of white blood cells, Meas. J. Int. Meas. Confed., 55 (2014) 58–65.

8. J. Malašauskiene, R. Milašius, Investigation and estimation of structure of web from electrospun nanofibres, J. Nanomater., 2013 (2013).

9. F. Brun, G. Turco, A. Accardo, S. Paoletti, Automated quantitative characterization of alginate/hydroxyapatite bone tissue engineering scaffolds by means of micro-CT image analysis, J. Mater. Sci. Mater. Med., 22 (2011) 2617–2629.

10. H. Ramoser, V. Laurain, H. Bischof, R. Ecker, Leukocyte segmentation and classification in blood-smear images, Annu. Int. Conf. IEEE Eng. Med. Biol. Soc., 4 (2005) 3371–3374.

11. N. Guo, L. Zeng, Q. Wu, A method based on multispectral imaging technique for White Blood Cell segmentation, Comput. Biol. Med., 37 (2007) 70–76.

12. C. Di Ruberto, A. Dempster, S. Khan, B. Jarra, Analysis of infected blood cell images using morphological operators, Image Vis. Comput., 20 (2002) 133–146.

13. Q. Liao, Y. Deng, An accurate segmentation method for white blood cell images, Proc. - Int. Symp. Biomed. Imaging, (2002) 245–248.

14. S.H. Rezatofighi, H. Soltanian-Zadeh, Automatic recognition of five types of white blood cells in peripheral blood, Comput. Med. Imaging Graph., 35 (2011) 333–343.

15. Ö. Kasım, A.E. Kuzucuoğlu, Lökosit hücrelerinin preparat görüntüsünden tespiti ve sınıflandırılması, Gazi Üniv. Müh. Mim. Fak. Der., 30 (2015) 95–109.

16. N. Dehghan, M.A. Tavanaie, P. Payvandy, Morphology study of nanofibers produced by extraction from polymer blend fibers using image processing, Korean J. Chem. Eng., 32 (2015) 1928–1937.

17. E.S. Gelsema, Application of the Method of Multiple Thresholding to White Blood Cell Classification, Comput. Biol. Med., 18 (1988) 65–74.

18. L. Zhao, K. Li, M. Wang, J. Yin, E. Zhu, C. Wu, S. Wang, C. Zhu, Automatic cytoplasm and nuclei segmentation for color cervical smear image using an efficient gap-search MRF, Comput. Biol. Med., 71 (2016) 46–56.

19. X. Bai, P. Wang, C. Sun, Y. Zhang, F. Zhou, C. Meng, Finding splitting lines for touching cell nuclei with a shortest path algorithm, Comput. Biol. Med., 63 (2015) 277–286.

20. D. Yu, T.D. Pham, X. Zhou, Analysis and recognition of touching cell images based on morphological structures, Comput. Biol. Med., 39 (2009) 27–39.

21. J.J. Stanger, N. Tucker, N. Buunk, Y.B. Truong, A comparison of automated and manual techniques for measurement of electrospun fibre diameter, Polym. Test., 40 (2014) 4–12.

22. H. Shen, A.S. Goldstein, G. Wang, Biomedical Imaging and Image Processing in Tissue Engineering, in: N. Pallua, C. V. Suschek (Eds.), Tissue Eng. From Lab to Clin., 1st ed., Springer-Verlag Berlin Heidelberg, New York, 2011: pp. 155–178.

23. P.M. Kulkarni, E. Barton, M. Savelonas, R. Padmanabhan, Y. Lu, K. Trett, W. Shain, J.L. Leasure, B. Roysam, Quantitative 3-D analysis of GFAP labeled astrocytes from fluorescence confocal images, J. Neurosci. Methods, 246 (2015) 38–51.

24. G. Lin, U. Adiga, K. Olson, J.F. Guzowski, C.A. Barnes, B. Roysam, A hybrid 3D watershed algorithm incorporating gradient cues and object models for automatic segmentation of nuclei in confocal image stacks, Cytometry, 56A (2003) 23–36.

25. F. Piccinini, A. Tesei, G. Paganelli, W. Zoli, A. Bevilacqua, Improving reliability of live/dead cell counting through automated image mosaicing, Comput. Methods Programs Biomed., 117 (2014) 448–463.

26. H.L. More, J. Chen, E. Gibson, J.M. Donelan, M.F. Beg, A semi-automated method for identifying and measuring myelinated nerve fibers in scanning electron microscope images, J. Neurosci. Methods, 201 (2011) 149–158.

27. T.T. Demirtaş, G. Kaynak, M. Gumuşderelioҙlu, Bone-like hydroxyapatite precipitated from 10×SBF-like solution by microwave irradiation, Mater. Sci. Eng. C, 49 (2015) 713–719.

28. A.I. Van Den Bulcke, B. Bogdanov, N. De Rooze, E.H. Schacht, M. Cornelissen, H. Berghmans, Structural and rheological properties of methacrylamide modified gelatin hydrogels, Biomacromolecules, 1 (2000) 31–38.

29. G. Irmak, T.T. Demirtaş, M. Gümüşderelioğlu, Highly Methacrylated Gelatin Bioink for Bone Tissue Engineering, ACS Biomater. Sci. Eng., 5 (2019) 831–845.

30. F. Jin, P. Fieguth, L. Winger, E. Jernigan, Adaptive Wiener filtering of noisy images and image sequences, in: Proc. 2003 Int. Conf. Image Process. (Cat. No.03CH37429), IEEE, 2003: pp. III-349–52.

31. P. Shukla, A. Boyat, Image Denoising using Local Adaptive Wiener Filter in Spatial and Temporal Domain, Int. J. Adv. Res. Electron. Commun. Eng., 4 (2015) 2019–2024.

32. J. Sen Lee, Digital Image Enhancement and Noise Filtering by Use of Local Statistics, IEEE Trans. Pattern Anal. Mach. Intell., PAMI-2 (1980) 165–168.

33. J.S. Lim, Two-Dimensional Signal and Image Processing, 1st ed., Printice Hall, Englewood Cliffs, New Jersey, 1990.

34. J.S. Lee, Refined filtering of image noise using local statistic, Comput. Graph. Image Process., 24 (1983) 255–269.

35. M.S. Nixon, A.S. Aguado, Feature Extraction & Image Processing for Computer Vision, 3rd ed., Elsevier Inc., London, 2012.

36. M.P. Wand, C.M. Jones, Kernel Smoothing, First Edit, Chapman & Hall, New York, 1995.

37. R. Gonzalez, R. Woods, B. Masters, Digital Image Processing, Third Edition, Third Edit, Upper Saddle River, New Jersey, 2007.

38. M. Bizrah, S.C. Dakin, L. Guo, F. Rahman, M. Parnell, E. Normando, S. Nizari, B. Davis, A. Younis, M.F. Cordeiro, A semi-automated technique for labeling and counting of apoptosing retinal cells, BMC Bioinformatics, 15 (2014) 169.

39. A.M. Abd El-Aziz, A. El-Maghraby, A. Ewald, S.H. Kandil, In-vitro cytotoxicity study: cell viability and cellmorphology of carbon nanofibrous scaffold/hydroxyapatite nanocomposites, Molecules, 26 (2021) 1552.

40. R. Dittmar, E. Potier, M.v. Zandvoor, K. Ito, Assessment of Cell Viability in Three-Dimensional Scaffolds Using Cellular Auto-Fluorescence, Tissue Engineering: Part C, 18 (2012) 198-204.

41. B. Gantenbein, A.S. Croft, M. Larraillet, Mammalian Cell Viability Methods in 3D Scaffolds for Tissue Engineering, in: N. Grigoryeva (Eds.), Fluorescence Methods for Investigation of Living Cells and Microorganisms, 1st ed., Intech Open, London, 2020: pp. 1-25.

Use of Composite Barrier in Radioactive Waste Repositories

Radyoaktif Atık Depolarında Kompozit Bariyer Kullanımı

Rüveyda Kübra İleri Durmuş[●], **Sema Akyil Erentürk**[*●]

Department Energy Institute, Istanbul Technical University, İstanbul, Turkey.

ABSTRACT

In this study, the performance of PAN/Zeolite-based composite barrier material was evaluated for the removal of ^{126}Sn and ^{79}Se radionuclides from an aqueous solution. Performance evaluation of the composite barrier material was performed separately for ^{126}Sn and ^{79}Se radionuclides using SWOT analysis. In addition, the risks to non-human organisms in case of accidental release of these radionuclides from radioactive waste landfills have been evaluated. These risks were evaluated by calculating the total doses of freshwater and terrestrial biota using the ERICA assessment tool. The exposed total dose range of reference biota as such crustaceans, phytoplankton, and vascular plants in freshwater was decreased to 4.02E6-3.87E9 µG h^{-1} for ^{126}Sn isotope, and 3.35E07-1.92E12 µG h^{-1} for ^{79}Se isotope using composite barrier material. In terrestrial reference biota such as annelids, grasses and grasses, lichens and bryophytes, mammals and trees, the exposed total dose range was decreased to 4.51E06-7.41E04 µG h^{-1} for ^{126}Sn and 2.15E06-5.53E09 µG h^{-1} for ^{79}Se.

Key Words

Radioactive waste repositories, composite barrier, Tin-126, Selenium-79, risk assessment.

ÖZ

Bu çalışmada, sulu bir çözeltiden ^{126}Sn ve ^{79}Se radyonüklidlerin uzaklaştırılması için PAN/Zeolit bazlı kompozit bariyer malzemesinin performansı değerlendirildi. Kompozit bariyer malzemesinin performans değerlendirmesi ^{126}Sn ve ^{79}Se radyonüklidleri için SWOT analizi kullanılarak ayrı ayrı yapılmıştır. Ayrıca, radyoaktif atık depolama alanlarından bu radyonüklitlerin yanlışlıkla salınması durumunda, insan dışı canlılara yönelik riskler değerlendirilmiştir. Bu riskler ERICA assessment tool kullarak tatlı su ve karasal biotaların alacağı toplam dozlar hesaplanarak değerlendirilmiştir. Tatlı sudaki kabuklular, fitoplankton ve vasküler bitkiler gibi referans biyotaların maruz kaldığı toplam doz aralığı, kompozit bariyer malzemesi kullanılarak ^{126}Sn izotopu için 4.02E6-3.87E9 µG h^{-1}'e ve ^{79}Se izotopu için 3.35E07-1.92E12 µG h^{-1}'e düşürülmüştür. Annelidler, çimenler, likenler ve briyofitler, memeliler ve ağaçlar gibi karasal referans biyotasında, maruz kalınan toplam doz aralığı ^{126}Sn için 7.41E04-4.51E06 µG h^{-1}'ya ve ^{79}Se için 2.15E06-5.53E09 µG h^{-1}'e düşürülmüştür.

Anahtar Kelimeler

Radyoaktif atık depoları, kompozit bariyer, Kalay-126, Selenyum-79, risk değerlendirmesi.

INTRODUCTION

Nuclear power plants seem to key solution for the increasing energy demand by the high capacity factor, preventing climate change; nevertheless, the radioactive wastes problem because of their high radioactivity are waiting for a permanent solution like conducting studies on the storage and disposal of radioactive waste repositories. The main concern of the waste repositories is to attain the water to the waste repository and to migrate the radionuclides in the waste packages to the biosphere. In order to protect the waste repository from the water and prevent the migration of the radionuclides in waste packages, the multi-barrier concepts composed of the engineered barriers and geological formation were developed and has been studied by researchers and authorities since the 1970s [1,2].

The main reason for developing the engineered barrier is the adsorption of the radionuclides having a long half-life and extension of the time that attain the radionuclides to the biosphere; therefore, the concentration of the radionuclides is decreased and they will not jeopardize human and ecosystem health. In order words, Engineered barriers work for the extension of the time to attain the radionuclides to the biosphere and for prevention of the attain the water to the waste repository; therefore, they work bi-directional. In the absence of the engineered barrier, water succeeds to meet the waste repository and radionuclides migrate to the biosphere earlier and more concentration than expected without adsorption [1,2].

In the design phase of the multi-barrier, the design of the engineered barriers is shaped by the geological formation and radioactive waste repositories. However, one of the engineered barriers is generally made of the buffer material where radionuclides contact firstly. The buffer materials should be designed to adsorb more radionuclides having a long half-life. Furthermore, the buffer materials should be designed with high chemical, physical and structural properties such as low permeability, high plasticity, and high cation exchange capacity [3-8].

^{79}Se and ^{126}Sn are remarkable radionuclides in the waste packages because they are long half-live fission products and radiologically harmful in the spent nuclear fuel [9-11]. The fission efficiency for ^{126}Sn and ^{79}Se are 0.0236% and 0.04%, respectively [11,12]. The half-life of ^{126}Sn is 2.35×10^5 and it is a dangerous beta (max = 252 keV) and gamma (87.6, 86.94 or 64.3 keV) emitter by thermal neutrons although it has a relatively low production of about 0.056% is a fission product. The half-life of ^{79}Se is 65000 years and it is potentially dangerous for beta radiation (max = 0.056 MeV) [12]. According to the Belgian deep geological repository, ^{79}Se is seemed to the main contributor to the activity release. Selenium is also redox-sensitive radionuclides that shows oxidation states as -II, 0, IV and VI in aquatic media.

According to the recommendation of the International Commission on Radiological Protection (ICRP) in 1978, while defending the view that "if people are sufficiently protected, other living organisms will also be adequately protected". In 1991, it was stated that environmental control is also necessary for humans to be adequately protected, that other species should not be at risk, that non-human organisms may occasionally be harmed, but cannot endanger endangered species or create an imbalance between species. This change in the paradigm of the ICRP has accelerated the work carried out within the framework of the protection of non-human species from radiation. Since it will not be possible to evaluate the effects of radiation on all species in the ecosystem, separate assessments are made for reference organisms, exposure routes and terrestrial, freshwater and marine environments. With the ERICA (Environmental Risk from Ionizing Contaminants: Assessment and Management) program, which is a modelling simulation developed for this purpose, it is possible to predict the transfer of environmental or radionuclide pollution on the reference plants or animals, to determine the equivalent dose amount to which the biota will be exposed, and to evaluate the impact [13].

Within the framework of this paradigm, the doses to be exposed to non-human biota as a result of the release of ^{126}Sn and ^{79}Se into the environment as a result of an accident that may occur in radioactive waste repository areas were calculated using the ERICA Tool Program. The exposed total doses of selected freshwater and terrestrial reference biota were evaluated separately in the presence and absence of the composite barrier material used in the waste storage area. SWOT analysis was used to show strengths, weaknesses, opportunities, and threats of the composite barrier material.

MATERIALS and METHODS

ERICA assessment tool is a product developed within the 6th Framework project ERICA and is one of the most inclusive assessments that has been recognized and used by international organizations such as ICRP, IAEA. ERICA Assessment Tool is used for determination of the amount of equivalent dose to which it will be exposed and effect evaluation on reference plant or animal that is determined by IAEA and UNSCEAR by transfer of environmental or radionuclide contamination [14,15]. Ionizing radiation exposure, effects and risks, chemical and environmental risk characterization and environmental management can be performed in order to protect the ecosystem structure and function using this computer-based software [16].

ERICA has 3 tiered approaches and it can be adapted to the specific assessment of using reference organisms. In Tier 1, only the selected elements of a specific area can be examined according to appropriate reference organisms and the risk assessment is made according to result by comparing against Environmental Media Concentration Limits (EMCL). The results are given as Risk Quotients (RQ):

$$RQ = \sum_{1}^{n} \frac{M_n}{EMCL_n}$$

where, RQ= Total Risk quotient, M_n= measured or predicted maximal activity concentration for radionuclide "n" in the medium in Bq L^{-1} for water, Bq kg^{-1} (dry weight) for soil or sediment or Bq m^{-3} for air; EMCL$_n$= Environmental Media Concentration Limit for radionuclide "n" (same units as media) [16].

In Tier 2, selected elements in the specific area can be examined according to selected reference organisms and, the risk assessment is made according to the result. Selected reference organisms are representing the range of typical organisms from aquatic, terrestrial and marine environments. The results enable the calculation of doses and identification of the potentially most exposed reference organism by using the concentration value (CR) in Bq kg^{-1} and distribution coefficient (K_d) in Bq kg^{-1}. Tier 2 is important for determining the uncertainties within the effects analysis part of the assessment [16].

In Tier 3, these results can be evaluated according to probability estimates. This tier enables to enter of the data for the site-specific probability distribution functions and gives the uncertainties in the final dose-rate results. Sensitivity analysis is important for the parameters on the effects on the model output and this helps to quantities the uncertainties especially cost-effective research [16].

In this study, ERICA Assessment Tool is used for the effect of the barrier on the dose exposure in the freshwater biota, i.e., crustacean, phytoplankton, vascular plant, and terrestrial biota i.e., annelid, grasses and herbs, lichen and bryophytes, mammal, shrub, tree. Initial Se and Sn concentration and remaining concentration in the solution after adsorption were converted to activity by using the following formula:

$$A = \frac{ln2}{t_{1/2}} x \frac{mN_A a}{M}$$

where A is activity (Bq), $t_{1/2}$ is half-life of the nuclei (s), M is the molarity of the substance (kg mol^{-1}), m is mass of substance (kg), NA is Avogadro's number (mol^{-1}), a is the abundance.

In order to calculate to the subjected dose of the freshwater reference biota in the ERICA Tool Assessment Program, the required distribution coefficient (K_d) value was calculated as:

$$K_d = \frac{A_i - A_e}{A_e} x \frac{V}{m}$$

where A_i is the activity concentration of the initial solution (Bq mL^{-1}), A_e is the activity concentration of the solution in equilibrium (Bq mL^{-1}), V is the volume of the solution (mL), m is the amount of the adsorbent (0.05 g).

RESULTS and DISCUSSION

In the event of an accident that may occur in radioactive waste storage, the risks of the spread of waste radionuclides to the environment have also been evaluated. The tin and selenium concentrations in the solution before and after the adsorption process were converted into activity units, and the performance of the barrier material to reduce the migration of tin and selenium ions into the ecosystem was investigated.

Table 1. Total ^{126}Sn dose range for freshwater biota.

Sn	Freshwater					
	Without barrier			With barrier		
	Crustaen	Phytoplankton	Vascular Plant	Crustaen	Phytoplankton	Vascular Plant
Max. Dose (µG h^{-1})	1.24E+10	2.41E+08	1.08E+10	3.87E+09	7.49E+07	7.49E+07
Min. Dose (µG h^{-1})	9.44E+08	4.01E+07	8.32E+08	2.37E+08	4.02E+06	4.02E+06

Table 2. Total ^{126}Sn ddose range for terrestrial biota.

Sn	Terrestrial											
	Without barrier						With barrier					
	Annelid	Grasses & Herbs	Lichen &bryophytes	Mammal	Shrub	Tree	Annelid	Grasses & Herbs	Lichen &bryophytes	Mammal	Shrub	Tree
Max. Dose (µG h^{-1})	1.45E+07	5.45E+06	6.20E+06	1.35E+07	5.46E+06	4.43E+06	4.51E+06	1.69E+06	1.93E+06	4.20E+06	1.70E+06	1.38E+06
Min. Dose (µG h^{-1})	9.66E+05	3.63E+05	4.13E+05	9.00E+05	3.64E+05	2.95E+05	2.42E+05	9.11E+04	1.04E+05	2.26E+05	9.14E+04	7.41E+04

Table 3. Total ^{79}Se dose range for freshwater biota.

Se	Freshwater					
	Without barrier			With barrier		
	Crustaen	Phytoplankton	Vascular Plant	Crustaen	Phytoplankton	Vascular Plant
Max. Dose (µG h^{-1})	7.13E+12	1.01E+09	1.07E+12	1.92E+12	2.73E+08	2.87E+11
Min. Dose (µG h^{-1})	4.75E+11	6.77E+07	7.11E+10	2.35E+11	3.35E+07	3.52E+10

Table 4. Total ^{79}Se dose range for terrestrial biota.

Se	Terrestrial											
	Without barrier						With barrier					
	Annelid	Grasses & Herbs	Lichen &bryophytes	Mammal	Shrub	Tree	Annelid	Grasses & Herbs	Lichen &bryophytes	Mammal	Shrub	Tree
Max. Dose (µG h^{-1})	1.52E+09	5.78E+08	2.06E+10	6.50E+07	1.86E+09	1.86E+09	4.09E+08	1.56E+08	5.53E+09	1.75E+07	4.99E+08	4.99E+08
Min. Dose (µG h^{-1})	1.01E+08	3.86E+07	1.37E+09	4.33E+06	1.24E+08	1.24E+08	5.02E+07	1.91E+07	6.79E+08	2.15E+06	6.13E+07	6.13E+07

The different activity ranges between the 1.14E09 and 1.71E10 Bq L^{-1} activity values, the ERICA Tool Assessment program evaluated how much aquatic and terrestrial biota could receive as a result of leakage into the environment without barrier material in the waste area and the presence of barrier material. In the absence of barrier material, crustaceans, phytoplankton, and vascular plants, which are studied as freshwater biota, will be exposed to significant doses. The total dose range to which this biota will be exposed varies between 1.60E7 and 1.24E10 µG h^{-1} from the radioactive isotope of tin, and between 6.77E07 and 7.13E12 µG h^{-1} from the radioactive isotope of selenium (Table 1 and Table 3). In the case of using barrier material, the total dose

Strengths

■The use of composite barrier materials around the container containing waste in radioactive waste repository areas significantly reduces the spread of radioactive wastes to the environment and the biosphere.

■Composite barrier materials protect people and the environment from potential hazards in accidents that may occur during the disposal of radioactive waste, and also increase the safety of the disposal facility.

■It is important to examine the characteristics of the designed barrier system in terms of isolating the waste from the environment and people and evaluating its long-term performance.

Weaknesses

■Composite barrier materials may not provide the desired performance in preventing the release of every radionuclide into the environment.

■In the event of an unexpected accident, the doses to be taken by human and non-human creatures may increase.

SWOT

Opportunities

■By changing the components in the composite barrier materials, their performance against different radionuclides can be increased.

Threats

■One of the disadvantages of composite barrier materials is that they degrade over time and decrease their mechanical strength.

Figure 1. SWOT analysis for the composite barrier materials.

range to which this biota will be exposed decreases to 4.02E6 to 3.87E9 µG h^{-1} for radioactive tin isotope, and 3.35E07 to 1.92E12 µG h^{-1} for radioactive selenium isotope. In the case of using a barrier, the external dose is reduced by approximately 70%.

In terrestrial reference biota such as annelids, grasses and grasses, lichens and bryophytes, mammals and trees, the observed total dose range in the case of not using barrier material is between 2.95E05 and 1.45E07 µG h^{-1} for tin, and between 4.33E06 and 2.06E10 µG h^{-1} for selenium (Table 2 and Table 4). In the case of using barrier material, the dose range to which this biota will be exposed has decreased by 70% and it is 4.51E06 to 7.41E04 µG h^{-1} for tin and 2.15E06 to 5.53E09 µG h^{-1} for selenium. Since the exposure to freshwater and terrestrial biota from the total doses originating from radioactive waste repositories has not been examined in another study before with the ERICA program, it was not possible to compare with the literature.

SWOT analysis was used to evaluate the strengths, weaknesses, opportunities, and threats of the use of composite barrier materials in the spread of radionuclides, which are dangerous for living things due to their long half-lives and activities in radioactive waste repository areas. The results of the SWOT analysis are given in Fig.

1. Weaknesses can be improved for different radionuclides by using composite barrier materials of different compositions. In addition, by investigating the interactions of different radionuclides with the barrier materials in more detail, it can be suggested to use different composite barrier materials according to the radionuclide inventory of radioactive wastes.

CONCLUSION

In this study, the effectiveness of a composite barrier material for ^{126}Sn and ^{79}Se used in radioactive waste repository areas was evaluated. In accordance with the recommendation of the International Commission on Radiological Protection (ICRP), the ERICA Tool Program was used to assess the total exposures of selected freshwater and terrestrial reference biota. The doses of freshwater and terrestrial biota originating from ^{126}Sn and ^{75}Se are significantly reduced in the presence of the composite barrier material. Some of the freshwater and terrestrial biota are more exposed to these doses.

In line with the results obtained, the usability of the composite barrier material was evaluated in terms of strengths, weaknesses, opportunities, and threats using SWOT analysis.

References

1. B. Grambow, Mobile fission and activation products in nuclear waste disposal, J. Contam. Hydrol., 102 (2008) 180–186.

2. C. Bruggeman, A. Maes, J. Vancluysen, P. Vandemussele, Selenite reduction in Boom clay: Effect of FeS$_2$, clay minerals and dissolved organic matter, Environ. Pollut., 137 (2005) 209–221.

3. H.S. Ahn, H.Y. Jo, Influence of exchangeable cations on hydraulic conductivity of compacted bentonite, Appl. Clay Sci., 44 (2009) 144–150.

4. S. Kaufhold, M. Pohlmann-Lortz, R. Dohrmann, R. Nüesch, About the possible upgrade of bentonite with respect to iodide retention capacity, Appl. Clay Sci., 35 (2007) 39–46.

5. B. Riebe, S. Dultz, C. Bunnenberg, Temperature effects on iodine adsorption on organo-clay minerals: I. Influence of pretreatment and adsorption temperature, Appl. Clay Sci., 28 (2005) 9–16.

6. J. Manjanna, T. Kozaki, S. Sato, Fe(III)-montmorillonite: Basic properties and diffusion of tracers relevant to alteration of bentonite in deep geological disposal, Appl. Clay Sci., 43 (2009) 208–217.

7. A. Gosman, I. Hvozdova, J.L.M. Nieto, Measuring The Diffusion and Sorption of the Trace Elements and Radionuclides in Soil, Clay and Bentonite, Czechoslov. J. Phys., 49 (1999) 847-853.

8. C. Hurel, N. Marmier, A. Bourg, F. Fromage, Sorption of Cs and Rb on purified and crude MX-80 bentonite in various electrolytes, J. Radioanal. Nucl. Chem., 279 (2008) 113–119.

9. S.A. Catlow, G.L. Troyer, D.R. Hansen, R.A. Jones, Half-life measurement of [126]Sn isolated from Hanford nuclear defense waste, J. Radioanal. Nucl. Chem., 263 (2005) 599–603.

10. G. Jörg, R. Bühnemann, S. Hollas, N. Kivel, K. Kossert, S. Van Winckel, C.L. Gostomski, Preparation of radiochemically pure [79]Se and highly precise determination of its half-life, Appl. Radiat. Isot., 68 (2010) 2339–2351.

11. A.L. Nichols, D.L. Aldama, M. Verpelli, International Atomic Energy Agency INDC International Nuclear Data Committee Handbook of Nuclear Data for Safeguards: Database Extension, INDC (NDS)-0534, Vienna, 2008.

12. V. Silliková, S. Dulanská, Sequential determination of ^{99}Tc and [126]Sn in radioactive concentrate, Acta Chim. Slovaca, 10 (2017) 61–64.

13. ICRP, Publication 29: Radionuclide release into the environment: assessment of doses to man, Pergamon, New York, 1978.

14. J.E. Brown, B. Alfonso, R. Avila, N.A. Beresford, D. Copplestone, G. Prohl, A. Ulanovsky, The ERICA Tool, J. Environ. Radioact., 99 (2008) 1371-1383.

15. N. Beresford, J. Brown, D. Copplestone, J. Garnier-Laplace, B. Howard, C.M. Larsson, D. Oughton, G. Pröhl, I. Zinger, D-ERICA: An integrated approach to the assessment and management of environmental risks from ionising radiation, Description of purpose, methodology and application, EC Contract FI6RCT-2004-508847, European Commission Report, https://wiki.ceh.ac.uk/download/attachments/115017395/D-Erica.pdf, (2004).

16. D.H. Oughton, G. Strømman, B. Salbu, Ecological risk assessment of Central Asian mining sites: application of the ERICA assessment tool, J. Environ. Radioact., 123 (2013) 90-98.

Antiproliferative Properties and Evaluation of Antioxidant of Different Cornelian Cherry Genotypes and Analysis of Phenolic and Sugar Compounds by HPLC,

Farklı Kızılcık Meyvelerinin Genotiplerinin Antiproliferatif Özellikleri ve Antioksidanlarının Değerlendirilmesi ve HPLC ile Fenolik ve Şeker Bileşiklerinin analizi

Yılmaz Uğur[1], Emine Şalva[2], Fırat Ege Karaat[3], Selim Erdoğan[2]

[1]Department of Pharmacy Services, Health Services Vocational School, Inonu University, Malatya, Turkey.
[2]Faculty of Pharmacy, Inonu University, Malatya, Turkey.
[3]Faculty of Agriculture, Adıyaman University, Adıyaman, Turkey.

ABSTRACT

The aim of this study was to investigate the chemical composition (vitamin C, phenolic, and sugar compounds), the cytotoxic effect on healthy (L-929) and lung cancer (A-549) cells, and the antioxidant capacity of fruits belong to thirteen cornelian cherry (Cornus mas L.) genotypes grown under the same conditions in Turkey. Fruit samples were extracted by the ASE technique. The chemical composition was analyzed by HPLC-DAD-RID. A reversed-phase Clipeus C18 reversed-phase column (250 mm × 4.6 mm, 5 μm) were used. For gradient elution mobile phase A contained 4.5 % acetic acid in water; solution B acetonitrile were used as mobile phase with flow rate 1.0 mL/min. Antioxidant capacity, total phenolic, and total anthocyanin content were determined using spectrophotometric methods. Cytotoxic effects were evaluated by MTT assay in L-929 and A-549 cell lines for 48 h. No toxic effect of the fruit extracts was observed on L-929 healthy mouse fibroblast cells, while it was determined to reduce cell proliferation (approximately 50%) on A-549 lung cancer cells. The featured genotypes were 44-03, 44-20, 44-21, 77-09, and 44-21, 44-16, 77-05, respectively. The featured genotypes for antioxidant capacity and cytotoxic effects on A-549 cells were 44-03, 44-20, 44-21, 77-09, and 44-21, 44-16, 77-05, respectively. The results have brought out that there are significant differences between the genotypes ($p \leq 0.05$) and cornelian cherry fruits have a significant antioxidant capacity and potential for antiproliferative effects.

Key Words
Cornus mas L., phenolic compounds, vitamin C, antioxidant capacity, antiproliferative effect, lung cancer.

ÖZ

Bu çalışmanın amacı, kızılcık meyvelerinin kimyasal bileşimi (C vitamini, bireysel fenolik ve şeker bileşikleri) ve antioksidan kapasitesinin yanında, meyve ekstrelerinin sağlıklı (L-929) ve akciğer kanseri (A-549) hücreleri üzerindeki sitotoksik etkisini araştırmaktır. Türkiye'de aynı koşullarda yetiştirilen on üç kızılcık (Cornus mas L.) genotipi meyve örnekleri ASE tekniği ile optimum koşullarda ekstrakte edildikten sonra kimyasal bileşim, HPLC-DAD-RID ile analiz edildi. Clipeus C18 ters faz kolonu (250 mm x 4.6 mm, 5 um) kullanıldı. Gradiyen elüsyon uygulanarak yapılan belirlemede dakikada 1 ml akış oranında, mobil faz olarak solvent A: %4,5 asetik asit solüsyonu ve solvent B: asetonitril kullanıldı. Antioksidan kapasitesi, toplam fenolik ve toplam antosiyanin içeriği spektrofotometrik yöntemler kullanılarak belirlendi. Sitotoksik etkiler, 48 saat boyunca L-929 ve A-549 hücre hatlarında MTT testi ile değerlendirildi. Meyve ekstraktlarının L-929 sağlıklı fare fibroblast hücreleri üzerinde toksik etkisi gözlenmezken, A-549 akciğer kanseri hücrelerinde hücre proliferasyonunu (yaklaşık %50) azalttığı belirlendi. A-549 hücreleri üzerindeki antioksidan kapasite ve sitotoksik etkiler için öne çıkan genotipler sırasıyla 44-03, 44-20, 44-21, 77-09 ve 44-21, 44-16, 77-05 olduğu belirlendi. Elde edilen sonuçlar, genotipler ($p \leq 0.05$) arasında önemli farklılıklar olduğunu ve kızılcık meyvelerinin önemli bir antioksidan kapasiteye ve antiproliferatif etki potansiyeline sahip olduğunu ortaya koymuştur.

Anahtar Kelimeler
Kızılcık (Cornus mas L.), fenolikler, C vitamin, antioksidan kapasite, antiproliferative effect, akciğer kanseri.

INTRODUCTION

Fruits and vegetables are sources of natural antioxidants thanks to their secondary metabolites as well as being a food source. Antioxidants that have a preventive effect against harmful free radicals causing cancer, heart diseases, and many other diseases have been drawn attention due to their beneficial effects on human health [1]. Free radicals may comprise from the oxidation and reduction reactions that normally occur in the organisms, as well as harmful sources such as toxic products of cell metabolism, radiation, viruses, ultraviolet beams, and cigarette smoke. These reactive species cause oxidative damage in lipids, proteins,nucleic acids, and various pathological events. It is known that the relevant reactive species cause molecular changes and gene mutations in cells, and play a role in aging, cellular damage, and tissue destruction.

Antioxidants that neutralize free radicals and prevent their formation by giving their electrons serve a protective function in the human body. They are found in foods and the body in lower concentrations than oxidizable substrates and delay or prevent the oxidation of the substrate that causes oxidative damage [2]. Vitamins, carotenoids, and polyphenols are among the natural sources of antioxidants. Polyphenols are compounds found in many vegetables, fruits, and beverages such as tea and red wine and contain mainly flavonoids and phenolic acids. These compounds have the radical scavenging effect either by breaking free radicals chain reactions or directly by suppressing free radicals [3]. Polyphenols, commonly found in most plants, have pharmacological activity due to their ability to remove/prevent the reactive oxygen species causing destructive damage to the cells [4].

There are some problems with the use of synthetic anticancer agents following: Effecting without distinction between the normal tissue and tumor, their sensitivity to induced drug resistance, the severe side effects, etc. Such issues raise the interest in using natural bioactive ingredients as cancer preventive or healing agents [4].

Cornelian cherry is a tree plant growing naturally. Its fruits are generally consumed freshly or as jam, marmalade, syrup, jelly, compote, dried layers of fruit pulp, tarhana, and juice [5-6]. Besides, its fruit, leaf, root, and shell are used in folk medicine as an antipyretic, diarr-hea preventive, and removing kidney stones. Cornelian cherry fruits have a rich content of anthocyanin, flavonoid, and phenolic compounds. Many studies have revealed the antiseptic, antioxidant, antidiabetic, and antimicrobial properties of the cornelian cherry [4-5, 7-13]. Based on a scientific basis use of herbal medicine for the prevention of diseases such as cancer, obesity, diabetes, and cardiovascular, the studies to reveal the therapeutic properties of plants are increasing, and cornelian cherry attracts attention from this aspect as well. In the genotypes used in the current study, there is no study on the individual phenolic compounds and cytotoxic activity. The aim of this study is to determine the phenolic content and antioxidant capacity properties of fruits of different cornelian cherry genotypes from the Malatya Province of Turkey and investigate the in-vitro cytotoxic effects of fruit extracts on lung cancer cells.

MATERIALS and METHODS

The fruit material used in the study was obtained from the cornelian cherry genetic resources collection orchard belonging to Apricot Research Institute, located in Malatya Province of Turkey. Fruit samples were taken from fourteen cornelian cherry genotypes. The fruit samples removing the kernel were pulped with a blender. Fruit puree was dried with lyophilizer (Christ Alpha 1-2 LD plus, Germany) and powdered. The obtained fruit powder was used in all analyzes.

Extraction Procedure and Spectrophotometric Analyses

Analyses Accelerated Solvent Extraction (ASE) 200 system (Dionex, Sunnyvale, CA, USA) with 11-60 mL stainless steel ASE vessels used for the pressurized liquid extraction was used for the extraction of polyphenol from the fruit samples. The fruit samples were extracted in the solvent mixture of methanol:water:HCl (70:29.9:0.1 v/v/v) at 25°C, 1500 psi for 60 min [14]. The obtained extract evaporated to dryness by rotavapor under reduced pressure. The dry residue was redissolved in a 4 mL solvent mixture of methanol:water (1:1 v/v), and then was filtered through a 0.45 µm PVDF (polyvinylidene difluoride) filter. The filtrate was used in all analyzes except sugar and vitamin C analyzes. The total phenolic content (TPC) was determined by the Folin-Ciocalteu method [15], and the results were expressed as mg gallic acid/100 gDW (dry weight). UV/VIS Spectrophotometer (Shimadzu 2000S Model, Japan) was used for detection of TPC in the cornelian cherry samp-

les. To determine the antioxidant capacity, DPPH radical scavenging and reducing power tests were performed. DPPH radical scavenging test was performed by using the method of Yen and Hung [16]. The reducing power test was performed by using the method of Hwang et al. [15]. Results were compared with a standard curve prepared with Trolox, and expressed as mg Trolox (TE)/100 gDW. Total anthocyanin content (TAN) was determined using the pH-differential method [17] and expressed as mg cyanidin-3-O-glucoside (c3g)/100 gDW.

Analysis of Phenolic Compounds

The qualitative and quantitative determination of polyphenols was carried out using a Shimadzu HPLC, equipped with Shimadzu DGU-20A5 model vacuum degasser and Shimadzu 20 ADXR solvent pump. Separations were performed using a Clipeus C18 5 µm reversed-phase column (250 mm × 4.6 mm). Detection was performed with a Shimadzu SPD-M20A photodiode array detector. To prepare analytically pure polyphenol standards, 1000 mg/L stock solutions were prepared by dissolving 0.010 g polyphenol into deionized pure water and completed with 10 mL met-

hanol and water (1:1 v/v). By using these stock solutions standard solutions of each polyphenol were prepared daily. The determination of phenolic compounds was carried out by the HPLC-DAD system. In the determination by applying gradient elution, Solvent A: 4.5% acetic acid solution and Solvent B: acetonitrile were used as mobile phases. The elution conditions are given in Table 1. The content of the phenolic compounds was determined according to its calibration curve and expressed as mg/100 gDW.

Validation Studies

Limit of detection (LOD) and limit of quantification (LOQ) was calculated by multiplying 3.3 and 10 by the standard deviation of the blank solution(s) respectively. To determine the % recovery, the sample was spiked a known amount of phenolic compound standard, and then both spiked sample and unspiked sample were measured to determine amount of phenolic compound by HPLC.

Table 1. The gradient program applied by HPLC.

Analysis time (min)	Solvent B (%)	Flow rate (mL/min)	Column temp. (°C)	Injection vol. (µL)	Wavelength (nm)
0.01	0				271, 273
7	5				
12	15				278, 279
20	40	1	30	20	
25	100				
30	100				325, 354
40	5				

Table 2. The validation parameter values from HPLC for phenolic compounds.

Phenolic compounds	Retention Time (min)	LOD*	LOQ*	Calibration Curve	R2	Linear Range*	Recovery (%)	Precision intra-day RSD %	Precision inter-day RSD %
Gallic acid	5.44	0.033	0.048	y=605.33x+34.12	0.9999	0.05-10	90.39	4.84	7.95
Catechin	14.37	0.034	0.060	y=111.68x+3.29	0.9999	0.06-5.0	77.47	6.92	9.50
Chlorogenic acid	15.15	0.005	0.010	y=559.62x+12.41	0.9999	0.025-5.0	77.00	8.91	10.07
Epigal**	16.61	0.044	0.060	y=20.244x-2.04	0.9999	0.25-25.0	80.00	4.40	6.72
Epicatechin	16.93	0.026	0.043	y=13.296x+4.29	0.9998	0.05-5.0	77.40	3.22	8.03
Rutin	18.94	0.012	0.019	y=308.2x+5.50	0.9999	0.025-2.5	98.44	2.37	6.73

*mg/100 mL, **Epigallocatechin gallate

The percentage of recovery was calculated using Equation (1):

$$\% \, Recovery = \frac{C1 - C0}{C(spike)} x100$$

(1)

where C1 is the measured concentration of the spiked sample, C0 is the measured concentration of the unspiked sample and C(spike) is the added concentration of phenolic compound standard. The validation parameter values calculated for the phenolic compounds are given in Table 2.

Analyses of Sugar Compounds and Vitamin C

Sugar analysis in fruit samples was carried out by HPLC-RID (refractive index detector) (Shimadzu RID-10A). Separations were performed using a Carbohydrate 5μm column (250 mm × 4.6 mm). The solvent mixture of acetonitrile:water (77:23 v/v) was used as mobile phase. 0.50 g fruit sample was weighed into a centrifuge tube, and then 10 mL ultrapure water was added on. Tubes were mixed well by vortex and then centrifuged at 6000 rpm for 5 min. The upper phase was taken and filtered through a 0.45 μm PVDF filter. Sugar content was determined by injecting to HPLC the filtrate.

The determination of vitamin C was carried out by the HPLC-DAD (Diode-Array Detection) system (Shimadzu SPD-M20A). Separations were performed using a Phenomenex C18 5μm column (250 mm × 4.6 mm). The ultrapure water (pH: 2.2) was used as mobile phase. 2.50 g fruit sample was weighed into a centrifuge tube wrapped with aluminium foil, and then 10 mL 6% metaphosphoric acid was added on. Tubes were mixed well by vortex and then centrifuged at 6000 rpm for 2 min. The upper phase was taken and filtered through a 0.45 μm PVDF filter. Vitamin C content was determined by injecting to HPLC the filtrate, at 254 nm [18].

In-vitro Cytotoxic Activity

L-929 (normal mouse fibroblast cell line, ATCC, CCL-1) and A-549 (human lung cancer cell line, ATCC, CCL-185) cells were grown and maintained in Dulbecco's Modified Eagle's Medium (DMEM) containing 10% fetal bovine serum (FBS), 1% penicillin and streptomycin and were incubated at 37 °C in a humidified atmosphere of 5% CO2. Stock cultures were passaged at 2 to 3-day intervals.

The MTT [2, 5- diphenyl - tetrazolium bromide, and 3 - (4, 5-dimethyl thiazolyl)] test was used to evaluate the cell viability. The test is based on producing a blue formazan product from mitochondrial dehydrogenase that indicates the normal functions of mitochondria and as a result of the measurement method of the resulting cell viability and cytotoxicity [19]. L-929 and A-549 cells at a density of 1x104 cells/well were seeded into 96- well plates in DMEM containing 10% FBS. Then, the cells were treated with different concentrations (100-200 μg/mL) of the extract. 48 h after the treatment, the medium of each plate was changed with a fresh medium containing MTT solution. After 4 h of incubation, the incubated media was added to the solubilization buffer. Then, the absorbance of each well was read at a wavelength of 570 nm using Elisa Reader (Epoch, Biotek, USA). Cell proliferation was obtained by proportioning the absorbance values obtained from the negative control to the absorbance values of the experimental groups. The absorption value from controls (cells not treated with extracts) was considered having 100% cell viability [20, 21].

Statistical analysis

Analyses were performed with three replicates. All data were subjected to variance analyses. Significant differences among applications were determined according to LSD multiple comparison test at p < 0.05. In addition, correlation coefficients between results of the analysis were calculated. The chemical compositions and cytotoxic effects on L929 and A549 cell lines of the tested fruit samples were compared using principal components analysis (PCA). Besides, Pearson's Correlation Test (p < 0.01 and p < 0.05) was applied to evaluate the relations among the assessed fruit characteristics. All of the statistical analyzes were performed using IBM SPSS Statistics 22 software.

RESULTS and DISCUSSION

TPC, total anthocyanin and antioxidant capacity

TPC values of fruit extracts belonging to cornelian cherry genotypes were measured using the calibration graph prepared in the spectrophotometer with concentrations of 1.00, 2.50, 10.00, 25.00, and 50.00 mg/100 mL of gallic acid standard. Results expressed as gallic acid equivalent (GAE) are given in Figure 1A. The TPC values of the fruits ranged from 201.45-
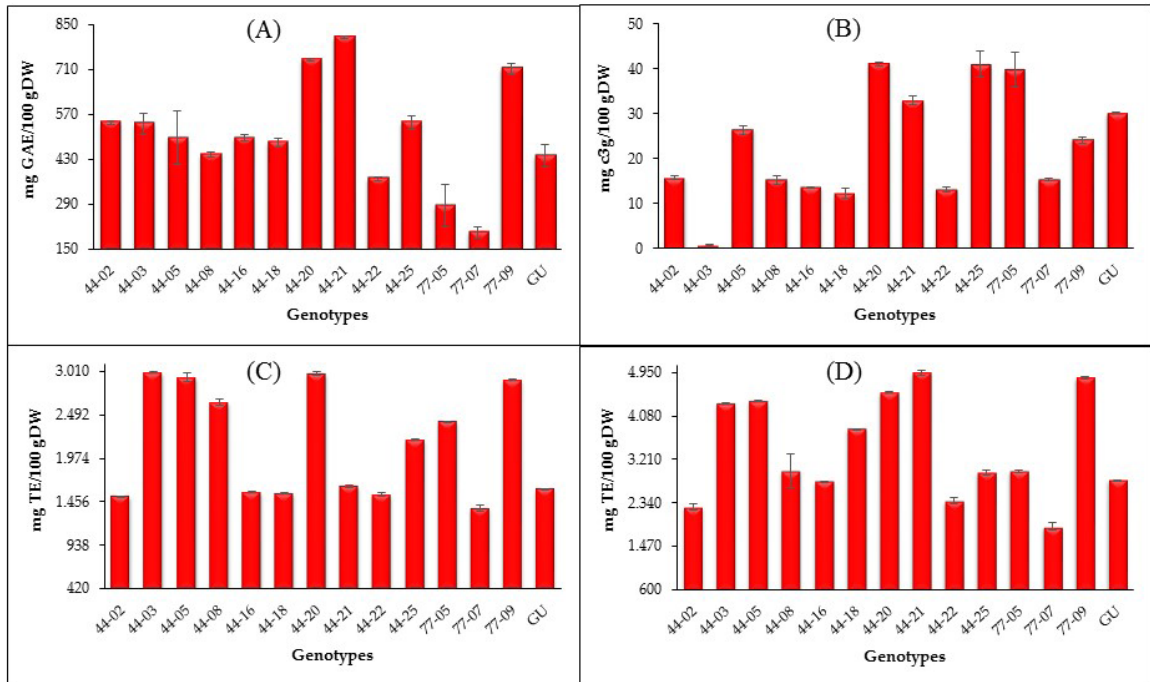
Figure 1. Total phenol (A) and total anthocyanin (B) contents, antioxidant capacity to DPPH radical scavenging (C), and reducing power (D) tests of cornelian cherry fruit extracts (GU: Güney Uzun).

808.73 mg GAE/100 gDW, and the genotypes with the highest phenolic content were 44-21 (808.73±7.27 mg GAE/100DW), 44-20 (739.64±10.91 mg GAE/100 gDW) and 77-09 (710.55±32.73 mg GAE/100 gDW), respectively. Genotype 77-07 contained the lowest phenolic content (201.45±32.73 mg GAE/100gDW). These results are in agreement with those obtained by Stiropoulos et al. (280-560 mg GAE/100 g), Tural and Koca (281-579 mg GAE/100 g), De Biaggi et al. (196.68 mg GAE/100 g), Cosmulescu et al. (163.69-359.28 mg GAE/100 g), Kucharska and Letowska (261.70-464.12 mg GAE/100 g) and Cetkovska et al. (217.4-614.3 mg GAE/100 g) [7-9, 22-24]. However, there are also higher and lower values in the literature compared to the results of our study. For instance, Yousefi et al. [25] and Pantedis et al. [10] reported that TPC is 1310.2 and 2611mg GAE/100 g (higher than the results of our study) in cornelian cherry fruit, respectively, while Klymenko et al. [26] within the range of 91.34-200.00 mg GAE/100 g (lower than the results of our study).

TAN results of fruit extracts belonging to cornelian cherry genotypes are given in Figure 1B. TAN values ranged from 0.67 to 41.08 mg c3g/100 gDW. The genotype 44-20 (41.08±0.73 mg c3g/100 gDW) came into

prominence with the highest total anthocyanin content, while the genotype 44-03 (0.67±0.27 mg c3g/100 gDW) had the lowest.

Anthocyanins are pigments that give pink, red, blue, and purple colors to fruits and vegetables [17]. The results of our study are in agreement with those reported by Karaaslan (12.0-23.3 mg/100 g), Kantar (32-36 mg/100 g), and Cetkovska (6.1-34.7 mg/100 g) [17, 24, 27]. Compared to our results, either higher or lower results were reported in the previous studies. For example, De Biaggi et al. (134.71 mg/100 g), Moldovan et al. (92.23 mg/100 g), Pantelidis et al. (223 mg/100 g) and Popovic et al. (0.00058-0.03 mg/100 g) etc. [5, 8, 10, 11].

Fruit extracts were analyzed for their antioxidant capacity using DPPH radical scavenging and reducing power assays. Results are given in Figure 1C (DPPH) and 1D (reducing power). According to the DPPH assay, antioxidant capacity values varied between 1377.22-3003.91 as mg TE/100 gDW, and 75.22-88.89 as % inhibition. Genotypes 44-03 (3003.91±7.77), 44-20 (2991.82±25.24), 44-05 (2945.76±49.75), and 77-09 (2910.25±7.42 mg TE/100 gDW) showed the highest antioxidant capacity. According to the reducing power assay, antioxi-

dant capacity values varied between 1869.16-4943.36 mg TE/100 gDW. Genotypes 44-21 (4943.76±59.97), 77-09 (4847.65±21.58), 44-20 (4559.67±19.02), 44-05 (4375.19±14.43) and 44-03 (1339.88±14.68 mg TE/100 gDW) showed the highest antioxidant capacity according to reducing power assay. In a study conducted on six cornelian cherry genotypes, antioxidant capacity (DPPH) values of three genotypes were 76.32-82.37% (in agreement with our results), while the other three genotypes were reported to be between 38.98-60.86% (lower than our results) [12]. In another study in which different solvents were used, the antioxidant capacities (reducing power) of extracts obtained from ethanol and methanol solvents were 3531.91 and 2734.56, respectively, while it was 5894.99 for acetone, 1207.73 for acetonitrile, and 920.65 mg TE/100 g for water [17]. The use of different extraction solvents may be the reason for the difference in results.

Phenolic compounds

Phenolic component determinations of extracts obtained after extraction from fruits belonging to fourteen cornelian cherry genotypes were made by the HPLC-DAD system. In all genotypes, gallic acid, catechin, epicatechin, chlorogenic acid, epigallocatechin gallate (Epigal), and rutin compounds were determined in different concentrations. 44-20 and 44-21 with their gallic acid, chlorogenic acid, Epigal, and epicatechin contents, 44-20 and 44-02 with their catechin content, and 44-25 with its rutin content were determined as the prominent genotypes (Table 3). There are many previous reports on phenolic compounds of cornelian cherry fruits. The gallic acid, catechin, chlorogenic acid, epicatechin and rutin contents of the examined samples were between 21.91-55.07, 10.35-30.41, 4.09-33.98, 6.83-17.58, 7.60-36.33 and 3.69-15.68 mg/100 gDW respectively, in agreement with previous studies (gallic acid: from 0.05 to 166; catechin: from 0.39 to 395; chlorogenic acid: from 1.29 to 15; epicatechin: from 0.40 to 211; rutin: from 0.29 to 81 mg/100 g) [8, 9, 11, 13, 28-39]. In this current study, Epigal content of the examined samples was between 6.83-17.58 mg/100 gDW, lower than the result (19 mg/100 g) of Harnly et al. [40], who studied in unripped cornelian cherry fruits. As a matter of fact, the contents of some phenolic compounds unripe fruits are higher than those of ripe fruits [41]. Data from both previous studies and the present study have appeared on a wide scale. The different polarities of the phenolic compounds may affect those extraction yields depending on the polarity of the extraction solvents. Many factors, such as the solvent used in extraction, the extraction technique, genotype/variety feature, growing location, altitude, and plant nutrition status, may be the reason for the variation in the results.

Table 3. Phenolic compounds in cornelian cherry fruit extracts (mg/100 gDW); data are expressed as mean±SD (n = 3); means in the same column bearing different letters are significantly different (p < 0.05).

Genotype Name	Gallic Acid	Catechin	Chlorogenic Acid	Epigal	Epicatechin	Rutin
44-02	23.08±4.61gh	30.12±1.33a	24.49±0.27c	7.61±0.67ef	10.06±1.54def	9.60±0.32cd
44-03	27.19±1.65efg	20.05±1.80bc	10.92±0.36e	6.83±0.60f	14.54±1.11c	10.57±0.81c
44-05	30.42±2.33def	17.14±1.83cd	17.58±1.66d	12.83±0.42c	11.32±1.66cdef	7.88±0.65ef
44-08	22.95±0.85gh	10.35±0.13g	4.09±0.11g	6.96±0.03f	8.26±0.64ef	3.69±0.09g
44-16	38.48±0.61bc	13.43±0.75efg	8.81±0.18f	6.85±0.86f	9.65±0.41def	6.54±0.48f
44-18	39.31±5.36b	19.94±3.13bc	11.03±2.03e	13.46±2.37bc	12.48±3.41cd	13.77±2.81b
44-20	55.07±3.61a	30.41±0.22a	32.35±0.83a	17.45±1.48a	35.14±5.59a	8.45±0.80de
44-21	54.75±2.16a	21.41±5.05b	33.98±0.17a	17.58±1.64a	36.33±0.16a	10.90±0.19c
44-22	38.61±3.57bc	21.15±2.41b	27.04±2.04b	10.74±0.36d	18.95±3.05b	7.47±0.87ef
44-25	25.66±1.58fgh	21.99±2.11b	27.35±1.43b	13.36±0.94bc	11.10±3.41cdef	15.68±1.08a
77-05	21.91±3.07h	12.91±2.98fg	17.34±2.45d	14.69±0.56b	10.06±2.03def	6.45±0.91f
77-07	30.97±0.99de	18.64±0.09bc	16.59±0.11d	6.94±0.18f	10.18±1.47def	8.34±0.45de
77-09	41.24±4.83b	16.61±1.46cde	16.34±0.00d	9.22±0.47de	11.70±0.01cde	7.68±0.28ef
GU	34.01±2.02cd	14.65±0.34def	10.30±0.14ef	7.89±0.05ef	7.60±0.70f	8.91±0.40de
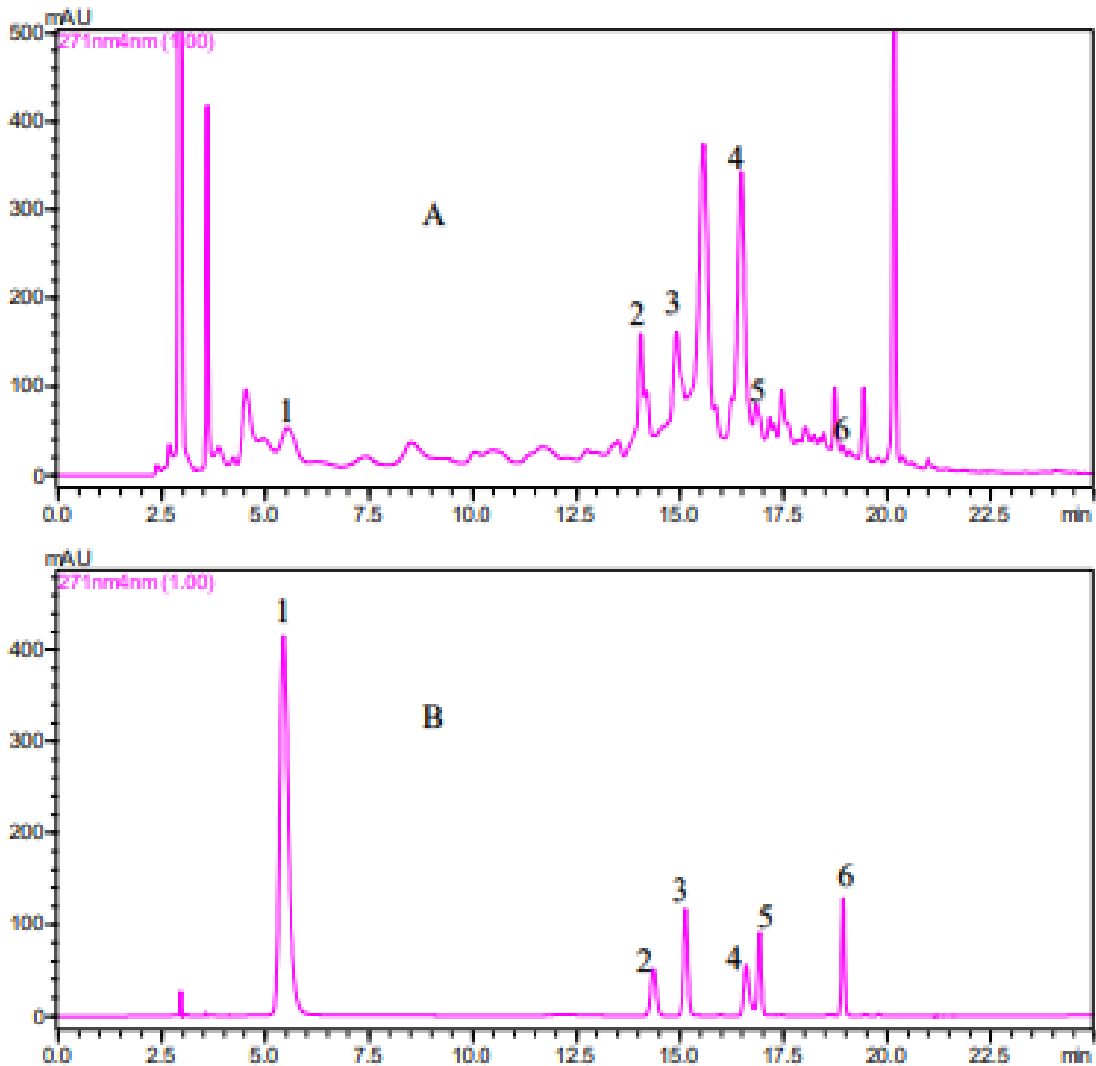
Figure 2. HPLC chromatograms of sample genotype 44-18 (A) and standards mix solution (B).
1: Gallic acid, 2: Catechin, 3: Chlorogenic acid, 4: Epigallocatechin gallate, 5: Epicatechin, 6: Rutin
Standards mix solution (1, 3, 4, and 6: 0.025 mg/100 mL; 2 and 5: 0.05 mg/100 mL).

Sugar Compounds and Vitamin C

Sugar compounds of cornelian cherry fruits was determined with the HPLC-RID, and the results are presented in Table 4. The differences in glucose contents among cornelian cherry genotypes were statistically insignificant (p > 0.05). Amounts of fructose, sucrose, and glucose ranged from 1.86-2.94, 0.03-0.12 and 3.05-4.59 % DW, respectively. Perova et al. [42] reported that fructose and glucose contents in cornelian cherry fruits were in the range of 2.2-3.8% and 2.5-7.0%, respectively. In a study of fresh and dried cornelian cherry fruits, fructose was found to be 1.90%, glucose 12.26% and sucrose 0.17% in fresh fruit samples. In a study [43] of fresh and dried cornelian cherry fruits, fructose was found to be 1.90%, glucose 12.26% and sucrose 0.17% in fresh fruit samples. In dried fruit samples fructose was found to be 2.63%, glucose 7.45% and sucrose 0.25%. In another study [44], it was reported that fructose and glucose contents in cornelian cherry fruits were 3.7% and 5.4%, respectively. Antolak et al. [45] reported that cornelian cherry juice contained 5.56g/100 mL fructose and 2.97g/100 mL glucose. The results of fructose and glucose reported by us were near to these literature data, while the sucrose results were lower than.

Table 3. Phenolic compounds in cornelian cherry fruit extracts (mg/100 gDW); data are expressed as mean±SD (n = 3); means in the same column bearing different letters are significantly different (p < 0.05).

Genotype Name	Vitamin C	Glucose*	Fructose	Sucrose
44-02	69.86±1.35j	4.35±0.66	2.69±0.42ab	0.10±0.02c
44-03	126.76±2.39ı	4.32±0.44	2.43±0.30abc	0.05±0.01g
44-05	198.35±1.29e	3.60±0.70	2.32±0.34abc	0.08±0.01d
44-08	254.38±0.08b	4.59±0.71	2.94±0.47a	0.08±0.01d
44-16	258.42±3.40b	4.06±0.85	2.90±0.63a	0.07±0.01de
44-18	264.68±3.12a	4.42±0.39	2.36±0.33abc	0.11±0.01bc
44-20	247.41±2.80c	3.46±0.64	2.02±0.40bc	0.07±0.02ef
44-21	216.17±5.64d	3.05±0.59	2.01±0.39bc	0.05±0.01fg
44-22	139.53±1.27g	3.71±0.51	2.81±0.62a	0.08±0.01de
44-25	8.48±0.45l	4.52±0.61	1.90±0.05c	0.12±0.01ab
77-05	132.36±0.04h	3.20±0.46	2.07±0.61bc	0.03±0.01h
77-07	213.28±8.20d	3.97±0.65	2.54±0.54abc	0.08±0.01d
77-09	21.96±0.72k	4.40±0.81	1.86±0.02c	0.12±0.01a
GU	146.16±2.95f	3.86±0.36	2.09±0.27bc	0.12±0.01ab

The vitamin C results of cornelian cherry fruits ranged from 8.48 to 264.68 mg/100 gDW (Table 4). The genotype 44-18 had the highest vitamin C content in its fruits (264.68±3.12 mg/100 gDW). The vitamin C contents of cornelian cherry fruits were reported as being between 16.0 and 299.5 mg/100 g in previous studies [7, 10, 12, 23, 24]. Vitamin C results for other genotypes except the 44-25 genotype (8.48±0.45 mg/100 gDW) are consistent with the literature data.

In-vitro Cytotoxic Activity

The cytotoxic effects of the fruit extracts on healthy cells (L-929) are presented in Figure 2. 100 and 200 µg/mL extract doses of the studied cornelian cherry genotypes showed no toxic effects on L-929 cells. The cytotoxic effects of the extracts on lung cancer cells (A-549) are given in Figure 3. The significant cytotoxic activity was observed against lung cancer cells in both extract doses of the studied genotypes, especially 44-16 and 44-21. The extracts of other genotypes were observed to reduce the proliferation of lung cancer cells, too (p ≤ 0.05). In some genotypes (44-05, 44-08, 44-22, GU), the cytotoxic activity on A-549 (lung) cells increased by increasing the extract dose.

Yousefi et al. [25] reported that cornelian cherry fruit extracts showed anticancer potential and increased the apoptosis in SKOV3 (ovarian), MCF-7 (breast), PC-3 (prostate), and A-549 (lung) carcinogenic cell lines. Also, cornelian cherry leaves [4] and fruit juice [46] were stated to reduce cancer cell proliferation. Hosseini et al. [47] reported that the cornelian cherry extracts significantly reduced cell proliferation in the gastric carcinoma cell lines and thus could be used as a potent inhibitor of cancer cell proliferation. However, they found that when administered a 10 mg/mL extract dose in L-929 cells, the cell proliferation was reduced by approximately 80%. Depending on increasing doses, it was specified that cornelian cherry fruit extracts shown a high level of cytotoxic effect on healthy cells.

The results of correlation analysis between biochemical fruit characteristics and cytotoxic properties of cornelian cherry genotypes examined within the scope of the study are presented in Table 5. Accordingly, different correlation levels were determined among most of the evaluated fruit characteristics, which are statistically significant (at 0.01 and 0.05 significance levels).

TPC showed positive correlations in a low level with DPPH, moderate level with CAT, CA and Epigal, and a high level with RP, GA and Epicat. In addition to TPC, DPPH was found correlated with RP but in a high level (r = 0.62). A moderate positive correlation was found between RP and GA, Epigal and Epicat, and a low-level negative correlation (r = -0.39) with Fructose. TAN highly
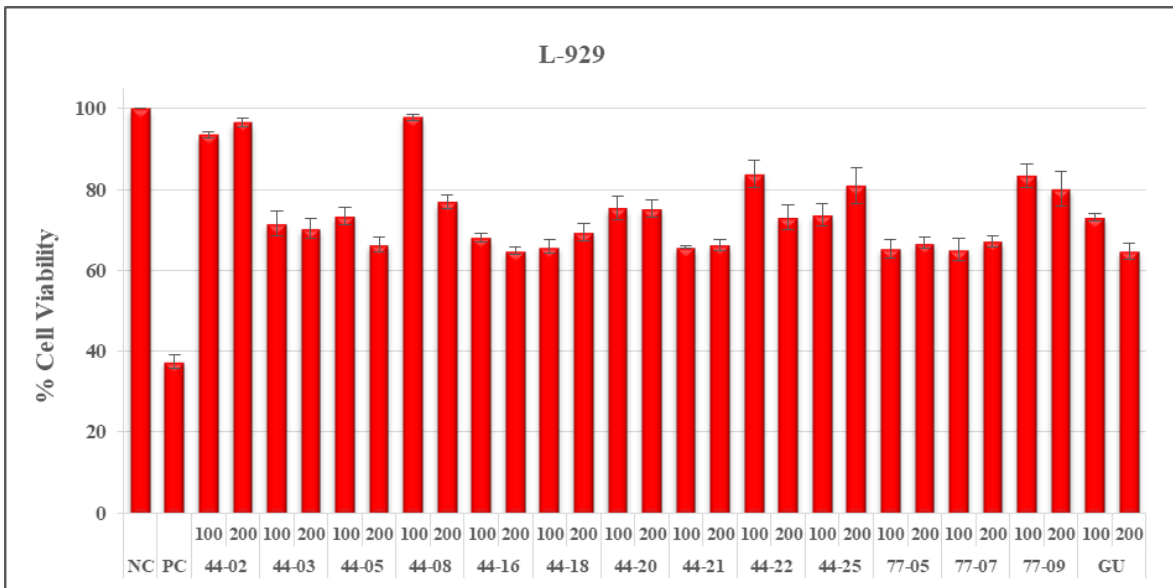
Figure 3. Cell proliferation inhibitory activities of cornelian cherry fruit extracts (100 and 200 µg/mL) against L929 healthy cell lines. The vertical bars represent mean±SD of three individual experiments (NC: Negative Control; PC: Positive Control).
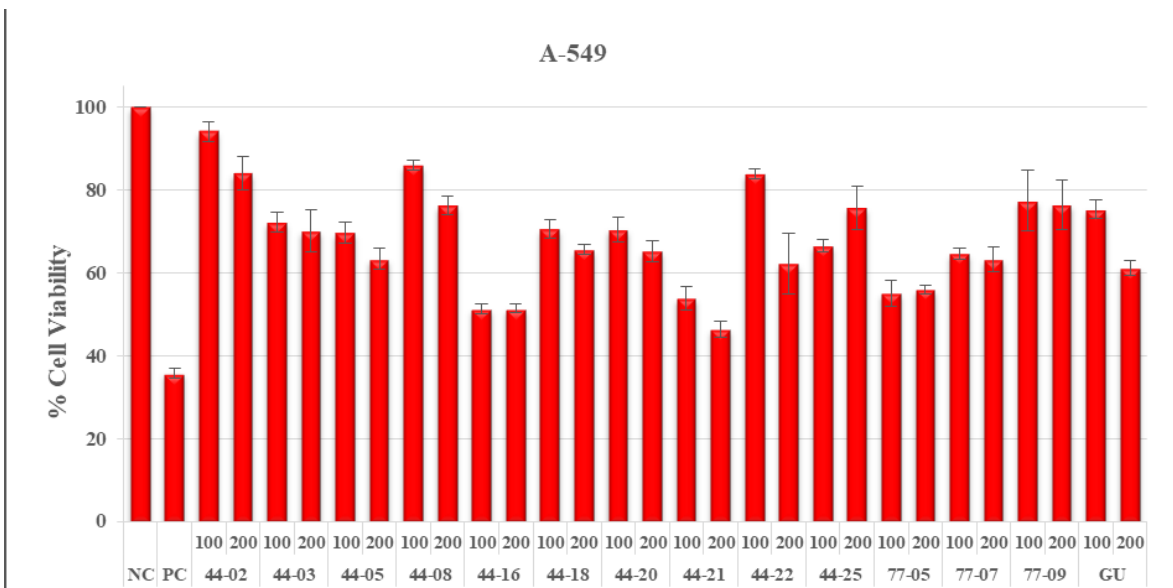
Figure 4. Cell proliferation inhibitory activities of cornelian cherry fruit extracts (100 and 200 µg/mL) against A549 lung cancer cell lines. The vertical bars represent mean±SD of three individual experiments (NC: Negative Control; PC: Positive Control).

correlated with Epigal, moderately with CA and Fructose and in a low level with Epicat, Glucose and A-100, but the directions of the correlations were different. Low level of correlations were found for GA with CAT, VitC, Glucose, medium level with CA, Epigal and A-200, high level but different directions with Epicat. CAT showed a low level of positive correlation with Epigal (r = 0.38), a moderate level of positive correlation with Epicat, Rutin

and L-200, and a high level of positive cor relation with CA (r = 0.72). CA showed positive correlation with Rutin (r = 0.37), negative and low-level correlation with Glucose (r = -0.35), and a high level of positive correlation with Epigal and Epicat. Similarly, Epigal also showed a high level of positive correlation with Epicat, besides it showed a positive low level of correlation with Rutin, a low level of negative correlation with A-100 and A-200,

Table 5. Correlation coefficients among the assessed variables obtained from Pearson's Correlation Test.

	DPPH	RP	TAN	GA	CAT	CA	Epigal	Epicat	Rutin	VitC	Glucose	Fructose	Sucrose	L-100	L-200	A-100	A-200
TPC	0.33*	0.73**	0.28	0.62**	0.43**	0.45**	0.43**	0.62**	0.26	-0.09	-0.06	-0.30	0.09	0.10	0.23	-0.02	0.00
DPPH		0.62**	0.19	-0.04	-0.05	-0.06	0.16	0.10	-0.20	-0.15	0.02	-0.24	-0.21	0.17	0.06	0.07	0.24
RP			0.20	0.55**	0.11	0.21	0.50**	0.54**	0.15	0.06	-0.16	-0.39**	-0.12	-0.16	-0.15	-0.20	-0.12
TAN				0.24	0.16	0.54**	0.70**	0.35*	0.17	-0.19	-0.33*	-0.50**	-0.01	-0.17	-0.01	-0.32*	-0.14
GA					0.35*	0.50**	0.54**	0.82**	0.15	0.35*	-0.31*	-0.22	-0.06	-0.28	-0.27	-0.30	-0.40**
CAT						0.72**	0.38*	0.55**	0.48**	-0.17	-0.05	-0.11	0.10	0.11	0.49**	0.24	0.24
CA							0.69**	0.75**	0.37*	-0.24	-0.35*	-0.30	-0.11	-0.07	0.24	-0.07	-0.09
Epigal								0.72**	0.37*	0.12	-0.42**	-0.42**	-0.23	-0.34*	-0.15	-0.37*	-0.32*
Epicat									0.18	0.26	-0.40**	-0.22	-0.34*	-0.17	-0.10	-0.22	-0.31*
Rutin										-0.31*	0.14	-0.32*	0.34*	-0.34*	0.11	-0.12	0.11
VitC											-0.19	0.30	-0.36*	-0.24	-0.51**	-0.28	-0.46**
Glucose												-0.27	0.43**	0.37*	0.27	0.34*	0.43**
Fructose													-0.10	0.22	0.06	0.15	0.07
Sucrose														0.30	0.36*	0.44**	0.47**
L-100															0.68**	0.80**	0.63**
L-200																0.68**	0.68**
A-100																	0.71**

TPC: Total Phenolics, RP: Reducing Power, TAN: Total Anthocyanin, GA: Gallic Acid, CAT: Catechin, CA: Chlorogenic Acid, Epigal: Epigallocatechin gallate, Epicat: Epicatechin, VitC: Vitamin C

and a moderate negative correlation with Glucose and Fructose. Epicat was also found negatively correlated with Sucrose and A-200 in a low level and moderate level with Glucose. Rutin showed negative correlations with VitC, Fructose and L-100, and positive but low correlations with Sucrose. VitC also showed correlations with Sucrose (r = -0.36) and a moderate negative correlation with L-200 and A-200 (r = -0.51 and r= -0.46, respectively). Glucose showed positive correlations with Sucrose, L-100, A-100 and A-200, whereas Sucrose with L-200, A-100 and A-200. All cytotoxic properties were found significant and positively correlated with each other in high and very high levels.

The eigen and variance values of the first four components out of a total of eighteen components obtained as a result of the principal component analysis of the fruit characteristics of the cornelian cherry genotypes examined within the scope of the study are summarized in Table 6.

As a result of the analysis, it was seen that the first two components expressed 52.02% of the total variance, with the first and second components being 30.34% and 21.69%, respectively. This was followed by the third and fourth components with 10.68% and 10.09%, and the cumulative variance expressed with the fourth component reached 72.79%. As a result of their study on 21 cornelian cherry varieties grown in New Zealand, Lu et al. [48], reported that the cumulative variance of the first two components was 67.9% in the results of the principal components analysis performed with 6 different physical fruit characteristics. The higher value obtained in this current study would be due to the relatively lower variance in the population in terms of the characteristics examined, as well as the lower number of biochemical properties examined.

The component score results of the characters and the genotypes of the first two components, which represent the majority of the obtained variance and express almost all of the characters examined as a result of the principal component analysis, are presen ted in the bi-plot charts given in Figure 4. When the figure is examined, similar to the results reported by Brown et al. [49], it was observed that the genotypes were distributed around the chart based on their distinguishing characteristics instead of forming clusters whose boundaries could be sharply determined.

Table 3. Phenolic compounds in cornelian cherry fruit extracts (mg/100 gDW); data are expressed as mean±SD (n = 3); means in the same column bearing different letters are significantly different (p < 0.05).

Variable	Vitamin C	Glucose*	Fructose	Sucrose
TPC	0.58	0.52	0.34	-0.02
DPPH	0.14	0.22	0.76	-0.40
RP	0.63	0.20	0.56	-0.30
TAN	0.58	0.21	-0.15	-0.28
GA	0.78	0.05	0.10	0.23
CAT	0.37	0.67	-0.24	0.40
CA	0.68	0.49	-0.27	0.29
Epigal	0.87	0.16	-0.07	-0.04
Epicat	0.86	0.20	0.15	0.35
Rutin	0.31	0.40	-0.61	-0.24
VitC	0.21	-0.59	0.24	0.38
Glucose	-0.51	0.31	-0.03	-0.39
Fructose	-0.41	-0.29	0.09	0.68
Sucrose	-0.35	0.50	-0.31	-0.22
L-100	-0.53	-0.56	0.39	0.28
L-200	-0.34	-0.81	0.00	0.23
A-100	-0.56	-0.62	0.19	0.27
A-200	-0.54	-0.68	0.11	-0.03
Eigen values	5.46	3.90	1.92	1.82
Variance (%)	30.34	21.69	10.68	10.09
Cumulative variance (%)	30.34	52.02	62.70	72.79

TPC: Total Phenolics, RP: Reducing Power, TAN: Total Anthocyanin, GA: Gallic Acid, CAT: Catechin, CA: Chlorogenic Acid, Epigal: Epigallocatechin gallate, Epicat: Epicatechin, VitC: Vitamin C

As a result of the analysis, most of the phytochemical fruit characteristics were represented by the first component. The most important characters affecting the first component were respectively; Epigal (0.87), Epicat (0.86), GA (0.78), RP (0.63), TAN (0.58), TPC (0.58), and Glucose (-0.51).

Positive PC1 values points the genotypes with higher values in terms of these traits, except for Glucose, which gives negative value. In support the genotypes '44-20' and '44-21' were with their higher RP, GA, Epicat and Epigal contents. All of the cytotoxic parameters were represented by the second component as well as CAT (0.67), VitC (-0.59), and Sucrose (0.50). For example, the genotype '44-02' was distinguished with higher cytotoxic properties. DPPH (0.76) and Rutin (-0.61) affected the third component and Fructose (0.68) the fourth of which effect on the distribution of the genotypes examined in the first two components was weak.
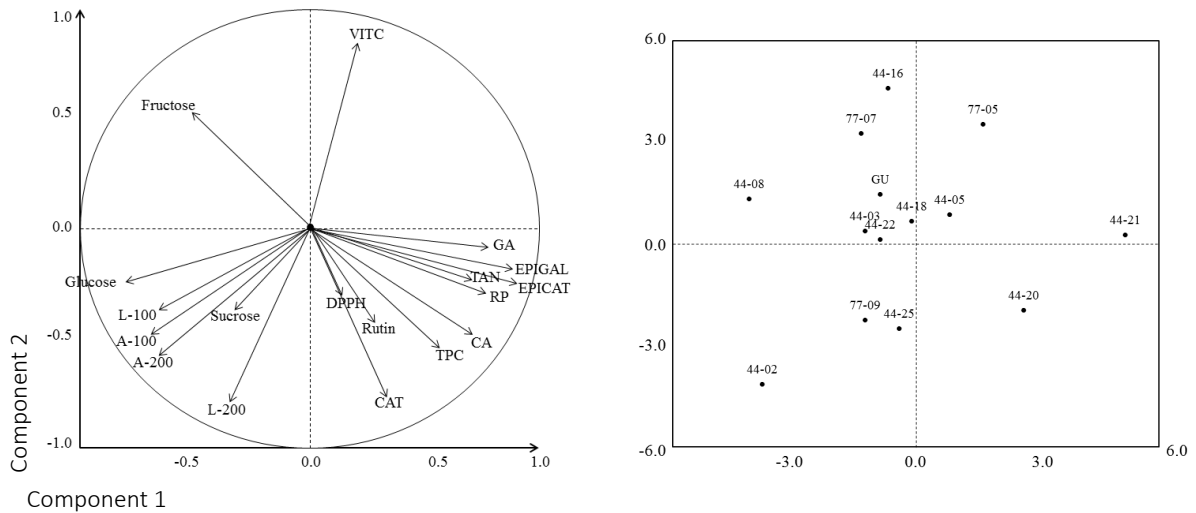
Figure 5. Segregation of apricot cultivars according to pomological and phytochemical characteristics determined by principal component analysis (TPC: Total Phenolics, RP: Reducing Power, TAN: Total Anthocyanin, GA: Gallic Acid, CAT: Catechin, CA: Chlorogenic Acid, EPIGAL: Epigallocatechin gallate, EPICAT: Epicatechin, VITC: Vitamin C).

Studies show that using cornelian cherry fruits as a functional food gains importance due to their high phenolic content and potential therapeutic benefits. Phenolic compounds are the main compounds responsible for pharmacological activity. Its health-supporting effects arising from its potent antioxidant activities were stressed in many studies. In this study, the antioxidant potential of cornelian cherry fruit extracts and their cytotoxic effects on A-549 (lung) cancer cells were investigated. Results of the present study showed that the fruit extract inhibited cell proliferation by showing the cytotoxic effect on A-549 cells. The phytochemical contents of the fruits used in the study were also determined. 44-21, 44-16, and 77-05 genotypes were the genotypes with the highest cytotoxic effects (approximately 50%) on A-549 cells. Many mechanisms may be responsible for these beneficial effects. Singlet oxygen and free radical scavenging antioxidant activity are possible action mechanisms of cornelian cherry extracts, and this activity was observed in vitro. Cornelian cherry extracts have the potent to reduce the riskof various cancer diseases. Well-designed long-term clinical studies are needed to confirm these results.

References

1. G. Shui, LP. Leong, Residue from star fruit as valuable source for functional food ingredients and antioxidant nutraceuticals, Food Chem., 97 (2006) 277–284.
2. E. Büyüktuncel, Toplam fenolik içerik ve antioksidan kapasite tayininde kullanilan baslica spektrofotometrik yöntemler, Marmara Pharm. J. 2 (2013) 93–103.
3. A. Ekbul, Diyetsel Polifenoller ve Kardiyovasküler Sistem. Turkiye Klin J Cardiol 17 (2004) 48–54.
4. K. Šavikin, G Zdunić, T Janković, T Stanojković, Z Juranić, N Menković, In vitro cytotoxic and antioxidative activity of Cornus mas and Cotinus coggygria, Nat. Prod. Res. 23 (2009) 1731–1739.
5. B.M. Popović, D. Štajner, K. Slavko, B. Sandra, Antioxidant capacity of cornelian cherry (Cornus mas L.) comparison between permanganate reducing antioxidant capacity and other antioxidant methods Food Chem., 134 (2012) 734–741.
6. S. Celik, I. Bakirci, I.G. Sat, Physicochemical and organoleptic properties of yogurt with cornelian cherry paste, Int. J. Food Property. 9 (2006) 401–408.
7. S. Tural, I. Koca, Physico-chemical and antioxidant properties of cornelian cherry fruits (Cornus mas L.) grown in Turkey, Sci. Hort., 116 (2008) 362-366.
8. B.M. De, D Donno, MG Mellano, L Riondato, EN Rakotoniaina, GL Beccaro, Cornus mas (L.) fruit as a potential source of natural health-promoting compounds: physico-chemical characterisation of bioactive components, Plant Foods Hum Nutr 73 (2018) 89–94.
9. S. Cosmulescu I. Trandafir, F. Cornescu, Antioxidant capacity, total phenols, total flavonoids and colour component of cornelian cherry (Cornus mas L.) wild genotypes, Not .Bot Horti. Agrobo., 47 (2019) 390-394.

10. G.E. Pantelidis, M. Vasilakakis, G.A. Manganaris, G. Diamantidis, Antioxidant capacity, phenol, anthocyanin and ascorbic acid contents in raspberries, blackberries, red currants, gooseberries and cornelian cherries, Food Chem., 102 (2007) 777-2783.

11. B. Moldovan, A. Filip, S. Clichici, R. Suharoschi, P. Bolfa, L. David, Antioxidant capacity of cornelian cherry (Cornus mas L.) fruits extract and the in vivo evaluation of ıts anti-inflammatory effects, J. Functional Foods, 26 (2016) 77- 87.

12. H. Hamid, H. Yousef, H. Jafar, A. Mohammad, Antioxidant capacity and phytochemical properties of cornelian cherry (Cornus mas L.) genotypes in Iran, Sci. Hort., 129 (2011) 459–463.

13. A.S. Milenkovic-Andjelkovic, M.Z. Andjelkovic, A.N. Radovanovic, B.C. Radovanovic, V. Nikolic, Phenol composition, DPPH radical scavenging and antimicrobial activity of cornelian cherry (Cornus mas) fruit and leaf extracts, Hem. Ind., 69 (2015) 331–337.

14. S. Erdoğan, S. Erdemoğlu, Evaluation of polyphenol contents in differently processed apricots using accelerated solvent extraction followed by high-performance liquid chromatography–diode array detector, Int. J. Food Sci. Nutr., 62 (2011) 729–739.

15. J.Y. Hwang, Y.S. Shue, H.M. Chang, Antioxidative activity of roasted and defatted peanut kernels, Food Res. Int., 34 (2001) 639–647.

16. G.C. Yen, C.Y. Hung, Effects of alkaline and heat treatment on antioxidative activity and total phenolics of extracts from Hsian-tsao (Mesona procumbens Hemsl.), Food Res. Int., 33 (2000) 487-492.

17. N.M. Karaaslan, (2012) Kiraz (Prunus avium), Çilek (Fragaria vesca) ve Kızılcık (Cornus Mas L.) Meyvelerindeki Antosiyanin Bileşiklerinin HPLC-ESI-MS İle Tayini ve Karakterizasyonu. PhD. Thesis, Faculty of Science, Fırat University, Elazığ, Turkey.

18. B. Cemeroğlu, (2007) Gıda Analizleri. Gıda Teknolojisi Yayınları. No:34 Ankara. s: 168-171.

19. F.S. Hosseini, M. Noroozi Karimabad, M.R. Hajizadeh, A. Khoshdel, S.K. Falahati-Pour, M.R. Mirzaei, S.M. Mirmohamadi, M. Mahmoodi, Evaluating of Induction of Apoptosis by Cornus mas L. Extract in the Gastric Carcinoma Cell Line (AGS), Asian Pacific J. Cancer Prev., 20 (2019) 123–130.

20. Y. Baran, C. Oztekin, E.Y. Bassoy, Combination of Fludarabine and Imatinib Induces Apoptosis Synergistically Through Loss of Mitochondrial Membrane Potential and Increases in Caspase-3 Enzyme Activity in Human K562 Chronic Myleloid Leukemia Cells. Cancer Invest., 28 (2010) 623–628.

21. Y. Baran, A.U. Ural, U. Gunduz, Mechanisms of cellular resistance to imatinib in human chronic myeloid leukemia cells, Hematology 12 (2007) 497–503.

22. T. Stiropoulos, A. Petridis, N. Koutinas, I. Therios, 'Ntoulia 1' and 'Ntoulia 2' cornelian cherries (Cornus mas L.), Hort Science, 46 (2011) 955-957.

23. A.Z. Kucharska, A.S. Letowska, Morphological, physical & chemical, and antioxidant profiles of Polish varieties of cornelian cherry fruit (Cornus mas L.), ŻYWNOŚĆ Nauka Technologia Jakość, 3 (2011) 78 – 89.

24. J. Cetkovska, P. Divis, J. Vespalcova, J. Porizka, V. Reznicek, Basic nutritional properties of cornelian cherry (Cornus mas L.) cultivars gown in the Czech Republic, A Alim., 44 (2015) 549-557.

25. B. Yousefi, M. Abasi, M.M. Abbasi, R. Jahanban-Esfahlan, Antiproliferative properties of Cornus mas fruit in different human cancer cells, Asian Pac. J. Cancer Prev., 16 (2015) 5727-5731.

26. S. Klymenko, A.Z. Kucharska, A. Sokół-Łętowska, N. Piórecki, Antioxidant activities and phenolic compounds in fruits of cultivars of cornelian cherry (Cornus mas L.), Agr. Bio. Div. Impr. Nut. Health Life Qual., 3 (2019) 484–499.

27. N.K. Kantar, (2019) Kızılcık Meyvesinden (Cornus mas) Ohmik Destekli Mikrodalga ve Ultrasonik Yöntemleri İle Fenolik Bileşiklerin Ekstraksiyonu. PhD. Thesis, Faculty of Engineering, Ankara University, Ankara, Turkey.

28. B.C. Radovanovic, A.S.M. Andelkovic, A.B. Radovanovic, M.Z. Andelkovic, Antioxidant and antimicrobial activity of polyphenol extracts from wild berry fruits grown in Southeast Serbia, Tropical J. Pharmaceut. Res., 12 (2013) 813-839.

29. G. Tian, T. Zhang, F. Yang, Y. Ito, Separation of gallic acid from Cornus officinalis Sieb. Et Zucc by High-Speed Counter-Current Chromatography, J. Chromatogr., A, 886 (2000) 309–312.

30. W. Du, H. Cai, M. Wang, X. Ding, H. Yang, B. Cai, Simultaneous determination of six active components in crude and processed fructus corni by High Performance Liquid Chromatography, J. Pharm. Biomed. Anal., 48 (2008) 194–197.

31. J. Sochor, T. Jurikova, S. Ercisli, J. Mlcek, M. Baron, S. Balla, S.O. Yılmaz, T. Necas, Charcterization of cornelian cherry (Cornus mas L.) genotypes–genetic resources for food production in Czech Republic, Genetika, 46 (2014) 915–924.

32. G. Cao, Y. Zhang, J. Feng, H. Cai, C. Zhang, M. Ding, X. Cong, B. Cai, A rapid and sensitive assay for determining the main components in processed fructus corni by UPLC-Q-TOF-MS, Chromatographia, 73 (2011) 135–141.

33. M.H. Lin, H.K. Liu, W.J. Huang, C.C. Huang, T.H. Wu, F.L. Hsu, Evaluation of the potential hypoglycemic and beta-cell protective constituents ısolated from corni fructus to tackle ınsulin-dependent diabetes mellitus, J. Agric. Food Chem., 59 (2011) 7743–7751.

34. S. Cosmulescu, I. Trandafir, V. Nour, Phenolic acids and favonoids profiles of extracts from edible wild fruits and their antioxidant properties, Int. J. Food Prop., 20 (2017) 3124–3134.

35. Z. Liu, Z.Y. Zhu, H. Zhang, G.G. Tan, X.F. Chen, Y.F. Chai, Qualitative and quantitative analysis of fructus corni using ultra sound assisted microwave extraction and high performance liquid chromatography coupled with diode array UV detection and time-of fight mass spectrometry, J. Pharm. Biomed. Anal., 55 (2011) 557–562.

36. H. Cai, G. Cao, B. Cai, Rapid simultaneous ıdentification and determination of the multiple compounds in crude fructus corni and its processed products by HPLC– MS/MS with multiple reaction monitoring mode, Pharm. Biol., 51 (2013) 273–278.

37. S. Deng, B.J. West, C.J. Jensen, UPLC-TOF-MS characterization and ıdentification of bioactive iridoids in Cornus mas fruit, J. Anal. Meth. Chem., (2013) Article ID 710972, 7 pages.

38. A. Begic-Akagic, P. Drkenda, A. Vranac, P. Orazem, M. Hudina, Influence of growing region and storage time on phenolic profile of cornelian cherry jam and fruit, Eur. J. Hort. Sci., 78 (2013) 30–39.

39. P. Drkenda, A. Spahic, A. Begic-Akagic, F. Gasi, A. Vranac, M. Hudina, M. Blanke, Pomological characteristics of some autochthnous genotypes of cornelian cherry (Cornus mas L.) in Bosnia and Herzegovina, Erwerbs-Obstbau, 56 (2014) 59–66.

40. J.M. Harnly, R.F. Doherty, G.R.A. Beecher, J.M. Holden, Flavonoid content of U.S. fruits, vegetables, and nuts, J. Agric. Food Chem., 54 (2006) 9966–9977.

41. S. Erdoğan. (2008) Çeşitli Kayısı Örneklerinde Bakır Spesiasyonu (Türlendirme). PhD. Thesis, Faculty of Science, İnönü University, Malatya, Turkey.

42. I.B. Perova, A.A. Zhogova, A.V. Poliakova, K.I. Éller, G.V. Ramenskaia, I.A. Samylina, Biologically active substances of cornelian cherry fruits (Cornus mas L.), Vopr. Pitan., 83 (2014) 86-94.

43. N.T. Petkova, M.H. Ognyanov, Phytochemical characteristics and in vitro antioxidant activity of fresh, dried and processed fruits of cornelian cherries (Cornus mas L.), Bulgarian Chem. Commun., 50 (2018) 302 –307.

44. T. Tarko, A. Duda-Chodak, P. Satora, P. Sroka, P. Pogoń, J. Machalica, Chaenomeles japonica, Cornus mas, Morus nigra fruits characteristics and their processing potential, J. Food Sci. Technol. 51 (2014) 3934–3941.

45. H. Antolak, A. Czyzowska, M. Sakac, A. Misan, O. Duragic, D. Kregiel, Phenolic compounds contained in little-known wild fruits as antiadhesive agents against the beverage-spoiling bacteria asaia spp., Molecules, 22 (2017) 1256.

46. A. Kourpeti-Tiptiri, E. Fitsiou, K. Spyridopoulou, Evaluation of antioxidant and antiproliferative properties of Cornus mas L. fruit juice, Antioxidants, 8 (2019) 377.

47. F.S. Hosseini, M.N. Karimabad, M.R. Hajizadeh, A. Khoshdel, Evaluating of induction of apoptosis by Cornus mas L. extract in the Gastric Carcinoma Cell Line (AGS), Asian Pac. J. Cancer Prev., 20 (2018) 123-130.

48. Y. Lu, B.N. Pekerti, Z.S. Toh, F. Broom, G. Savage, S.Q. Liu, D. Huang, Physicochemical parameters and proanthocyanidin profiles of cranberries cultivated in New Zealand, J. Food Compos. Anal., 63 (2017) 1-7.

49. P.N. Brown, S.J. Murch, P. Shipley, Phytochemical diversity of cranberry (Vaccinium macrocarpon Aiton) cultivars by anthocyanin determination and metabolomic profiling with chemometric analysis, J. Agric. Food Chem., 60 (2012) 261-271. .

Molecular Docking Mediated Virtual Drug Screening for GABA$_A$ Receptor: Promising Digoxin Derivatives

Moleküler Yanaştırma Yöntemiyle GABAA Reseptörü için Sanal İlaç Tarama: Umut Veren Digoksin Türevleri

Hüseyin Saygın Portakal[ID]

Izmir University of Economics, Genetics and Bioengineering, Izmir, Turkey.

ABSTRACT

In the central nervous system (CNS) of mammalian species, γ-aminobutyric acid (GABA) is the primary inhibitory neurotransmitter due to it regulates neuronal development through leading neural differentiation, proliferation, migration, etc. GABAA receptor is the major GABA receptor since it has the highest expression level among the other GABA receptors within CNS. Many pieces of evidence prove that the defects in the GABAergic pathway might give rise to serious diseases such as schizophrenia, epilepsy, anxiety, depression, insomnia, etc. In this study drug library with a totally of 8170 ligands consists of three distinct datasets which are FDA-approved Drugs, Drugs Approved by World but not FDA, and Non-human Metabolites have been screened for the allosteric site of the GABAA receptor with PyRx Virtual Screening Tool and ligand-receptor interactions have been analyzed with Biovia Discovery Studio software. Results reveal that Digoxin and its two distinct derivatives (DD1 and DD2), as well as Conivaptan, are promising in the treatment of GABAergic pathway-based disorders. The findings of this report should be verified with further molecular dynamics (MD) simulations and the ligands should be tested by both *in vitro* and *in vivo* studies.

Key Words

Virtual drug screening, molecular docking, GABA, GABAergic pathway, central nervous system, nervous disorders.

ÖZ

Memeli türlerinin merkezi sinir sisteminde (MSS) γ-aminobütirik asit (GABA), nöral farklılaşma, çoğalma, göç vb. yolları düzenleyen nöronal gelişim için birincil inhibitör nörotransmiterdir. GABA$_A$ reseptörü MSS içindeki diğer GABA reseptörleri arasında en yüksek ekspresyon seviyesine sahip olduğu için majör GABA reseptörüdür. GABAerjik yolaktaki bozuklukların şizofreni, epilepsi, anksiyete, depresyon, uykusuzluk gibi ciddi hastalıklara yol açabileceğini gösteren pek çok kanıt bulunmaktadır. Bu çalışmada FDA Onaylı İlaçlar, Dünyaca Onaylı Ama FDA Onaylı Olmayan İlaçlar ve İnsan Dışı Metabolitler olarak üç farklı verisetinden oluşan toplam 8170 ligand içeren ilaç kütüphanesi GABA$_A$ reseptörünün allosterik bölgesi için PyRx Virtual Screening Tool ile taranmış ve ligand-reseptör etkileşimleri Biovia Discovery Studio yazılımı ile analiz edilmiştir. Sonuçlar, Digoksin ve iki farklı türevinin (DD1 ve DD2) ve ayrıca Conivaptan'ın GABAerjik yolak temelli bozuklukların tedavisinde umut verici olduğunu ortaya koymaktadır. Bu raporun bulguları daha ileri moleküler dinamik (MD) simülasyonları ile doğrulanmalı ve ligandlar hem in vitro hem de in vivo çalışmalarla test edilmelidir.

Anahtar Kelimeler

Sanal ilaç tarama, moleküler yanaştırma, GABA, GABAerjik yolak, merkezi sinir sistemi, sinir sistemi bozuklukları.

INTRODUCTION

γ-aminobutyric acid (GABA) is the primary inhibitory neurotransmitter in the mammalian central nervous system (CNS). Through the GABAergic pathway, GABA acts a significant role in neuronal development by regulating neural differentiation, migration, proliferation, etc [1], [2]. Fundamentally, the functions of GABA are exhibited by binding to three distinct receptors which are $GABA_A$, $GABA_B$, and $GABA_C$ receptors [3]. While $GABA_A$ and $GABA_C$ are chloride ion (Cl^-) transporter ionotropic and ligand-gated receptors, $GABA_B$ is a metabotropic receptor [4]. Differentiation in GABA expression, GABA metabolism, synaptic receptors' activity, and differentiation on Cl^- ion concentration across the cell membrane is the primary parameters defining the regulation of neuronal activity [5].

Among the GABA receptors, $GABA_A$ has the highest expression level along with the CNS and is primarily responsible for fast inhibition in the brain [6]. The chemical structure of $GABA_A$ receptors contains five distinct subunits which are $α_{(1-6)}$, $β_{(1-3)}$, $γ_{(1-3)}$, δ, ε, Θ, π, $ρ_{(1-3)}$ [7]. In general, $GABA_A$ receptors that are widely expressed in the mammalian brain contain two α, two β, and one γ chains, and this conformation of $GABA_A$ receptors enables phasic inhibition which is fast and temporaneous through rapid desensitizing of postsynaptic receptors. In addition, tonic (long-term) activation within mammalian organisms is mediated by extrasynaptic $GABA_A$ receptors containing α5 subunit in the hippocampus and π subunit in the brain [8]–[10]. This tonic activation acts a prominent role in neuronal development since it regulates neural cell growth, formation of synapses, migration, and proliferation. Furthermore, $GABA_A$ receptors' localization over the synapses provides strong communication between neural cells [11]. As such, $GABA_A$ receptor expression profile, construction of its structure, and regular process of GABAergic pathway through these receptors are the main parameters for neuronal network creation and development within CNS [12].

Many discoveries demonstrate that the defects of the GABAergic pathway might cause serious diseases [13]. Among these diseases, schizophrenia takes the lead as one of the most significant neurodevelopmental disorders [14]. The primary symptoms of schizophrenia such as psychotic thoughts, hallucinations, delusions, and behavioral alterations are sourced from disrupted neuronal communications [15]. Various researches have reported that the inhibition of α5 subtype $GABA_A$ receptor by enhanced binding affinity of GABA gives rise to schizophrenic behavior patterns [16]. In addition, enhanced immune reactivity of α2 subtype $GABA_A$ receptor which is sourced from prenatal infections also might create schizophrenic pathogenesis [17]. Besides, the observation of attenuation on $GABA_A$ receptor expression and GABAergic pathway might cause other serious neuronal disorders such as epilepsy [18], anxiety [19], depression [20], insomnia [21], etc. For instance, it's been reported that extreme anxiety, avoidance behavior, and traumatic memories may be sourced by inhibition of $GABA_A$ receptors and be treated with to increase GABAergic transmission by various chemical compounds such as benzodiazepines [22]. Moreover, surprisingly it's recently been discovered that GABA metabolites secreted by B-cells inhibit $CD8^+$ T cell activity and suppress anti-tumor immune response through binding to $GABA_A$ receptors expressed on the surface of $CD8^+$ T cells [23]. Those findings indicate the great potential of $GABA_A$ receptors to treat several diseases from neuronal disorders to cancer and to date, various inhibitors have been developed such as Suramin [24], Broflanilide [25], Clozapine [26], etc.

In this study, virtual drug screening targeting the $GABA_A$ receptor's allosteric site has been carried out with a molecular docking-based approach. As such, 1609 FDA-Approved Drugs, 4254 Drugs Approved by World but not FDA, and 2307 Non-human Metabolites -a total of 8170 ligands- have been investigated during the virtual screening. Furthermore, the ligand that is included in the chemical structure of $GABA_A$ receptor (Benzamidine) has been re-docked and 7 distinct known inhibitors have been analyzed in order to validate the research. Findings demonstrate that two distinct Digoxin derivatives (ZINC000118915215 (DD1) and ZINC000118915217 (DD2)) from the Drugs Approved by World but not FDA dataset have the highest binding affinity to the allosteric site of $GABA_A$ receptor. In addition, the Digoxin drug (ZINC000242548690) from the FDA-Approved Drugs dataset has been revealed as one of the ligands having the highest binding affinity after Conivaptan (ZINC000012503187). Therefore, Digoxin and its derivatives are evaluated as promising compounds in the treatment of GABAergic pathway-based diseases.

MATERIALS and METHODS

Receptor Preparation

Crystal structure of GABA$_A$ receptor and grid box sizes selection were carried out by following the research published by Sahila and his colleagues in 2015 [27]. The GABA$_A$ crystal structure with PDB ID: 4COF was retrieved in .pdb format from Protein Data Bank (PDB). X-ray diffraction analysis of the selected GABA$_A$ receptor has a 2.97 Å resolution, 0.226 R-value (free), and 0.206 R-value (observed). The downloaded receptor structure was imported in UCSF Chimera software version 1.16. The ligands and heteroatoms of the GABA$_A$ receptor were removed from the structure and the receptor was prepared by following the Dock Prep module of UCSF Chimera [28]. During preparation solvent molecules (water) were removed, hydrogen atoms and partial charges were added, and the side chains were replaced by using Dunbrack 2010 rotamer library. Once the preparation had been completed, the prepared receptor was exported in .pdb format and imported into PyRx Virtual Screening Tool so that to be used in molecular docking studies.

Ligand Preparation

In order to perform virtual drug screening, a library containing a total of 8170 ligands was prepared including FDA-Approved Drugs dataset consisting of 1609 ligands, Drugs Approved by the World but not FDA dataset consisting of 4254 ligands, and Non-human Metabolites dataset consisting of 2307 ligands. The ligands constituting datasets were retrieved from the ZINC15 database. The datasets were imported in PyRx software separately, and the ligands were prepared by following the energy minimization module of the PyRx Virtual Screening Tool [29].

Molecular Docking

Virtual drug screening was conducted on the AutoDock Vina package loaded in PyRx Virtual Screening Tool by docking all ligand datasets to the allosteric site of the GABA$_A$ receptor [30]. During the molecular docking strategy, the file format of ligands was converted to .pdbqt, and grid box coordinates were defined as x= -20.224, y= -20.175, z= 126.3505 by following the Sahila et. al.'s publication and considering the benzamidine ligand location in the crystal structure of the protein [27].

Grid box dimensions were set to x= 40.143, y= 40.138, z= 40.053. Once the molecular docking had been completed, the data demonstrating binding affinity, rmsd/ub, and rmsd/lb of each dataset were exported in .csv format. The ligands with the highest binding affinity and mode with 0 value of each rmsd/ub, and rmsd/lb parameters had been selected, and receptor-ligand interactions' analysis was carried out in Biovia Discovery Studio Visualiser software.

Validation

In order to validate the molecular docking strategy, the structure of Benzamidine ligand found in the crystal structure of the receptor had been exported as .pdb format and re-docked to the receptor by following ligand preparation and molecular docking protocols. Besides, 7 known GABA antagonists which are Broflanilide (CHEBI: 131598), Clozapine (CHEBI: 3766), Flumazenil (CHEBI: 5103), Hydrochloride (CHEBI: 145121), Picrotoxinin (CHEBI: 8206), Suramin (CHEBI: 45906), Xenovulene A (CHEBI: 66336) were downloaded from ChEBI database and docked by conducting the same procedure.

ADME Study and Toxicity Profile

Absorption, Distribution, Metabolism, and Excretion (ADME) and toxicity properties of the three ligands exhibiting the highest binding affinity within the Drugs Approved by the World but not FDA and Non-human Metabolites datasets were analyzed with both OSIRIS Property Explorer tool [31] and swissADME server [32]. As such, physico-chemical properties (formula, molecular weight, molar refractivity, and topological polar surface area (TPSA)), lipophilicity parameters (iLOGP, XLOGP3, WLOGP, MLOGP, SILICOS-IT, and Consensus Log Po/w), solubility properties (Log S, SILICOS-IT solubility in both mg/ml and mol/l units, and solubility class), druglikeness properties (druglikeness and drug-score), pharmacokinetics parameters (GI absorption, BBB permeant, P-gp substrate, CYP1A2 inhibitor, CYP2C19 inhibitor, CYP2C9 inhibitor, CYP2D6 inhibitor, and CYP3A4 inhibitor), and toxicity profiles (mutagenicity, tumorigenicity, irritant effects, and reproductive effects) of related ligands were revealed. There was no requirement for ADME and toxicity analysis of the FDA-Approved Drugs dataset now that the ligands had been tested by FDA previously.

RESULTS and DISCUSSION

In order to reveal possible promising GABA antagonists, molecular docking mediated virtual drug screening was carried out. As such, a ligand library with a total of 8170 ligands consisting of three distinct datasets which are FDA-Approved Drugs (1609 ligands), Drugs Approved by World but not FDA (4254), and Non-human Metabolites (2307 ligands) were docked to the allosteric site of GABA$_A$ receptor. The binding affinity values and interacting receptor residues of the best 20 ligands of FDA-Approved Drugs, Drugs Approved by World but not FDA, and Non-human Metabolites are shown in Table 1, Table 2, and Table 3, respectively.

The molecular docking strategy was validated by re-docking the Benzamidine compound found in the crystal structure of the receptor. In this scope, the Benzamidine compound was exported as a separate file and re-docked to the allosteric site of the receptor. The binding affinity and the RMSD values of re-docked Benzamidine was determined as -6.7 kcal/mol, and 0.0 (rmsd/ub, and rmsd/lb), respectively. Furthermore, the Benzamidine-receptor interactions in both the downloaded crystal structure and the re-docked structure were performed in Biovia Discovery Studio (Figure 1). Results demonstrate that while Benzamidine in the crystal structure interacts with Tyr62, Phe200 residues through pi-pi stacked interactions and Tyr97, Glu155, Ser156, Tyr157, residues through conventional hydrogen bonds, re-docked Benzamidine interacts with Tyr62, Phe200 through pi-pi stacked interactions, Tyr97, Ser156, Tyr157 through conventional hydrogen bonds, Glu155, Tyr205 residues of the receptor through the salt bridge and pi cation interactions. Similarities of interacting residues of the receptor and the types of interactions demonstrate the sufficient accuracy of the molecular docking approach conducted in the study.

Furthermore, 7 known GABA antagonists were docked to the GABA$_A$ receptor's allosteric site and binding affinities were analyzed (Table 4). The chemical structures of the three best-scored ligands from each dataset were illustrated in Figure 2. Inhibitor docking findings demonstrate that the Suramin ligand has the highest binding affinity with -10.4 kcal/mol value. In addition, Broflanilide has -9.5 kcal/mol binding affinity, and Clozapine has -8.3 kcal/mol binding affinity. The receptor interactions of these three ligands and remaining inhibitors were analyzed in order to reveal common interacting residues of the GABA$_A$ receptor with GABA antagonists. As such it's revealed that Suramin might create conventional hydrogen bonds with Ala45, carbon-hydrogen bonds with Ser46, Asp48, Asn100, Lys102, Arg180, halogen (fluorine) interactions with Ile47, Asp48, Met55, alkyl and pi-alkyl interactions with Ala45, Leu99, Ala135, Met137, pi-cation interaction with Arg180 residues, Broflanilide might create carbon-hydrogen bonds and pi-anion interactions with Asp43, pi-pi stacked interaction with Tyr62, alkyl and pi-alkyl interactions with Tyr62, Leu99, Phe200, Ala201 residues, Clozapine might create carbon-hydrogen bond with Asp43, pi-sigma interactions with Tyr62, Phe200, conventional hydrogen bonds with Gln64, alkyl and pi-alkyl interactions with Leu99, Ala201, halogen (fluorine) interactions with Lys173 residues of the GABA$_A$ receptor (Figure 3). Considering the findings and interactions of remaining GABA antagonists, the common residues were revealed as; Asp43, Ala45, Ser46, Ile47, Tyr62, Leu99, Ala135, Met137, Tyr157, Arg180, Ile181, Phe200, Ala201. The number of common amino acids and their percentages in interaction have been analyzed by considering 20 best ligands of the three datasets as well as the inhibitors. The results are demonstrated in Table 5.

Among 1609 FDA-Approved Drugs, 7 drugs (ZINC000012503187, ZINC000242548690, ZINC000036701290, ZINC000203757351, ZINC000004099009, ZINC000095617679, ZINC000011679756) exhibited higher binding affinity then -10.4 kcal/mol which is the Suramin's binding affinity. In particular, the three best-scored ligands from the FDA-Approved Drugs dataset that are ZINC000012503187 (Conivaptan), ZINC000242548690 (Digoxin), ZINC000036701290 (Ponatinib) have been evaluated as promising with the binding affinities of -11.8 kcal/mol, -11.6 kcal/mol, and -10.9 kcal/mol, respectively. The receptor interactions of these ligands are demonstrated in Figure 4. Conivaptan is a Vasopressin receptors (V1a and V2) inhibitor [33] and is widely used in decreasing sodium levels in the blood and heart failure diseases [34]. Findings demonstrate that Conivaptan might create conventional hydrogen bonds with Asp43, carbon-hydrogen bonds with Ala45, Alkyl, and pi-alkyl interactions with Ala45, Leu99, Ala135, Ala201, pi-pi stacked, and pi-pi t-shaped interactions with Tyr157, Phe200, pi-sigma interaction with Asn100, and pi-cation interaction with Arg207. Digoxin is a molecule extracted from Digitalis lanata [35] and is used in the treatment of many cardiac diseases since it has activity on increasing

Table 1. Best 20 ligands, their binding affinities and interacting receptor residues of FDA-Approved Drugs dataset.

	FDA-Approved Drugs	
Ligand Name	Binding Affinity (kcal/mol)	Receptor Residues Interacting with Ligand
ZINC000012503187	-11.8	ASP43, ALA45, LEU99, ASN100, ALA135, TYR157, PHE200, ALA201, ARG207
ZINC000242548690	-11.6	ALA45, SER46, MET49, VAL53, MET55, TYR62, LEU99, ALA135, PRO184
ZINC000036701290	-10.9	ASN41, ASP43, ALA45, TYR62, GLN64, LEU99, PHE200, ALA201, ARG207
ZINC000203757351	-10.8	ASP43, ALA45, LEU99, ASN100, LYS102, ALA135, ARG180, ARG196, PHE200, ALA201, ARG207
ZINC000004099009	-10.6	ALA45, SER46, ASP48, ASP101, LYS102, ALA135, GLU182
ZINC000095617679	-10.6	ASP43, ALA45, TYR62, LEU99, MET115, TYR157, ARG180, PHE200, THR202, ARG207
ZINC000011679756	-10.5	ASN41, ASP43, TYR62, TYR157, PHE200, ALA201, THR202, TYR205
ZINC000006745272	-10.4	ASP43, ALA45, SER46, ASP48, TYR62, GLN64, LEU99, ASN100, ASP101, ALA135, PHE200
ZINC000100378061	-10.3	ALA45, TYR62, LEU99, ARG180, PHE200
ZINC000000538658	-10.2	ALA45, TYR62, LEU99, ARG180
ZINC000004097344	-10.2	ASP43, ALA45, LEU99, ALA135, MET137, GLU155, ALA201, THR202, TYR205
ZINC000040430143	-10.2	ASN41, ASP43, TYR62, PHE200, ALA201
ZINC000052955754	-10.2	ALA45, TYR62, MET137, ARG180, GLU182, PHE200, ARG207,
ZINC000068202099	-10.2	ASN41, ASP43, TYR62, TYR157, ARG169, GLY170, PHE200, ALA201
ZINC000169621231	-10.2	ALA45, ASN100, ARG180
ZINC000001493878	-10.1	ALA45, SER46, ASP48, TYR62, LEU99, ASP101, ARG129, GLU155, TYR157, PHE200, TYR205,
ZINC000006716957	-10.1	ALA45, LEU99, ALA135, MET137, THR151, GLU153, GLU182, LEU183, PRO184
ZINC000026985532	-10.1	ASP43, SER46, TYR62, LEU99, ASN100, ALA135, MET137, ARG180, PHE200, ARG207
ZINC000064033452	-10.1	ASP43, TYR62, SER156, TYR157, PHE200, ALA201
ZINC000070466416	-10.1	ASP43, ALA45, SER46, TYR62, ALA135, MET137

Table 2. Best 20 ligands, their binding affinities, and interacting receptor residues of Drugs Approved by World but not FDA dataset.

	Drugs Approved by World but not FDA	
Ligand Name	Binding Affinity (kcal/mol)	Receptor Residues Interacting with Ligand
ZINC000118915215	-11.9	ILE47, MET55, ALA135, MET137, ARG180, GLU182, LEU183, PRO184
ZINC000118915217	-11.9	MET49, TYR97, ALA135, MET137, ARG180, PRO184
ZINC000001542146	-11.3	ALA45, ILE47, TYR62, LEU99, ALA135, MET137, ILE181, GLU182, PHE200
ZINC000257362202	-11.2	ALA45, SER46, ASP48, MET49, GLU52, VAL53, MET55, LEU99, LYS102, ALA135, THR151, PRO184
ZINC000150339052	-10.9	ALA45, ASP48, MET55, LEU99, ALA135, CYS136, MET137, THR151, PRO184
ZINC000256630457	-10.9	ASP43, ALA45, TYR97, LEU99, ASN100, ALA135, MET137, GLU182, PHE200, ALA201
ZINC000118915214	-10.8	ILE47, VAL50, ASN54, ALA135, MET137, GLU153, LEU183, ARG196
ZINC000011616152	-10.7	ASP43, ALA45, TYR62, ARG180, PHE200, ALA201
ZINC000118915216	-10.7	ASP43, ASP48, VAL53, MET55, LEU99, ALA135, MET137, ARG180, LEU183, PRO184
ZINC000256109538	-10.7	SER46, ILE47, ASP48, MET49, GLU52, VAL53, MET55, ALA135, PRO184
ZINC000885764928	-10.7	TYR62, ALA135, ARG180, PHE200
ZINC000008143788	-10.6	TYR62, GLN64, PHE200
ZINC000095618690	-10.6	ASP48, TYR62, LEU99, ALA135, MET137, ARG180, GLU182
ZINC000000577115	-10.5	TYR62, GLU155, TYR157, PHE200, ALA201, TYR205
ZINC000043195321	-10.5	ASP43, ALA45, TYR62, LEU99, ARG180, PHE200, ALA201,
ZINC000100054749	-10.5	ALA45, SER46, ASP48, LEU99, ASN100, ASP101, LYS102, ALA135, CYS136, MET137, ASN149, THR151
ZINC000224657532	-10.5	ASP43, GLN64, GLU155, PHE200, ALA201, TYR205
ZINC000000537940	-10.4	ASN41, GLU155, TYR157, ARG169, ALA174, PHE200, ALA201, THR202, TYR205
ZINC000095618689	-10.4	TYR62, GLY127, TYR157, LYS173, GLU179, PHE200, ALA201, TYR205
ZINC000003872494	-10.3	TYR62, TYR97, GLU155, TYR157, PHE200, ALA201, TYR205

Table 3. Best 20 ligands, their binding affinities and interacting receptor residues of Non-human Metabolites dataset.

	Non-human Metabolites	
Ligand Name	Binding Affinity (kcal/mol)	Receptor Residues Interacting with Ligand
ZINC000028642721	-10.1	ALA45, SER46, ILE47, THR60, ASN100, ASP101, ALA135, CYS136, MET137, ARG180, GLU182
ZINC000100029436	-10.0	ALA45, SER46, ILE47, ASP48, TYR62, LEU99, ILE181, PHE200, ALA201, ARG207
ZINC000004098622	-9.9	ASP43, ALA45, SER46, TYR62, TYR97, LEU99, ASN100, ASP101, ARG180, PHE200, TYR205
ZINC000085432705	-9.8	ALA45, SER46, ASP48, TYR62, LEU99, ALA135, MET137, PHE200, ALA201
ZINC000003870412	-9.7	ALA45, SER46, ASP48, ASN54, MET55, LEU99, ASN100, ASP101, ALA135, MET137
ZINC000004096846	-9.7	SER46, ASP48, ASN54, ASN100, ASP101, ALA135, MET137, ARG180
ZINC000169335484	-9.6	ASP43, ALA45, ASP48, ASN54, MET55, LEU99, LYS102, ALA135, CYS136, MET137, GLU153, ARG180, GLU182, ARG207
ZINC000003874317	-9.5	ASN41, TYR62, GLN64, GLU155, SER156, TYR157, THR176, PHE200, ALA201, TYR205
ZINC000003255767	-9.4	ASP43, ALA45, TYR62, GLN64, LEU99, TYR157
ZINC000032052445	-9.4	ALA45, SER46, ASN100, ASP101, ALA135, ARG180
ZINC000038231587	-9.4	TYR62, TYR157, PHE200, ALA201, TYR205
ZINC000072180374	-9.4	TYR62, LEU99, ASN100, MET137, ASN149, CYS150, THR151, PHE200
ZINC000096006026	-9.4	ASP41, SER46, ASP48, MET55, GLN64, ALA135, CYS136, MET137, GLU153, TYR157, ARG180, GLU182
ZINC000100256265	-9.4	ASP43, ALA45, TYR62, LEU99, ASN100, CYS136, ASN149, THR151, ARG180, PHE200
ZINC000256095149	-9.4	ILE47, ASP48, MET137, ARG196, SER209
ZINC000257693609	-9.4	ASP43, ALA45, SER46, ASP48, TYR62, LEU99, ASN100, ARG180, GLU182, PHE200
ZINC000000156701	-9.3	ASN41, ASP43, TYR97, TYR157, ALA201, TYR205
ZINC000008215411	-9.3	ASP43, ALA45, SER46, ASP48, VAL53, ASN54, MET55, THR60, LEU99, ASN100, ASP101, CYS136, ARG180, GLU182, PRO184
ZINC000085552319	-9.3	ASN41, ASP43, GLN64, TYR97, GLU155, VAL198, VAL199, PHE200, ARG207
ZINC000096015174	-9.3	ILE47, ASP48, ASN149, ARG180, ILE181, GLU182, SER211

A)

B)
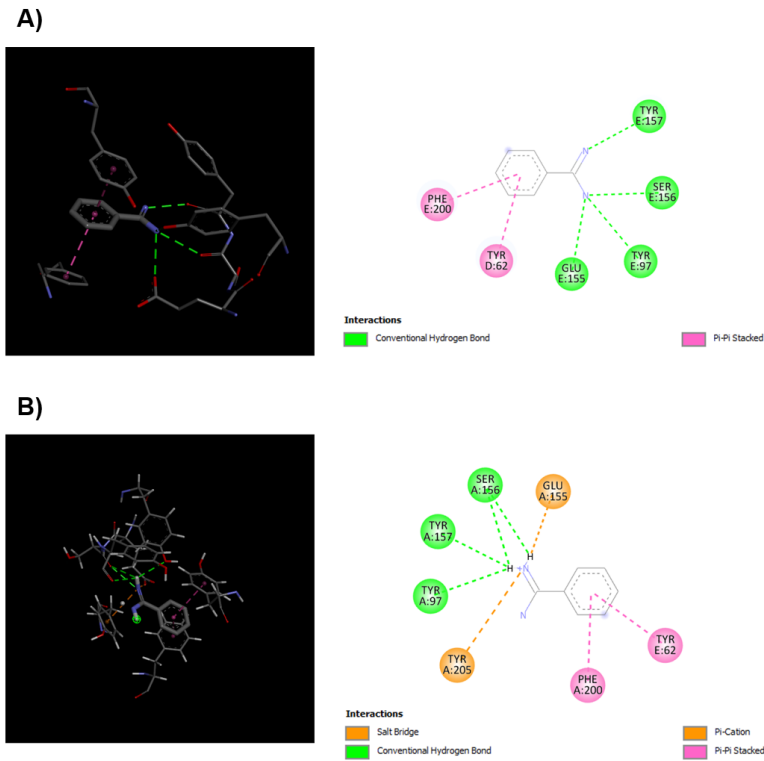
Figure 1. Interactions between the allosteric site of the GABAA receptor with Benzamidine; A) in crystal structure analysis B) re-docked result analysis.

Table 4. The ligands, their binding affinities, and interacting receptor residues of Inhibitors dataset including re-docked Benzamidine ligand.

Inhibitors Including Re-docked Benzamidine		
Ligand Name	Binding Affinity (kcal/mol)	Receptor Residues Interacting with Ligand
Suramin	-10.4	ALA45, SER46, ALA135, CYS136, MET137, ASN149, CYS150, THR151, GLU153, ARG180, VAL194, ARG196, PHE200, ARG207, SER209
Broflanilide	-9.5	ALA45, SER46, ILE47, ASP48, MET55, LEU99, ASN100, LYS102, ALA135, MET137, ARG180
Clozapine	-8.3	ASP43, TYR62, LEU99, PHE200, ALA201
Hydrochloride	-7.9	ASP43, ALA45, LEU99, MET115, TYR157, THR176, ALA201
Xenovulene	-7.3	ALA45, SER46, ILE47, ILE181
Flumazenil	-7.1	ASP43, TYR62, GLN64, LEU99, LYS173, PHE200, ALA201
Picrotoxinin	-6.8	SER46, ILE181
Benzamidine	-6.7	TYR62, TYR97, GLU155, SER156, TYR157, PHE200, TYR205

Table 5. The analysis of the frequency features of interacting common aminoacid residues of the allosteric site of GABA_A receptor within three datasets and the inhibitors.

Common Aminoacid Residues' Frequencies		
Aminoacid Name	Number	Percentage
ASP43	28	% 8.48
ALA45	37	% 11.21
SER46	23	% 6.96
ILE47	10	% 3.03
TYR62	35	% 10.61
LEU99	34	% 10.30
ALA135	30	% 9.10
MET137	24	% 7.27
TYR157	17	% 5.17
ARG180	26	% 7.87
ILE181	5	% 1.52
PHE200	37	% 11.21
ALA201	24	% 7.27
Total	330	% 100

myocardial contractility, blood pleasure, stroke volume, and reducing heart rate [36]. Results put forward that Digoxin might create alkyl and pi-alkyl interactions with Ala45, Met49, Leu99, Ala135, Pro184, carbon-hydrogen bonds with Ser46, Tyr62, Pro184, pi-sulfur bonds with Met55, conventional hydrogen bonds with Val53, and Met55 residues of the receptor. Ponatinib is the third FDA-approved drug among the ones with the highest binding affinity. It was approved by the FDA in 2012 as a tyrosine-kinase inhibitor [37] and is used in the treatment of leukemia [38]. It's revealed that Ponatinib might create conventional hydrogen bonds with Asn41, Asp43, Arg207, carbon-hydrogen bonds with Ala45, Gln64, pi-pi stacked, and pi-alkyl interactions with Ala45, Tyr62, Leu99, Phe200, and Ala201 residues of the receptor.

FDA-Approved Drugs
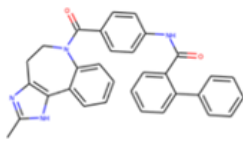
ZINC000012503187
(Conivaptan)
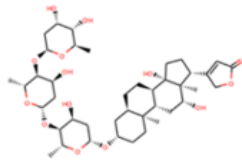
ZINC000242548690
(Digoxin)
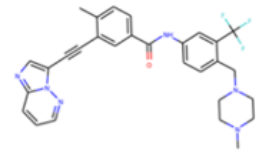
ZINC000036701290
(Ponatinib)

Drugs Approved by World but not FDA
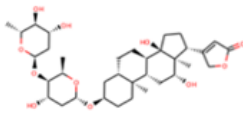
ZINC000118915215
(DD1)
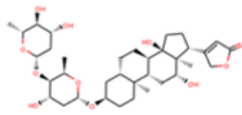
ZINC000118915217
(DD2)
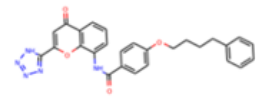
ZINC000001542146
(Pranlukast)

Non-human Metabolites
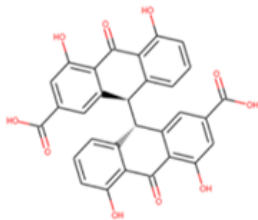
ZINC000028642721
(Sennidin A)
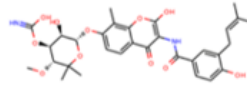
ZINC000100029436
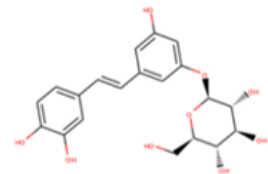
ZINC000004098622

Inhibitors
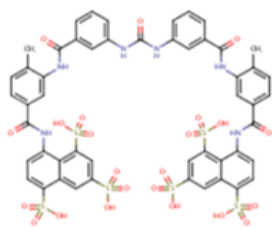
Suramin
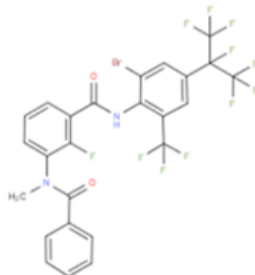
Broflanilide
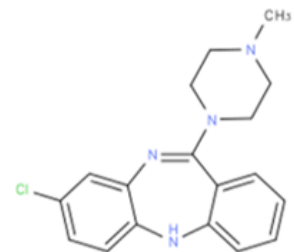
Clozapine

Figure 2. Three ligands with the highest binding affinity of each dataset from the molecular docking results.
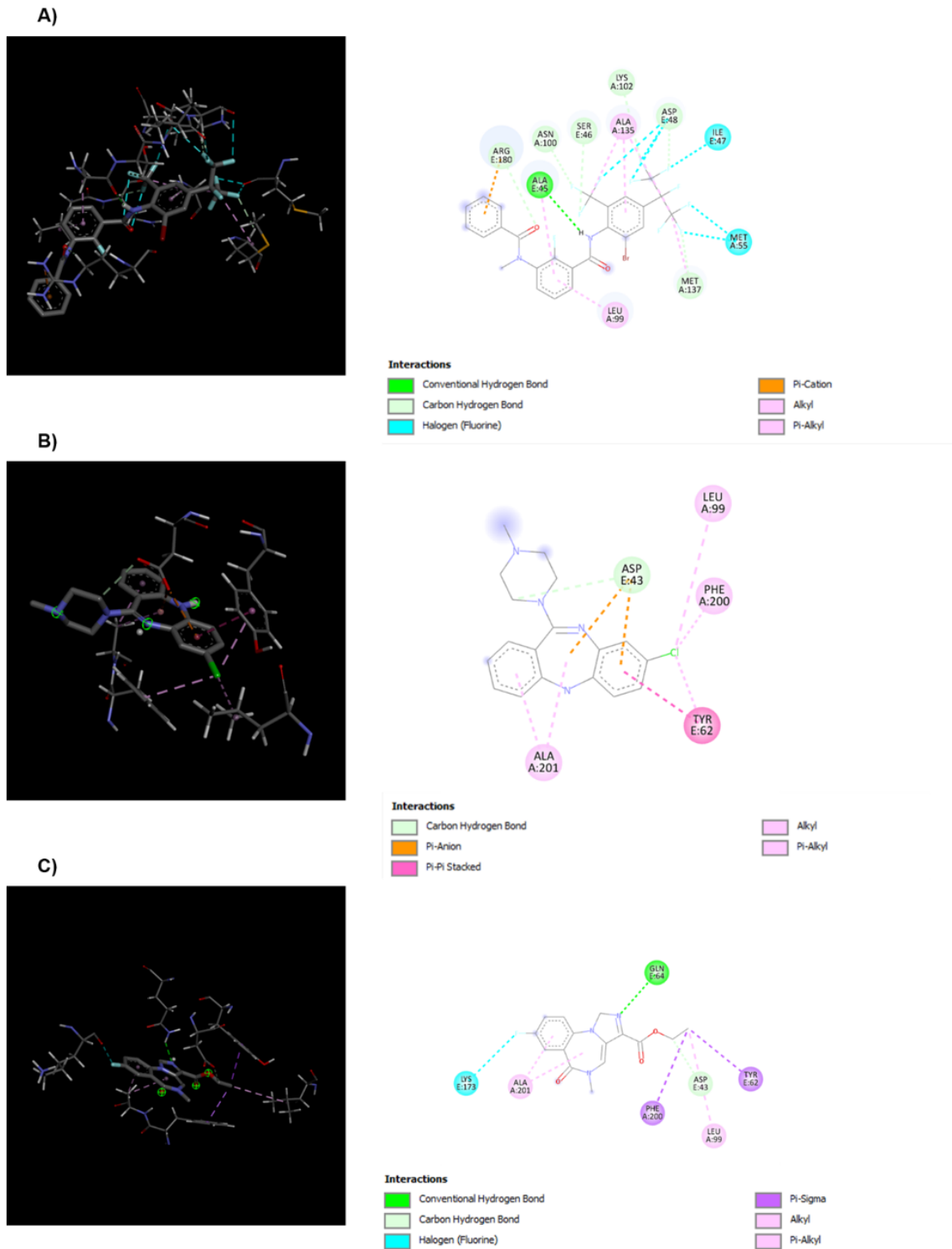
Figure 3. Interactions between the allosteric site of the GABA$_A$ receptor with the three best-scored ligands of Inhibitors; A) Suramin, B) Broflanilide, C) Clozapine.
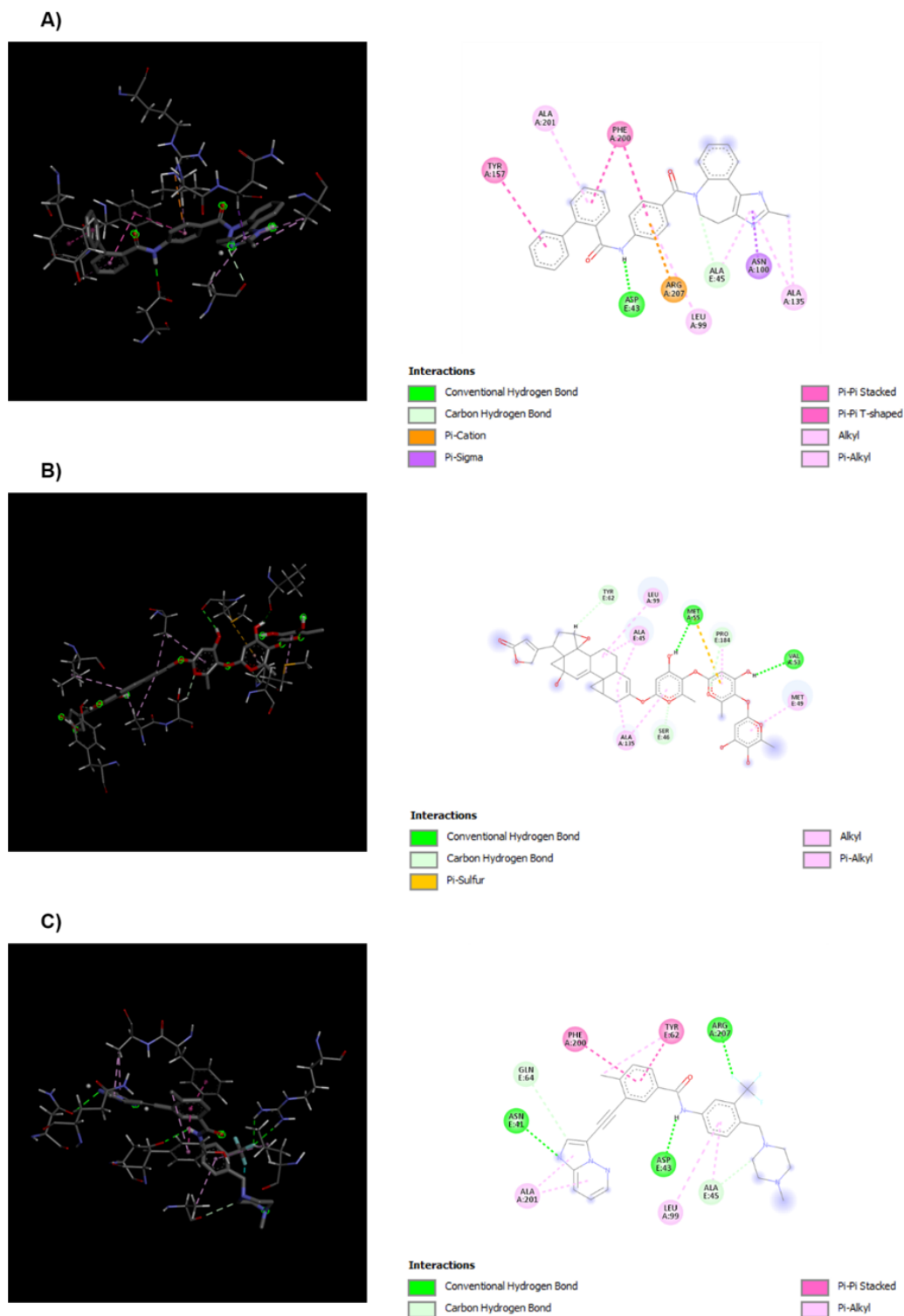
Figure 4. Interactions between the allosteric site of the GABAA receptor with three best-scored ligands of the FDA-Approved Drugs; A) ZINC000012503187 (Conivaptan) B) ZINC000242548690 (Digoxin), and C) ZINC000036701290 (Ponatinib).

In addition, 4254 ligands from the Drugs Approved by World but not FDA dataset had been docked to the allosteric site of the GABA$_A$ receptor, and 17 (ZINC000118915215, ZINC000118915217, ZINC000001542146, ZINC000257362202, ZINC000150339052, ZINC000256630457, ZINC000118915214, ZINC000011616152, ZINC000118915216, ZINC000256109538, ZINC000885764928, ZINC000008143788, ZINC000095618690, ZINC000000577115, ZINC000043195321, ZINC000100054749, ZINC000224657532) drugs were discovered with higher binding affinity than Suramin which is the best-scored ligand of the inhibitors. The three best-scored ligands which are ZINC000118915215 (DD1), ZINC000118915217 (DD2), and ZINC000001542146 (Pranlukast) were analyzed since they have the binding affinities of -11.9 kcal/mol, -11.9 kcal/mol, and -11.3 kcal/mol, respectively. The ligand-receptor interactions of the related ligands are demonstrated in Figure 5. While DD1 and DD2 are distinct derivatives of the Digoxin molecule, Pranlukast is a widely used drug as antiallergic and antiasthmatic since it's a cysteinyl leukotriene receptor-1 antagonist [39], [40]. Ligand-receptor interaction studies revealed that DD1 creates conventional hydrogen bonds with Ile47, Glu182, pi-sulfur bonds with Met55, alkyl and pi-alkyl interactions with Ala135, Met137, Leu183, Pro184, and carbon-hydrogen bond with Arg180, DD2 creates alkyl and pi-alkyl interactions with Met49, Ala135, Met137, Pro184, pi-sulfur bond with Met55, conventional hydrogen bond with Tyr97, carbon-hydrogen bond with Arg180, Pranlukast creates alkyl and pi-alkyl interactions with Ala45, Tyr62, Leu99, Ala135, Met137, Ile181, Phe200, conventional hydrogen bonds with Ile47, Glu182, pi-pi stacked interaction with Tyr62, pi-donor hydrogen bond with Met137, and carbon-hydrogen bond with Ile181 residues of the receptor.

Eventually, ligands of the Non-human metabolites dataset had been docked to the GABA$_A$ receptor and no ligand with a binding affinity higher than Suramin's was revealed among the 2307 ligands. However, 7 ligands (ZINC000028642721, ZINC000100029436, ZINC000004098622, ZINC000085432705, ZINC000003870412, ZINC000004096846, ZINC000169335484) had exhibited higher binding affinity than -9.5 kcal/mol which is the Broflanilide's (second-best inhibitor) binding affinity. Docking studies revealed that the three best-scored ligands of the Non-human

Metabolite dataset were ZINC000028642721 (Sennidin A), ZINC000100029436, and ZINC000004098622 with the binding affinities of -10.1 kcal/mol, -10.0 kcal/mol, and -9.9 kcal/mol, respectively. The receptor interactions of these ligands are demonstrated in Figure 6. The data demonstrate that ZINC000028642721 (Sennidin A) might create pi-sigma interaction with Ala45, conventional hydrogen bonds with Ser46, Ile47, Asp101, Ala135, Met137, Glu182, carbon-hydrogen bonds with Thr60, Asn100, Cys136, pi-alkyl interactions with Ala135, Arg180, ZINC000100029436 might create alkyl and pi-alkyl interactions with Ala45, Leu99, Phe200, Ala201, carbon-hydrogen bonds with Ser46, Asp48, Ile181, conventional hydrogen bonds with Ile47 pi-pi stacked interactions with Tyr62, Phe200, and ZINC000004098622 might create conventional hydrogen bonds with Asp43, Ser46, Tyr97, Leu99, carbon-hydrogen bond with Ala45, pi-alkyl interactions with Ala45, Leu99, pi-pi stacked interactions with Tyr62, Phe200, unfavorable donor-donor and unfavorable acceptor-acceptor interactions with Asp101, Arg180, pi-donor hydrogen bonds with Asn100, Tyr205 amino acid residues of the receptor.

In the light of the findings, 30 drugs with the highest binding affinity and their datasets were listed in Table 5. Data put forward that the five best ligands are DD1, DD2 (from Drugs Approved by World but not FDA), Conivaptan, Digoxin (from FDA Approved Drugs), and Pranlukast (from Drugs Approved by World but not FDA) with the binding affinities of -11.9 kcal/mol, -11.9 kcal/mol, -11.8 kcal/mol, -11.6 kcal/mol, and -11.3 kcal/mol, respectively. Since the Digoxin drug and its two distinct derivatives exhibited quite binding affinity, these compounds were evaluated as rather promising in order to be used in the treatment of GABAergic disorders. In addition, there is no evidence in literature demonstrating the binding profile of Digoxin to GABA$_A$ receptors' allosteric site, Gautam et al. have reported that GABAergic agent production increases during dose-dependent Digoxin treatment [41]. As such, the findings might keep light on the molecular mechanism of the increases in GABAergic agent production, and provide significant evidence in order to test Digoxin and its derivatives (DD1, and DD2) in the treatment of GABAergic disorders. Furthermore, Vasopressin receptors inhibitor Conivaptan and cysteinyl leukotriene receptor-1 antagonist Pranlukast might be repurposed for treatment of GABAergic disorders since they have quite binding affinity to the allosteric site of the GABA$_A$ receptor.
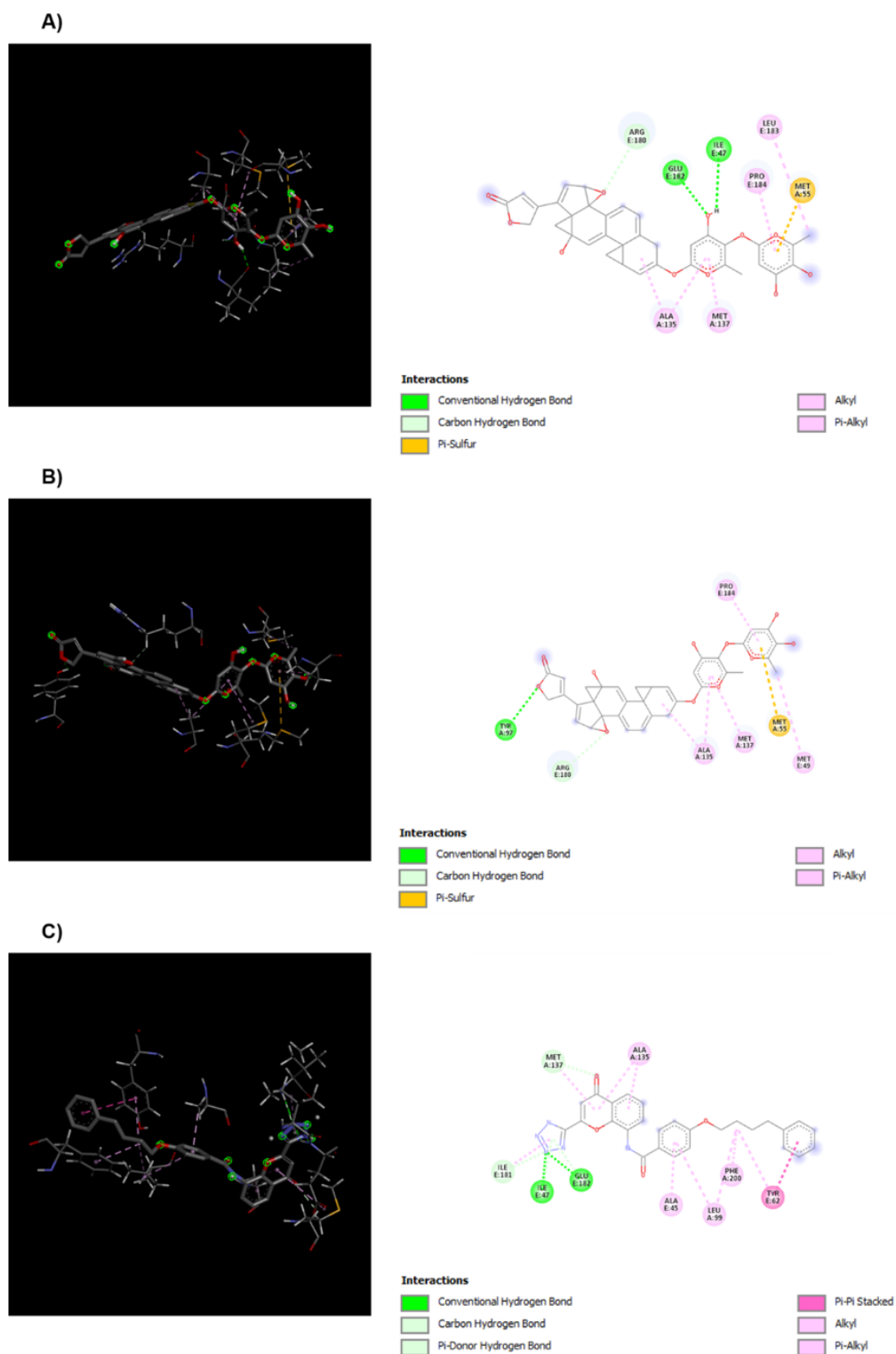
Figure 5. Interactions between the allosteric site of the GABAA receptor with three best-scored ligands of the Drugs Approved by World but not FDA; A) ZINC000118915215 (DD1), B) ZINC000118915217 (DD2), and C) ZINC000001542146 (Pranlukast).

Figure 6. Interactions between the allosteric site of the GABAA receptor with three best-scored ligands of the Non-human Metabolites; A) ZINC000028642721 (Sennidin A), B) ZINC000100029436, and C) ZINC000004098622.

Table 6. The scores, datasets, interacting receptor residues of the best scored 30 ligands from the molecular docking results.

30 Ligands with Best Scores			
Ligand Name	Score (kcal/mol)	Dataset	Receptor Residues Interacting with Ligands
ZINC000118915215	-11.9	Drugs Approved by World but not FDA	ILE47, MET55, ALA135, MET137, ARG180, GLU182, LEU183, PRO184
ZINC000118915217	-11.9	Drugs Approved by World but not FDA	MET49, TYR97, ALA135, MET137, ARG180, PRO184
ZINC000012503187	-11.8	FDA Approved Drugs	ASP43, ALA45, LEU99, ASN100, ALA135, TYR157, PHE200, ALA201, ARG207
ZINC000242548690	-11.6	FDA Approved Drugs	ALA45, SER46, MET49, VAL53, MET55, TYR62, LEU99, ALA135, PRO184
ZINC000001542146	-11.3	Drugs Approved by World but not FDA	ALA45, ILE47, TYR62, LEU99, ALA135, MET137, ILE181, GLU182, PHE200
ZINC000257362202	-11.2	Drugs Approved by World but not FDA	ALA45, SER46, ASP48, MET49, GLU52, VAL53, MET55, LEU99, LYS102, ALA135, THR151, PRO184
ZINC000036701290	-10.9	FDA Approved Drugs	ASN41, ASP43, ALA45, TYR62, GLN64, LEU99, PHE200, ALA201, ARG207
ZINC000150339052	-10.9	Drugs Approved by World but not FDA	ALA45, ASP48, MET55, LEU99, ALA135, CYS136, MET137, THR151, PRO184
ZINC000256630457	-10.9	Drugs Approved by World but not FDA	ASP43, ALA45, TYR97, LEU99, ASN100, ALA135, MET137, GLU182, PHE200, ALA201
ZINC000118915214	-10.8	Drugs Approved by World but not FDA	ILE47, VAL50, ASN54, ALA135, MET137, GLU153, LEU183, ARG196
ZINC000203757351	-10.8	FDA Approved Drugs	ASP43, ALA45, LEU99, ASN100, LYS102, ALA135, ARG180, ARG196, PHE200, ALA201, ARG207
ZINC000011616152	-10.7	Drugs Approved by World but not FDA	ASP43, ALA45, TYR62, ARG180, PHE200, ALA201
ZINC000118915216	-10.7	Drugs Approved by World but not FDA	ASP43, ASP48, VAL53, MET55, LEU99, ALA135, MET137, ARG180, LEU183, PRO184
ZINC000256109538	-10.7	Drugs Approved by World but not FDA	SER46, ILE47, ASP48, MET49, GLU52, VAL53, MET55, ALA135, PRO184
ZINC000885764928	-10.7	Drugs Approved by World but not FDA	TYR62, ALA135, ARG180, PHE200
ZINC000008143788	-10.6	Drugs Approved by World but not FDA	TYR62, GLN64, PHE200
ZINC000004099009	-10.6	FDA Approved Drugs	ALA45, SER46, ASP48, ASP101, LYS102, ALA135, GLU182
ZINC000095617679	-10.6	FDA Approved Drugs	ASP43, ALA45, TYR62, LEU99, MET115, TYR157, ARG180, PHE200, THR202, ARG207
ZINC000095618690	-10.6	Drugs Approved by World but not FDA	ASP48, TYR62, LEU99, ALA135, MET137, ARG180, GLU182
ZINC000000577115	-10.5	Drugs Approved by World but not FDA	TYR62, GLU155, TYR157, PHE200, ALA201, TYR205

Table 6. Continue

	30 Ligands with Best Scores		
Ligand Name	Score (kcal/mol)	Dataset	Receptor Residues Interacting with Ligands
ZINC000011679756	-10.5	FDA Approved Drugs	ASN41, ASP43, TYR62, TYR157, PHE200, ALA201, THR202, TYR205
ZINC000043195321	-10.5	Drugs Approved by World but not FDA	ASP43, ALA45, TYR62, LEU99, ARG180, PHE200, ALA201,
ZINC000100054749	-10.5	Drugs Approved by World but not FDA	ALA45, SER46, ASP48, LEU99, ASN100, ASP101, LYS102, ALA135, CYS136, MET137, ASN149, THR151
ZINC000224657532	-10.5	Drugs Approved by World but not FDA	ASP43, GLN64, GLU155, PHE200, ALA201, TYR205
ZINC000000537940	-10.4	Drugs Approved by World but not FDA	ASN41, GLU155, TYR157, ARG169, ALA174, PHE200, ALA201, THR202, TYR205
ZINC000006745272	-10.4	FDA Approved Drugs	ASP43, ALA45, SER46, ASP48, TYR62, GLN64, LEU99, ASN100, ASP101, ALA135, PHE200
ZINC000095618689	-10.4	Drugs Approved by World but not FDA	TYR62, GLY127, TYR157, LYS173, GLU179, PHE200, ALA201, TYR205
ZINC000003872494	-10.3	Drugs Approved by World but not FDA	TYR62, TYR97, GLU155, TYR157, PHE200, ALA201, TYR205
ZINC000011616153	-10.3	Drugs Approved by World but not FDA	ASP43, ALA45, SER46, ASP48, MET55, TYR62, ARG180, PHE200, ALA201
ZINC000022058728	-10.3	Drugs Approved by World but not FDA	ALA45, MET55, LEU99, ALA135, GLU182, PRO184, ARG207

Once the virtual drug screening had been completed, ADME analysis and toxicity profile of the three best-scored ligands from the Drugs Approved by World but not FDA and Non-human Metanolites datasets were carried out with swissADME server and OSIRIS Property Explorer tool. Since they had been tested by FDA previously, the ligands from FDA-Approved Drugs were not investigated in ADME and toxicity studies. The physico-chemical properties, lipophilicity, water-solubility, druglikeness properties, pharmacokinetics, and toxicity results of the ligands are listed in Table 6. Since DD1 and DD2 are structural isomers, the ADME and toxicity profiles of these derivatives have similar properties. Both derivatives were analyzed as water-soluble, they have no inhibitory activity on CYP isoforms, they have no permeation activity from the blood-brain barrier (BBB), and they have no possible side effects such as mutagenicity, tumorigenicity, irritant effects, and reproductive effects. While Pranlukast was found as insoluble in water as well as not permeant from BBB, its inhibitory effects on CYP2C19, CYP2C9, and CYP3A4 were observed. In addition, ADME and toxicity studies of Non-human Metabolites ligands revealed that ZINC000028642721 (Sennidin A) is poorly soluble, has a CYP2C9 inhibition activity, has no undesired effect, ZINC000100029436 is moderately soluble in water, has no CYP isoform inhibition activity, but has mutagenicity effect, and ZINC000004098622 is water-soluble, has no CYP isoform inhibition activity, but has a reproductive effect. In the light of the information on binding affinities, chemical interactions with the amino acid residues of the receptor, ADME analysis, and toxicity profiles of the ligands, FDA approved Digoxin drug and its derivatives (ZINC000242548690, ZINC000118915215, and ZINC000118915217) as well as Conivaptan which was approved by FDA and Pranlukast are evaluated as promising in order to be used in the treatment of GABAergic disorders.

Table 7. ADME and toxicity analysis of the best three ligands from Drugs Approved by World but not FDA and Non-human Metabolites datasets.

		ADME and Toxicity Analysis					
Properties		Drugs Approved by World but not FDA			Non-human Metabolites		
	Ligand Name	ZINC000118915215	ZINC000118915217	ZINC000001542146	ZINC000028642721	ZINC000100029436	ZINC000000409 8622
	Formula	C35H54O11	C35H54O11	C27H23N5O4	C30H18O10	C31H36N2O11	C20H22O9
Physico-chemical properties	Molecular Weight (g/mol)	650.80	650.80	481.50	538.46	612.62	406.38
	Molar Refractivity	166.04	166.04	135.27	138.55	161.88	102.03
	TPSA (topological polar surface area)	164.37 Å²	164.37 Å²	123.00 Å²	189.66 Å²	201.00 Å²	160.07 Å²
Lipophilicity	Log $P_{o/w}$ (iLOGP)	4.19	4.53	3.07	2.16	4.48	1.71
	Log $P_{o/w}$ (XLOGP3)	1.24	1.24	4.32	4.80	4.18	0.73
	Log $P_{o/w}$ (WLOGP)	2.34	2.34	4.44	3.96	3.85	-0.07
	Log $P_{o/w}$ (MLOGP)	1.17	1.17	3.07	1.27	0.51	-0.87
	Log $P_{o/w}$ (SILICOS-IT)	1.28	1.28	5.12	3.46	3.21	0.00
	Consensus Log $P_{o/w}$	2.04	2.11	4.00	3.13	3.25	0.30
Solubility	Log S (SILICOS-IT)	-1.86	-1.86	-10.46	-6.59	-5.84	-1.02
	SILICOS-IT Solubility (mg/ml)	8.92e+00	8.92e+00	1.68e-08	1.38e-04	8.90e-04	3.90e+01
	SILICOS-IT Solubility (mol/l)	1.37e-02	1.37e-02	3.49e-11	2.56e-07	1.45e-06	9.59e-02
	Solubility Class	Soluble	Soluble	Insoluble	Poorly soluble	Moderately soluble	Soluble
Druglikeness	Druglikeness	3.42	3.42	-4.02	0.52	0.93	-6.63
	Drug-score	0.41	0.41	0.21	0.32	0.17	0.25

Table 7. Continue

		ADME and Toxicity Analysis					
Properties		Drugs Approved by World but not FDA			Non-human Metabolites		
Pharmaco-kinetics	GI absorption	Low	Low	Low	Low	Low	Low
	BBB permeant	No	No	No	No	No	No
	P-gp substrate	Yes	Yes	Yes	No	No	No
	CYP1A2 inhibitor	No	No	No	No	No	No
	CYP2C19 inhibitor	No	No	Yes	No	No	No
	CYP2C9 inhibitor	No	No	Yes	Yes	No	No
	CYP2D6 inhibitor	No	No	No	No	No	No
	CYP3A4 inhibitor	No	No	Yes	No	No	No
Toxicity	Mutagenicity	No	No	No	No	Yes	No
	Tumorigenicity	No	No	No	No	No	No
	Irritant Effects	No	No	No	No	No	No
	Reproductive Effects	No	No	No	No	No	Yes

Conclusion

The GABAergic pathway is one of the most prominent pathways responsible for neuronal development and is managed through the interactions between γ-aminobutyric acid (GABA) which is the primary inhibitory neurotransmitter in CNS and its receptors which are $GABA_A$, $GABA_B$, or $GABA_C$ receptors. Among these receptors, the $GABA_A$ receptor has the highest expression level along with CNS and regulates neural cell migration, proliferation, growth, and synapse structures generation by performing phasic inhibition and tonic activation.

To date, much evidence has revealed that defects in the GABAergic pathway might cause several serious diseases such as schizophrenia, epilepsy, anxiety, depression, insomnia, etc. Besides, it's recently been reported that anti-tumor immune response is suppressed through the inhibition of CD8 T cell activity by GABA metabolite secreted by B-cells. As such, the discovery of novel inhibitors targeting the GABAergic pathway and the repurposing of approved drugs are quite promising approaches for the treatment of regarding disorders from schizophrenia to cancer.

In this study, a molecular docking mediated virtual drug screening strategy targeting the allosteric site of the GABA$_A$ receptor has been carried out with a total of 8170 ligands consisting of 1609 FDA-Approved Drugs, 4254 Drugs Approved by World but not FDA, and 2307 Non-human Metabolites. Furthermore, the developed strategy has been validated with the re-docking of the Benzamidine ligand which is found in the crystal structure of the receptor, and the docking of 7 known GABA antagonists. Results demonstrate that two Digoxin derivatives which are ZINC000118915215 (DD1) and ZINC000118915217 (DD2) from the Drugs Approved by World but not FDA dataset have the highest binding affinity to the allosteric site of the GABA$_A$ receptor. Furthermore, Digoxin drug (ZINC000242548690) from the FDA-approved Drugs dataset has been analyzed as one with the highest binding affinity after Conivaptan drug (ZINC000012503187). In addition, ADME and toxicity studies have revealed that DD1 and DD2 have quite a drug potential since they are water-soluble, have no inhibitory effect on CYP isoforms, and have no possible undesired effects such as mutagenicity, tumorigenicity, irritant effects, and reproductive effects. While Digoxin is a molecule produced by Digitalis lanata, it's widely used in several cardiac diseases. Besides, Conivaptan is a Vasopressin receptors (V1a and V2) inhibitor and is also widely used in heart failure diseases. As such, the great potential of Digoxin and its derivatives (DD1 and DD2) in the treatment of GABAergic pathway-based disorders is declared in this report. In addition, Conivaptan has great potential, too, since it has a quite binding affinity to the allosteric site of the GABA$_A$ receptor. However, the findings of the report should be analyzed with molecular dynamics (MD) simulation studies, and the potential of the related drugs should be tested by in vitro and in vivo studies.

Funding Declaration

Competing Declaration
The research have been carried out by only one author and the author has no relevant financial or non-financial interests to disclose.

Author Contribution Declaration
The research and submission have been carried out by only one author.

Data Availability Declaration
The datasets generated during and/or analysed during the current study are available from the corresponding author on reasonable request.

References

1. L. D. Ochoa-de la Paz, R. Gulias-Cañizo, E. D'Abril Ruíz-Leyja, H. Sánchez-Castillo, and J. Parodí, The role of GABA neurotransmitter in the human central nervous system, physiology, and pathophysiology, Rev. Mex. Neurocienc., 22 (2021) 67-76.
2. D. A. McCormick, GABA as an inhibitory neurotransmitter in human cerebral cortex, J. Neurophysiol., 62 (1989) 1018-1027.
3. A. Ghit, D. Assal, A. S. Al-shami, and D. E. E. Hussein, GABA A receptors : structure , function , pharmacology , and related disorders, J. Genet. Eng. Biotechnol., 123 (2021) 1-15.
4. A. N. Shrivastava, A. Triller, and W. Sieghart, Gaba a receptors: Post-synaptic co-localization and cross-talk with other receptors, Front. Cell. Neurosci., 5 (2011) 1-12.
5. F. C. Roth and A. Draguhn, GABA metabolism and transport: Effects on synaptic efficacy, Neural Plast., 2012 (2012) 1-12.
6. M. P. Serrano-Regal, L. Bayon-Cordero, R. P. Ordaz, E. Garay, A. Limon, R. O. Arellano, C. Matute, and M. V. Sanchez-Gomez, Expression and Function of GABA Receptors in Myelinating Cells, Front. Cell. Neurosci., 14 (2020) 1-15.
7. E. Sigel and M. E. Steinmann, Structure, function, and modulation of GABAA receptors, J. Biol. Chem., 287 (2012) 40224-40231.
8. V. Lee and J. Maguire, The impact of tonic GABAA receptor-mediated inhibition on neuronal excitability varies across brain region and cell type, Front. Neural Circuits, 8 (2014) 1-27.
9. V. Tretter and S. J. Moss, GABAA receptor dynamics and constructing GABAergic synapses, Front. Mol. Neurosci., 1 (2008) 1-13.
10. A. Scimemi, A. Andersson, J. H. Heeroma, J. Strandberg, B. Rydenhag, A. W. McEvoy, M. Thom, F. Asztely, and M. C. Walker, Tonic GABAA receptor-mediated currents in human brain, Eur. J. Neurosci., 24 (2006) 1157-1160.
11. G. Deidda, I. F. Bozarth, and L. Cancedda, Modulation of GABAergic transmission in development and neurodevelopmental disorders: Investigating physiology and pathology to gain therapeutic perspectives, Front. Cell. Neurosci., 8 (2014) 1-23.
12. B. Monesson-Olson, J. J. McClain, A. E. Case, H. E. Dorman, D. R. Turkewitz, A. B. Steiner, and G. B. Downes, Expression of the eight GABAA receptor α subunits in the developing zebrafish central nervous system, PLoS One, 13 (2018) 1-15.
13. P. L. Pearl, T. R. Hartka, J. L. Cabalza, J. Taylor, and M. K. Gibson, Inherited disorders of GABA metabolism, Future Neurol., 1 (2006) 631-636.
14. J. C. de Jonge, C. H. Vinkers, H. E. Hulshoff Pol, and A. Marsman, GABAergic mechanisms in schizophrenia: Linking postmortem and In vivo studies, Front. Psychiatry, 8 (2017) 118-130.
15. K. R. Patel, J. Cherian, K. Gohil, and D. Atkinson, Schizophrenia: Overview and treatment options, P. T., 39 (2014) 638-645.
16. T. C. Jacob, Neurobiology and Therapeutic Potential of α5-GABA Type A Receptors, Front. Mol. Neurosci., 12 (2019) 1-10.
17. E. Engin, J. Liu, and U. Rudolph, α2-containing GABAA receptors: A target for the development of novel treatment strategies for CNS disorders, Pharmacol. Ther., 136 (2012) 142-152.

18. P. Syed, N. Durisic, R. J. Harvey, P. Sah, and J. W. Lynch, Effects of GABAA Receptor α3 Subunit Epilepsy Mutations on Inhibitory Synaptic Signaling, Front. Mol. Neurosci., 13 (2020) 1-12.

19. S. K. Sanders and A. Shekhar, Regulation of anxiety by GABAA receptors in the rat amygdala, Pharmacol. Biochem. Behav., 52 (1995) 701-706.

20. [20] M. V. Fogaça and R. S. Duman, Cortical GABAergic dysfunction in stress and depression: New insights for therapeutic interventions, Front. Cell. Neurosci., 13 (2019) 1-20.

21. D. T. Plante, J. E. Jensen, and J. W. Winkelman, The role of GABA in primary insomnia, Sleep, 35 (2012) 741-742.

22. P. Nuss, Anxiety disorders and GABA neurotransmission: A disturbance of modulation, Neuropsychiatr. Dis. Treat., 11 (2015) 165-175.

23. B. Zhang, A. Vogelzang, M. Miyajima, Y. Sugiura, Y. Wu, K. Chamoto, R. Nakano, R. Hatae, R. J. Menzies, K. Sonomura, N. Hojo, T. Ogawa, W. Kobayashi, Y. Tsutsui, S. Yamamoto, M. Maruya, S. Narushima, K. Suzuki, H. Sugiya, K. Murakami, M. Hashimoto, H. Ueno, T. Kobayashi, K. Ito, S. Fagarasan, B cell-derived GABA elicits IL-10+ macrophages to limit anti-tumour immunity, Nature, 599 (2021) 471-476.

24. H. Luo, K. Wood, F. D. Shi, F. Gao, and Y. Chang, Suramin is a novel competitive antagonist selective to α1β2γ2 GABAA over ρ1 GABAC receptors, Neuropharmacology, 141 (2018) 148-157.

25. T. Nakao and S. Banba, Broflanilide: A meta-diamide insecticide with a novel mode of action, Bioorganic Med. Chem., 24 (2016) 372-377.

26. F. J. Michel and L. E. Trudeau, Clozapine inhibits synaptic transmission at GABAergic synapses established by ventral tegmental area neurones in culture, Neuropharmacology, 39 (2000) 1536-1543.

27. M. Sahila, P. P. Babitha, S. Bandaru, A. Nayarisseri, and V. A. Doss, Molecular docking based screening of GABA (A) receptor inhibitors from plant derivatives, Bioinformation, 11 (2015) 280-289.

28. E. F. Pettersen, T. D. Goddard, C. C. Huang, G. S. Couch, D. M. Greenbatt, E. C. Meng, T. E. Ferrin, UCSF Chimera - A visualization system for exploratory research and analysis, J. Comput. Chem., 25 (2004) 1605-1612.

29. S. Dallakyan and A. Olson, Small-Molecule Library Screening by Docking with PyRx, NY: Springer New York, 1263 (2015) 243-250.

30. O. Trott and A. J. Olson, AutoDock Vina: Improving the speed and accuracy of docking with a new scoring function, efficient optimization, and multithreading, J. Comput. Chem., 31 (2010) 455-461.

31. T. Sander, Molecular Properties Prediction - Osiris Property Explorer. [Online]. Available: https://www.organic-chemistry.org/prog/peo/. [Accessed: 18-Apr-2022].

32. A. Daina, O. Michielin, and V. Zoete, SwissADME: A free web tool to evaluate pharmacokinetics, drug-likeness and medicinal chemistry friendliness of small molecules, Sci. Rep., 7 (2017) 1-13.

33. F. Ali, M. A. Raufi, B. Washington, and J. K. Ghali, Conivaptan: A dual receptor vasopressin V1a/V2 antagonist, Cardiovasc. Drug Rev., 25 (2007) 261-279.

34. M. Z. Hoque, P. Arumugham, N. Huda, N. Verma, M. Afiniwala, and D. H. Karia, Conivaptan: Promise of treatment in heart failure, Expert Opin. Pharmacother., 10 (2009) 2161-2169.

35. H. Van Wietmarschen, H. Hagels, R. Peters, J. Heistek, J. Van Der Greef, and M. Wang, Optimizing growth conditions for digoxin production in Digitalis lanata Ehrh, World J. Tradit. Chinese Med., 2 (2016) 24-35.

36. S. Virgadamo, Digoxin: A systematic review in atrial fibrillation, congestive heart failure and post myocardial infarction, World J. Cardiol., 7 (2015) 808-816.

37. F. H. Tan, T. L. Putoczki, S. S. Stylli, and R. B. Luwor, Ponatinib: A novel multi-tyrosine kinase inhibitor against human malignancies, Onco. Targets. Ther., 12 (2019) 635-645.

38. S. Saussele, W. Haverkamp, F. Lang, S. Koschmieder, A. Kiani, K. Jentsch-Ullrich, F. Stagelmann, H. Pfeifer, P. L. Rosee, N. Goekbuget, C. Rieger, C. F. Waller, G. N. Franke, P. le Coutre, R. Kirchmair, and C. Junghanss, Ponatinib in the Treatment of Chronic Myeloid Leukemia and Philadelphia Chromosome-Positive Acute Leukemia: Recommendations of a German Expert Consensus Panel with Focus on Cardiovascular Management, Acta Haematol., 143 (2020) 217-231.

39. S. Yoshihara, Pranlukast hydrate in the treatment of pediatric bronchial asthma, Pediatr. Heal. Med. 4 (2013) 55-63.

40. S. Tomari, T. Shimoda, T. Kawano, K. Mitsusa, Y. Obase, C. Fukusjima, H. Matsuse, and S. Kohno, Effects of pranlukast, a cysteinyl leukotriene receptor 1 antagonist, combined with inhaled beclomethasone in patients with moderate or severe asthma, Ann. Allergy, Asthma Immunol., 87 (2001) 156-161.

41. S. K. Gautam and S. K. Kulkarni, GABA/BZ-and NMDA-receptor interaction in digoxin-induced convulsions in rats, Indian J. Exp. Biol., 29 (1991) 636-640.

Research Article

Preliminary Phytochemical Screening, GC-MS, FT-IR Analysis of Ethanolic Extracts of *Rosmarinus Officinalis*, *Coriandrum Sativum* L. and *Mentha Spicata*

GC-MS, FT-IR Analizi ile *Rosmarinus Officinalis*, *Coriandrum Sativum* L. ve *Mentha Spicata*'nın etanol ekstraktlarının Ön Fitokimyasal Taraması

Jamaluddeen Mohammed[1], **Oluwasuyi Ayobami Oba[2]**, **Nur Pasaoglulari Aydinlik[1]***

[1]Faculty of Arts and Sciences, Department of Chemistry, Cyprus International University, Nicosia, Turkey.
[2]Faculty of Engineering, Department of Environmental Sciences, Cyprus International University, Nicosia, Turkey.

ABSTRACT

Phytochemical and some proximate composition analysis was carried out on three (3) selected edible medicinal plants leaves which were believed to be of medicinal value and have physiological effects as anti-inflammatory, antibacterial, anti-pyretic, antioxidant, laxative etc. The significant aim of the research is to identify the phyto-components as well as compounds presents in the ethanolic extract of *Mentha Spicata* L. (Mint), *Rosemarinus Officinalis* (Rosemary), and *Coriandrum Sativum* (Coriander) using two different analytical methods, GC-MS, along with their functional groups using FT-IR. The GC-MS analysis reveals various compounds identified as major constituents and mostly all the compounds identified was found to possess medicinal properties. The data analysis from FT-IR spectrometry representing most of the strong absorptions bands which further indicates major functional groups such as aliphatic amines, alkanes, aromatic (primary and secondary) and carboxylic acids. While the preliminary phytochemical screening conducted indicates the presence of Flavonoids, Tannins, Triterpenoids, and Saponins from the ethanolic extracts of the plant extracts. Therefore the findings indicate that all the selected plant samples are potential sources of medicinal activities and can be applied in the field of phyto-medicine considering their diverse ethno-pharmacological importance.

Key Words
Medicinal Plants, phytochemical screening, phyto-medicine, phyto-components.

ÖZ

Fitokimyasal ve bazı yakın bileşim analizleri, tıbbi ve fizyolojik değeri olduğuna inanılan anti-inflamatuar, antibakteriyel, anti-pi-retik, antioksidan, yumuşatıcı vb. etkileri olan üç (3) seçilmiş yenilebilir bitki yaprağı üzerinde gerçekleştirilmiştir. Bu çalışmanın esas amacı *Mentha spicata* L (Nane), R*osemarinus officinalis* (Biberiye) ve *Coriandrum sativum* (Kişniş)'in etanolik ekstraktında bulunan fito-bileşenlerin yanı sıra bileşikleri iki farklı analitik yöntem, GC-MS, ile birlikte fonksiyonel gruplar için FT-IR kullanarak tanımlamaktır. GC-MS analizi, ana bileşenler olarak tanımlanan çeşitli bileşikleri ortaya çıkarır ve çoğunlukla tanımlanan tüm bileşiklerin tıbbi özelliklere sahip olduğu bulunmuştur. FT-IR spektrometrisinden elde edilen veri analizi, alifatik aminler, alkanlar, aromatik (birincil ve ikincil) ve karboksilik asitler gibi ana fonksiyonel grupları da gösteren güçlü absorpsiyon bantlarını göstermektedir. Yapılan ön fitokimyasal tarama, bitkilerin etanolik ekstraktlarından Flavonoidler, Tanenler, Triterpenoidler ve Saponinlerin varlığını gösterir. Bu nedenle bulgular, seçilen tüm bitki örneklerinin potansiyel tıbbi aktivite kaynağı olduğunu ve çeşitli etno-farmakolojik önemi dikkate alınarak fito-tıp alanında uygulanabileceğini göstermektedir.

Anahtar Kelimeler
Tibbi bitkiler, fitokimyasal tarama, bitkisel ilaç, fitokimyasal bileşenler.

INTRODUCTION

In the history of man-kind, plants and their derivatives have always been an important source of medicines for our health conditions for ages. The first knowledge and discovery of the various healing properties of plants has been traced back to ancient days. It is also known that plants are the most important rich source of drugs both in traditional system and that of modern medicines [1]. However, over time, humans have developed an interest in knowing and investigating the exact source and constituents responsible for most of the healing properties associated with the plants parts [2, 3]. As a result of these studies conducted on the plants species birth the word phytochemistry which is regarded as the science responsible for the compounds contained in plants extracts. In recent years, we have seen a revival of interest in the use of medicine from herbal sources, which is evidently possible because herbal medicine has been reported to be a safe with no adverse side effects compared with the synthetic drugs. Most of the medicinal values of these plants lies in some chemical substances that produce a definite physiological action on the human body [4-6]. *Coriandrum Sativum* L. (Apiaceace Family) was originated around the Mediterranean region and usually cultivated mainly in tropical areas. Coriander is among one of the edible plants from the Apiaceae family to be considered medicinal plants due to its exceptionally functional qualities and well documented medicinal history. Aside from its nutritional compositions as seen in Table 1, it is also well known for its sanative character for ages and its phytochemical constituents excel in all bioactive compounds which include, phenolic compound Flavonoids and ascorbic acid. Coriander also has curative and preventive properties such as anti-microbial and anti- carcinogenic. Coriander leaves are also a very vital and important crop that represents a unique position in flavoring substances because of its fragrance and it seeds are used in traditional medicine as an immune booster, and also used in the preparation of many household dishes as it is believed to have contained some medicinal curing abilities that help in curing bed cold, fever, and stomach disorders [7-9]

Rosmarinus officinalis (Rosemary) is a perennial edible plants with a specie name *Rosmarinus officinalis* and is a very popular herbs due to its enormous health properties. Table 2 reveals the chemical and mineral composition of the rosemary plant. Rosemary is an indigenous plant of Mediterranean region where it usually grow and being cultivated worldwide. The plant name arises from rosmarinus in Latin meaning 'dew of the sea' and it has been accepted as the plant with the highest

Table 1. Nutrient composition of coriander leaf as per USDA [2].

Nutrients	Amount (per 100 g)
Energy	279 kcal
Protein	21.93 g
Carbohydrates	52.10 g
Total lipids(fat)	4.78 g
Calcium, Ca	1246 mg
Magnesium, Mg	694 mg
Iron, Fe	42.46 mg
Phosphorus, P	481 mg
Zinc, Zn	4.72 mg
Potassium, K	4466 mg
Vitamin C	566.7 mg
Sodium, Na	211 mg
Thiamine	1.252 mg
Niacin	10.707 mg
Riboflavin	1.500 mg
Vitamin A,	293 ug
Vitamin B-12	0.00 ug
Fatty acids (MUFA)	2.232 g

Table 2. Chemical and minerals composition of rosemary plant [10].

Compounds	%Composition
α -Pinenene	9.72
α -Caryophyllene	8.38
Eucalyptol	5.11
Borneol	24.13
Camphor	5.01
Y-Terpinene	5.005
D-Verbenone	4.17
Limonene	2.29
Methyl jasmonate	2.24
α -Muurolene	1.58
Borneyl acetate	1.55
Myrecene	0.204
Eugenol	1.18
β- Germacrene	1.52
α -cardinene	0.63
farnesyl	0.32

Table 3. Chemical constituent of peppermint as per monographs of international pharmacopeia [13].

Compounds	Percentage composition (%)
Cineole	3.5 − 14.0
Limonene	1.0 − 5.0
Menthone	14.0 − 32..0
Isomenthone	1.5 − 10.0
Methyl acetate	2.8 -10.0
Isopulegol	Max 0.2
Pulegone	Max 4.0
Carvone	Max 1.0
Menthfuran	1.9 − 10.0

antioxidants activity and believed to possess phytochemical compounds such as Flavonoid, triterpenes, diterpenes and Steroids [10] Rosemary is a very tolerance plant that can withstand moderately harsh weather it usually grows averagely within temperature range of 25 -30 ℃. The plant can adopt and tolerate easily in almost all weather condition [11]. *Mentha spicata* (Mint) Mint is a very fast growing edible perennial plants with many different varieties that usually grow tall up to 3 feet tall which composes of varieties of chemical constituents (Table 3). The *Mentha spicata* species plant replicate well when exposed to sunlight and sometimes in under partial shades, they are usually planted early in raining seasons which is sometimes referred to as growing sea-

son, the plant required at least an average temperature of 25 − 35℃ (normally under moist soil condition) but excess or too much water will cause some diseases i.e. roots and leaf diseases [12, 13]. The significant goal of this paper is to identify and isolate volatile biologically active compounds from the ethanolic extracts of the plants and determine their pharmacological effects.

MATERIAL and METHODS
Collection and extraction of plant extracts
All the fresh plants samples were obtained from a farm garden in Lefkosa district of TRNC, and the plants samples were identified by a botanist from the TRNC ministry of agriculture and natural resources, all leaves are se-

parated from the main plant stalk, soaked and wash in water, air dried at room temperature 25°C. The dried sample were further weighed and crushed into powder. All the plants samples for the phytochemical analysis were extracted in ethanol and distilled water, the ethanolic extract of the plants leaves were prepared by soaking 50g of each of the dried powder of every sample individually in 500 mL of absolute ethanol solution and further allowed to stay for 48 hrs under room temperature condition in other to achieved thorough extraction. After two days, the resulting content was then filtered through a whatmann filter paper (No. 42, 125 mm) and kept for evaporation of the solvent to get the dried concentrated extracts. The dried portion of the extract was then frozen and stored at 5°C and the crude residue was weighed and used for all the preliminary phytoconstituent analysis.

Preliminary phytochemical screening

The preliminary phytochemical analysis for the ethanolic extract were performed to identify different phytochemical content in the plants samples by using standard procedure by Sofowora [14], Trease and Evans [15] and Ayoola et al. [16].

Test for Saponins (frothing test)

0.5 g of the crude ethanolic sample was weighed and added to 10 mL of distilled water in a test tube, the resulting solution was vigorously shaken and stable froth is observed if formed. Followed by adding 3 drops of olive oil to the froth formed sample and shaken vigorously after which the sample is further observed for the formation of emulsion.

Test for Tannins

Two qualitative analysis are used in testing for the presence of Tannins in any given samples.

KOH Test: 10mL of freshly prepared 10%KOH solution in a clean beaker, and 0.3 g of the crude ethanol extract was added and vigorously shaken to dissolve. And partial or dirty precipitate observed indicate the presence of Tannins.

Ferric chloride Test: 0.5 g of extract was dissolve in 10mL distilled water and boiled in a test tube and a few drops of ferric chloride solution was added to the boiled sample a formation of brownish green color is observed for the confirmation of Tannins.

Test for Flavonoids

2mL of sodium hydroxide (NaOH) was mixed with the crude extract of the plant a formation of concentrated yellow color was observed with further addition of 2 drops of diluted H_2SO_4 which later become colorless.

Test for Steroids

2mL of chloroform solution was added to 5mL of aqueous crude sample of the plant extract follow by 4mL of concentrated H_2SO_4 and indication of reddish color indicate the presence of Steroid in the sample.

Test for Terpenoids

5mL of aqueous ethanolic extract of the plant sample was mixed in 4 mL of chloroform and 1mL of acetic anhydride was added to the mixed solution follow by addition of 2 mL of concentrated H_2SO_4 formation of reddish violet color indicates the presence of triterpenoids in the sample.

Test for Glycosides

4 mL of concentrated acetic acid was mixed with 2mL of chloroform and aqueous extract of the plant sample the mixture was then cooled and concentrated H_2SO_4 was added and a formation of green color indicate the presence of glycoside in the given sample.

FTIR Spectroscopic Analysis

Fourier Transform Infrared Spectrophotometer (FTIR) is one of the most important analytical tools for the determination and identifying the types of functional group presents in a given compounds. FTIR method and technique was used for the determination and identification of various types of functional groups in each powdered leave extract of all the three sample used in the analysis as described by Yadav et al. [9]. The infrared spectroscopy spectrum (IR) was obtained using FTIR Shimadzu Japan in the range 400–4000 cm^{-1} with which 10mg of dried extract powdered sample of each of the plant sample was grounded in a mortar and pestle in order to obtain a fine powdered sample and the obtained extracts was subsequently used for the FTIR analysis.

GC-MS Specifications

All the plant extracts analyses were performed using a GC-MS system (GCMS-QP2010 SE plus Shimadzu Technology Japan) equipped with an HP-5MS capillary column (30 m x0.25 mm). The injection volume of each sample was 1 μL. And Helium was used as a carrier gas

with flow rate of 1 mL/min, the injection port temperature was 250°C and the program of the sample was set to a temperature ranges from 50°C to 300°C at a rate of 50°C/min and 10 min hold at 300°C for non- volatile constituents.

Peak Identification

The interpretation of mass spectrum of GC-MS and the constituents was identified by comparing their mass spectra with those in the Database of National Institute of Standard and technology (NIST). The spectrum of the unknown component was compared with spectrum of the known components stored in the NIST Library according to the chemical constituents present in the plant extracts.

RESULT and DISCUSSION

Preliminary phytochemical analysis

The Preliminary phytochemical analysis results revealed the presence of medically active compounds in the plants samples studied. As shown in Table 4, it could be seen that almost all the three selected plants contain various secondary metabolites such as Flavonoids, Saponins, Tannins, Triterpenoids and Steroids respectively, with the exception of Mints (*Mentha spicata* L) samples in which its test analysis results for Flavonoids test showed negative result. The positive results of the preliminary tests for Saponins, Flavonoids, and steroids are displayed in Fig .1. All the three (3) plants selected

for the study are very vital and mostly used for the treatment of many diseases as a results of their phytochemicals constituents which have been confirmed in so many studies conducted in the field of food and nutrition and have been reported to possess high medicinal value. Flavonoids are very vital bioactive polyphenols that are distributed widely in the plant kingdom and play an important role in photosynthesizing cells [17, 18]. Flavonoids have been reported to possess a wide range of biological activities such as antibacterial, anti-inflammatory and analgesic [19-21]. Furthermore these findings suggest that all the plants samples analyzed contain phytochemical nutrients in them, therefore all the three plants are a potential sources of natural antioxidants that could serve great importance in therapeutic purposes [22-24].

Gas chromatography Mass spectrometry (GCMS) Analysis

From Figure 2 and Table 5, the GC-MS analysis of the ethanolic extract of Rosemary (*Rosemarinus officinalis*) revealed the presence of various bioactive compounds. Some of the biologically active compounds revealed by the GC-MS are camphene a (monoterpenes) at a retention time of 5.33 with peak area of 43.2% which is known for its analgesic and anti- inflammatory property, and Eucalyptol(1,8-cineole) with retention time of 14.67 and peak area of 7.6% is used as antioxidant, anti-cancer and analgesic in drug formulation, while
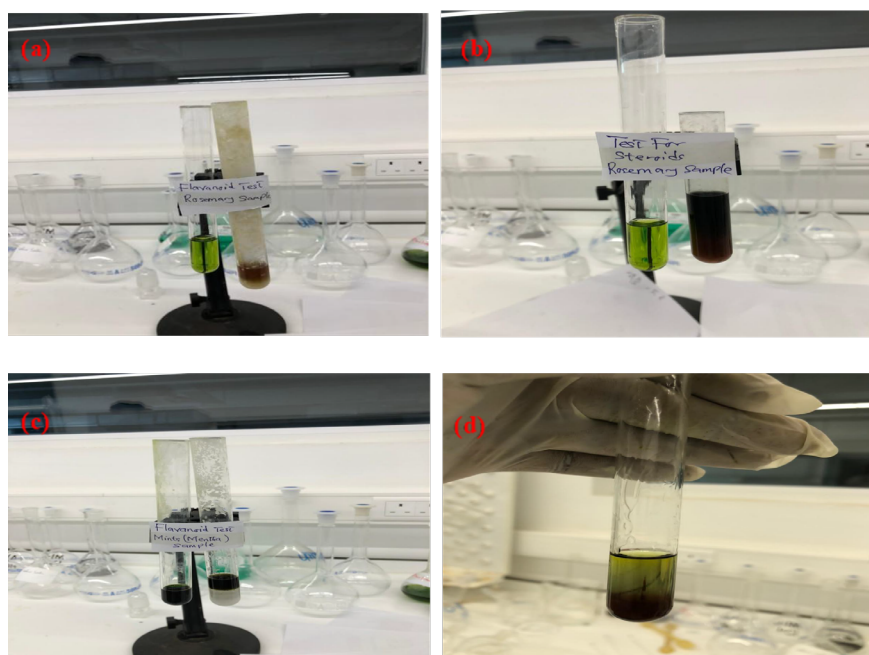
Figure 1. Preliminary phytochemical screening showing (a) Flavonoid test for rosemary, (b) Steroids test for rosemary, (c) Flavonoid test for *Mentha spicata*, (d) Steroids test for *Mentha spicata*.
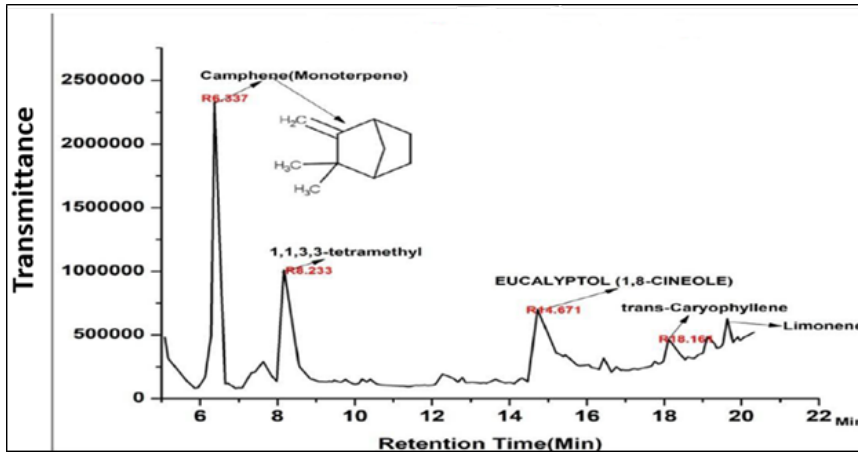
Figure 2. GC-MS Spectral Analysis of Ethanolic extract *Rosmarinus officinalis*.
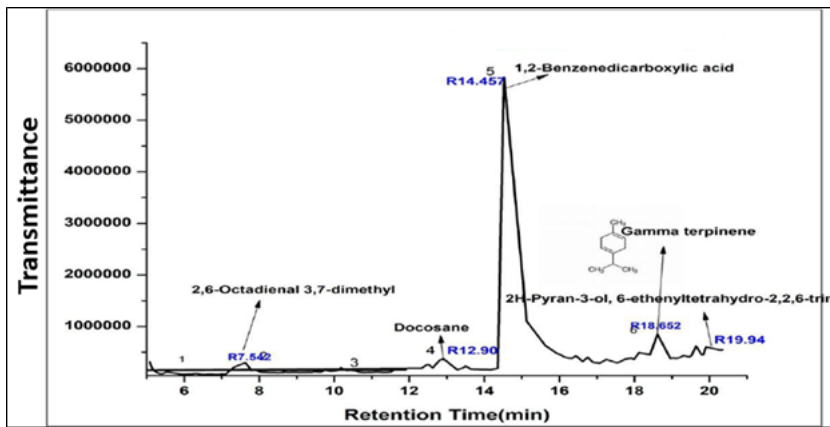
Figure 3. GC-MS Spectral Analysis of Ethanolic extract of *Coriandrum sativum*.
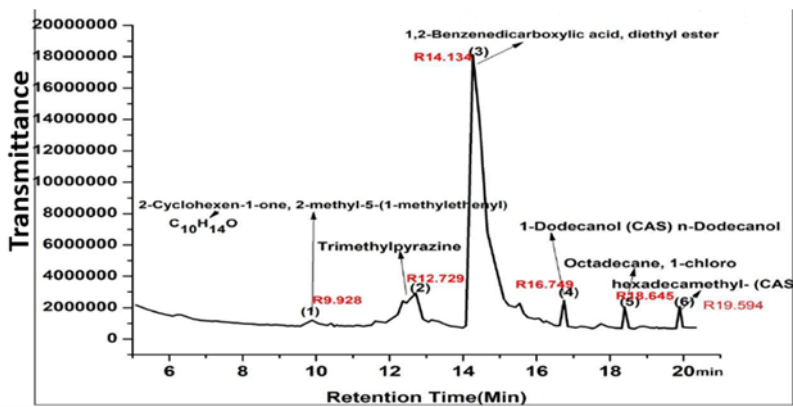
Figure 4. GC-MS Spectral Analysis of Ethanolic extract of Mint plant.

Table 4. Phytochemical constituents present in the plants extracts.

Plants	Percentage composition (%)				
	Flavonoids	Tannins	Saponins	Steroids	Triterpenoids
Mint	-	+	+	+	+
Rosemary	+	+	+	+	+
Coriander	+	+	+	+	+

- Negative result

+ Positive result
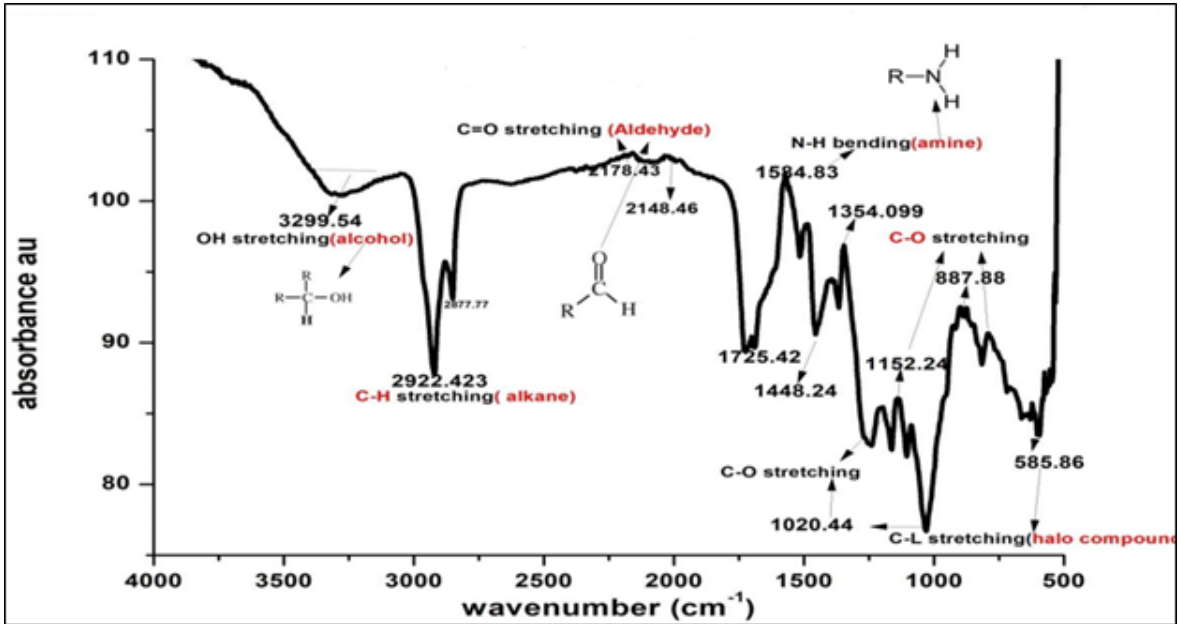
Figure 5. FTIR Analysis of *Rosmarinus officinalis* at solid state.

Table 5. Activity of Phyto-components identified in *Rosmarinus officinalis* by GC-MS.

Retention Time(Min)	Compounds Name	LRI	Peak Area %
5.337	Camphene (monoterpenes)	943	43.2
8.233	1,1,3,3-tetramethyl	1487	11.4
14.671	Eucalyptol (1,8- cineole)	1059	7.6
18.161	Trans-caryophyllene	1224	2.7
19.832	Limonene	1545	1.2
	Others		33.9

Table 6. Activity of Phyto-components identified in *Coriandrum sativum* by GC-MS.

Retention Time(Min)	Compounds Name	LRI	Peak Area %
5.62	2,6-octadienal 3,7-dimethyl	1024	0.45
12.90	Docosane	2208	0.25
14.457	1,2Benzenedicarboxylic acid	1620	24.7
18.652	Gamma terpene	1137	2.12
19.942	2H-Pyran-3-ol	1278	0.87
	Others		71.61

Table 7. Activity of Phyto-components identified in *Rosmarinus officinalis* by GC-MS.

Retention Time(Min)	Compounds Name	LRI	Peak Area %
9.928	2 Cyclohexen-1-one	873	0.76
12.729	Trimethylpyrazine	1008	0.94
16.749	1 Dodecanol(n-dodecanol)	1461	0.54
19.594	Hexadecamethyl	2097	0.3
18.645	Octadecane	1810	0.23
14.134	1,2,benzene dicarboxylic acid	1620	24.43
	Others		72.8

Trans- caryophyllene at retention time 18.161 with a peak area of 2.7% has an anti-microbial and anti- bacterial as a their biological activity. Also a bioactive compounds Limonene with a retention time of 19.832 and peak area of 1.2% has antimicrobial and antibacterial activity [25, 26].

As revealed in Figure 3 and Table 6 which shows the GC-MS analysis results of *Coriandrum sativum*. The phyto-constituents detected in ethanolic extract Coriander with their retention time and peak area are 2,6-octadienal 3,7-dimethyl with retention time of 5.62 and peak area 0.45%, Docosane with retention 12.9 and peak area 0.25%, 1,2-Benzenedicarboxylic acid (phthalic acid) with retention time of 14.45 and peak area of 24.7, Gamma terpene with retention time 18.65 and peak area of 2.12% and finally 2H-Pyran- 3-ol with retention time 19.94 and peak area of 0.8%. 2, 6-octadienal, 3, 7-dimethyl is used as Anti-fungal agent and also in Anti-cancer treatments. Biologically active compound Docosane also has antioxidant and anti-microbial properties and 1,2-Benzenedicarboxylic acid (phthalic acid) is used as anti-oxidant and antibacterial agents, also Gamma terpene has been reported to have a potent antioxidant property, and cardiovascular support and also provide neuro-protection [27]. While 2H-Pyran-3-ol serve as Antibacterial, antimicrobial as well as anti-oxidants.

The GC-MS analysis of *Mentha spicata* are shown in Figure 4 and Table 7. The phytoconstituents detected in ethanolic extract of Mints (*Mentha spicata*) sample extract using gas chromatography-mass spectrometry(GC-MS) with their retention time and peak area are 2 Cyclohexen-1-one at a retention time of 9.928 with a peak area of 0.76%, and its biological activities include Antioxidants, antibacterial agents used in drugs formulation. And Trimethylpyrazine (TMP) with retention time of 12.729 min with a peak area of 0.94% and is used in treatment of cardiovascular diseases, headache and vertigo and also used in preventing cell damage [28-30].

FTIR Analysis

Basically in this study the potential of FTIR Spectroscopy as analytical tools is used for identification of various functional groups responsible for medicinal properties in all the plant samples. The FTIR spectra of *Rosmarinus officinalis*, *Coriandrum sativum* and *Mentha Spicata* are revealed in Figure 5, 6 and 7 respectively. The results confirms the presence of many characteristics functional groups detected at different vibrational frequency

band in the IR spectrum. The various functional groups observed using FTIR spectrum indicates the presence of O-H group(alcohol), carboxylic acid, amine, sulphur derivatives ,amino acid, and nitro - compounds among others. From the summarized FTIR Spectrum the fingerprint at 3299.54 cm^{-1} in rosemary sample which is the representative for O-H group predict the presence of alcohol in the sample, and the analysis reveals that all the three plants samples contains O-H(alcohol) and CH (alkane) functional group in them [31]. The band at 2922.423, 2832.61, 2993.83, and 2981.63cm^{-1} represent – CH_2 and –CH_3 groups which is due to presence of chlorophyll groups in the samples the weak band at 1476.80 cm^{-1} in parsley sample which is the representative of N-H bending is as a result of the amino acid present in that sample [32, 33]. And also the bands at 1152.24, 1029.98 and 1057.85 cm^{-1} represent stretching vibration of (C-O) and are due to the presence of acid. As OH (alcohol group) group has the ability of forming hydrogen bonding capacity, presence of OH group probably indicates the higher potential of the sample towards inhibitory activity against microorganisms [34].

Conclusion

This present study has been performed to established different phytochemical parameters on three medically valued plants using two distinctive analytical techniques FTIR, and GC-MS. The GCMS chromatogram conducted on all the selected plant extracts revealed the presence of many bioactive compounds of medicinal value such as Camphene (monoterpenes), Eucalyptol (1,8- cineole), Trans-caryophyllene, Limonene, 2-Cyclohexen-1-one, Trimethylpyrazine(TMP), 1-Dodecanol (n-dodecanol), Octadecane, 1,2-benzendicarboxylic acid (phthalic acid), 2,6- octadienal 3,7-dimethyl, Gamma terpene, 2H-Pyran-3-ol, 1,4 Cyclohexadiene, and Metronidazole (anazole). While the FTIR analysis conducted showed the presence of many characteristics functional groups such as Carboxylic acids, amine amide, and OH group along with sulphur derivatives with some notable alkanes and alkynes. The preliminary phytochemical screening indicates the presence of various secondary metabolites such as Tannins, Flavonoids, Saponins, Triterpenoids and Steroids which is evident in the research carried out by [35, 36, 37]. Therefore, these findings suggest that all the three plants samples analyzed contain many phytochemical compounds in them, and conclusively are a potential sources of natural antioxidants that could serve great importance for varieties of therapeutic purposes.
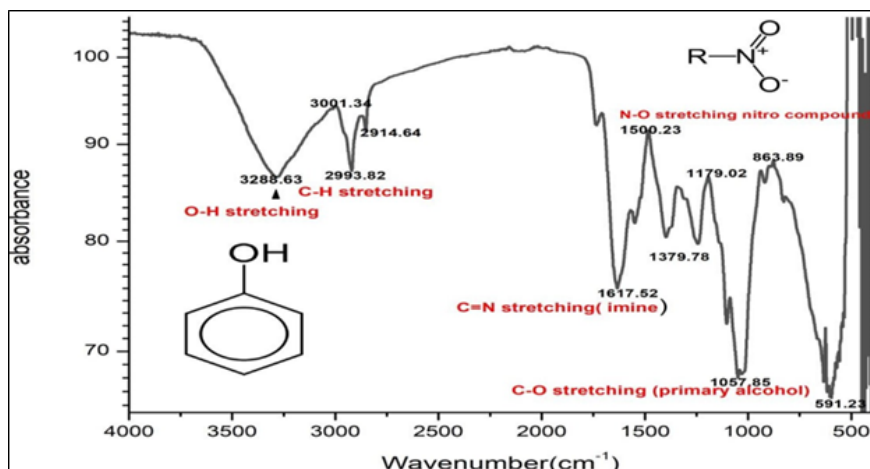
Figure 6. FTIR Analysis *Coriandrum sativum* at solid state.
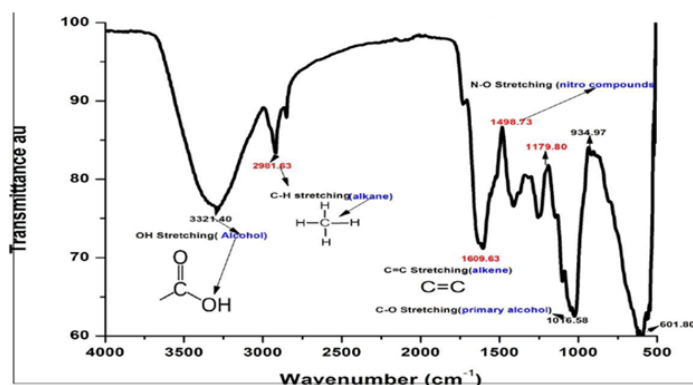
Figure 7. FTIR Analysis *Mentha Spicata* at solid state.

Conflict of Interest

The authors declare that they have no conflict of interest.

References

1. H.O. Edeoga, D.E. Okwu, B.O. Mbaebie, Phytochemical Constituents of some Nigerian Medicinal Plants, Afr. J. Biotechnol., 4 (2005) 685-688.
2. D. Kumar, P.J. Shrivastava, phytochemical analysis of miracle herb coriander sativum Indian J.Sci. Res, 13 (2017) 34-48.
3. I. Ahmad, Z. Mehmood, Screening of some Indian medical plants for their antimicrobial properties, J. Ethnopharmacol., 62 (2010) 183-193.
4. O.A. Aiyegoro, A. Okoh, Preliminary phytochemical screening and in vitro antioxidant activities of the aqueous extract of Helichrysum longifolium, BMC Complement Altern Med., 10 (2010) 21– 28.
5. G. Philomena, Concerns regarding the safety and toxicity of medicinal plants—an overview, J. Appl. Pharmaceut. Sci., 1 (2011) 40–44.
6. H. Yuan, Q. Ma, L. Ye, G. Piao, The traditional medicine and modern medicine from natural products, Molecules., 21 (2016) 559.
7. N.L. Pathak, S.B. Kasture, N.M. Bhatt, J.D. Rathod, phytopharmacological properties of Coriander as a potential medicinal plant, An overview journal of applied pharmaceuticals science, 4 (2011) 20 -27.
8. F. Malongane, L. McGaw, F.N. Mudau, The synergistic potential of various teas, herbs and therapeutic drugs in health improvement: a review, J. Sci. Food Agri., 97 (2017) 4679–4689.
9. R. Yadav, R.K. Khare, A. Singhal, Qualitative phytochemical screening of some selected medicinal plants of Shivpuri District (MP), Int. J. Life Sci. Sci. Res., 3 (2017) 844–847.
10. M.M. Özcan, J.C. Chalchat., Chemical composition and antifungal activity of rosemary (*Rosmarinus officinalis* L.) oil from Turkey, International Journal of Food Sciences and Nutrition., 59 (2008) 691-698.
11. N. Arnold, G. Valentini, B. Bellomaria, A. Hocine, Comparative study of the essential oils from Rosmarinus eriocalyx Jordan & Fourr. From Algeria and R. officinalis L. from other countries, Journal of Essential Oil Research, 9 (1997) 167-175.
12. K. Ashok, S. Chandra, P. Dutt, B. Lal Kaul, A. Tava, Essential oil composition of Mentha x piperita L. from different environments of north India, Flav Fragr., 14 (1999) 5-8.
13. D. Ganesh, K.S. Kiran, K.J. Prakash, S. Norayama, GCMS analysis of phytocomponents in the methanolic extracts of Mentha arvensis (corn mints), IJCPS., 6 (2014).
14. L.A. Sofowora, Medicinal plants and Traditional Medicine in Africa. Spectrum Books Ltd, Ibadan, (1993) 55-71.
15. G.E.Trease, W.C. Evans, Pharmacognosy 11th Ed., Tindall Ltd, London, (1989) 60-75.

16. G.A. Ayoola, H.A.B. Coker, S.A. Adesegun, A.A. Adepoju-Bello, K. Obaweya, E.C. Ezennia, T.O. Atangbayila, Phytochemical screening and antioxidant activities of some selected medicinal plants used for malarial therapy in South-Western Nigeria, Trop. J. Pharm. Res. 7 (2008) 1019-1024.

17. A.G. Gülbaba, N. Özkurt, M. Kürkçüoğlu, Mersin Adana yöresindeki doğal biberiye (*Rosmarinus officinalis* L.) populasyonlarının tespiti ve uçucu yağ verim ve bileşimLerinin belirlenmesi. Orman Bakanlığı Teknik Bülten, 193 (2002) 193 5-30.

18. A. Muhammad, S. Muhammad, J. Amer, Phytochemical spectrum of Essential Oil of Paganum harmala by GC-MS and antimicrobial activity using sequential solvents fractions and essential oil, Asian J. Chem., 26 (2014) 574–578.

19. A. Hussain, W. Shadma, R. Aleza, and H. Sarfaraj, Microscopial, anatomical and physico- chemical studies on leaves of foenuculum vulgare growing widely in eastern Uttar Pradesh region of India, Indian Journal of Natural Products and Resources., 1 (2011) 74-80.

20. J.K. Mensah, R.I. Okoli, J.O. Ohaju-Obodo, K. Eifediyi, Phytochemical, nutritional and medical properties of some leafy vegetables consumed by Edo people of Nigeria, Afr. J. Biotech., 7 (2018) 200-230.

21. A. Kathirvel, A.K. Rai, G.S. Maurya, V. Sujatha, Dryopteris cochleata Rhizome: a nutritional source of essential elements, phytochemicals, antioxidants and antimicrobials, Int. J. Pharm. Pharm. Sci,. 6 (2014) 179–188.

22. P. Ruthiran, R. Lokesh, I. S. Chinnadura, Phytochemical studies and GC-MS analysis of Spermadictyon suaveolens Roxb, Int. J. Pharm. Pharm. Sci., 9 (2017) 143–149.

23. Z.Z. Mohamed, S. Benedict, Phytochemical constituents of the leaves of Leucaena leucocephala from Malaysia, Int. J. Pharm. Pharm. Sci., 8 (2016) 174–179.

24. P.G Jiji, M.P. Subin, Qualitative phytochemical screening and GC-MS analysis in the leaf methanolic extracts of Kamettia caryophyllata (Roxb.) Nicolson and Suresh, Paripex Indian J. Res., 6 (2017) 470–479.

25. G.S Kumar, K.N. Jayaveera, C.K. Ashok Kumar, U.P. Sanjay, B.M. Vrushabendra Swamy, D.V. Kishore Kumar, Screening of antioxidant activity, total phenolic and GC-MS study of Vitexnegundo. Trop. J. Pharm. Res., 6 (2007) 717-723.

26. K.S. Sunil, S. Akki, B.D. Ashika, L.R. Chitrali, S. Naresh, S. Balasubramanian, GCMS And FTIR analysis on the methanolic extract of *coriandrum sativum* leaves, European journal of pharmaceutical and medical research, 5 (2018) 455-457.

27. K. Ashish, J. Bhat, GC-MS analysis of methanol extract of Acacia nilotica (L.) Leaves. Int. J. Pharma. Chem., 6 (2016) 50–53.

28. K.B. Santhos, D. Manickam, P. Sri Kamatchi, S. Shyama, S. Subramaniam, GC-MS analysis of an Ayurvedic medicine Modified Arjunarishta, Int. J. Curr. Res. Chem. Pharm. Sci. 4 (2017) 46–50.

29. K.S. Thanga Krishna, S. Muthukumarasamy, V. R Mohan, GC-MS analyses of ethanol extract of Sarcostemma secamone (L) bennet (Asclepiadaceae). Sci. Res., 2 (2012) 187–191.

30. R.L. Shrestha, GC-MS analysis, antibacterial and antioxidant study of Amomum subulatum, J. Med. Plants Stud., 5 (2017) 126–129.

31. A. Balasubramanian, S. Akki, B.D. Ashika, S. Naresh, GCMS and FTIR analysis on the methanolic extract of coriadrum sativum L leaves, ejpmr., 5 (2018).

32. P. Rajiv, A. Deepa, P. Vanathi, D. Vidhya, Screening for phytochemical and FTIR analysis of Myristica Dacttyloids fruits extracts, International journal of pharmaceuticals science (2020) 316-318.

33. F.N. Iheagwam, O.O. Ogunlana, O.E. Ogunlana, I. Isewon, J. Oyelade, Potential anti-cancer flavonoids isolated from Caesalpinia bonduc young twigs and leaves: Molecular docking and in silico studies. Bioinform. Biol. Insights., 13 (2019) 1–16.

34. M. Gunjan, K. Goutam, A.K. Jham M. Umashankar, Pharmacognostic and antihyperglycemic study of Coccinia indica, International Journal of Phytomedicine., 2 (2010) 36-40.

35. X. Li, T. Tian, Phytochemical Characterization of *Mentha spicata* L. Under Differential Dried-Conditions and Associated Nephrotoxicity Screening of Main Compound With Organ-on-a-Chip, Front.pharmacol., 28 (2018) 10-67.

36. B.D. Ashika, R.L. Chitrali, S. Naresh, K. Sunil, S. Akki, S. Balasubramanian, phytochemical studies on the methanolic extract of coriander sativum leaves – an in vitro approach, European journal of biomedical and pharmaceutical sciences., 5 (2018) 494-500.

37. R. Kalinda, N. Rioba, Phytochemical Analysis and Efficacy Of Rosemary (*Rosmarinus Officinalis*) and Mint (*Mentha Spicata*) Extracts Against Fall Armyworm (Spodoptera Frugiperda) on Baby Corn (Zea Mays), Acta chemical sciendo., 4 (2020) 24-58.

Research Article

Evaluation of Antimicrobial Activities of Various Herbal Oils Against *Helicobacter pylori* and their Cytotoxic Effects on HUVEC Cell Line

Çeşitli Bitkisel Yağların *Helicobacter pylori*'ye Karşı Antimikrobiyal Etkinlikleri ve HUVEC Hücre Hattı Üzerindeki Sitotoksik Etkilerinin Değerlendirilmesi

Tuğçe Deniz Tanalp[1], Başak Aru[2] and Kayhan Çağlar[3]

[1]Department of Medical Services and Techniques, Gazi University Health Services Vocational School, Ankara, Turkey.
[2]Department of Immunology, Faculty of Medicine, Yeditepe University, İstanbul, Turkey.
[3]Department of Clinical Microbiology, Faculty of Medicine, Gazi University, Ankara, Turkey.

ABSTRACT

*H*elicobacter pylori (H. pylori) infection is accepted as the most important chronic bacterial infection. In recent years, it is reported that the bacteria are developing resistance against the applied antibiotics. In order to increase the success rate, decrease recurrence and achieve eradication, it is very important to investigate nontoxic biocompatible herbal resources to be used in addition to antibiotic therapy. Herbal oils, obtained from plants are being used for various purposes for a long time, particularly in commercial and scientific fields. Therefore, in our study, we chose various herbal oils *(Eucalyptus globulus, Juniperus communis, Rosmarinus officinalis, Thymus vulgaris)* that are known to be effective against gastric and gastrointestinal tract diseases which do not have adequate investigations over *H. pylori* in the literature, and we aimed to investigate their antimicrobial activity over *H.pylori* and cytotoxic activity on Human Umbilical Vein Endothelial Cells (HUVEC) cell line. The antimicrobial activity is investigated by microdilution assay (MIC, MBC), and cytotoxic activity is investigated by MTT and LDH assays. As a result, it was found that *Eucalyptus globulus* (MIC: 2,81 %v/v, MBC: 5,62 %v/v), *Juniperus communis* (MIC: 0,35 %v/v, MBC: 0,70 %v/v), *Rosmarinus officinalis* (MIC: 2,81 %v/v, MBC: 5,62 %v/v), *Thymus vulgaris* (MIC: 0,70 %v/v, MBC: 1,40 %v/v) oils were effective against *H. pylori*. Besides, it was determined that *Thymus vulgaris* herbal oil had the highest cytotoxic effect, and *Eucalyptus globulus* herbal oil had the lowest cytotoxic effect on the HUVEC cell line.

Key Words
Helicobacter pylori, herbal oil, antibacterial activity, cytotoxicity.

ÖZ

*H*elicobacter pylori (H. pylori) enfeksiyonu en önemli kronik bakteriyel enfeksiyon olarak kabul edilmektedir. Son yıllarda tedavide kullanılan antibiyotiklere karşı bakterinin direnç geliştirdiği rapor edilmiştir. Tedavide başarı oranının yükselmesi ve rekürrensin azalması için, toksik olmayan biyouyumlu bitkisel kaynakların araştırılarak sistemik antibiyotik tedavisine ek olarak kullanılması ve eradikasyonun sağlanması son derece önemlidir. Bitkilerden elde edilen yağlar uzun yıllardan beri çeşitli amaçlara yönelik, özellikle ticari ve bilimsel alanlarda kullanılmaktadır. Bu nedenle çalışmamızda; genellikle mide ve gastrointestinal sistem rahatsızlıklarına iyi geldiği bilinen ve literatürde *H. pylori* üzerinde yapılmış yeterli çalışması bulunmayan çeşitli bitkisel yağlar (*Eucalyptus globulus, Juniperus communis, Rosmarinus officinalis, Thymus vulgaris*) seçilmiş ve *H. pylori*'ye karşı antimikrobiyal etkinlikleri ile Human Umbilical Vein Endothelial Cells (HUVEC) hücre soyu üzerindeki sitotoksik etkilerinin araştırılması amaçlanmıştır. Bitkisel yağların antimikrobiyal etkinlikleri mikrodilüsyon yöntemi ile (MIC, MBC), sitotoksik etkinlikleri ise MTT ve LDH yöntemleri ile incelenmiştir. *H. pylori*'ye karşı antimikrobiyal etkisini araştırdığımız, *Eucalyptus globulus* (MIC: 2,81 %v/v, MBC: 5,62 %v/v), *Juniperus communis* (MIC: 0,35 %v/v, MBC: 0,70 %v/v), *Rosmarinus officinalis* (MIC: 2,81 %v/v, MBC: 5,62 %v/v) ve *Thymus vulgaris* (MIC: 0,70 %v/v, MBC: 1,40 %v/v) 'in etkili olduğu gözlemlenmiştir. Aynı zamanda HUVEC hücre soyu üzerinde *Thymus vulgaris* bitkisel yağının en yüksek, *Eucalyptus globulus* bitkisel yağının ise en düşük sitotoksik etkiye sahip olduğu tespit edilmiştir.

Anahtar Kelimeler
Helicobacter pylori, bitkisel yağ, antibakteriyel aktivite, sitotoksitite.

INTRODUCTION

It is thought that *H.pylori* and other helicobacteria found in the digestive system are as old as the first living organisms and settled as the main flora bacteria in the digestive systems of large mammals and the first primates [1]. *H. pylori,* which was produced in the laboratory for the first time in 1982, was thought to belong to this genus due to its similarities to the genus *Campylobacter* and was defined as *Campylobacter pyloridis* [2]. However, in later studies, it was revealed that many phenotypic and genotypic characteristics were different from the Campylobacter genus, and therefore this new genus was named *Helicobacter* [3]. *H. pylori*, which is highly motile, gram-negative, and spiral-shaped, has been found to colonize the mucus layer on the gastric mucosal epithelium in individuals with ulcer or gastritis disease [4]. Marshall and Warren, who discovered colonies formed by spiral-shaped microorganisms on the surface of the medium in their study, and then succeeded in producing spiral microorganisms in biopsy samples from more than 11 patients, concluded that the formation of some gastroduodenal diseases may be associated with these bacteria [5]. Proving the relationship between this spiral-shaped microorganism and gastroduodenal diseases is considered as one of the important developments that left its mark on medicine in the 20th century.

Today, *H. pylori* infection is accepted as the most important chronic bacterial infection and the most important cause of chronic gastritis [6]. It is known that *H. pylori*, which can survive in the stomach for life if left untreated, is associated with diseases such as peptic ulcer, gastritis, gastric cancer, and mucosal-associated lymphoid tissue (MALT) lymphoma [7]. According to the 2005 III. Maastricht Consensus reports of the European *H.pylori* study group, it is less common in developed countries than in developing countries, while this rate is 20%-30% in developed countries, it is 85%-95% in developing countries, and more than 50% of the world population is reported to be infected with this bacterium. *H.pylori* was first described as a group 1 carcinogen by IARC (International Agency for Research on Cancer) in 1994. Therefore, the treatment of *H.pylori* is very important. The primary reservoir of *H.pylori* is the human gastric mucosa. However, the passageway to this region, the factors affecting the passageway, and the rates of passage are still being investigated. Treatment of the infection is combined antibiotic therapy known

as "triple therapy", which is administered to patients for 7-10 days. Clarithromycin and amoxicillin (or metronidazole) are administered in combination with proton pump inhibitors, but this treatment does not provide 100% eradication. This treatment protocol was determined by the 1997 report of the European *Helicobacter pylori* Working Group. Initially, the success of this combination was very high, but in recent years success rates have decreased, and recurrences have increased. It is thought that there are many factors such as antibiotic resistance, patient compliance, bacterial virulence and density, geographical features, and genetic differences [8,9]. *H.pylori* was first isolated from the oral flora by Krajden and Shames in 1989 [10], then in dental plaque by Majmudar et al. in 1990 [11], Dowsett et al. in 1999 on the dorsum of the tongue [12], and Oshowo et al. in saliva in 1998 [13], and they thought that the oral cavity could be a reservoir like the gastric mucosa. Although the current systemic antibiotic therapy is effective on the stomach, eradication is not successful because antibiotics cannot penetrate the dental plaque biofilm [14]. This situation has been reported in developed western countries that the treatment success has decreased at unacceptable rates. For this reason, it is thought that the drugs used in the treatment of *H.pylori* are insufficient. These problems encountered in treatment have led researchers to develop new antibacterial drugs to support treatment. More attention is paid to the search for new antibacterial drugs, especially herbal medicines, against *H. pylori*. Therefore, to increase the success rate of the treatment and decrease its recurrence, it is extremely important to search for non-toxic biocompatible herbal sources and to use them in addition to systemic antibiotic treatment and to ensure eradication. Essential oils obtained from plants have been used for various purposes for many years, especially in commercial and scientific fields [15,16]. Herbal oils, which have a wide range of uses, have been the subject of interest of many scientists in recent years and their biological activities have been investigated by examining their structures. Today, the research of medicinal plants and their essential oils is very important both scientifically and economically. Herbal oils are among the drugs used in the treatment from ancient times to the present day. Considering the purpose of use in folk medicine, some biological activities have been scientifically explained as a result of pharmacological studies on these herbal oils [17-19]. Therefore, in our study; various herbal oils, which are known to be good for stomach and gastrointestinal system disorders in folk medicine and for which

there are no adequate studies on *H.pylori* in the literature, were selected and it was aimed to investigate their antimicrobial activities against *H.pylori* as well as their cytotoxicity on human endothelial cells. For this purpose, antimicrobial activities of herbal oils against *H.pylori* were investigated by microdilution method and their cytotoxic properties were evaluated on HUVEC cell line by MTT and LDH methods.

MATERIALS and METHODS

H.pylori culture

Cells were extracted from cryobank and incubated overnight in 37 °C CO_2 containing incubator, using solid medium. After incubation, petri dishes were evaluated morphologically for the production of different colonies. Cells, collected by inoculation loop were evaluated for motility and contamination with 40X magnification. The cells cultivated in the petri dish were collected by sterile cotton bud which was mixed in medium containing eppendorf and homogenous spreading cultivation was performed to a new petri dish with the same cotton bud for cell passaging and incubated for a night long. Following incubation, bacteria reproduced in the petri dish were collected by steril cotton bud and transferred to a FBS and antibiotic containing liquid medium and left in the mixing incubator (37 °C, 100 rpm) for a night long. Following incubation, cell count was performed in the spectrophotometry device to determine the number of bacteria to be used in the antimicrobial activity tests and cell characterization was also performed.

Gram staining

Ten µl of the medium was dropped to one side of the slide. A little amount of cells were collected from the cells in the petri dish by inoculation loop and dropped over the medium on the slide. After drying, the slide was fixed by crossing over the flame three times. Afterwards, the slide was consecutively dyed with crystal violet for 1 minute, washed with water, dyed with lugol for 1 minute, washed and decolorized with alcohol and lastly washed with aqueous fuchsine for 1 minute, washed and left for drying. After drying, immersion oil was dropped over the preparate, evaluated with 100X magnifying objective and photopgraphs were obtained.

Evaluation of properties of *H.pylori* with urease and cathalase tests

The bacteria obtained from fresh culture were cultivated over urea medium prepared in 1.5 ml eppendorf tubes and left for incubation in 37 °C. Turning of the medium color from yellow to pink was accepted as positivity of the presence of *H.pylori* in the medium. For the cathalase test, colony obtained from fresh culture was placed over the slide and 3% hydrogen peroxide was dropped. Bubble formation was accepted as the positivity fro the presence of *H. pylori*.

H.pylori cell count

In order to produce a time-growth curve of the cells, cell counts were made every 2 hours for 48 hours to create a growth curve of cells. At the end of the 2nd hour from bacteria passaged from solid medium to liquid medium, 20 µL was collected from the bacteria passaged from solid medium to aqueous medium, 980 µL of medium was added and measurement was performed in UV-VIS spectroscopy in 600 nm wave form.

Antimicrobial effects of the herbal oils against *H. pylori*

Minimal Inhibitory Concentration (MIC) test was performed in 96 well plates by microdilution method which was based on reference method recommended by the NCCLS. After determination of inhibition concentrations, minimal bactericidal concentrations were determined by MBC test [20-22].

MIC and MBC tests

MIC values were determined by broth dilution method. To each well of the 96 well plate, 100 µl, 10% FBS containing Brucella broth medium was added for testing concentrations. 90 µl oil and 10 µl DMSO were mixed in sterile eppendorf tube by vortexing and added to the first well that contained 100 µl Brucella broth medium. Two times serial dilutions of the herbal oils, starting from 45% in the first well and including 8 different concentrations were prepared. Then, $10^6/100$ µl CFU bacteria suspension was added to each well. Amoxycillin and DMSO were used as positive and negative control, consecutively. At the same time, growth of *H.pylori* in a well without addition of any herbal oil or DMSO oil mixture over medium in another well was evaluated as control group. 25 µg in 8 µl of 250 mg 80 ml Amoxina suspension was added to positive control well. Also 10 µl DMSO was added to negative control well and tested. Plate was left for incubation in 37 °C for 24 hours. After incubation, % oil concentration in the first well without growth was identified as MIC value. For MBC, 10 µl was obtained from wells and cultivated to Brucella agar containing petri dishes with separate compartments for

each concentration and left for 24 hours incubation in 37 °C. After incubation, % oil concentration in the first well without growth was identified as MBC concentration.

Chemicals & Treatment

The herbal oils were obtained from Aksuvital Natural Products Corporation. Essential oils were produced from leaves or flowers by hydrodistillation method according to the type of plant and fixed oils were obtained from squeezing of the oily seeds of the plants by cold press machine. Cytotoxicity of herbal oils were evaluated on the human umbilical vein endothelium cell line (HUVEC ATCC® CRL-1730™).

Determination of cytotoxicity

For assessment of cytotoxicity, HUVEC cell line, cultured with DMEM/F12 culture medium (Thermo Fisher Scientific, Catalog No: 11320033) supplemented with 10% fetal bovine serum (Sigma-Aldrich, Catalog No: F7524) and 1% antibiotic solution (Thermo Fisher Scientific, Catalog No: 15140122) was used. 5×10^3 cells per well were seeded into 96-well cell culture plates as triplicates and incubated under humid environment containing 5% CO_2 at 37 °C tissue culture incubator overnight to allow attachment. Stock solutions of herbal oils were prepared by mixing with DMSO at 500 mg/mL concentration, and diluted to 1, 50, 100, 250 ve 500 ug/ml final concentrations by mixing with cell culture medium. Cells were incubated with the media containing herbal oils for 48 hours, and cytotoxicity was measured via LDH and MTT assays. For the evaluation of LDH release, commercial LDH cytotoxicity assay kit was used according to manufacturer's instructions (Cell Bio Labs CytoSelect LDH Cytotoxicity Assay Kit (Catalog No: CBA241)). For negative control, cell culture medium was used whereas for positive control, cells lysed by the addition of Triton X-100 solution provided by the kit was used. The absorbance was measured at 450 nm by a microplate spectrophotometer (BioTek Epoch Microplate Spectrophotometer) [23].

Relative cytotoxicity was calculated according to manufacturer's protocols:

$$\text{Relative Cytotoxicity (\%)} = \frac{OD\ Compound\ treated\ sample\ -\ OD\ negative\ control}{OD\ positive\ control\ -\ OD\ negative\ control} \times 100$$

Toxicity was also evaluated by MTT assay, which relies on the reduction of tetrazolium dye MTT (3-(4,5-Di-methylthiazol-2-yl)-2,5-diphenyltetrazolium bromide)

to insoluble formazan by the activity of mitochondrial enzyme succinate dehydrogenase. For the determination of toxicity by MTT assay, cells were incubated with herbal oils as defined as in the LDH assay; at the end of the incubation period, the culture medium was replaced with 200 µl medium containing 10% MTT reagent (Sigma-Aldrich, Catalog No:TOX1-1KT). The non-treated group was served as positive control while plain cell culture medium was used as negative control. At the end of incubation time, formazan crystals were dissolved by the addition of solubilization solution provided with the kit. The resulting solutions (violet in color) were transferred to another 96 well plate as triplicates. The absorbance was measured by a microplate spectrophotometer at a wavelength of 570 nm [24-26]. Viability was calculated as given below.

$$\text{Relative Cellular Viability (\%)} = \frac{OD\ Compound\ treated\ sample\ -\ OD\ negative\ control}{OD\ positive\ control\ -\ OD\ negative\ control} \times 100$$

Statistical Analysis

The statistical analysis of dose and percentage cytotoxicity analysis were performed using "SPSS software for Windows version 17,0 (Statistical Package for the Social Sciences Inc, Chicago, IL, USA)" software. Continuous variables were defined by "Mean ± Standart Deviation". The 24th and 48th hour values within their own groups were evaluated using Friedman test ($p < 0,05$ was accepted as statistically significant) and comparison of 24th and 48th hour values were performed using Mann Whitney-U test ($p < 0,05$ was accepted as statistically significant). Multiple comparison of the groups were performed by Kruskal-Wallis test and dual comparison of the groups were performed by Mann Whitney-U test.

RESULTS and DISCUSSION

Antimicrobial effects of herbal oils

The MIC and MBC values were found as follows: *Eucalyptus globulus* (MIC: 2.81% v/v, MBK: 5.62% v/v), *Juniperus communis* (MIC: 0.35% v/v). v/ v, MBC: 0.70% v/v), *Rosmarinus officinalis* (MIC: 2.81% h/v, MBC: 5.62% v/v), and *Thymus vulgaris* (MIC: 0.70% h/v, MBC: 1.40% v/ v) (Table 1). As seen in the literature, Esmaili et al. [27] evaluated the anti-*H.pylori* activities of essential oils of *Thymus vulgaris* and *Eucalyptus globulus* by the agar diffusion method and found the anti-*H. pylori* activities for *T. Vulgaris* and *E. globulus* to be 10.8 and 46.4 µg/ mL, respectively. Therefore, *T. Vulgaris* had a better inhibitory effect against *H.pylori* than *E. globulus*, in

Table 1. MIC and MBC values of herbal oils against H.pylori (% v/v).

Herbal Oils	Tested Concentrations of Herbal Oils (% v/v)	MIC (% v/v)	MBC (% v/v)
Eucalyptus globules		2.81	5.62
Juniperus communis	45-0.35	0.35	0.70
Rosmarinus officinalis		2.81	5.62
Thymus vulgaris		0.70	1.40

agreement with our study. In the study of Mahady et al. [28], it was reported *Rosmarinus officinalis* as MIC: 25 µg/mL. The activity of *Juniperus communis* extract was also found to be weak (MIC: 100 µg/mL). Antimicrobial effects of *Rosmarinus officinalis* and *Juniperus communis* against *H. pylori* were observed in our study, which is in accordance with the study. However, *Juniperus communis* was found to be more effective than *Rosmarinus officinalis* in our study.

Cytotoxic effects of herbal oils

It is a desirable feature for a drug that will have the potential to be used in medicine, not only showing the expected effect but also not showing any toxic effects. In this context, as the next step, the cytotoxic effects of 4 herbal oils, which we found antimicrobial effect against *H. pylori*, on the HUVEC cell line were also investigated in our study. The viability of the HUVEC cell line was over 80% as a result of the application of *Eucalyptus globulus* at all concentrations. While the viability rate of *Rosmarinus officinalis* was above 100% at concentrations up to 500 µl/mL, it was observed that the viability rate decreased below 20% at 500 µl/mL concentration. It was observed that the viability of *Juniperus communis* decreased significantly in response to increasing concentrations, while the viability of the HUVEC cell line was observed to be significantly lower at all concentrations of *Thymus vulgaris* . In this situation; on HUVEC cell lines treated with 1, 5, 50, 100, 250 µl/ml concentrations of *Rosmarinus officinalis* and 500 µl/ml *Eucalyptus globulus*, the 24th hour viability rates were found to be the highest. When 48 hour the viability values of cells were compared (Table 2), the viability of cells were were above 80% up to 50 µl/mL concentration of *Eucalyptus globulus*, whereas the viability decreased below %50 significantly at higher doses of oils. Similar results were obtained with the increasing concentrations of *Rosmarinus officinalis* extract oil. It was observed

that the viability of *Juniperus communis* was between 60-80% up to a concentration of 50 µl/mL, while at higher doses, the viability rate decreased significantly below 20%. Although the viability of the HUVEC cell line was significantly lower at all concentrations of *Thymus vulgaris* , it was noted that the viability rates increased from 20% to 40% with the increase in concentration. In this situation; The highest viability rates at the 48th hour were detected on HUVEC cell line treated with *Eucalyptus globulus* at 1, 5, 50, 100, 250 µl/ml concentrations and *Thymus vulgaris* at 500 µl/ml concentration.

Cabral et al. [29],. investigated the cytotoxicity of the essential oil of *Juniperus communis* subsp. alpina (Suter) čelak needles by MTT method, and they reported the essential oil decreased the human keratinocyte HaCaT cell viability as 65.65% ± 1.195 (at 1.25 µl/mL concentration); 21.47 ± 4.078 (at 0.64 µl/mL), and 1.59% ± 1.206 (at 0.32 µl/mL concentration) compared to the control. Similarly, in our study, it was observed that the viability rate of the HUVEC cell line that we studied in response to the increasing concentrations of J.communis decreased.

Döll-Boscardin et al. [30] investigated the cytotoxic effects of the essential oils of young and mature leaves of *Eucalyptus benthamii* on various cancer cells and reported that no cytotoxic effect was observed on the HeLa cell line, but a very weak cytotoxic effect on Jurkat cells. In our study, as a result of the application of E.globulus on the HUVEC cell line at all concentrations, the viability rate was above 80% at the end of the 24th hour. When the exposure time was prolonged, it was observed that the viability rate decreased below 50% at concentrations above 50 µl/mL at the end of the 48th hour.

Cattaneo et al. [31] investigated the efficacy of hydroalcoholic extracts of *Rosmarinus officinalis* on human

Table 2. Statistical values of the viability of herbal oils on HUVEC cell line measured by MTT method.

C	1 µl/ml (n:3)	5 µl/ml (n:3)	50 µl/ml (n:3)	100 µl/ml (n:3)	250 µl/ml (n:3)	500 µl/ml (n:3)	p*
			Eucalyptus globules				
24. hr	0.90 ± 0.01	0.87 ± 0.02	0.94 ± 0.02	0.96 ± 0.02	0.98 ± 0.01	0.98 ± 0.02	0.021
48. hr	0.97 ± 0.01	0.85 ± 0.01	0.81 ± 0.06	0.53 ± 0.01	0.44 ± 0.01	0.12 ± 0.01	0.012
p**	< 0.001	< 0.001	< 0.001	< 0.001	< 0.001	< 0.001	
			Juniperus communis				
24. hr	1.21 ± 0.06	1.10 ± 0.03	0.90 ± 0.24	0.70 ± 0.15	0.25 ± 0.04	0.14 ± 0.02	0.012
48. hr	0.75 ± 0.01	0.60 ± 0.01	0.75 ± 0.01	0.15 ± 0.02	0.03 ± 0.01	0.06 ± 0.01	0.010
p**	< 0.001	< 0.001	> 0.05	< 0.001	< 0.001	< 0.001	
			Rosmarinus officinalis				
24. hr	1.33 ± 0.08	1.18 ± 0.06	1.15 ± 0.06	1.15 ± 0.07	1.15 ± 0.02	0.12 ± 0.01	0.079
48. hr	0.86 ± 0.02	0.73 ± 0.01	0.53 ± 0.01	0.51 ± 0.01	0.04 ± 0.02	0.07 ± 0.01	0.010
*p**	< 0.001	< 0.001	< 0.001	< 0.001	< 0.001	< 0.001	
			Thymus vulgaris				
24. hr	0.26 ± 0.13	0.13 ± 0.10	0.35 ± 0.06	0.38 ± 0.03	0.41 ± 0.02	0.46 ±0.07	< 0.001
48. hr	0.11 ± 0.08	0.13± 0.08	0.13± 0.08	0.26 ± 0.20	0.41 ± 0.20	0.46 ± 0.11	< 0.001
p**	0.005	0.005	< 0.001	0.23	0.35	0.89	

C: Concentrations

* Friedman test

** Mann-Whitney U test

melanoma A375 cell line viability by MTT and Trypan blue methods. The results showed that *R.officinalis* extract decreased cell proliferation in a time and dose-dependent manner. In our study, it was observed that the viability rate was above 100% despite the application of R.officinalis essential oil at very high doses (up to 500 µl/mL) at the end of the 24th hour, and when the exposure time was extended to 48 hours, the viability rate gradually decreased with increasing doses.

Ayesh et al. [32] investigated the effects of *Thymus vulgaris* L. ethanol extract on cellular viability and cytotoxicity by MTT and LDH methods on THP-1 leukemia cell line and freshly isolated peripheral blood mononuclear cells (PBMCs). As a result, they reported that the extract significantly reduced the number of viable THP-1 and PBMCs in a concentration-dependent manner. In our study, it was observed that *T. vulgaris* herbal oil significantly reduced the viability of the HUVEC cell line at all concentrations.

When the % cytotoxicity rates of the oils measured by the LDH method on the HUVEC cell line were compared at the 24th hour (Table 3), *Thymus vulgaris* had the highest cytotoxicity at all concentrations, and it was observed the cytotoxicity rates increased from 60% to over 75% with the increase in dose. The cytotoxicity of *Juniperus communis* and *Rosmarinus officinalis* increased with increasing concentration, but the cytotoxicity of *Eucalyptus globulus* was observed at the lowest level at all concentrations and did not exceed %10-15. Thus, at all concentrations, *Thymus vulgaris* was detected as the herbal oil with the highest cytotoxicity at the 24th hour on the HUVEC cell line. When the % cytotoxicity rates of the oils measured by the LDH method on the HUVEC cell line were compared at the 48th hour (Table 3), it was shown that the cytotoxic effects of all oils increased significantly at increasing concentrations. In this situation; *Eucalyptus globulus* at concentrations of 1,100 μl/ml; *Thymus vulgaris* at concentrations of 5,500 μl/ml; and *Rosmarinus officinalis* at concentrations of 50, 250 μl/ml on HUVEC cell line were found to have the highest toxicity at the 48th hour.

Table 3. Statistical values of cytotoxic activities of herbal oils measured by LDH method on HUVEC cell line.

C	1 μl/ml (n: 3)	5 μl/ml (n: 3)	50 μl/ml (n: 3)	100 μl/ml (n: 3)	250 μl/ml (n: 3)	500 μl/ml (n: 3)	p*
Eucalyptus globules							
24. hr	0.11 ± 0.01	0.11 ± 0.01	0.14 ± 0.01	0.10 ± 0.01	0.12 ± 0.01	0.12 ± 0.01	0.024
48. hr	0.25 ± 0.01	0.26 ± 0.01	0.35 ± 0.01	0.68 ± 0.17	0.44 ± 0.01	0.65 ± 0.01	0.019
p**	< 0.001	< 0.001	< 0.001	< 0.001	< 0.001	< 0.001	
Juniperus communis							
24. hr	0.15 ± 0.01	0.16 ± 0.01	0.17 ± 0.01	0.21 ± 0.01	0.23 ± 0.01	0.60 ± 0.01	0.012
48. hr	0.10 ± 0.01	0.16 ± 0.01	0.19 ± 0.01	0.29 ± 0.01	0.30 ± 0.01	0.57 ± 0.01	0.010
p**	0.05	0.5	0.05	0.05	0.05	0.12	
Rosmarinus officinalis							
24. hr	0.18 ± 0.01	0.21 ± 0.01	0.22 ± 0.01	0.23 ± 0.20	0.48 ± 0.01	0.63 ± 0.01	0.026
48. hr	0.14 ± 0.01	0.25 ± 0.01	0.37 ± 0.01	0.50 ± 0.01	0.64 ± 0.02	0.73 ± 0.02	0.010
p**	0.05	0.05	0.05	0.05	0.05	0.05	
Thymus vulgaris							
24. hr	0.60 ± 0.01	0.57 ± 0.01	0.65 ± 0.01	0.65 ± 0.01	0.65 ± 0.01	0.74 ± 0.01	0.017
48. hr	0.04 ± 0.01	0.43± 0.10	0.36 ± 0.01	0.66 ± 0.01	0.46 ± 0.40	0.82± 0.02	0.055
p**	0.05	0.05	0.05	0.27	0.50	0.05	

K: Concentrations

* Friedman test

** Mann-Whitney U test

Comparisons of the efficacy of herbal oils on the HUVEC cell line evaluated by MTT and LDH methods are given in Figures 1-4.

In Figure 1; the highest viability rates at 24 hours were determined on the HUVEC cell line treated with *Rosmarinus officinalis* at a concentration of 1, 5, 50, 100, 250 μl/ml and *Eucalyptus globulus* at 500 μl/ml.

In Figure 2; the highest viability rates at 48 hours were determined on the HUVEC cell line treated with *Eucalyptus globulus* at concentrations of 1, 5, 50, 100, 250 μl/ml and *Thymus vulgaris* at 500 μl/ml concentration.
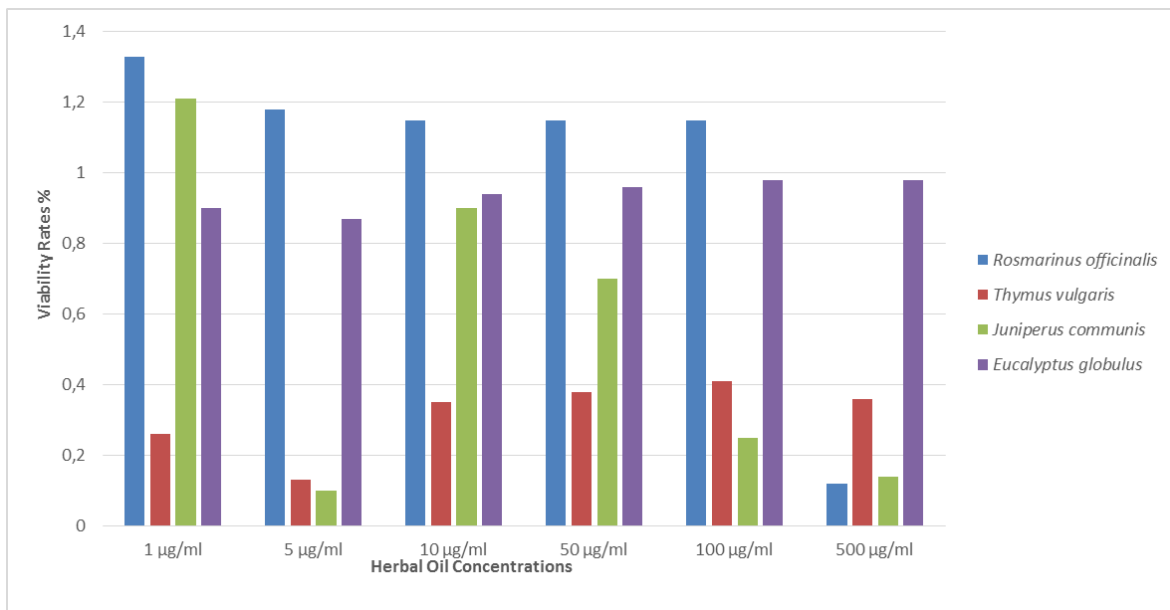
Figure 1. Comparison of the % viability of vegetable oils on HUVEC cell line at the 24th hour measured by MTT method.
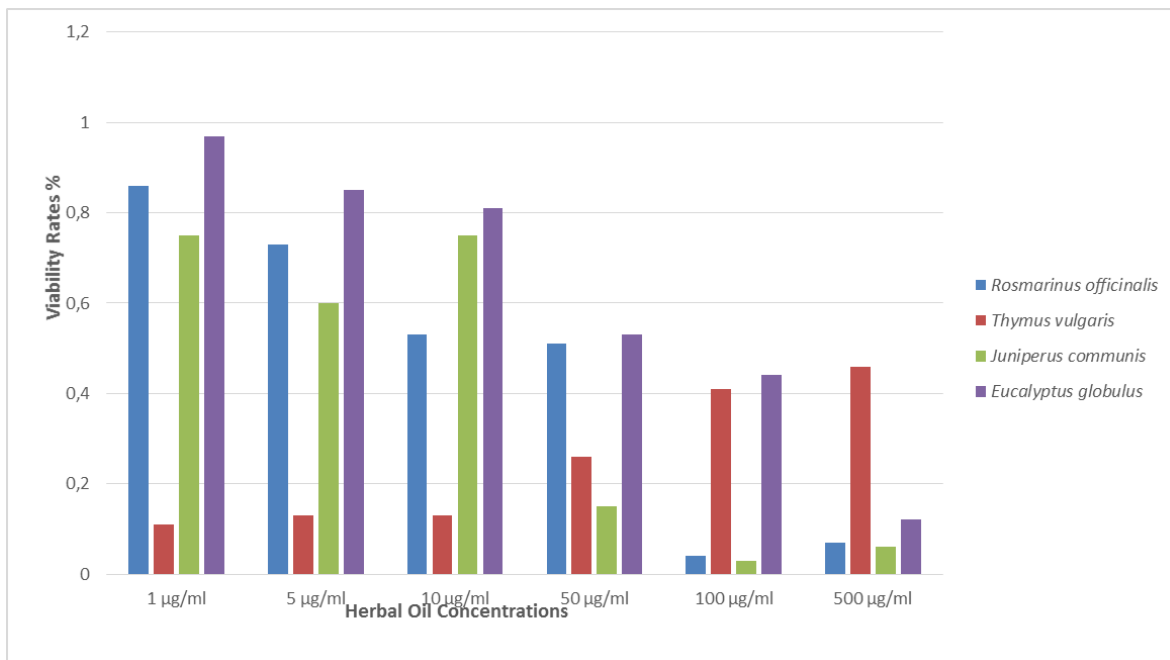
Figure 2. Comparison of the % viability of vegetable oils on HUVEC cell line at the 48th hour measured by MTT method.
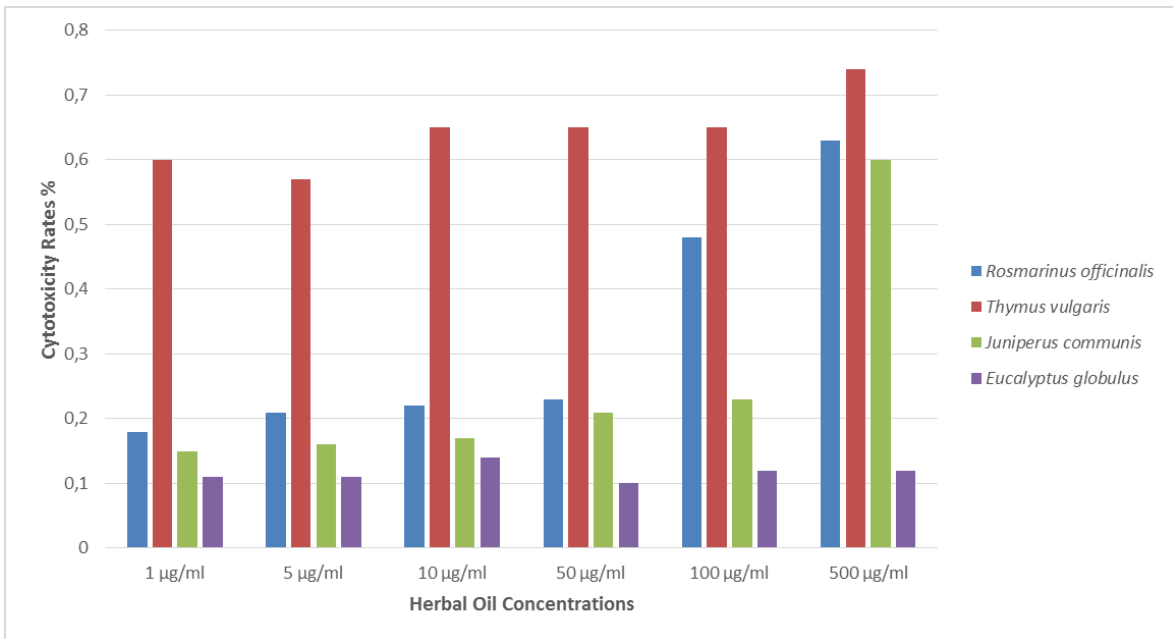
Figure 3. Comparison of % cytotoxicity rates of vegetable oils on HUVEC cell line at the 24th hour measured by LDH method.
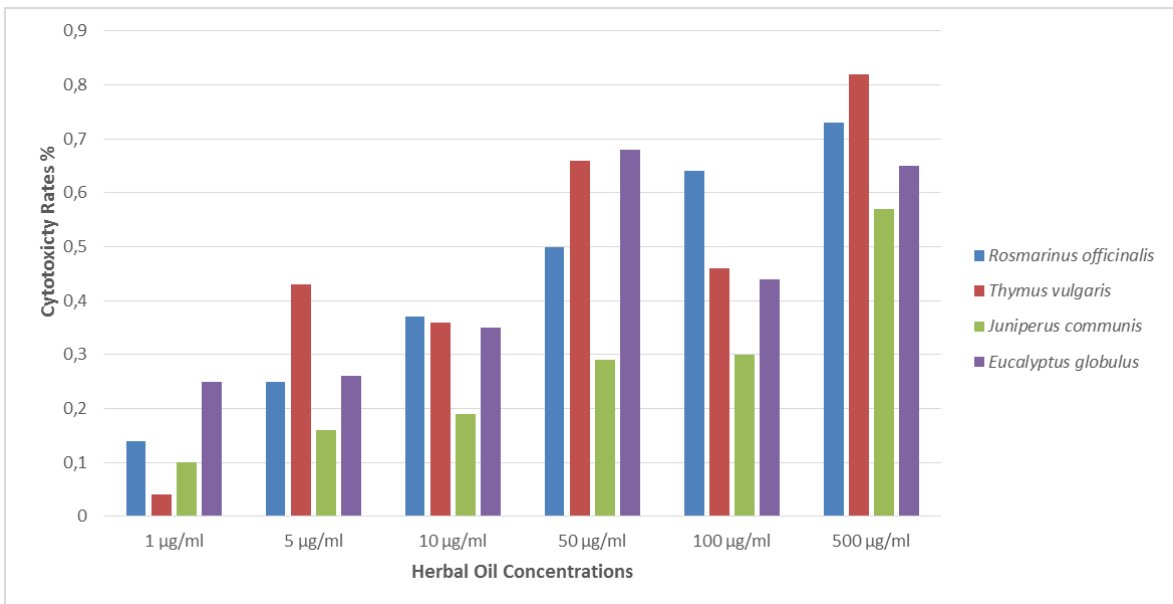
Figure 4. Comparison of % cytotoxicity rates of vegetable oils on HUVEC cell line at the 48th hour measured by LDH method.

In figure 3; at all concentrations, *Thymus vulgaris* was detected as the highest cytotoxic herbal oil against Huvec cell line at 24. hour.

In Figure 4, *Eucalyptus globulus* at concentrations of 1,100 µl/ml, *Thymus vulgaris* at concentrations of 5,500 µl/ml, and *Rosmarinus officinalis* at concentrations of 50, 250 µl/ml on HUVEC cell line were found to have the highest toxicity at 48 hours.

CONCLUSION

Vegetable oils have been used for thousands of years in food preservation, medicine, alternative medicine, and natural treatments. As a result of pharmacological studies on these vegetable oils, considering their intended use, some of their biological activities have been scientifically explained. Studies show that vegetable oils, which have a wide range of uses, have antimicrobial activities against various microorganisms. In our study, 4 different vegetable oils, which are generally known to be good for stomach and gastrointestinal system disorders and for which there are no adequate studies in the literature, were selected, and their antimicrobial activities against *H.pylori* and their cytotoxic effects on HUVEC cell line were examined. As a result, we believe that the findings of our study will contribute to the literature. The fact that *Eucalyptus globulus*, *Juniperus communis*, *Rosmarinus officinalis*, and *Thymus vulgaris*, which have been used in the treatment of gastrointestinal diseases in folk medicine for many years, have shown significant antibacterial activity against *H.pylori* constitutes very valuable findings for further research. Unlike our study, the cytotoxic effects of selected vegetable oils on healthy cell lines have not been adequately addressed in the literature.

In the light of the information we presented in our study, can be concluded that further in vitro and in vivo studies aiming to determine the efficacy and toxicity of the active chemical compounds of vegetable oils, which was found to have anti H pylori activity, on strains with different virulence, will contribute significantly to the development of adjuvant herbal medicines that will increase the eradication rates.

References

1. D. Falush, T. Wirth, J.K. Pritchard, M. Stephens, M. Kidd, M.J. Blaser, D.Y. Graham, S. Vacher, G.I. Perez-Perez, Y. Yamaoka, F. Megraud, K. Otto, U. Reichard, E. Katzowitsch, X. Wang, M. Achtman, and S. Suerbaum, Traces of human migrations in *Helicobacter pylori* populations, Science, 299 (2003) 1582-1585.

2. S.C. Goodwin, J.A. Armstrong, T. Chilvers, M. Peters, M.D. Collins, L. Sly, W. Mcconnell, and W.E.S. Harper, Transfer of *Campylobacter pylori* and *Campylobacter mustelae* to Helicobacter gen. nov. as *Helicobacter pylori* comb. nov. and *Helicobacter mustelae* comb. Nov. Respectively, Int. J. Syst. Bacteriol., 39(1989) 397-405.

3. B.J. Marshall, and J.R. Warren, Unidentified curved bacilli in the stomach of patients with gastritis and peptic ulceration, Lancet, 1 (1984) 1311-1315.

4. R.J. Hopkins, and J.G. Morris, *Helicobacter pylori*: The missing link in perspective, Am. J. Med., 97 (1994) 265-277.

5. S. Suerbaum, and P. Michetti, *Helicobacter pylori* infection, New Eng. J. Med., 347 (2002) 1175-1186.

6. M. Kidd, and I.M. Modlin, A century of *Helicobacter pylori*, Digestion, 59 (1998) 1-15.

7. J.M. Luck, and T.N. Seth, The physiology of gastric urease, Biochem. J., 19 (1925) 357-365.

8. A. Nagorni, *Helicobacter pylori* at the end of the second millenium, FU. Med. Biol., 7 (1999) 15-25

9. B.M. Gökçekuyu, *Helicobacter pylori* eradikasyonunda birinci basamak tedavide kullanılan antibiyotiklerin direnç durumları, Doktora Tezi, Dokuz Eylül Üniv. Tıp Fak., İzmir, (2011).

10. B. Shames, S. Krajden, M. Fuksa, C. Babida, J.L. Penner, Evidence for the occurrence of the same strain of *Campylobacter pylori* in the stomach and dental plaque, J. Clin. Microbiol., 27 (1989) 2849-2850.

11. P. Majmudar, S.M. Shah, K.R. Dhunjibhoy, and H.G. Desai, Isolation of *Helicobacter pylori* from dental plaques in healthy volunteers, Indian J. Gastroenterol., 9 (1990) 271-272.

12. S.A. Dowsett, L. Archila, V.A. Segreto, C.R. Gonzales, A. Silva, K.A. Vastola, R.D. Bartizek, and M.J. Kowolik, *Helicobacter pylori*: Infection in ındigenous families of Central America: Serostatus and oral and fingernail carriage, J. Clin. Microbiol., (1999) 2456–2460.

13. A. Oshowo, D. Gillam, A. Botha, M. Tunio, J. Holton, P. Boulos, and M. Hobsley, *Helicobacter pylori*: The mouth, stomach, and gut axis, Ann. Periodontol., 37 (1998) 276-280.

14. S.S. Socransky, and A.D. Haffajee, Dental biofilms: Difficult therapeutic targets, Periodontol. 2000, 28 (2002) 12–55.

15. M. Valdivieso-Ugarte, C. Gomez-Llorente, J. Plaza-Díaz, Á. Gil, Antimicrobial, Antioxidant, and Immunomodulatory Properties of Essential Oils: A Systematic Review, Nutrients, 11 (2019) 2786.

16. M. D'agostino, N. Tesse, J.P. Frippiat, M. Machouart, A. Debourgogne, Essential Oils and Their Natural, Active Compounds Presenting Antifungal Properties, Molecules, 24 (2019) 3713.

17. E. Çelik, G. Yuvalı Çelik, Bitki uçucu yağlarının antimikrobiyal özellikleri, Orlab On-Line Mikrobiyoloji Dergisi, 5 (2007) 1-6.

18. L.L. Cogo, C.L.B. Monteiro, M.D. Miguel, O.G. Miguel, M.M. Cunico, M.L. Ribeiro, E.R. Camargo, G.M.B. Kussen, K.S. Nogueira, and L.M.D. Costa, Anti-*Helicobacter pylori* activity of plant extracts traditionally used for the treatment of gastrointestinal disorders, Braz. J. Microbiol., 41 (2010) 304–309.

19. M. Kıvanç, A. Akgül, Antibacterial activities of essential oils from turkish spices and citrus, Flavour Fragr. J., 1 (1986) 175-179.

20. H. Sakkas, P. Gousia, V. Economou, V. Sakkas, S. Petsios, and C. Papadopoulou, In vitro antimicrobial activity of five essential oils on multidrug resistant Gram-negative clinical isolates, J. Intercult. Ethnopharmacol., 5(2016) 212-218.

21. G. Güzeldağ, L. Kadioglu, A. Mercimek, and F. Matyar, Preliminary examination of herbal extracts on the inhibition of *Helicobacter pylori*, Afr. J. Tradit. Complement. Altern. Med., 11 (2014) 93-96.

22. S.M. Ali, A.A. Khan, I. Ahmed, M. Musaddiq, K.S. Ahmed, H. Polasa, L.V. Rao, C.M. Habibullah, L.A. Sechi, N. Ahmed, Antimicrobial activities of Eugenol and Cinnamaldehyde against the human gastric pathogen *Helicobacter pylori*, Ann. Clin. Microbiol. Antimicrob., 4 (2005) 1-7.

23. G. Fotakis, J.A. Timbrell, In vitro cytotoxicity assays: comparison of LDH, neutral red, MTT and protein assay in hepatoma cell lines following exposure to cadmium chloride, Toxicol. Lett., 160 (2006) 171-7.

24. M.V. Berridge, P.M. Herst, A.S. Tan, Tetrazolium dyes as tools in cell biology: new insights into their cellular reduction, Biotechnol. Annu. Rev., 11 (2005) 127-152.

25. L. Su-Wen, L. Hwei-San, T. Kang-Nee, D.B. Tracey, Reduction of MTT to Purple Formazan by Vitamin E Isomers in the Absence of Cells, Trop. Life Sci. Res., 26 (2015) 111–120.

26. K.M. Sanjeev, C. Prakash, R. Seog-Woo, In vitro Models, Endpoints and Assessment Methods for the Measurement of Cytotoxicity, J. Toxicol. Environ. Health., 2 (2010) 87-93.

27. D. Esmaili, A.M. Mobarez, A. Tohidpour, Anti-*Helicobacter pylori* activities of shoya powder and essential oils of *Thymus vulgaris* and *Eucalyptus globulus*, Open Microbiol. J., 6 (2012) 65-69.

28. G.B. Mahady, S.L. Pendland, A. Stoia, F.A. Hamill, D. Fabricant, B.M. Dietz, L.R. Chadwick, In vitro susceptibilityof *Helicobacter pylori* to botanical extracts used traditionally fort he treatment of gastrointestinal disorders, Phytother. Res., 19 (2005) 988-991.

29. C. Cabral, V. Francisco, C. Cavaleiro, M.J. Gonçalves, M.T. Cruz, F. Sales, M.T. Batista, L. Salgueiro, Essential oil of *Juniperus communis* subsp. alpina (Suter) Čelak needles, chemical composition, antifungal activity and cytotoxicity, Phytother. Res., 26 (2012) 1352-1357.

30. P.M. Döll-Boscardin, A. Sartoratto, B.H.L.N.S. Maia, J.P. Paula, T. Nakashima, P.V. Farago, C.C. Kanunfre, In Vitro Cytotoxic Potential of Essential Oils of *Eucalyptus benthamii* and Its Related Terpenes on Tumor Cell Lines, Evid.-Based Complementary Altern. Med., 2012 (2012) 1-8.

31. Cattaneo, L., Cicconi, R., Mignogna, G., Giorgi, A., Mattei, M., Graziani, G., Ferracane, R., Grosso, A., Aducci, P., Schininà, M.E. and Marra, M, Anti- Proliferative Effect of *Rosmarinus officinalis* L. Extract on Human Melanoma A375 Cells. Plos One, 10 (2015) 1-18.

32. B.M. Ayesh, A.A. Abed, D.M. Faris, In vitro inhibition of human leukemia THP-1 cells by *Origanum syriacum* L. and *Thymus vulgaris* L. Extracts, BMC Res. Notes, 7 (2014) 1-6.

Research Article

Analysis of Conformational Differences of Copper and Alkali Metal Complexes of Insulin Using Trapped Ion Mobility-Mass Spectrometry Technique

Tuzaklamalı İyon Hareketliliği-Kütle Spektrometrisi Tekniği Kullanılarak İnsülinin Bakır ve Alkali Metal Komplekslerinin Konformasyonel Farklılıklarının Analizi

Mehmet Atakay[*]

Department of Chemistry, Hacettepe University, 06800, Ankara, Turkey.

ABSTRACT

Molecular recognition, protein folding, and formation of supramolecular structures that occur at the molecular level of biological processes are based on noncovalent interactions. Interactions between metal atoms and proteins are also based on noncovalent interactions that underlie the mechanisms involved in many cellular processes. The activities of enzymes are highly dependent on the interactions of such protein groups with cofactors, substrates, metal ions, and other proteins. The compositions and binding stoichiometry of protein-metal complexes can be determined with high accuracy performing mass spectrometry (MS) analysis. The conformational features of protein-metal complexes can be studied additionally using a mass spectrometer with ion mobility spectrometry (IMS) capability. This study focuses the monitoring the differences in the conformational changes of insulin protein during the formation of its complex with copper and alkali metals using trapped ion mobility spectrometry – time-of-flight (TIMS–TOF) mass spectrometer instrument. The compaction of the insulin structure by the formation of the insulin-copper complexes in the gas phase was determined with TIMS-TOF-MS analyses. However, no change was observed in the insulin structure with the addition of H, Na, and K atoms as adducts at the same analysis conditions.

Key Words

Noncovalent interactions, protein-metal complexes, conformational change, trapped ion mobility-mass spectrometry.

ÖZ

Moleküler tanıma, protein katlanması ve supramoleküler yapıların oluşumu gibi moleküler düzeyde meydana gelen biyolojik süreçler kovalent olmayan etkileşimlere dayanır. Metal atomları ve proteinler arasındaki etkileşimler de birçok hücresel süreçte yer alan mekanizmaların temelini oluşturan kovalent olmayan etkileşimlere dayanmaktadır. Enzimlerin aktiviteleri, bu tür protein gruplarının kofaktörler, substratlar, metal iyonları ve diğer proteinlerle olan etkileşimlerine büyük ölçüde bağlıdır. Protein-metal komplekslerinin bileşimi ve bağlanma stokiyometrileri, yüksek doğrulukta kütle spektrometrik (MS) analiz ile belirlenebilir. Protein-metal komplekslerinin konformasyonel özellikleri ise iyon hareketliliği spektrometrisi (IMS) özelliğine sahip bir kütle spektrometresi kullanılarak ek olarak incelenebilmektedir. Bu çalışmada tuzaklamalı iyon hareketliliği spektrometrisi - uçuş zamanlı (TIMS-TOF) kütle spektrometresi kullanılarak bakır ve alkali metallerle komplekslerinin oluşumu sırasında insülin proteininin konformasyonel değişimlerindeki farklılıkların izlenmesine odaklanılmaktadır. İnsülin-bakır komplekslerinin oluşmasıyla insülin yapısının gaz fazında daha kompakt hale geldiği TIMS-TOF-MS analizleri ile belirlenmiştir. Ancak aynı analiz koşullarında H, Na ve K atomlarının eklenmesiyle insülin yapısında herhangi bir değişiklik gözlenmemiştir.

Anahtar Kelimeler

Kovalent olmayan etkileşimler , protein-metal kompleksleri, konformasyonel değişim, tuzaklamalı iyon hareketliliği-kütle spektrometrisi.

INTRODUCTION

Metal ions interact with proteins and form metal-protein complexes in many biological processes. Such processes, which include folding and stabilizing protein structures and acquiring their biological functions, take place in the presence of metal ions [1]. Besides the formation of coordination complexes between metals and proteins, there are also complex formations based on noncovalent interactions such as hydrogen bonding, π-stacking, and hydrophobicity [2]. Protein structures can undergo structural changes specific to the interaction sites for target recognition by forming complexes with metals [3]. Proteins can interact with metals through functional groups such as amine, hydroxyl, phosphate, sulfonate, and carboxylic acid located in their structures. The amine groups at the N-terminus of the protein chains and the carboxylic acid groups at the C-terminus are also potential binding sites for metals [4]. Complexes involving such interactions are characterized by various analytical techniques such as calorimetry, X-ray crystallography, circular dichroism, and nuclear magnetic resonance spectroscopy. In addition to the analytical advantages of these techniques, they also have some shortcomings in the analysis of noncovalent complexes. The necessity for large amounts of samples, long analysis times, complicated interpretation of data due to the interference of signals, the problems encountered in the crystallization of such samples, and the inability to detect complexes using spectroscopic methods are the most prominent shortcomings of these techniques [5-6]. Mass spectrometry (MS) techniques that allow monitoring such interactions with high accuracy and sensitivity can produce ionic species in their both native and gas-phase forms during or after the ionization. In fact, with the development of soft ionization techniques in MS, analyses can be performed to preserve noncovalent interactions in complex structures while transferring from the solution to the gas phase [7-8]. Strong interactions between metal ions and biomolecules in the solution phase are generally not disrupted during electrospray ionization (ESI) [9]. The preservation of the structures of metal-protein complexes based on noncovalent interactions during the soft ionization process makes it possible to analyze these species in their intact forms. The bonding ratios and stoichiometry of the complexes formed due to noncovalent interactions of metals and proteins can be determined by evaluating the mass spectra obtained from the ESI-MS analysis [10-11]. Conformational chan-

ges resulting from the binding of metals to proteins can be monitored using the ion mobility-mass spectrometry (IM-MS) technique. The ion mobility units of the IM-MS instruments separate the ions into different ion packets according to their arrival time differences in the gas phase depending on their collision cross section (CCS) values [4]. Such problems in previously mentioned analytical techniques are not encountered in IM-MS analyses. Thus, IM-MS has become prominent among other analytical techniques in the structural analysis of protein-metal complexes.

In this study, the noncovalent complexes of the insulin protein with copper and alkali metals were compared and analyzed in terms of changes in protein's conformational features using the trapped ion mobility spectrometry – time-of-flight – mass spectrometry (TIMS-TOF-MS) technique. Copper is an essential trace element in several redox processes in living organisms. Trace elements which are very important for many biological activities, regulate many physiological reactions by forming complexes with biomolecules [12]. Many living organisms use a certain amount of copper metal to survive and maintain their physiological functions correctly [13]. It is an essential metal ensuring the correct functioning of the proteins and enzymes in the vital biological pathways. It must also be included in metabolic processes to functionalize many enzymes in organisms [12, 14]. Insulin is a hormone that consists of 51 amino acids and is secreted from the pancreas in the body [15]. It regulates glucose, protein, and fat metabolisms in the blood [16]. Proper functioning of insulin metabolism is vital for human health and this metabolism needs to be regulated for patients with diabetes. Insulin commonly forms complexes with metals such as copper, magnesium, sodium, and potassium, in addition to zinc and calcium [17-18]. Pancreatic β-cells within these metabolic activities form insulin-zinc coordination complexes [19]. Group I and II metal ions such as K^+, Na^+, Ca^{2+}, and Mg^{2+} are also involved in insulin secretion from pancreatic β-cells [20].

MATERIALS and METHODS

Chemicals

Insulin human, copper (II) nitrate hydrate (99.999% trace metals basis), methanol, and water (LC-MS grade) were purchased from Sigma-Aldrich (St Louis, MO, USA). The mass and mobility calibration of methods were performed using the standard tune mixture purchased from Agilent Technologies (Santa Clara, CA, USA).

Trapped Ion Mobility-Mass Spectrometry Analyses

Trapped Ion Mobility Spectrometry − Time-of-Flight (TIMS−TOF) mass spectrometer (Bruker Daltonics, Bremen, Germany) was used in mass spectrometry (MS) and ion mobility-mass spectrometry (IM-MS) analyses of insulin and insulin- copper (II) nitrate mixtures. TIMS technique applies an electric field in a funnel to keep ions in a gas flow. Following the ion trapping event, the electric field is gradually reduced by decreasing voltage to allow sequential elution of trapped ions with ascending mobilities [20].

Insulin human protein was dissolved in water at 0.5 mg/mL concentration. The protein solution was diluted with water:methanol mixture (7:3, v/v) to 0.01 mg/mL final concentration prior to TIMS−TOF-MS analyses. Copper (II) nitrate solution was also prepared in water at 1.0 mg/mL concentration. Then, 1.0 μL of the copper (II) nitrate solution was added to the insulin solution before TIMS-TOF-MS analyses. The sample solutions were directly infused into the ESI source at a flow rate of 3.0 μL/min. MS and IM-MS analyses were performed using the following ESI source settings: 4500 V capillary voltage, 0.5 bar nebulizer gas pressure, 4.0 L/min drying gas flow, and 150 °C drying gas temperature. TIMS parameter settings: IMS ramp start: 0.50 V.s/cm², ramp end

2.00 V.s/cm²; ramp time 350 ms; ΔV deflection transfer and capillary exit: 20 V, funnel 1 and deflection transfer: 120 V, ramp start and accumulation exit: 120 V. Nitrogen was used as source gas which is filled in the TIMS unit of the instrument. The mass and mobility calibrations were performed externally using the Agilent ESI-L Low Concentration Tuning Mix [22-23]. DataAnalysis 5.0 software provided by Bruker was used for processing the acquired data.

RESULTS and DISCUSSION

Insulin protein has a molecular weight of approximately 5.7 kDa and contains two chains linked by two disulfide bonds in its structure [24]. The signals of multiply charged ions of the insulin protein are obtained in the mass spectrum as a result of ESI-MS analysis of insulin in the positive ion mode. The m/z values of the signals observed in the mass spectrum generally vary depending on the charge states of the ions formed in the gas phase. The net charges of the ions in the gas phase differ according to the number of protons or metal atoms adducted to the protein structure.
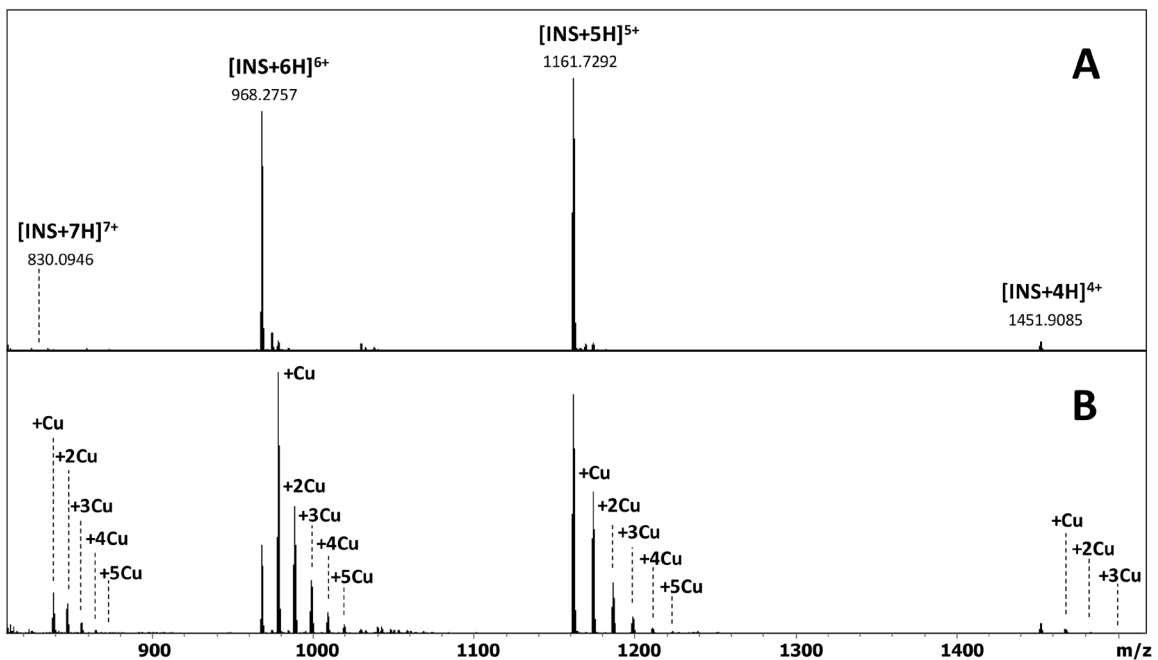
Figure 1. ESI mass spectra of (A) Insulin (B) Insulin with the addition of Cu(NO$_3$)$_2$. The numbers of attached Cu atoms to insulin are indicated for each peak in the mass spectrum.

Table 1. The m/z list of obtained ions in the TIMS-TOF-MS analyses of insulin and its mixture with Cu(NO$_3$)$_2$ between 4+ and 7+ charge states.

7+						
INS + 7H	INS + 6H + Na	INS + 6H + K	INS + 5H + Na + K	INS + 5H + 2K	INS + 4H + Na + 2K	INS + 3H + 2Na + 2K
830.0946	833.2323	835.5153	838.6562	840.9356	844.0789	847.214

INS + Cu		INS + 2Cu		INS + 3Cu	INS + 4Cu		INS + 5Cu
838.7953		847.4976		856.3426	865.0437		874.0313

6+						
INS + 6H	INS + 5H + Na	INS + 5H + K	INS + 4H + Na + K	INS + 4H + 2K	INS + 3H + Na + 2K	INS + 3H + 3K
968.2757	971.9408	974.6005	978.2634	980.9256	984.5878	987.2500

INS + Cu		INS + 2Cu		INS + 3Cu	INS + 4Cu		INS + 5Cu
978.4267		988.5789		998.7314	1009.0504		1019.2023

5+						
INS + 5H	INS + 4H + Na	INS + 4H + K	INS + 3H + Na + K	INS + 3H + 2K	INS + 2H + Na + 2K	INS + 2H + 3K
1161.7292	1166.1269	1169.3200	1173.7143	1176.9083	1181.3046	1184.4981

INS + Cu		INS + 2Cu		INS + 3Cu	INS + 4Cu		INS + 5Cu
1173.9100		1186.0929		1198.2752	1210.6593		1223.2418

4+						
INS + 4H	INS + 3H + Na	INS + 3H + K	INS + 2H + Na + K	INS + 2H + 2K	INS + H + Na + 2K	INS + H + 3K
1451.9085	1457.4058	1461.3972	1466.8898	1470.8836	1476.3755	1480.3865

INS + Cu			INS + 2Cu			INS + 3Cu	
1467.1353			1482.6146			1498.0901	

Firstly, human insulin was analyzed in the study in the positive ion mode by the ESI-MS technique without adding any acid or salt. In the mass spectrum obtained from these ESI-MS analyses, signals of the insulin protein ions having charges between 4+ and 7+ were observed (Figure 1). When the signal intensities in the ESI-MS spectrum, which are directly proportional to the relative abundances of the ions, are compared, it is seen that the signal intensities of 5+ (m/z 1161.7292) and 6+ (m/z 968.2757) charged ions of the insulin protein are much higher than the signal intensities of 4+ (m/z 1451.9085) and 7+ (m/z 830.0946) charged ions in the ESI mass spectrum (Figure 1A). In the same mass spectrum, signals of Na+ and K+ adduct ions are also observed at low intensity. Numbers and types of adducted atoms with corresponding m/z ratios of the ions observed at different charge states are given in Table 1.

When the insulin sample was analyzed after mixing with Cu(NO$_3$)$_2$ salt, it was observed in the obtained ESI-MS spectrum that different numbers of Cu atoms were attached to the insulin protein structure in the 4+ / 7+ charge state range (Figure 1B). These signals observed in the mass spectrum indicate that different numbers of copper atoms can bind to the insulin structure in the gas phase. While up to five copper atoms were bound to insulin at 5+, 6+, and 7+ charge states, maximum of three copper atoms could attach to the same protein in lower charge states (e.g., 4+ charge state). The numbers of attached copper atoms with corresponding m/z ratios of copper adduct ions observed at different charge states are also given in Table 1.

Ion mobility-mass spectrometry (IM-MS) analyses were also performed for the same samples. In IM-MS analyses, ion mobility diagrams are acquired, in which the mobility (1/K$_0$) and m/z data are located on the y- and x-axis, respectively. In these diagrams, the signal intensities of the ions are expressed by choosing an appropriate color range. Areas appearing in light color on the diagram indicate higher signal intensity. The signals of the 4+ and 7+ charged insulin ions are observed as straight linear lines extending from the corresponding mobility ranges in the ion mobility diagram obtained from the TIMS-TOF-MS analyses of the insulin sample (Figure 2A). It can be noticed that the signals of alkali metal adduct insulin ions form partial lines towards the upper right corners of the linear lines corresponding to each charge

state at higher mobility values. (Figure 2A). This data indicates that the protein structure expands as expected due to the increase in m/z value with the addition of alkali metal atoms to the insulin structure.

Signals of copper adduct protein ions were also observed in the ion mobility diagrams obtained from IM-MS analyses after the addition of $Cu(NO_3)_2$ salt to the insulin sample. (Figure 2B). This diagram shows signals belonging to copper adduct insulin ions in the 4+ and 7+ charge range as straight linear lines extending through their

corresponding mobility ranges. It can be seen in Figure 2B that ions with higher numbers of copper atoms in their structure form lines towards the lower right corner with lower mobility values, depending on the change in the number of copper atoms in the copper adduct ions. The m/z values of the total structures increase due to the binding of copper atoms to the insulin protein. The fact that this increase in the m/z values of the ions corresponds to the decrease in their mobility ($1/K_0$) indicates that the structures become more compact in the gas phase due to copper atom binding.
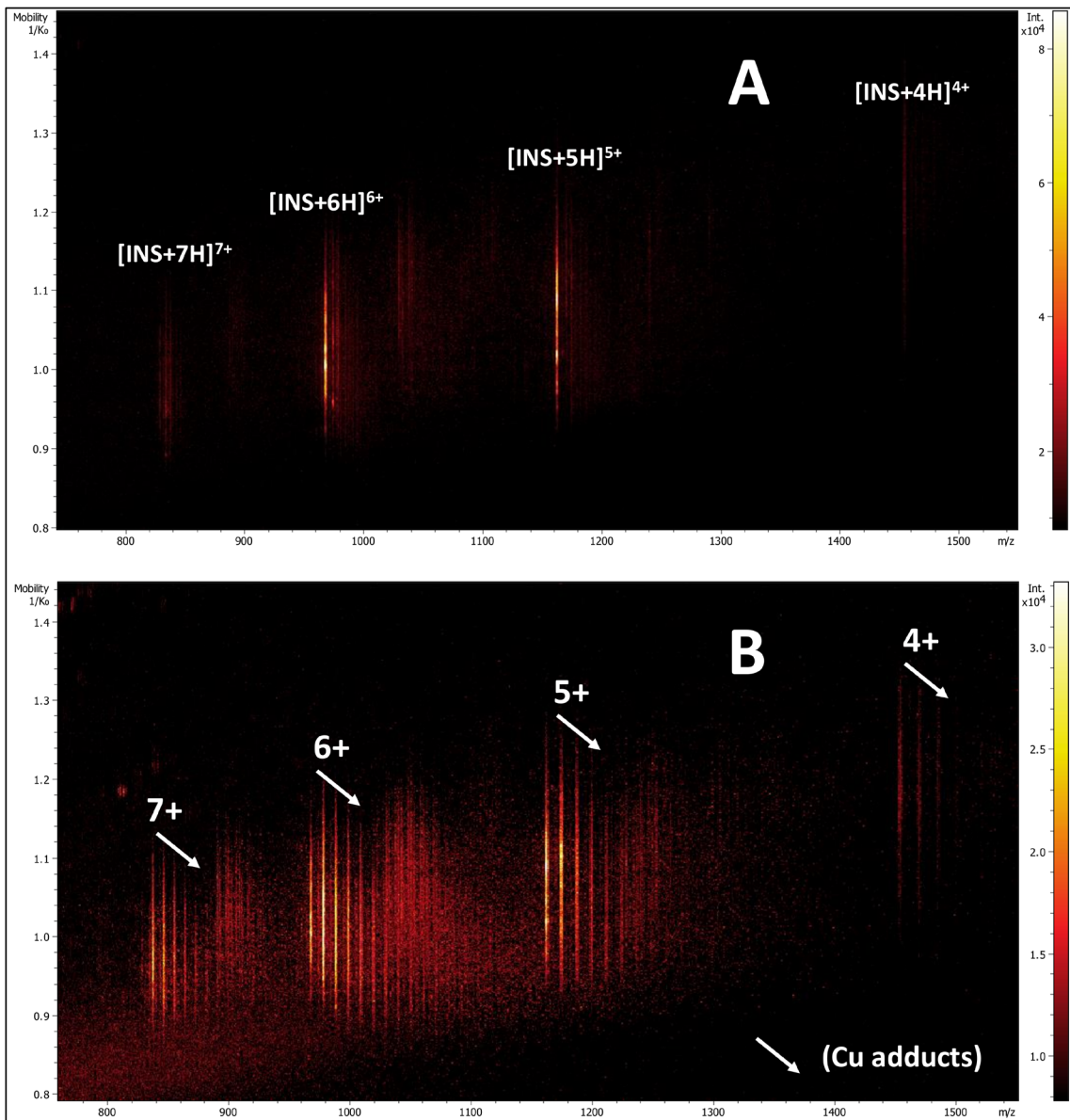
Figure 2. 2D TIMS-MS contour plots of (A) human insulin (B) human insulin with the addition of $Cu(NO_3)_2$. White arrows show the Cu adducts of the insulin ions between 4+ and 7+ charge states.

The mobility values in the data obtained from the ion mobility diagrams were converted to CCS values according to the Mason-Schamp equation [25-26]. The y-axis is proportional to the relative abundances of the ions, while the x-axis corresponds to the CCS (Å²) values in the plots obtained after the conversion. The shifts of the curves in these plots on the CCS axis (x-axis) make it possible to determine the extent to which the analyzed species contains compact or extended forms in the gas phase and to monitor the formation of these conformers. Extracted ion mobilograms of various copper adduct insulin ions between 4+ and 7+ charged states obtained from TIMS-TOF-MS analyzes are given in Figu-

re 3A-D. The conformational change in each charge state is evaluated individually. At the highest charge state (7+ charge state), it is seen that the CCS value of the structure decreases significantly as the number of copper atoms attached to the insulin structure increases (Figure 3A). This plot shows that the green-colored curve (INS+5Cu) has a higher intensity signal in the lower CCS region compared to the other curves. It is seen that the curve intensity increases in this compact CCS region from the black-colored curve (INS+Cu) to the green-colored curve (INS+5Cu). This data shows that with the addition of copper atoms to the insulin structure, the abundance of the compact form of the structure incre-
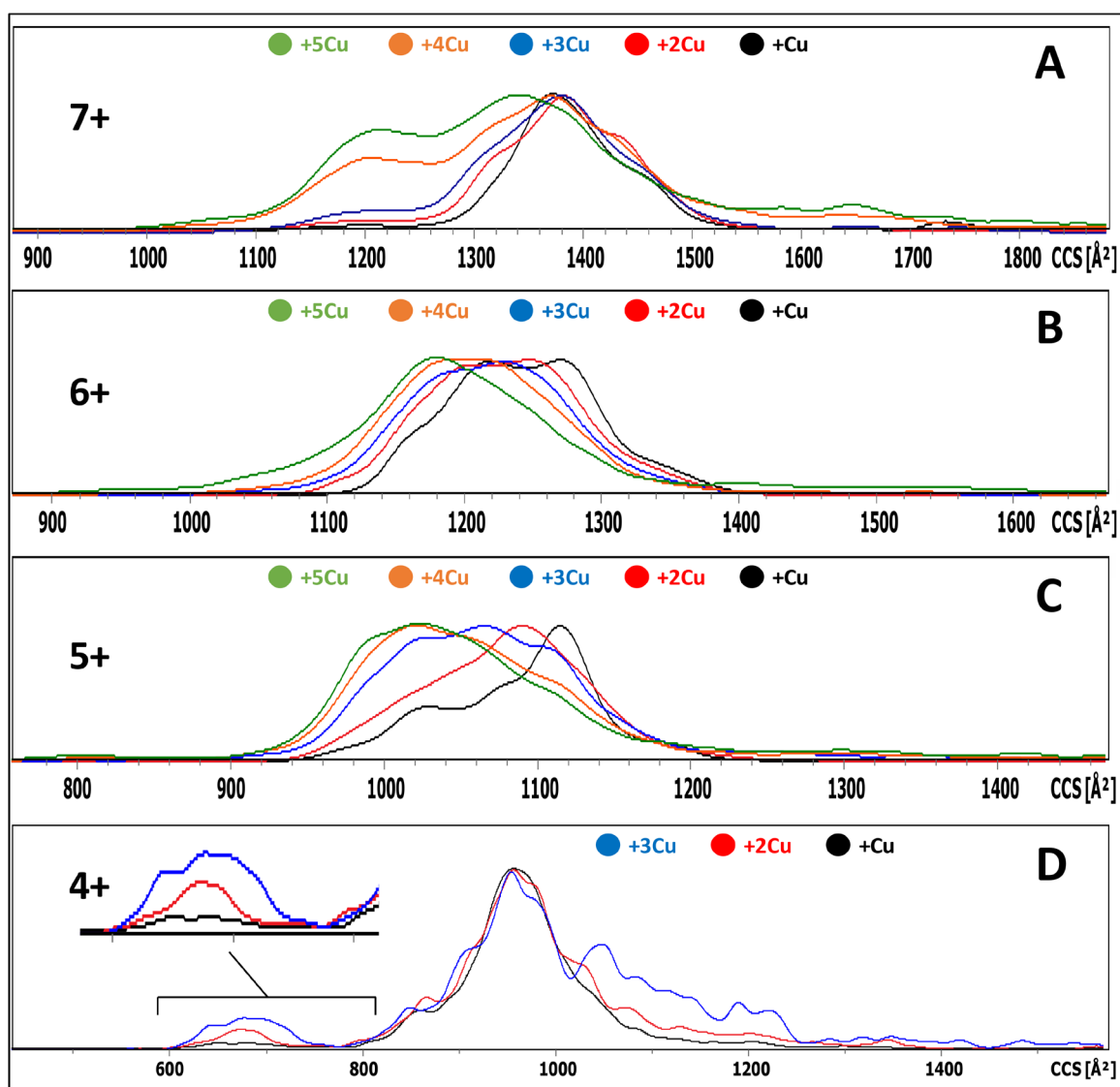
Figure 3. Extracted ion mobilograms of various Cu adducts of insulin ions between 4+ and 7+ charged states obtained from TIMS-TOF-MS analyses (A-D). The numbers of attached Cu atoms to insulin protein are shown at each set of mobilograms with their correlated colors.

ases significantly at the 7+ charge state. These nonspecific interactions between metals and proteins usually cause the compaction of the proteins in the gas phase [27-28]. Similarly, in the 6+ and 5+ charge states, the curves shifted to lower CCS values as the copper atom binds to the insulin protein, indicating that the addition of the copper atom makes the protein more compact in the gas phase (Figures 3B and 3C).

It is expected that the addition of copper atoms carrying extra charge to the protein will be less tolerated by the protein at the lowest charge state (4+ charge state). For this reason, the mobilograms obtained in this charge state, where only three copper atoms can be added to the insulin protein, are given in Figure 3D. The signals having lower intensity could be obtained at this lower charge state compared to the others due to the lower stability of the copper adduct protein ions. Therefore, it is more difficult to notice conformational changes from the signals in the mobilograms obtained at this charge state. It is seen that the signal intensities at lower CCS values increase due to the increase in the number of copper atoms attached to the protein from the black-colored curve (INS+Cu) to the blue-colored curve (INS+3Cu) (Figure 3D). This data also supports the inference that copper atom bonding increases the relative abundance of the compact form of the insulin protein in the gas phase.
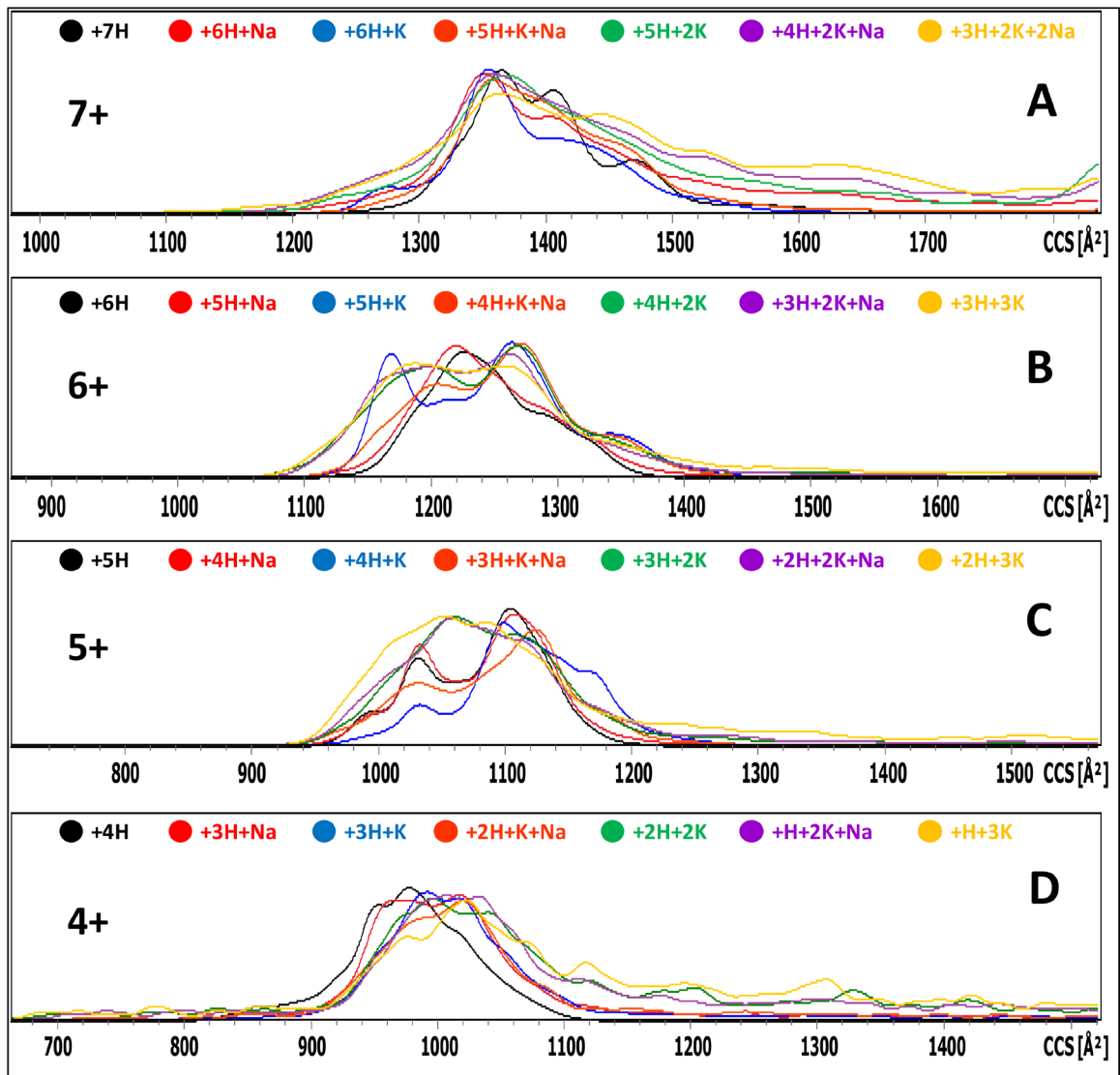
Figure 4. Extracted ion mobilograms of various H, Na, and K adducts of insulin ions between 4+ and 7+ charged states obtained from TIMS-TOF-MS analyses (A-D). The numbers of attached H, Na, and K atoms to insulin protein are shown at each set of mobilograms with their correlated colors.

MS analyses performed in positive ion mode have a high probability of binding sodium and potassium alkali metals to the analytes. The alkali metal adduction can be observed even at very low salt levels. In contrast, at higher salt concentrations, it can cause the presence of dominant signals of adducted ions in the mass spectrum. Especially in ESI-MS analyses that provide multiply charged ion formation, it is highly probable that more than one sodium and potassium ions bind to a single species even in a very low amount of salt. The formation of ions by binding alkali metals to peptides and proteins can also cause changes in the conformation of these species in the gas phase [29]. The insulin protein was analyzed by the IM-MS technique without adding any metal salt to the sample. Thus, the signals of H, Na, and K adduct protein ions with different combinations of these atoms were also evaluated for conformational analysis. The mobilograms obtained for these ions at different charge states are given in Figure 4A-D. The different colored extracted ion mobilograms of various H, Na, and K adduct insulin ions between 4+ and 7+ charged states obtained from TIMS-TOF-MS analyses are evaluated on the CCS axis (x-axis) of the mobilograms depending on different numbers and types of adduct atoms. It is seen that they do not show apparent shifts in the corresponding x-axis (Figure 4 A-D). In addition, no significant change was detected in the intensities of the curves in the mobilograms at both low and high CCS values corresponding to the compact and extended forms of the protein, respectively. The IM-MS data containing these signals with random distributions show that no obvious conformational change in the insulin protein structure occurs with the addition of H, Na, K atoms, and their different combinations. In some cases, the addition of such atoms increases the CCS value slightly with the increase in molecular mass, but it does not even cause a net change in the CCS value.

The data in the mobilograms given in Figures 3 and 4 are obtained under the same analysis conditions. According to these mobilograms, it was determined that the protein-metal complexes formed as a result of the nonspecific binding of copper atoms (monoisotopic mass of Cu: 62.9296 Da) to the insulin protein became more compact than the single insulin protein in the gas phase. However, there is no change in the protein structure such as compaction as a result of the addition of atoms such as H (1.0078 Da), Na (22.9898 Da), and K (38.9637 Da), which are smaller than the copper atom. These results showed that copper metal and alkali metals interact with insulin protein in different ways in the gas phase and this difference can be monitored through conformational changes with IM-MS analysis [30-31].

Conclusion

Mass spectrometry techniques that allow monitoring noncovalent interactions with high accuracy and sensitivity can produce ionic species in their intact forms during or after ionization. Various types of ionic species of the same sample can be transferred to the mass analyzer by performing ionization, where many parameters are effective. As a result of these ionization processes, protonation or metal ion adduction may occur according to the chemical environment of the analyte. In MS analyses, metal complex structures are detected due to ion-ion/ion-neutral interactions occurring in the gas phase. Therefore, analyzing the formation and conformational features of such dynamic metal inclusion complexes requires reliable analytical methods with high sensitivity. The ESI-MS technique provides many advantages over other biophysical techniques, especially high sensitivity and speed, in the characterization of biological complexes containing noncovalent interactions. In addition, mass spectrometry enables direct determination of m/z values with high accuracy, making it possible to determine the compositions and stoichiometry of complexes. Besides determining the chemical structures of the noncovalent complexes, conformational features of the complexes and changes in their shape during the complex formation can also be monitored dynamically using the IM-MS technique. The IM-MS instruments provide conformational data by performing the characterization of the analytes according to their masses, charge states, and shapes simultaneously in the gas phase. The signals of protonated ions were dominant with the presence of Na+ and K+ adduct ion signals in the ESI mass spectrum obtained in this study from the IM-MS analysis of human insulin in the positive ion mode. The IM-MS data indicated no noticeable conformational change in the structure of the insulin protein with the binding of H, Na, K atoms and their different combinations. Signals of copper adduct insulin ions from 4+ to 7+ charge states were observed in the ESI mass spectrum obtained from IM-MS analysis after the addition of $Cu(NO_3)_2$ salt to the insulin sample. The shift of extracted ion mobilograms of copper adduct insulin ions to lower CCS values with the addition of copper atoms to the insulin structure proves that the abundance of the compact form of the insulin increases in the gas phase. The data obtained from the

IM-MS analyses of insulin-metal complexes show that alkali metals and copper bind to insulin by different mechanisms. The changes in the protein conformation caused by the attachment of various metals to the insulin protein can be distinguished with high sensitivity and accuracy by performing IM-MS analyses.

References

1. C.M. Crittenden, E.T. Novelli, M.R. Mehaffey, G.N. Xu, D.H. Giles, W.A. Fies, K.N. Dalby, L.J. Webb, J.S. Brodbelt, Structural Evaluation of Protein/Metal Complexes via Native Electrospray Ultraviolet Photodissociation Mass Spectrometry, J Am Soc Mass Spectrom 31(5) (2020) 1140-1150.

2. E. Meggers, From conventional to unusual enzyme inhibitor scaffolds: the quest for target specificity, Angewandte Chemie International Edition 50(11) (2011) 2442-2448.

3. S.J. Archibald, R. Smith, Protein-Binding Metal Complexes: Noncovalent and Coordinative Interactions, Comprehensive Inorganic Chemistry II2013, pp. 661-682.

4. L.A. Angel, Study of metal ion labeling of the conformational and charge states of lysozyme by ion mobility mass spectrometry, Eur J Mass Spectrom (Chichester) 17(3) (2011) 207-15.

5. N. Potier, H. Rogniaux, G. Chevreux, A. Van Dorsselaer, Ligand–Metal Ion Binding to Proteins: Investigation by ESI Mass Spectrometry, Biological Mass Spectrometry2005, pp. 361-389.

6. A.B. Ilesanmi, T.C. Moore, L.A. Angel, pH dependent chelation study of Zn(II) and Ni(II) by a series of hexapeptides using electrospray ionization – Ion mobility – Mass spectrometry, International Journal of Mass Spectrometry 455 (2020).

7. J.A. Loo, R.R.O. Loo, H.R. Udseth, C.G. Edmonds, R.D. Smith, Solvent-induced conformational changes of polypeptides probed by electrospray-ionization mass spectrometry, Rapid Communications in Mass Spectrometry 5(3) (1991) 101-105.

8. S.K. Chowdhury, V. Katta, B.T. Chait, An electrospray-ionization mass spectrometer with new features, Rapid Communications in Mass Spectrometry 4(3) (1990) 81-87.

9. E.N. Yousef, L.A. Angel, Comparison of the pH-dependent formation of His and Cys heptapeptide complexes of nickel(II), copper(II), and zinc(II) as determined by ion mobility-mass spectrometry, J Mass Spectrom 55(3) (2020) e4489.

10. J.A. Loo, Studying noncovalent protein complexes by electrospray ionization mass spectrometry, Mass spectrometry reviews 16(1) (1997) 1-23.

11. S. Banerjee, S. Mazumdar, Electrospray ionization mass spectrometry: a technique to access the information beyond the molecular weight of the analyte, International journal of analytical chemistry 2012 (2012).

12. R. Mukherjee, The bioinorganic chemistry of copper, (2003).

13. Z. Zhang, H. Wang, M. Yan, H. Wang, C. Zhang, Novel copper complexes as potential proteasome inhibitors for cancer treatment (Review), Mol Med Rep 15(1) (2017) 3-11.

14. H. Tapiero, D.á. Townsend, K. Tew, Trace elements in human physiology and pathology. Copper, Biomedicine & pharmacotherapy 57(9) (2003) 386-398.

15. Z. Fu, E. R Gilbert, D. Liu, Regulation of insulin synthesis and secretion and pancreatic Beta-cell dysfunction in diabetes, Current diabetes reviews 9(1) (2013) 25-53.

16. A.R. Saltiel, C.R. Kahn, Insulin signalling and the regulation of glucose and lipid metabolism, Nature 414(6865) (2001) 799-806.

17. M. Gülfen, A. Özdemir, J.L. Lin, C.H. Chen, Investigation of non-covalent complexations of Ca (II) and Mg (II) ions with insulin by using electrospray ionization mass spectrometry, Rapid Communications in Mass Spectrometry 30(19) (2016) 2171-2182.

18. M. Gülfen, A. Özdemir, J.-L. Lin, C.-H. Chen, Quantifying Na (I)-insulin and K (I)-insulin non-covalent complexes by ESI–MS method and calculation of their equilibrium constants, International Journal of Biological Macromolecules 103 (2017) 910-918.

19. M.F. Dunn, Zinc–ligand interactions modulate assembly and stability of the insulin hexamer–a review, Biometals 18(4) (2005) 295-303.

20. M. Gulfen, A. Ozdemir, C.H. Chen, Monitoring Silver(I)-Insulin Complexes with Electrospray Ionization Quadrupole Ion Trap Mass Spectrometry, J Am Soc Mass Spectrom (2021).

21. J.M. Spraggins, K.V. Djambazova, E.S. Rivera, L.G. Migas, E.K. Neumann, A. Fuetterer, J. Suetering, N. Goedecke, A. Ly, R. Van de Plas, High-performance molecular imaging with MALDI trapped ion-mobility time-of-flight (timsTOF) mass spectrometry, Analytical chemistry 91(22) (2019) 14552-14560.

22. C.G. Vasilopoulou, K. Sulek, A.-D. Brunner, N.S. Meitei, U. Schweiger-Hufnagel, S.W. Meyer, A. Barsch, M. Mann, F. Meier, Trapped ion mobility spectrometry and PASEF enable in-depth lipidomics from minimal sample amounts, Nature communications 11(1) (2020) 1-11.

23. L.V. Tose, P. Benigni, D. Leyva, A. Sundberg, C.E. Ramirez, M.E. Ridgeway, M.A. Park, W. Romao, R. Jaffe, F. Fernandez-Lima, Coupling trapped ion mobility spectrometry to mass spectrometry: trapped ion mobility spectrometry-time-of-flight mass spectrometry versus trapped ion mobility spectrometry-Fourier transform ion cyclotron resonance mass spectrometry, Rapid Commun Mass Spectrom 32(15) (2018) 1287-1295.

24. M. Weiss, D.F. Steiner, L.H. Philipson, Insulin biosynthesis, secretion, structure, and structure-activity relationships, (2015).

25. M.E. Ridgeway, M. Lubeck, J. Jordens, M. Mann, M.A. Park, Trapped ion mobility spectrometry: A short review, International Journal of Mass Spectrometry 425 (2018) 22-35.

26. E.A. Mason, E.W. McDaniel, Transport properties of ions in gases, Wiley Online Library1988.

27. T. Wyttenbach, M. Grabenauer, K. Thalassinos, J.H. Scrivens, M.T. Bowers, The effect of calcium ions and peptide ligands on the relative stabilities of the calmodulin dumbbell and compact structures, The Journal of Physical Chemistry B 114(1) (2010) 437-447.

28. T.G. Flick, S.I. Merenbloom, E.R. Williams, Effects of metal ion adduction on the gas-phase conformations of protein ions, Journal of the American Society for Mass Spectrometry 24(11) (2013) 1654-1662.

29. T. Solouki, R. Fort, A. Alomary, A. Fattahi, Gas phase hydrogen deuterium exchange reactions of a model peptide: FT-ICR and computational analyses of metal induced conformational mutations, Journal of the American Society for Mass Spectrometry 12(12) (2001) 1272-1285.

30. E.M. Martin, F.D. Kondrat, A.J. Stewart, J.H. Scrivens, P.J. Sadler, C.A. Blindauer, Native electrospray mass spectrometry approaches to probe the interaction between zinc and an anti-angiogenic peptide from histidine-rich glycoprotein, Scientific reports 8(1) (2018) 1-13.

31. A. Noor, S. Qayyum, F. Jabeen, A.U. Rehman, Mononuclear Tricoordinate Copper (I) and Silver (I) Halide Complexes of a Sterically Bulky Thiourea Ligand and a Computational Insight of Their Interaction with Human Insulin, Molecules 27(13) (2022) 4231.

Research Article

Benchmarking Polymeric Cryogels for Immobilized Metal Affinity Chromatography

Immobilize Metal Afinite Kromatografisi için Polimerik Kriyojellerin Karşılaştırması

Yeşeren Saylan

Hacettepe University, Department of Chemistry, Ankara, Turkey.

ABSTRACT

Cryogels are polymers prepared in frozen milieu, and garnered significant attention in the field as new separation matrices. They have denoted significant benefits including supermacroporosity, short diffusion path, low pressure, and resistance for both adsorption and elution. Macro- and connected pores give polymeric cryogels a unique spongy structure. Immobilized metal affinity chromatography (IMAC) is a standard analytical separation method for the purification of biomolecules. Several transition ions generate stable complexes with electron-rich compounds. IMAC sorbent is obtained by complexing first-order transition metal ions over chelating agents. On the other hand, lysozyme is an enzyme found in various vertebrate cells and secretions. Common applications include its use as a cell disrupting agent, as an anti-bacterial agent, as a meal additive, and as a medicine against infections and ulcers. In this study, cryogel-based polymeric material was prepared by free-radical polymerization method with hydroxyethyl methacrylate/glycidyl methacrylate monomer pair that were covalently interacted with iminodiacetic acid metal chelating agent. The regions showing affinity for lysozyme enzyme were formed by binding with Ni(II) metal ions. The polymeric cryogel was first characterized using Fourier transform infrared spectrophotometer, scanning electron microscopy, thermal gravimetric analysis, X-ray photoelectron spectroscopy and swelling degree test. Then, the effects of pH, concentration, temperature, salt concentration and flow rate on enzyme adsorption capacity were evaluated, and optimum conditions were found. According to the optimization experiments, the maximum adsorption capacity of polymeric cryogel was reported as 11.82 mg/g at pH 7.4 and 25°C with a 0.5 mL/min flow rate and without ionic strength.

Key Words

Enzyme adsorption, immobilized metal affinity chromatograpy, cryogel.

ÖZ

Kriyojeller, donmuş ortamda hazırlanan polimerlerdir ve yeni ayırma matrisleri olarak bu alanda büyük ilgi görmüştür. Süpermakrogözenekliliği, kısa difüzyon yolu, düşük basıncı ve hem adsorpsiyona hem de elüsyona karşı gösterdiği az direnç gibi önemli faydalar sağlamışlardır. Büyük ve bağlı gözenekler polimerik kriyojellere özgün süngersi yapı özelliği kazandırır. İmmobilize metal afinite kromotografisi (IMAC), biyomoleküllerin saflaştırılması için kullanılan standart analitik bir ayırma yöntemidir. Birçok geçiş iyonu elektronca zengin bileşiklerle kararlı kompleksler oluştururlar. Birinci sıra geçiş metal iyonları şelatlayıcı ajanlar üzerinden kompleksleştirilerek IMAC sorbenti elde edilir. Lizozim çeşitli omurgalı hücreleri ve salgılarında bulunan bir enzimdir. Yaygın uygulamaları arasında bakteri hücre içi ürünlerin çıkarılması için bir hücre parçalayıcı madde, oftalmolojide anti-bakteriyel bir madde, süt ürünlerinde bir gıda katkı maddesi, enfeksiyon ve ülser tedavisi için bir ilaç olarak kullanılmaları sayılabilir. Bu çalışmada, hidroksietil metakrilat/glisidil metakrilat monomer çifti ile serbest radikal polimerizasyonu yöntemi ile hazırlanan kriyojel-temelli polimerik malzeme iminodiasetik asit metal şelatlayıcı ajanı ile kovalent olarak etkileştirilmiş ve Ni(II) metal iyonları ile bağlanarak lizozim enzimine afinite gösteren bölgeler oluşturulmuştur. Hazırlanan polimerik kriyojel önce Fourier transform spektrofotometresi, taramalı elektron mikroskopisi, termal gravimetrik analiz, X-ışını fotoelektron spektroskopisi ve şişme derecesi testi ile karakterize edilmiştir. Daha sonra, lizozim adsorplama kapasitesine pH, derişim, sıcaklık, tuz derişimi ve akış hızı etkileri araştırılarak optimum koşullar bulunmuştur. Optimizasyon deneylerine göre, polimerik kriyojelin maksimum adsorpsiyon kapasitesi, pH 7.4'de, 25°C'de, 0.5 mL/dk akış hızında ve iyonik kuvvet olmadan 11.82 mg/g olarak rapor edilmiştir.

Anahtar Kelimeler

Enzim adsorpsiyonu, immobilize metal afinite kromatografisi, kriyojel.

INTRODUCTION

Conventional chromatographic techniques have some restrictions including high pressure drop, reduced flow rate, low prolificacy, and complexities [1]. For overcoming these restrictions, new techniques have been advanced and utilized successively in polymeric forms [2]. Cryogels are supermacroporous polymeric materials prepared at sub-zero Celsius degrees employing a suitable activator/initiator pair [3]. The free-radical polymerization happens in the solvent and frozen monomer solution in the forming sides between the ice crystals. These ice crystals behave as porogen suppliers and a supermacroporous polymer is obtained following the thawing step [4]. They show low pressure drop and high flow rate compared with conventional methods. Moreover, they are low-cost and easy-going materials and have sponge-like forms with high mechanical stability and durability [5,6]. These properties offer distinctive applications to cryogels for several adsorption studies [7-9]. Immobilized metal ion affinity chromatography called as IMAC is a significant analytical technique for various biomolecules [10]. This method contains covalently bonded chelating sides to interact with metals. These metals are utilized for various biomolecules adsorption by coordinative binding features of amino acid sides of proteins [11]. IMAC also has more benefits including high healing yield with usage of non-denaturing desorption condition [12]. Different transition metals can obtain consistent complex with electron-rich compounds and arrange O-, N-, and S-containing molecules via ion-dipole bindings [13]. Metal-ion coordination with biomolecules is well suited for molecular recognition due to its specificity and stability, directing the biomolecules as a mediator to form a stable complex with high selectivity [14]. The tight binding and bond strength can be adjusted by selecting the appropriate metal ion for the biomolecule. The cost-friendly metal ions and ease-regeneration of adsorbents are charming properties of metal-chelate separation [15]. As a biomolecule, lysozyme is a hydrolase enzyme found in body secretions such as saliva, tears, sweat, mucus, and also milk, and egg whites. It cleaves β-1-4 glycosidic bonds, contains 129 amino acids, and weighs 14.4 kDa [16]. Common usage fields include anti-bacterial, anti-viral, anti-tumor, anti-inflammatory, anti-histaminic agent, and antimicrobial agent [17, 18]. High purity needs for therapeutic and natural biomolecules along with pressures to decrease costs have warned more simple, efficient, and less expensive adsorption methods in the last years [19,20].

Here, poly(2-hydroxyethyl methacrylate (HEMA)/glycidyl methacrylate (GMA)) cryogel was prepared with a free-radical polymerization method. The iminodiacetic acid (IDA) was modified to this cryogel as a chelating agent and then Ni(II) ions were incorporated into this cryogel for affinity binding of lysozyme. The cryogel was characterized employing scanning electron microscope (SEM), Fourier transform infrared spectroscopy (FTIR), thermal gravimetric analysis (TGA), X-ray photoelectron spectroscopy (XPS), and swelling degree studies. Following the characterization experiments, optimum lysozyme adsorption conditions (pH, concentration, temperature, salt concentration, and flow rate) were investigated in an aqueous solution. The mathematical calculations were utilized to compare experimental data with theoretical data for clarifying adsorption properties.

MATERIALS and METHODS

Chemicals

2-Hydroxyethyl methacrylate (HEMA), glycidyl methacrylate (GMA), ammonium persulfate (APS), N,N'-methylene bisacrylamide (MBA), N,N,N',N'-tetramethylethylenediamine (TEMED), iminodiacetic acid (IDA), nickel nitrate hexahydrate and lysozyme were acquired from Sigma. Other chemicals were reagent grades and the water utilized in the experiments was purified by Barnstead ROpure LP®.

Preparation of cryogel

The monomer mixture was made ready by mixing 0.283 g of MBA added in 10 mL of H_2O, 1.3 mL of HEMA, and 100 μL of GMA prepared in 3.7 mL of H_2O for preparation of cryogel. After that, 20 mg of APS and 25 μL of TEMED were stirred to this mixture. The final mixture was added into a syringe with a covered outlet. The syringe was kept at -12°C for a one day for free-radical polymerization and thawed at 25°C. Following the washing step for removing the impurities and unreacted monomers, the cryogel was used for the next steps. For the next step, 10 mg/mL of IDA solution (pH 11.0) was covalently modified to the PHEMA-GMA cryogel utilizing a peristaltic pump at 75°C for 6 h. Finally, PHEMA-GMA-IDA cryogel was cleared with CH_3COOH and H_2O to eliminate excess IDA and the pH 4.5 of Ni(II) solution interacted with PHEMA-GMA-IDA cryogel at 25°C for 2 h to chelate Ni(II) ions. The PHEMA cryogel was also prepared as a control polymer by employing same method with no GMA, IDA and Ni(II) ions.

Characterization of cryogel

The characterization experiments of cryogel were performed using SEM (QUANTA 400F Field Emission), XPS (Thermo Fisher Scientific, K-Alpha), TGA (Q500 V20.13), FT-IR (Thermo Fisher Scientific, Nicolet iS10), and swelling degree analysis for the examination of topology, elemental, physical and chemical properties, respectively. The FT-IR spectrum was obtained between 400 cm^{-1} and 4000 cm^{-1} wavenumbers. The surface topology and pore structure of cryogel were examined by SEM analysis. The cryogel was covered with a gold layer before being placed in the sample holder. Thermal stability of cryogel was performed at a heating rate of 10°C/min under N_2 by means of a thermogravimetric analyzer. The elemental property of cryogel was analyzed with XPS. Dried cryogel was attached to the sample holder with copper tapes and vacuumed for 30 min. Following surveying the general elemental map of the composition, the analysis was finalized. Dried cryogel was weighed (W_0) before swelling to determine equilibrium swelling degree of cryogel and then dropped into 10 mL of water and swollen cryogel was weighed (W_{sw}) at regular intervals (0-30 min) and calculated the following equation:

$$Swelling\ degree = \frac{W_0 - W_{sw}}{W_0} x100\%$$

Lysozyme adsorption of cryogel

The benchmarking adsorption of cryogel was performed in accordance with the effects of pH (4.0-8.0), lysozyme concentration (0.05-2.0 mg/mL), temperature (4-45°C), salt concentration (0-1.0 M NaCl) and flow rate (0.25-2.0 mL/min). For adsorption studies, the lysozyme was prepared in 10 mL of pH solutions, and reacted with cryogel using peristaltic pump for 2 h. Following this experiment, the adsorbed lysozyme was desorbed with desorption solution (0.1 M NaCl) for 1 h and cleaned with water for 1 h. The ultraviolet-visible absorbance values of samples were evaluated at 280 nm. The adsorbed lysozyme was calculated following equation:

$$Q = \left(Ci - Cf\right) \times \frac{V}{m}$$

Q is adsorbed lysozyme amount (mg/g), C_i and C_f are first and last lysozyme concentration (mg/mL), V is volume (mL) and m is cryogel mass (g). All adsorption experiments were done three times.

Mathematical calculations

The interaction between lysozyme and cryogel was determined with two adsorption models including Langmuir and Freundlich using experimental data. Langmuir adsorption model interests homogeneous interaction between adsorbed biomolecules and polymers and is defined by equation:

$$\frac{1}{Qeq} = \left[\frac{1}{QmaxbCeq}\right] + \left[\frac{1}{Qmax}\right]$$

Q_{max} and Q_{eq} are maximum and equilibrium adsorbed lysozyme amount (mg/g), C_{eq} is an equilibrium concentration (mg/L), and b is Langmuir constant belongs to adsorption energy. Q_{max} and b can be computed from the slope and intercept of plot of C_{eq} against C_{eq}/Q_{eq}.

The Freundlich adsorption model interests to heterogeneous binding between adsorbed biomolecules and polymers and is described by equation:

$$lnQeq = lnKf + \left(\frac{1}{n}\right) \times lnCeq$$

1/n and K_f are Freundlich mathematical constants belongs to heterogeneity and adsorption capacity and they can be computed from the slope and intercept of plot of lnQ_{eq} against lnC_{eq}.

RESULTS and DISCUSSION

Characterization of cryogel

The cryogels were characterized using SEM, XPS, TGA, FT-IR, and swelling degree analysis for examination of topology, elemental, physical, and chemical properties, respectively. The surface morphologies of cryogels were investigated at several magnifications via SEM analysis (Figure 1). It could be noticed that the cryogels had supermacroporous structures and the pore size was highly bigger than size of lysozyme, letting it to penetrate simply. The existence of channels with a diameter (around 50-100 μm) was obtained in the voids of dense thick polymeric walls. Moreover, the roughness difference between the PHEMA and PHEMA-GMA-IDA cryogels showed that the modification was successfully accomplished in the polymer structure [21].
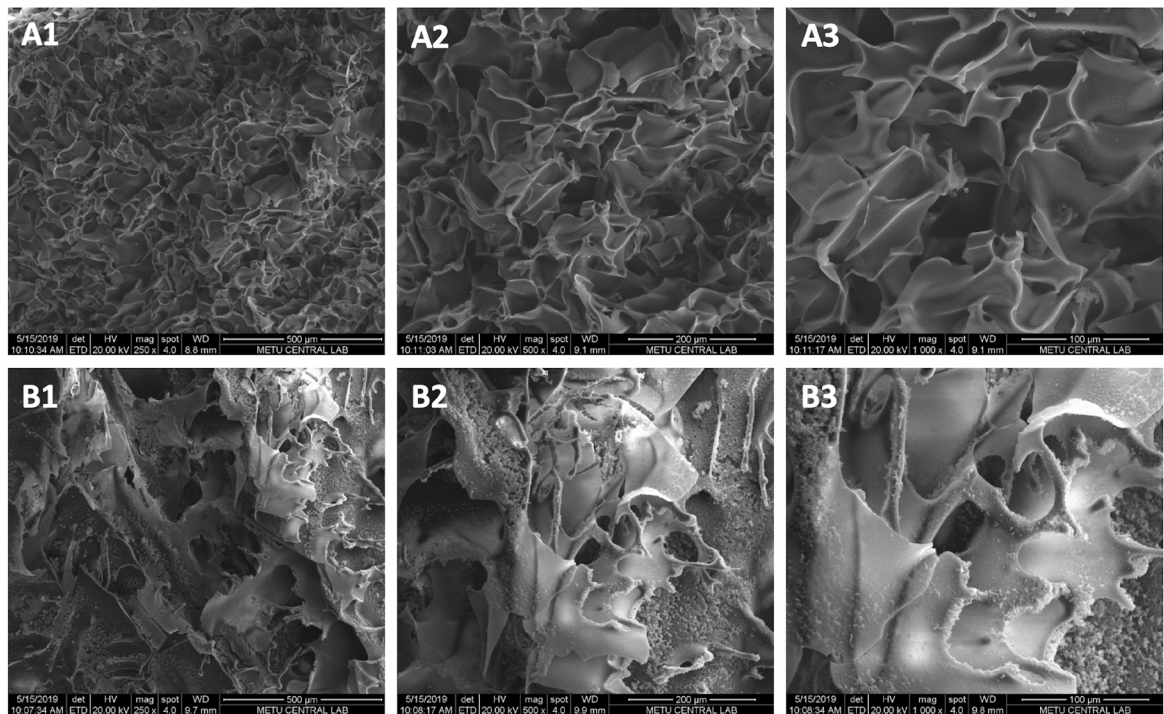
Figure 1. SEM images of PHEMA (A1-A3) and PHEMA-GMA-IDA (B1-B3) cryogels.

As depicted in Figure 2, the peaks belonging to functional groups were observed in the XPS spectra of the C, O, and N elements of the PHEMA-GMA-IDA cryogel. The corresponding chemical groups along with their binding energies (eV) were stated on the plots. Briefly, the presence of C=O was observed at 288.29 eV and 533.46 eV from carbon and oxygen data. The shoulder on the main peak at 286.25 eV and 532.18 eV correlated with the C-O groups in the cryogel [22].

The thermal stability of PHEMA-GMA-IDA cryogel was tested with TGA analysis (Figure 3A). TGA spectra result showed that cryogel lost only 3.6% of water and impurities up to 200°C and the sharp mass loss between 300-500°C was due to the breakdown of bonds in cryogel. Furthermore, it was observed that 4.0-4.7% mass of PHEMA-GMA-IDA cryogel was preserved at 800°C [23]. FT-IR spectrum of
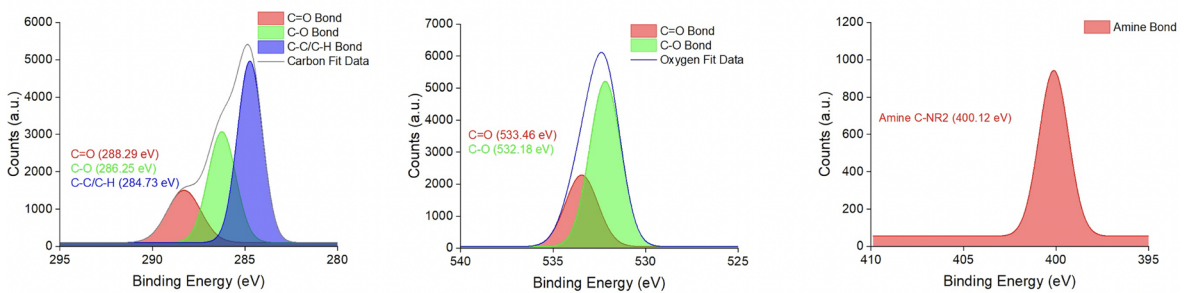
Figure 2. XPS spectra of PHEMA-GMA-IDA cryogel.
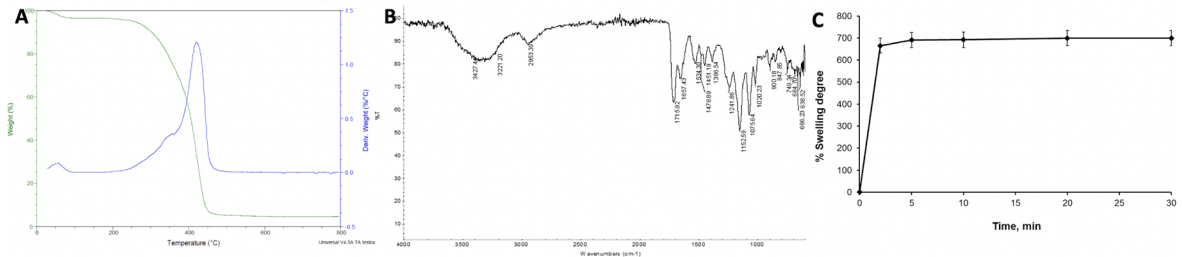
Figure 3. TGA (A) FT-IR (B) spectrum and swelling degree (C) of PHEMA-GMA-IDA cryogel.

PHEMA-GMA-IDA cryogel was demonstrated in Figure 3B. According to the spectra, the characteristic peaks of cryogel were broad peaks from 3200 to 3500 cm^{-1} designing to OH stretching, the peaks at 2953 cm^{-1} and 3221 cm^{-1} designing to CH and CH$_3$ stretchings. A peak at 1716 cm^{-1} indicated C=O configuration of HEMA and GMA. The C-O stretching of the carbonyl showed up at 1240 cm^{-1}. In addition, 1076 cm^{-1} was belonged to C-N functional group and the peak of the epoxy, C-O-C weakened at 900 cm^{-1} and 750 cm^{-1} that indicating the presence of IDA in the cryogel [24]. Finally, %swelling degree of PHEMA-GMA-IDA was calculated as 714.1g H$_2$O/g cryogel, respectively. It was observed that PHEMA-GMA-IDA cryogel began to swell in a short time (2 min) and after 10 min, its water holding capacity was stabilized (Figure 3C) [25].

Lysozyme adsorption of cryogel

The optimum parameters effects were carried out for evaluating the performance of PHEMA-GMA-IDA cryogel for the calculation of lysozyme adsorption capacity values. The pH effect on the adsorbed lysozyme was examined using several buffers (pH 4.0, 5.0, 6.0, 7.0, 7.4, and 8.0) including 0.5 mg/mL of lysozyme at 25°C without ionic strength (I.S.) at a 0.5 mL/min flow rate (F.R.). As Figure 4A demonstrated the maximum adsorbed lysozyme capacity was obtained at pH 7.4. The isoelectric point of lysozyme molecule is around pH 11.0, it carries a net negative charge at a pH above its pI owing to the surface-accessible amino acid residues. Thus, the PHEMA-GMA-IDA cryogel was simply electrostatically bonded lysozyme with at this pH [26].
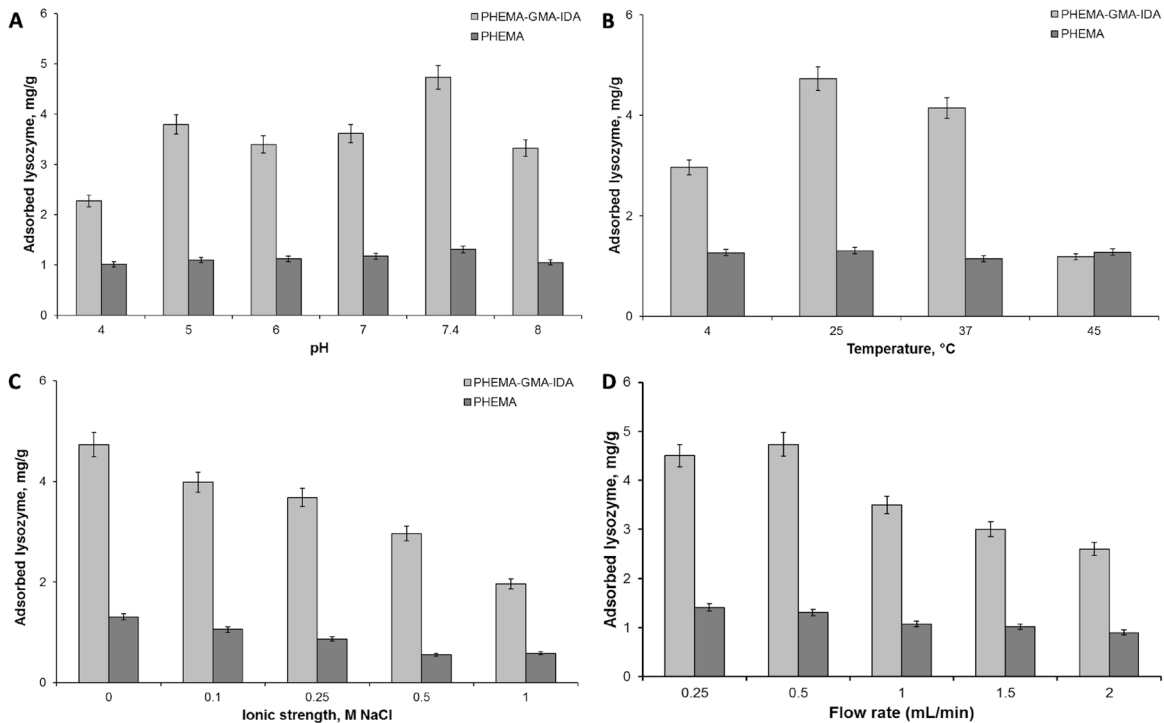
Figure 4. pH (A), temperature (B), ionic strength (C) and flow rate (D) effects on the adsorbed lysozyme. The adsorption experiments conditions: (A): C$_{lysozyme}$=0.5 mg/mL, T=25°C, I.S.=0 M, F.R.= 0.5 mL/min (B): C$_{lysozyme}$=0.5 mg/mL, pH 7.4, I.S.=0 M, F.R.= 0.5 mL/min, (C): C$_{lysozyme}$=0.5 mg/mL, pH 7.4, T=25°C, F.R.= 0.5 mL/min, (D): C$_{lysozyme}$=0.5 mg/mL, pH 7.4, T=25°C, I.S.=0 M.

The relation between adsorbed lysozyme and temperature provided significant information to appoint the interaction. As depicted in Figure 4B, several temperatures (4°C, 25°C, 37°C, and 45°C) were investigated with 0.5 mg/mL of lysozyme sample solutions at pH 7.4 without I.S. at a 0.5 mL/min F.R. The maximum adsorbed lysozyme amount was noticed at 25°C. As the bindings between lysozyme and PHEMA-GMA-IDA cryogel started to decline as temperature rise continued, the adsorbed lysozyme amount also reduced. The adsorption on IMAC supported an effect of electrostatic, hydrophobic, and/or donor-acceptor interactions [27]. Moreover, the I.S. effect (0.1 M NaCl, 0.25 M NaCl, 0.5 M NaCl and 1.0 M NaCl) on lysozyme adsorption was assessed with 0.5 mg/mL of lysozyme sample solutions at pH 7.4 at 25°C with a 0.5 mL/min F.R. Increment of the amount of NaCl followed in the adsorbed lysozyme reduction due to the bonds weakening between lysozyme and PHEMA-GMA-IDA cryogel. The NaCl molecules may react with lysozyme using electrostatic interactions and prevent the binding sites [28] (Figure 4C). Finally, the interaction between lysozyme and PHEMA-GMA-IDA cryogel varied at several F.R. As observed in Figure 4D, the maximum lysozyme adsorption was found at a 0.5 mL/min F.R. At higher rates, the lysozyme and PHEMA-GMA-IDA cryogel could not interact each other [29].

Mathematical calculations

The PHEMA-GMA-IDA cryogel interacted with lysozyme samples with different concentrations (0.05 mg/mL, 0.1 mg/mL, 0.25 mg/mL, 0.5 mg/mL, 0.75 mg/mL, 1.0 mg/mL, 1.5 mg/mL and 2.0 mg/mL) at pH 7.4 and 25°C with a 0.5 mL/min F.R. and no I.S. The adsorbed lysozyme amount increased with concentration increment (Figure 5A). It was observed that the PHEMA-GMA-IDA cryogel showed a high lysozyme capacity owing to binding sites being well-fitted with lysozyme [30]. The maximum adsorbed lysozyme amount was obtained as 11.82 mg/g for PHEMA-GMA-IDA cryogel. But, the PHEMA cryogel had only 2.19 mg/g adsorption capacity because of the non-specific interactions. It was also concluded from these results that affinity of lysozyme to the cryogel was increased specifically with attachment of IDA and Ni(II). The adsorption type of PHEMA-GMA-IDA cryogel was estimated by Langmuir and Freundlich models (Figure 5B, Figure 5C, Figure 5D, and Table 1). In accordance with the mathematical calculations, the regression coefficients (R^2 = 0.9911 for Langmuir, R^2 = 0.9867 for Freundlich) and the maximum adsorbed lysozyme amounts (Q_{max} = 12.86 mg/g for Langmuir, Q_{max} = 30.14 mg/g for Freundlich) were compared and noticed that the interaction between lysozyme and PHEMA-GMA-IDA cryogel was coherent with Langmuir adsorption mo-
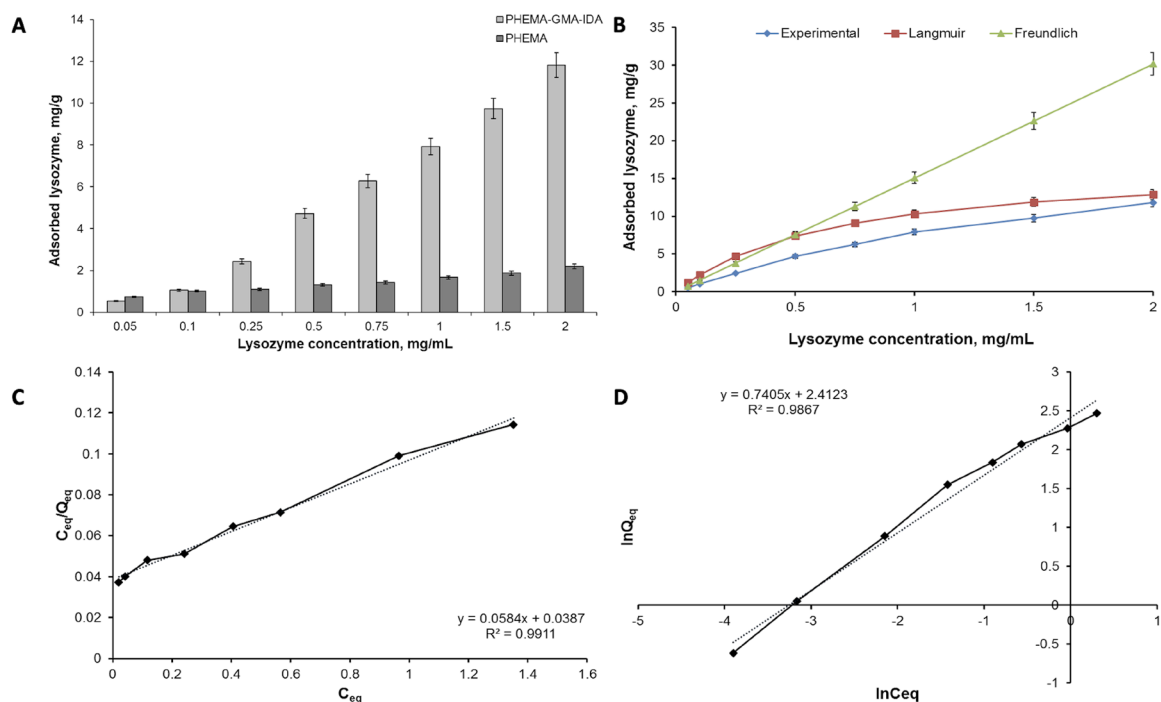
Figure 5. The effect of concentration on the adsorbed lysozyme (A), comparison experimental results with adsorption models (B), Langmuir (C) and Freundlich (D) models. The adsorption experiments conditions: pH 7.4, T=25°C, I.S.=0 M, F.R.= 0.5 mL/min.

Table 1. Adsorption model coefficients.

Langmuir				Freundlich		
Q_{eq} (mg/g)	Q_{max} (mg/g)	b (mL/mg)	R^2	Kf	1/n	R^2
11.82	12.84	1.5	0.9911	11.16	1.35	0.9867

Table 2. Comparing polymers in terms of the metal type, interaction, polymer, target, and adsorption capacity.

References	Metal	Interaction	Polymer	Target	Capacity
[32]	Cu^{2+}	PHEMA-IDA	Magnetic beads	Human serum albumin	28.4 mg/g
[33]	Cu^{2+}	PHEMA-MAH	Beads	Cytochrome c	31.7 mg/g
[34]	Cu^{2+}	PGMA-IDA	Beads	Immunoglobulin G	171.2 mg/g
[35]	Cu^{2+}	PHEMA-GMA-IDA	Bead-embedded cryogel	Immunoglobulin G	257 mg/g
[36]	Cu^{2+}	PGMA-IDA	Beads	Hemoglobin	130.3 mg/g
[37]	Ni^{2+}	PHEMA-GMA-IDA	Cryogel	Urease	11.30 mg/g
[38]	Zn^{2+}	PHEMA-GMA-IDA	Cryogel	Yeast alcohol dehydrogenase	9.94 mg/g
[39]	Cu^{2+}	PGMA-IDA	Magnetic beads	Human serum albumin	37.7 mg/g
[40]	Fe^{3+}	PAAm-GMA-IDA	Cryogel	Catalase	12.99 mg/g
This study	Ni^{2+}	PHEMA-GMA-IDA	Cryogel	Lysozyme	11.82 mg/g

del which referred the interaction type was monolayer, homogeneous, and binding sites had similar affinity for lysozyme. So, lysozyme reached to the interaction sites with no diffusion problems [31].

CONCLUSION

In this study, the preparation of PHEMA-GMA-IDA cryogel for the efficient adsorption of lysozyme was reported. The PHEMA-GMA-IDA cryogel was synthesized using free-radical polymerization and then modified for IMAC technology to create binding sites for lysozyme. This simple, stable, and low-priced preparation and adsorption process can be more distant used for various polymers-based systems for purification, separation, adsorption and sensor applications. Other polymers-based systems were summarized in Table 2 to compare the polymers in terms of the metal type, interaction, target, and adsorption capacity. As compared with existing polymer-based systems, this study was described for the first time and carries great potency for enzyme adsorption. Furthermore, this work demonstrates an adaptable method which can be distributed to the other biomolecules separation and adsorption and supplies a novel platform to synthesize new-generation biomaterial.

R e f e r e n c e s

1. J. Thömmes, M. Etzel, Alternatives to chromatographic separations, Biotechnol. Prog., 23 (2007) 42-45.

2. Y. Saylan, A. Denizli, Supermacroporous composite cryogels in biomedical applications, Gels, 5 (2019) 20.

3. M. Andaç, I.Y. Galaev, A. Denizli, Affinity based and molecularly imprinted cryogels: Applications in biomacromolecule purification, J. Chromatogr. B, 1021 (2016) 69-80.

4. V.I. Lozinsky, Cryostructuring of polymeric systems. 50.† cryogels and cryotropic gel-formation: Terms and definitions, Gels, 4 (2018) 77-89.

5. S. Akgönüllü, H. Yavuz, A. Denizli, Preparation of imprinted cryogel cartridge for chiral separation of l-phenylalanine, Artif. Cell. Nanomed. Biotechnol., 45 (2017) 800-807.

6. G.C. Ingavle, L.W.J. Baillie, Y. Zheng, E.K. Lis, I.N. Savina, C.A. Howell, S.V. Mikhalovsky, S.R. Sandeman, Affinity binding of antibodies to supermacroporous cryogel adsorbents with immobilized protein A for removal of anthrax toxin protective antigen, Biomaterials, 50 (2015) 140-153.

7. K. Çetin, A. Denizli, 5-Fluorouracil delivery from metal-ion mediated molecularly imprinted cryogel discs, Coll. Surf. B, 126 (2015) 401-406.

8. C.Y. Kuo, C.H. Chen, C.Y. Hsiao, J.P. Chen, Incorporation of chitosan in biomimetic gelatin/chondroitin-6-sulfate/hyaluronan cryogel for cartilage tissue engineering, Carbohydr. Polym., 117 (2015) 722-730.

9. N.K. Singh, R.N. Dsouza, M. Grasselli, M. Fernández-Lahore, High capacity cryogel-type adsorbents for protein purification, J. Chromatogr. A, 1355 (2014) 143-148.

10. J. Porath, Immobilized metal ion affinity chromatography, Protein Expr. Purif., 3 (1992) 263-281.

11. E.K.M. Ueda, P.W. Gout, L. Morganti, Current and prospective applications of metal ion-protein binding, J. Chromatogr. A, 988 (2003) 1-23.

12. N. Tüzmen, T. Kalburcu, A. Denizli, Immobilization of catalase via adsorption onto metal-chelated affinity cryogels, Process Biochem. 47 (2012) 26-33.

13. S. Mallik, R.D. Johnson, F.H. Arnold, Selective recognition of bis-imidazoles by complementary bis-metal ion complexes, JACS, 115 (1993) 2518-2520.

14. A. Denizli, Purification of antibodies by affinity chromatography, Hacettepe J. Biol. Chem., 39 (2011) 1-18.

15. E. Tamahkar, A. Denizli, Metal ion coordination interactions for biomolecule recognition: a review, Hittite J. Sci. Eng., 1 (2014) 21-26.

16. N. Bereli, Y. Saylan, L. Uzun, R. Say, A. Denizli, L-histidine imprinted supermacroporous cryogels for protein recognition, Sep. Purif. Technol., 82 (2011) 28-35.

17. Y. Saylan, E. Tamahkar, A. Denizli, Recognition of lysozyme using surface imprinted bacterial cellulose nanofibers, J. Biomater. Sci. Polym. Ed., 28 (2017) 1950-1965.

18. A. Vasilescu, Q. Wang, M. Li, R. Boukherroub, S. Szunerits, Aptamer-based electrochemical sensing of lysozyme, Chemosensors, 4 (2016) 10-30.

19. Y. Saylan, F. Yılmaz, A. Derazshamshir, E. Yılmaz, A. Denizli, Synthesis of hydrophobic nanoparticles for real-time lysozyme detection using surface plasmon resonance sensor, J. Mol. Recog., 30 (2017) e2631.

20. C. Ocana, A. Hayat, R.K. Mishra, A. Vasilescu, M. del Valle, J.L. Marty, Label free aptasensor for lysozyme detection: a comparison of the analytical performance of two aptamers, Bioelectrochem., 105 (2015) 72-77.

21. G. Öztürk, Y. Saylan, A. Denizli, Designing composite cryogel carriers for tyrosine adsorption, Sep. Purif. Technol., 254 (2021) 117622.

22. A. Baimenov, D. Berillo, S. Azat, T. Nurgozhin, V. Inglezakis, Removal of Cd^{2+} from water by use of super-macroporous cryogels and comparison to commercial adsorbents, Polymers, 12 (2020) 2405.

23. B. Wan, J. Li, F. Ma, N. Yu, W. Zhang, L. Jiang, H. Wei, Preparation and properties of cryogel based on poly(2-hydroxyethyl methacrylate-co-glycidyl methacrylate), Langmuir, 35 (2019) 3284-3294.

24. R.H. Şenay, S.M Gökalp, E. Türker, E. Feyzioğlu, A. Aslan, S. Akgöl, A new morphological approach for removing acid dye from leather waste water: Preparation and characterization of metalchelated spherical particulated membranes (SPMs), J. Environ. Manage., 151 (2015) 295-302.

25. E. Yeşilova, B. Osman, A. Kara, E. Tümay Özer, Molecularly imprinted particle embedded composite cryogel for selective tetracycline adsorption, Sep. Purif. Technol., 200 (2018) 155-163.

26. T. Matsunaga, T. Hishiya, T. Takeuchi. Surface plasmon resonance sensor for lysozyme based on molecularly imprinted thin films, Anal Chim Acta., 591 (2007) 63-67.

27. S. Öztürk, N. Demir, Development of a novel IMAC sorbent for the identification of melamine in dairy products by HPLC, J. Food Compos. Anal., 100 (2021) 103931.

28. I. Göktürk, I. Perçin, A. Denizli, Catalase purification from rat liver with iron-chelated poly(hydroxyethyl methacrylate-N-methacryloyl-(l)-glutamic acid) cryogel discs, Prep. Biochem. Biotechnol., 46 (2016) 602-609.

29. Y. Saylan, N. Bereli, L. Uzun, A. Denizli, Monolithic boronate affinity columns for IgG separation, Sep. Sci. Technol., 49 (2014) 1555-1565.

30. Y. Saylan, L. Uzun, A. Denizli, Alanine functionalized magnetic nanoparticles for reversible amyloglucosidase immobilization, Ind. Eng. Chem. Res., 54 (2015) 454-461.

31. F. Inci, Y. Saylan, A.M. Kojouri, M.G. Ogut, A. Denizli, U. Demirci, A disposable microfluidic-integrated hand-held plasmonic platform for protein detection, Appl. Mat. Today, 18 (2020) 100478.

32. M. Odabaşı, L. Uzun, A. Denizli, Porous magnetic chelator support for albumin adsorption by ımmobilized metal affinity separation, J. Appl. Polym. Sci., 93 (2004) 2501-2510.

33. S. Emir, R. Say, H. Yavuz, A. Denizli, A new metal chelate affinity adsorbent for cytochrome c. Biotechnol. Prog., 20 (2004) 223-228.

34. E.B. Altıntaş, N. Tüzmen, L. Uzun, A. Denizli, Immobilized metal affinity adsorption for antibody depletion from human serum with monosize beads, Ind. Eng. Chem. Res., 46 (2007) 7802-7810.

35. N. Bereli, G. Şener, E. B. Altıntaş, H. Yavuz, A. Denizli, Poly(glycidyl methacrylate) beads embedded cryogels for pseudo-specific affinity depletion of albumin and immunoglobulin G, Mat. Sci. Eng. C, 30 (2010) 323-329.

36. E.B. Altıntas, D. Türkmen, V. Karakoç, A. Denizli, Hemoglobin binding from human blood hemolysate with poly(glycidyl methacrylate) beads, Coll. Surf. B Bioint., 85 (2011) 235-240.

37. M. Uygun, B. Akduman, S. Akgöl, A. Denizli, A new metal-chelated cryogel for reversible ımmobilization of urease, Appl. Biochem. Biotechnol., 170 (2013) 1815-1826.

38. B. Akduman, M. Uygun, D. Aktaş Uygun, S. Akgöl, A. Denizli, Purification of yeast alcohol dehydrogenase by using immobilized metal affinity cryogels, Mat. Sci. Eng. C, 33 (2013) 4842-4848.

39. F. Kartal, A. Denizli, Surface molecularly imprinted magnetic microspheres for the recognition of albumin, J. Sep. Sci., 37 (2014) 2077-2086.

40. D. Aktaş Uygun, M. Uygun, S. Akgöl, A. Denizli, Reversible adsorption of catalase onto Fe^{3+} chelated poly(AAm-GMA)-IDA cryogels. Mat. Sci. Eng. C, 50 (2015) 379-385.